

**FUSED & BRIDGED EXPANDED PORPHYRINS AND
EXPANDED CALIXPHYRIN: STRUCTURAL DIVERSITY AND
RECEPTOR PROPERTY**

By

G. KARTHIK
(CHEM07201004005)

National Institute of Science Education and Research
(NISER-Institute of Physics)
Bhubaneswar

*A thesis submitted to the
Board of Studies in Chemical Sciences
In partial fulfillment of requirements
For the Degree of*

DOCTOR OF PHILOSOPHY

of

HOMI BHABHA NATIONAL INSTITUTE



January, 2014

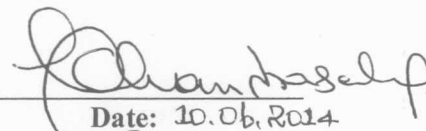
Thesis Title :

Homi Bhabha National Institute¹

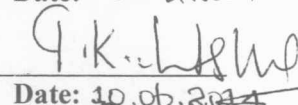
Recommendations of the Viva Voce Committee

As members of the Viva Voce Committee, we certify that we have read the dissertation prepared by <Candidate Name> entitled <" Title" > and recommend that it may be accepted as fulfilling the thesis requirement for the award of Degree of Doctor of Philosophy.

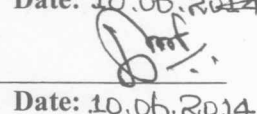
Prof. V. CHANDRASEKHAR
Chairman - <Name>


Date: 10.06.2014

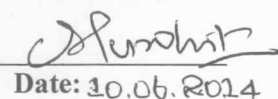
Prof. T.K. CHANDRASHEKHAR
Guide / Convener - <Name>


Date: 10.06.2014

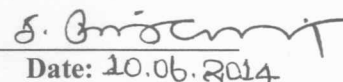
Prof. A. SRINIVASAN
Co-guide - <Name> (if any)


Date: 10.06.2014

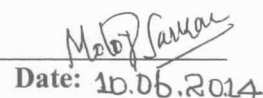
Dr. C. S. PURDHIT
Member 1 - <Name>


Date: 10.06.2014

Dr. S. PERUNCHERALATHAN
Member 2 - <Name>


Date: 10.06.2014

Dr. MOLLOY SARKAR
Member N - <Name>


Date: 10.06.2014

Final approval and acceptance of this thesis is contingent upon the candidate's submission of the final copies of the thesis to HBNI.

I/We hereby certify that I/we have read this thesis prepared under my/our direction and recommend that it may be accepted as fulfilling the thesis requirement.

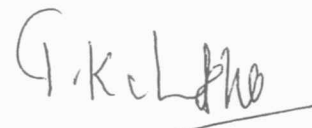
Date: 10.06.2014



<Signature>

Co-guide (if applicable)

Place: NISER,
BHUBANESWAR



<Signature>

Guide

¹ This page is to be included only for final submission after successful completion of viva voce.

STATEMENT BY AUTHOR

This dissertation has been submitted in partial fulfillment of requirements for an advanced degree at Homi Bhabha National Institute (HBNI) and is deposited in the Library to be made available to borrowers under rules of the HBNI.

Brief quotations from this dissertation are allowable without special permission, provided that accurate acknowledgement of source is made. Requests for permission for extended quotation from or reproduction of this manuscript in whole or in part may be granted by the Competent Authority of HBNI when in his or her judgment the proposed use of the material is in the interests of scholarship. In all other instances, however, permission must be obtained from the author.



(G. Karthik)

DECLARATION

I, hereby declare that the investigation presented in the thesis has been carried out by me. The work is original and has not been submitted earlier as a whole or in part for a degree / diploma at this or any other Institution / University.



(G. Karthik)

LIST OF PUBLICATIONS ARISING FROM THE THESIS

Journal

1. Core-Modified meso-Aryl Hexaphyrins with an Internal Thiophene Bridge: Structure, Aromaticity, and Photodynamics, **G. Karthik**, M. Sneha, V. P. Raja, J. M. Lim, D. Kim, A. Srinivasan, T. K. Chandrashekar, *Chem. Eur. J.* **2013**, *19*, 1886 – 1890.
2. Calix[2]thia[4]phyrin: An Expanded Calixphyrin with Aggregation-Induced Enhanced Emission and Anion Receptor Properties, **G. Karthik**, P. V. Krushna, A. Srinivasan, and T. K. Chandrashekar, *J. Org. Chem.* **2013**, *78*, 8496–8501.
3. Conformational Change from a Twisted Figure-Eight to an Open Extended Structure in Doubly Fused 36π Core-Modified Octaphyrins Triggered by Protonation: Implication on Photodynamics and Aromaticity, **G. Karthik**, J. M. Lim, A. Srinivasan, C. H. Suresh, D. Kim, T. K. Chandrashekar, *Chem. Eur. J.* **2013**, *19*, 17011-17019.
4. Photophysical Properties of Thiophene Bridged Core-modified expanded Porphyrins, J. M. Lim, **G. Karthik**, A. Srinivasan, T. K. Chandrashekar, D. Kim. *Chem. Commun.* **2014**, *50*, 4358-4361.
5. Meso-Aryl Core-Modified Fused Sapphyrins: Syntheses and Structural Diversity, **G. Karthik**, A. Srinivasan, T. K. Chandrashekar, *Org. Lett.* **2014**, DOI:10.1021/ol501395t

Conferences

1. Poster Presentation: Fused and Bridged Expanded Porphyrins for NLO applications at Chemical Research Society of India (CRSI), Feb 4-6, 2011, conducted by NISER-Bhubaneswar.
2. Oral Presentation: Fused and Bridged Expanded Porphyrins at Chemistry Research Scholars Meet-2011, IGCAR-DAE, Kalpakkam, Chennai.



(G. Karthik)

DEDICATIONS

To my parents.....

Acknowledgements

I am extremely thankful to my thesis supervisor **Prof. T. K. Chandrashekar**, for his valuable guidance, constant support, encouragement, motivation and sincere interest throughout my entire Ph.D. I am highly obliged to him for his constructive criticism, valuable suggestions and sharing his abundance of knowledge with me.

I would like to give special thanks to my thesis co-supervisor, **Prof. A. Srinivasan**, for his guidance and his valuable advice at all times. This work might not have been possible without his encouragement and support.

I would like to thank my thesis monitoring committee members Dr. S. Peruncheralathan and Dr. C. S. Purohit and also for useful discussion on organic reactions and crystallography respectively.

I would like to thank Dr. V. Krishnan & Dr. Arun kumar for solving the X-Ray crystal structures, Dr. Arindam Ghosh for useful discussion on NMR analysis and Dr. U. Lourderaj & Dr. H. Biswal for useful discussion on Theoretical studies.

I wish to express my gratitude to Prof. Dongho Kim and his group members Dr. Jong Min Lim and Won-Young Cha, Yonsei University, Korea for their timely help in photophysical studies described in this thesis.

I would like to extend my gratitude to Mr. Deepak, Mr. Sanjaya, Mr. Amit and Mr. Rajkumar for recording the single crystal X-Ray, NMR and Mass spectral analysis.

I thank all my teachers who taught throughout my academic life for raising me to this position. I am greatly indebted to Prof. A. Ilangovan and Dr. R. Ganesh Kumar, Bharathidasan University, Trichy for their help and encouragement during my early part of my career.

I would like to thank my labmates Dr. Arvind, Arindham, Rishab, Kushboo and friends.

I wish to thank my family members for their continuous support and encouragement. One and above all, I thank almighty for showing me right direction in my life.



G. Karthik

Contents

	<u>Page No.</u>
Synopsis	01
List of Figures / Tables	14
List of Abbreviations	20
Chapter 1: General Introduction	21
Chapter 2: General experimental methods and techniques	53
Chapter 3: Core-modified Bridged Expanded porphyrins	71
Chapter 4: Core-modified Fused Expanded porphyrins	116
Chapter 5: Calix[2]thia[4]pyrin: An expanded calixphyrin with AIEE and anion receptor properties	157
References	183



Homi Bhabha National Institute

Ph. D. PROGRAMME

- 1. Name of the Student** : G. KARTHIK
- 2. Name of the Constituent Institution** : Institute of Physics-
National Institute of Science Education and
Research (NISER),
Bhubaneswar, Odisha
- 3. Enrolment No.** : CHEM07201004005
- 4. Title of the Thesis** : Fused & Bridged Expanded Porphyrins and
Expanded Calixphyrin: Structural Diversity
and Receptor Property
- 5. Board of Studies** : Chemical Sciences

SYNOPSIS

1. Introduction

Porphyrins are ubiquitous molecule in nature and have been referred as “pigments of life.” It consists of four pyrrole rings connected by four methine carbon bridges, has 18π electrons in conjugation and considered as Hückel aromatic molecule. These heterocyclic macromolecules are classified depending on the number of π -electrons, *meso*-bridges, type of heterocyclic rings, connectivity, etc into normal, expanded, N-confused, inverted, fused and bridged derivatives [1-8]. In recent years, research on expanded porphyrins and its core-modified derivatives received much attention due to their diverse applications as new-generation organic nonlinear optical (NLO) materials [9], photosensitizers for photodynamic therapy (PDT) [10,11], anion, cation and neutral substrate receptors [12-13], and magnetic resonance imaging (MRI) contrasting agents [14].

2. Organization of the thesis

This thesis is mainly divided into five chapters and a brief description of each chapter is discussed below:

Chapter 1: General introduction

Chapter 2: General experimental methods and techniques

Chapter 3: Core-modified bridged expanded porphyrins

Chapter 4: Core-modified fused expanded porphyrins

Chapter 5: Calix[2]thia[4]pyrin: An expanded calixpyrin with AIEE and anion receptor properties

Chapter 1: General introduction

This chapter mainly focuses on brief introduction about the porphyrin derivatives in general and expanded porphyrins in particular. The first expanded porphyrin, sapphyrin, was serendipitously synthesized by Woodward and co-workers. However, the efficient synthetic

methodology was reported by Vogel and Sessler groups [1,15]. Vogel and co-workers have demonstrated the synthesis of range of octaphyrin analogues, while Sessler and co-workers have mainly focused on the rational synthesis of 22π sapphyrin, 26π rubyrin, 24π rosarin, amethyrin, 28π heptaphyrin and 40π turcasarin by using stable precursors and were reported in good yields [15]. They have reported not only developing efficient synthetic methods and also stable building blocks, such as, tripyrromethanes, dipyrromethanes and quaterpyrroles required for the synthesis of expanded porphyrins in simple and efficient way. These derivatives have large red-shifted absorption spectrum, multi-metal coordination site, ability to adopt various conformations and increased number of π -electrons in its conjugation pathway [1,9,15].

The extended π -electron conjugation promotes the expanded porphyrins for diverse applications. However, upon increasing the macrocycle size with more than six heterocyclic rings lead to deviate from planarity both in solution as well as in the solid state, and as a result, the delocalization of π -electrons along the molecular framework is not smooth. Hence, the larger expanded porphyrins with distorted topologies exhibit; (a) broad and ill-defined Soret band absorption spectra without Q-band or very weak bands, (b) low singlet and triplet excited state lifetime and (c) low NLO coefficient [9]. Considering the demerits, the overall molecular structure is an important factor to determine the electronic structures of expanded porphyrins by the extent of π -conjugation, the control of molecular topology is foremost important and relevant for understanding the molecular structure-property relationship in expanded porphyrins.⁹

It is obvious that topology control become one of the important solutions for maintaining the planarity and aromaticity in expanded porphyrin. Various attempts have been made to rigidify the expanded porphyrins such as metal coordination, temperature control, solvent change, protonation with appropriate acids, and functional group modifications [2-9]. However, only recently, the fused and bridged strategies to control the topology and retain

the planarity become an interesting topic, which does not alter the porphyrin intrinsic properties. Such expanded porphyrin analogues which are known in the literature is mainly discussed in this chapter. later part of this chapter highlights the syntheses of various normal and expanded calixphyrins and its important properties [16-18].

Chapter 2: General experimental methods and techniques

This chapter describes the detailed experimental procedure for the important precursors used in this thesis and experimental techniques used for characterization of the compounds. In general, we have used dithienothiophene (DTT) as one of the building blocks for the synthesis of bridged and fused expanded porphyrin. DTT has many advantages than other fused precursors, such as rigid core, electron donor, easy modification, etc. Other precursors required for the synthesis of macrocycle such as heterocyclic-diol, dithienothiophene and its derivative and tripyrrmethane (Chart 1) are also discussed in this chapter.

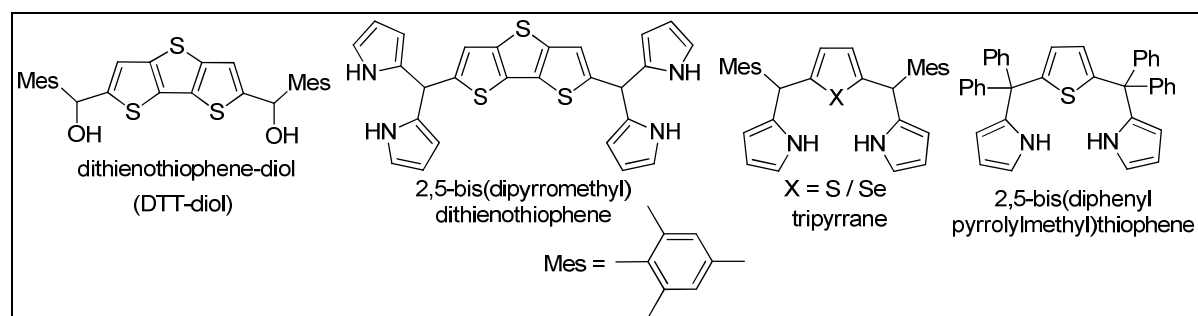


Chart 1. Precursors for the synthesis of expanded porphyrins and calixphyrin

Chapter 3: Core-modified Bridged Expanded porphyrins

This chapter describes the syntheses of two new internally heterocycle bridged expanded porphyrin derivatives, their structural and photodynamic properties. The internally *meso* thiophene-bridged core-modified hexaphyrins **1** and **2** (Chart 2) were synthesized by acid-catalyzed condensation of tripyrrane and thiophene-dialdehyde followed by oxidation with 2,3-dichloro-5,6-dicyano-1,4-benzoquinone (DDQ) in 10-12% yield. The synthetic methodology adopted here is simple and straight-forward. All the compounds were

characterized by ESI-mass spectrometry, electronic absorption spectroscopic studies, NMR and single crystal X-ray diffraction analysis.

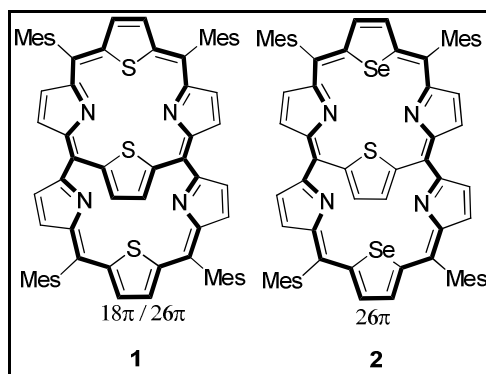


Chart 2. Thiophene bridged hexaphyrins

Interestingly, depending on the heteroatom present in the core such as Sulfur or Selenium atom, the participation of bridging thiophene ring in the π -electron conjugation pathway are different. Further, these bridged hexaphyrins exhibits the hybrid aromatic character which was revealed by spectroscopic studies. The structural analyses further confirm that the hexaphyrin macrocycle was planar and aromatic and that the internal bridging thiophene ring deviates from the mean plane of *meso* carbon atoms. For **1**, the deviation is 49° , while it is 73° for **2** (Figure 1). Compound **2** exhibits the expected 26π hexaphyrin electron conjugation, while the conjugation pathway for **1** has a hybrid character with contributions from both the 18π porphyrin-like skeleton and 26π hexaphyrin skeleton in the free-base form.

A comparison of structures of bridged hexaphyrins **1** and **2** with the corresponding hexaphyrins without an internal bridge (Figure 2) reveal the following; (a) introduction of internal bridging group makes the hexaphyrin skeleton rigid, thus preventing ring inversion of heterocyclic ring; and (b) the hexaphyrin skeleton in the bridged structure are more planar, thus facilitating better π conjugation pathway and therefore increasing the aromaticity.

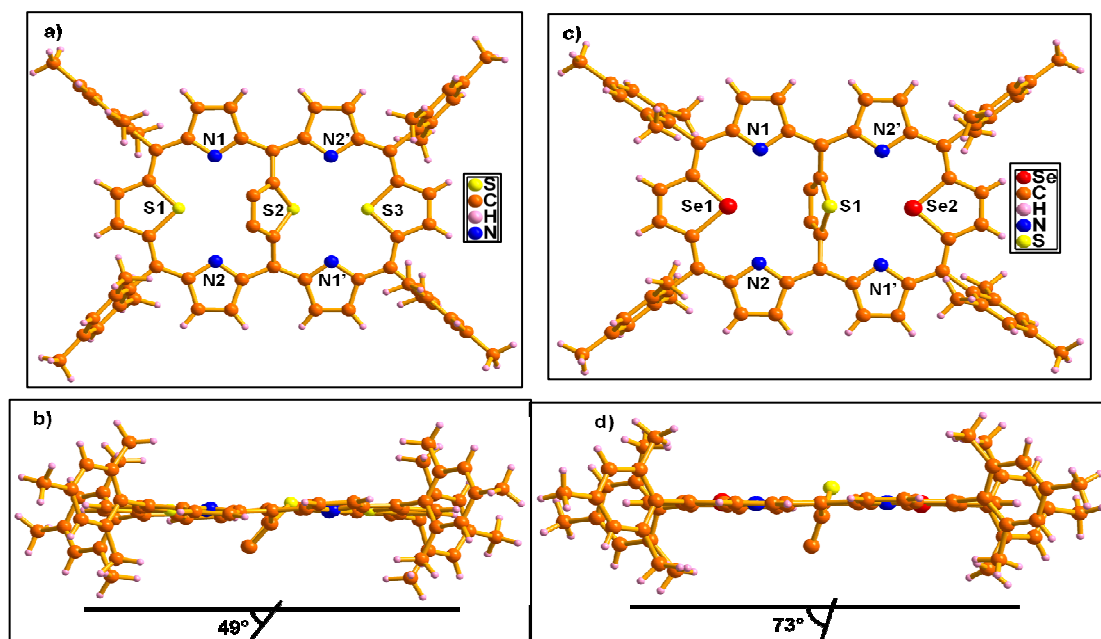


Figure 1. Single crystal X-ray structure of **1** (a & b) and **2** (c & d)

Such structural modifications lead to change in the electronic structure, which are important from the point of view of their application as NLO materials. The preliminary photophysical studies reveal an increase of singlet lifetime by two times upon introduction of bridge, which is presumably due to increased rigidity of the macrocycle. Overall, the present work demonstrated the first example of core-modified analogues of internally bridged expanded porphyrins with dual aromatic character.

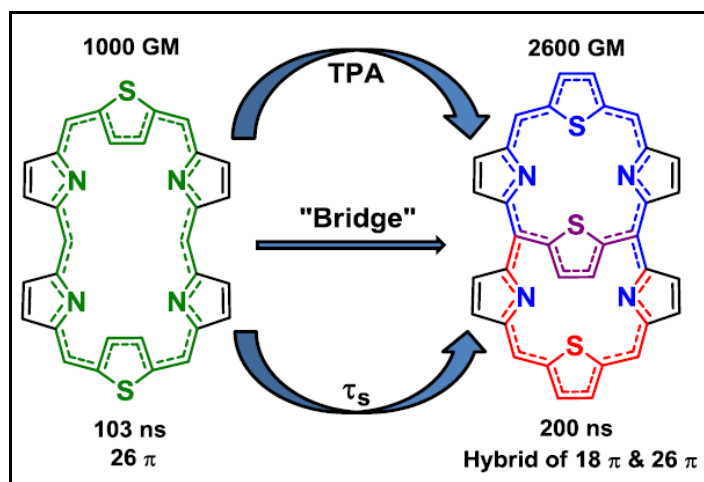


Figure 2. Photophysical properties of thiophene-bridged hexaphyrin **1**

In order to validate the bridging approach further the higher homologue of expanded bridged octaphyrins **3** and **4** are synthesized by using DTT as the bridging moiety (Chart 3), which is mainly focused on the second part of this chapter. The acid-catalyzed condensation of dithienothiophene-bis(dipyrromethane) with bithiophene diol or dithienothiophene diol afforded **3** or **4** in 6-8% yield. The spectral analysis reveals extended π conjugation than its non-bridged congener.

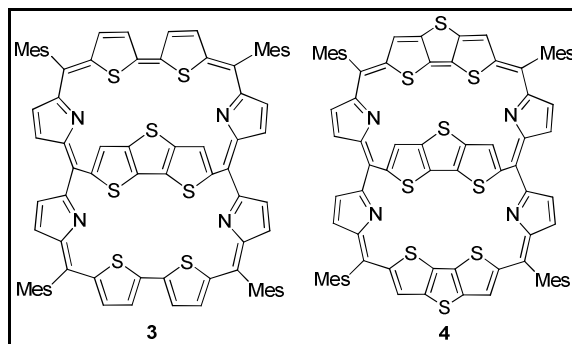
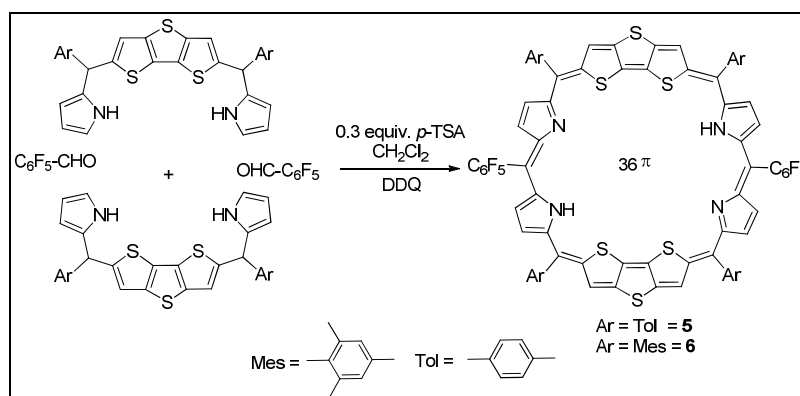


Chart 3. Dithienothiophene bridged Octaphyrins

Chapter 4: Core-modified Fused Expanded porphyrins

This chapter describes the synthesis, spectral, structural and photophysical characterization of fused derivative of expanded porphyrin such as doubly fused octaphyrin and mono fused sapphyrin.



Scheme 1. Synthesis of doubly fused octaphyrins

The syntheses of two fused octaphyrins **5** and **6** were achieved by simple acid-catalyzed condensation of dipyrromethane unit containing DTT moiety with

pentafluorobenzaldehyde followed by oxidation with DDQ. The single-crystal X-ray structure of **6** shows a figure-eight twisted conformation with two DTT moieties oriented in a staggered conformation with a π -cloud distance of 3.7 Å (Figure 3). Spectroscopic and quantum mechanical calculations reveal that both **5** and **6** conform to a $[4n]\pi$ nonaromatic molecule.

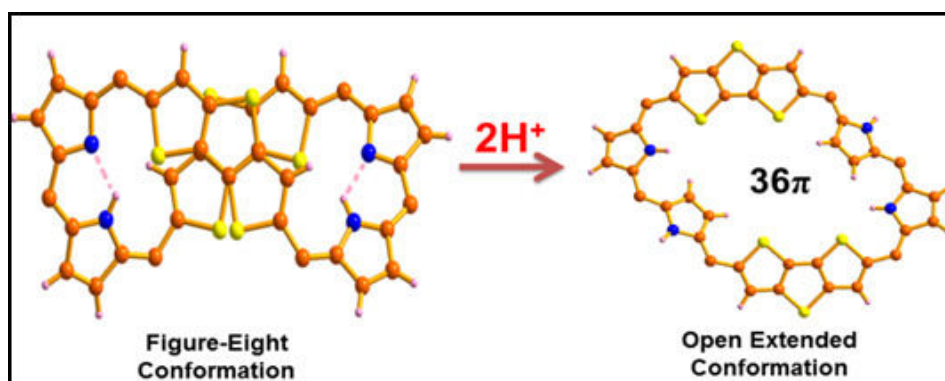


Figure 3. Conformational change of doubly fused octaphyrin by protonation

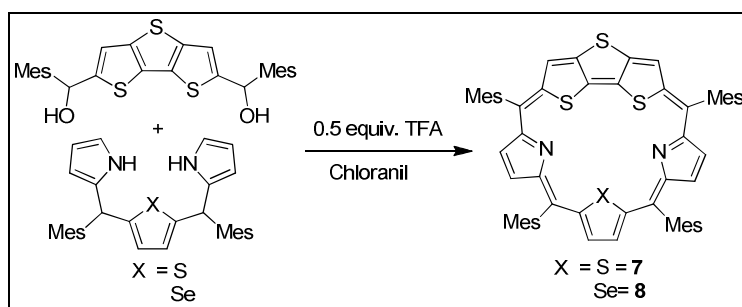
Protonation of imine pyrrole nitrogen of the **5** and **6** results in dramatic structural change, which led to (a) a large redshift and sharpening of absorption bands in electronic absorption spectrum, (b) a large change in chemical shift of pyrrole β -CH and -NH protons in the ^1H NMR spectrum, (c) a small increase in singlet lifetimes (τ_s), (d) a moderate increase in two-photon absorption cross-section (σ^2) values, and (e) a small increase in harmonic oscillator model of aromaticity (HOMA) values and a moderate decrease in the bond length alteration (BLA) value. Furthermore, nucleus-independent chemical shift (NICS) values calculated at various geometrical positions show positive values and anisotropy-induced current density (AICD) plots indicate paratropic ring-currents for the diprotonated form of **5** (Table 1). The single-crystal X-ray structure of the diprotonated form of **5** shows an extended structure, in which one of the pyrrole rings of each dipyrroin subunit undergoes a 180° ring-flip (Figure 3). Four trifluoroacetic acid (TFA) molecules are bound above and below the molecular plane defined by *meso*-carbon atoms and are held by N-H \cdots O, N-H \cdots F, and C-

H...F intermolecular hydrogen-bonding interactions. The extended-open structure upon protonation allows smooth delocalization of π -electrons and the electronic structure conforms to a $[4n]\pi$ Hückel antiaromatic in the diprotonated state as evidenced from above theoretical and structural characterization.

5	ϵ ($10^4 \text{ cm}^{-1}\text{M}^{-1}$) (nm)	τ_s (ps)	σ^2 / GM (1400nm)	HOMA	NICS (0)/ppm	Topology
Freebase	3.27 (369) 4.48 (521) 1.45 (723)	0.6	1600	0.454	+0.2	Twisted figure-eight $[4n]\pi$ nonaromatic
Mono- protonated	12.6 (631) 10.9 (701)	12.1	3200	--	--	Open extended conjugation
Di-protonated	8.4 (505) 10.7 (706)	9.6	2700	0.587	+9.94	$[4n]\pi$ Antiaromatic

Table 1. Photophysical properties of doubly fused octaphyrin **5**

The second part of this chapter discusses the synthesis of mono-fused sapphyrins **7** and **8**. The macrocycles are synthesized by acid-catalyzed condensation reaction of fused DTT-diol with core-modified tripyrromethane followed by oxidation with *p*-chloranil afforded **7** or **8** in 9-10% yield (Scheme 2). Both exhibit red shifted absorption spectrum and higher diatropic ring current in NMR, which reflects the enhanced aromatic properties than their non-fused derivatives.

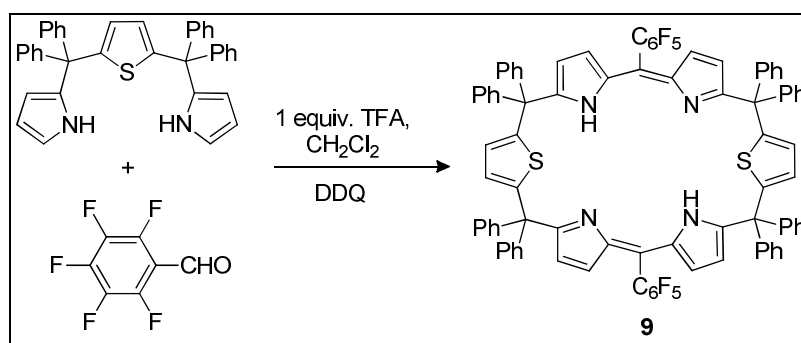


Scheme 2. Synthesis of sapphyrins

Chapter 5: Calix[2]thia[4]phyrin: An expanded calixphyrin with AIEE and Anion Receptor Properties

Fifth chapter demonstrates the core-modified expanded calixphyrin synthesis and their important properties such as aggregation-induced enhanced emission (AIEE) and anion

receptor properties [16-18]. The synthesis of calix[2]thia[4]phyrin, **9**, is outlined in Scheme 3. The synthetic methodology followed here is basically an acid-catalyzed condensation reaction of bis-pyrrolyl thiophene with pentafluorobenzaldehyde in the presence of TFA followed by oxidation with DDQ afforded **9** in 20% yield and trace amount of higher analogue, calix[3]thia[6]phyrin.



Scheme 3. Synthesis of core-modified calixphyrin **9**.

9 is highly soluble in common organic solvents, however, insoluble in water. Upon increasing addition of water, **9** exhibit an aggregation-induced enhanced emission (AIEE) phenomenon. This is attributed to the restricted intramolecular rotation of *meso* aryl rings present on the sp³ carbon of the bridge. Scanning electron microscope (SEM) studies reveal the formation of aggregation in acetonitrile/water mixture with an average diameter of aggregate in the range of 0.38-2.08 μm. When different compositions of the acetonitrile/water mixture were used, nano particles with average diameters from 150 nm (30:70) to 122 nm (10:90) were detected in the DLS studies. The photoluminescence quantum yield of **9** in water/acetonitrile (9:1) mixture is fivefold higher relative to the quantum yield in the acetonitrile solvent alone.

Single crystal X-ray analysis of **9** in freebase reveals a chair like conformation stabilized by N-H...N and C-H...π intramolecular H-bonding interactions. Fluorine atoms on the *meso* pentafluorophenyl groups are involved in C-H...F intermolecular hydrogen bonding interactions to generate two dimensional supramolecular assemblies in the solid state.

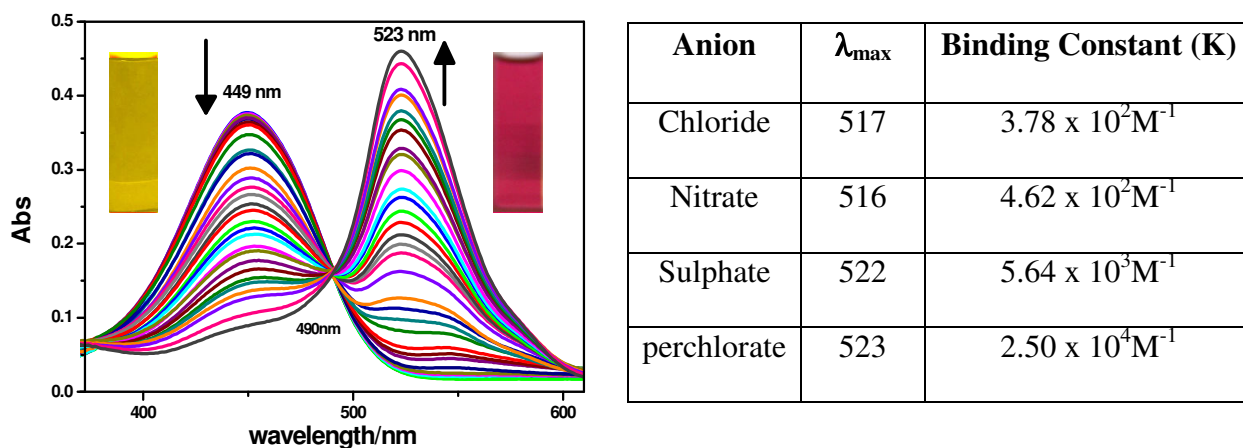


Figure 4. Changes in the absorption spectra of **9** upon addition of ClO_4^- ions in CH_2Cl_2 . Table 2. Absorption maxima (λ_{\max}) and binding constants (K) for binding of anions with **9** ($\lambda_{\max} = 449 \text{ nm}$)

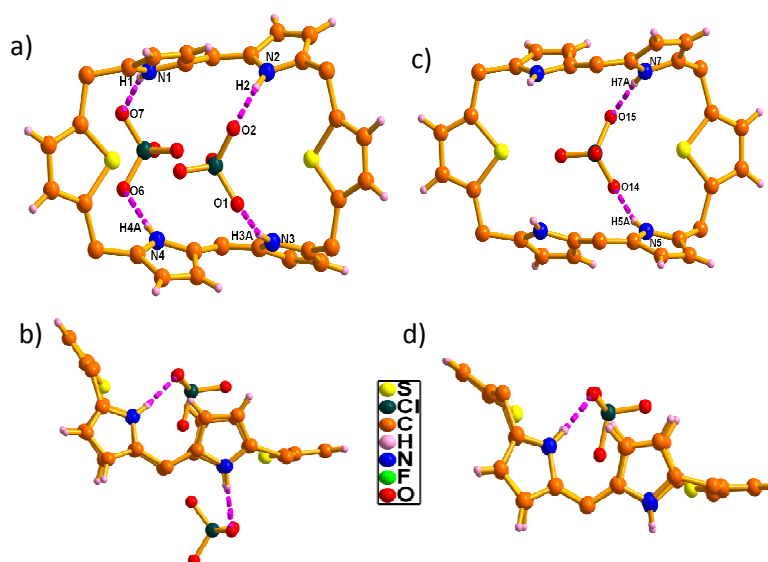


Figure 5. Single crystal X-ray structure of **9.2H²⁺** with perchlorate 1:2 complex (a & b) and 1:1 complex (c & d).

In the diprotonated state, **9** have affinity for anions and form 1:1 complexes with SO_4^{2-} , NO_3^- , Cl^- , and ClO_4^- (Figure 4) in solution. The tetrahedral anions bind more strongly relative to other anions (Table 2). The single crystal X-ray structure studies on ClO_4^- anion complex with **9** reveals formation of both 1:1 and 1:2 complex in solid state. Further, the host and the guest are held by N-H...O hydrogen bonding interactions (Figure 5).

3. References:

1. Sessler, J. L.; Weghorn, S. J. *Expanded, Contracted & Isomeric Porphyrins*; Tetrahedron Organic Chemistry Series, Pergamon, New York, Vol. 15, **1997**.
2. Chandrashekar, T. K.; Venkatraman, V. *Acc. Chem. Res.* **2003**, *36*, 676–691.
3. Vogel, E.; Bröring, M.; Fink, J.; Rosen, D.; Schmickler, H.; Lex, J.; Chan, K. W. K.; Wu, Y–D.; Plattner, D. A.; Nendel, M.; Houk, K. N. *Angew. Chem. Int. Ed. Engl.* **1995**, *34*, 2511-2514.
4. Furuta, H.; Asano, T.; Ogawa, T. *J. Am. Chem. Soc.* **1994**, *116*, 767-768.
5. Chmielewski, P. J.; Latos–Grażynski, L.; Rachlewicz, K.; Glowiak, T. *Angew. Chem. Int. Ed. Engl.* **1994**, *33*, 779-781.
6. Yoon, Z. S.; Osuka A.; Kim, D. *Nat. Chem.* **2009**, *1*, 113–122.
7. Anand, V. G.; Saito, S.; Shimizu, S.; Osuka, A. *Angew. Chem. Int. Ed.* **2005**, *44*, 7244–7248.
8. Suzuki, M.; Osuka, A. *J. Am. Chem. Soc.* **2007**, *129*, 464–465.
9. Senge, M. O.; Fazekas, M.; Notaras, E. G. A.; Blau, W. J.; Zawadzka, M.; Locos, O. B.; Mhuirheartaigh, M. N. *Adv. Mater.* **2007**, *19*, 2737–2774.
10. Bonnett, R. *Chem. Soc. Rev.* **1995**, *24*, 19-42.
11. Karunakaran, C. R.; Saneesh Babu, P. S.; Bollapalli, M.; Betsy, M.; Albish, K. P.; Nair, A.S.; Rao, K. S.; Srinivasan, A.; Chandrashekar, T. K.; Rao, C. M.; Pillai, R.; Ramaiah, D. *ACS Chem. Biol.* **2013**, *8*, 127-136.
12. Jasat, A.; Dolphin, D. *Chem. Rev.* **1997**, *97*, 2267-2313.
13. Sridevi, B.; Narayanan, S. J.; Rao, R.; Chandrashekar, T. K.; English, U.; Ruhlandt-Senge, K. *Inorg. Chem.* **2000**, *39*, 3669-3674.
14. Winter, M. B.; Klemm, P. J.; Phillips-Piro, C. M.; Raymond, K. N.; Marletta, M. A. *Inorg. Chem.* **2013**, *2*, 2277-2282.

15. Kadish, K. M.; Smith, K. M.; Guillard, R. *The Porphyrin Handbook*; Academic Press, San Diego, CA, 2000.
16. Sessler, J. L.; Zimmerman, R. S.; Bucher, C.; Král, V.; Andrioletti, B. *Pure. Appl. Chem.* **2001**, *73*, 1041–1057.
17. Salini, P. S.; Thomas, A. P.; Sabarinathan, R.; Ramakrishnan, S.; Sreedevi, K. C. G.; Reddy, M. L. P.; Srinivasan, A. *Chem. Eur. J.* **2011**, *17*, 6598 – 6601.
18. Zeng, Q.; Li, Z.; Dong, Y.; Di, C.; Qin, A.; Hong, Y.; Ji, L.; Zhu, Z.; Jim, C. K. W.; Yu, G.; Li, Q.; Li, Z.; Liu, Y.; Qin, J.; Tang, B. Z. *Chem. Commun.* **2007**, 70–72.

S. No	List of Figures: Figure Caption	Page No.
1.	Figure 1.1: Aggregation mode of π stacking molecules	50
2.	Figure 3.1: ESI-Mass spectrum of 12	77
3.	Figure 3.2: ESI-Mass spectrum of 16	77
4.	Figure 3.3: ESI-Mass spectrum of mono-condensed porphyrin 13	78
5.	Figure 3.4: ESI-Mass spectrum of Dithiaporphyrin 14	78
6.	Figure 3.5: ^1H spectrum of 12 in CD_2Cl_2 at 298K	80
7.	Figure 3.6: ^1H - ^1H COSY spectrum of 12 in CD_2Cl_2 at 298K	80
8.	Figure 3.7: ^1H NMR spectral changes of 12 in CDCl_3 at 298K with 0.1, 1.0, 2.0, 3.0, 4.0 equiv of TFA	81
9.	Figure 3.8: ^1H NMR spectrum of 12 in CD_2Cl_2 at 183K with 2 (top) and 4 (bottom) equiv of TFA	82
10.	Figure 3.9: ^1H NMR spectrum of 16 in CDCl_3 at 298K	83
11.	Figure 3.10: Electronic absorption spectra of 12 , 16 and their protonated forms	83
12.	Figure 3.11: MO energy diagram of 12 (left) and 16 (right)	84
13.	Figure 3.12: AICD plots for bridged core-modified hexaphyrins 12 (a) and 16 (b). The direction of external magnetic field is perpendicular to the hexaphyrin macrocycle	86
14.	Figure 3.13: The NICS (0) values of 12 (A) and 16 (B) calculated within inner and outside cavities. The purple points indicates the point at which NICS(0) values have been calculated	87
15.	Figure 3.14: Single crystal X-ray structures of 12 and 16 with disorder	88
16.	Figure 3.15: Single crystal X-ray structure of 12 , Top view and side view. <i>meso</i> -Mesityl units are omitted for clarity	89
17.	Figure 3.16: One dimensional array of 12 .	90
18.	Figure 3.17: Single crystal X-ray structure of 16 , Top view and side view.	91
19.	Figure 3.18: Cyclic Voltammogram (solid line) and Differential Pulse Voltammogram (dotted line) of 12	93

20. Figure 3.19: Cyclic Voltammogram (solid line) and Differential Pulse Voltammogram (dotted line) of 16	93
21. Figure 3.20: ESI-Mass spectrum of 12-R	94
22. Figure 3.21: Electronic absorption spectrum of 12-R in CH ₂ Cl ₂	95
23. Figure 3.22: Femtosecond transient absorption spectra and decay profiles of a) thiophene-substituted [26]hexaphyrin, b) 12 , and c) 16	96
24. Figure 3.23: one photon (OPA) and two photon absorption (TPA) spectra of 12	97
25. Figure 3.24: ESI-Mass Spectrum of octaphyrin 21	99
26. Figure 3.25: Mass Spectra of rubyrin	100
27. Figure 3.26: ESI-Mass Spectra of heptaphyrin	100
28. Figure 3.27: ESI-Mass Spectrum of octaphyrin 22	100
29. Figure 3.28: Electronic absorption spectrum of 21 and its protonated form	101
30. Figure 3.29: Electronic absorption spectrum of 22 and its protonated form	102
31. Figure 3.30: ¹ H NMR spectrum of 21 in CD ₂ Cl ₂ at 273K	103
32. Figure 3.31: ¹ H- ¹ H COSY spectrum of 21 in CD ₂ Cl ₂ at 273K	103
33. Figure 3.32: ¹ H NMR spectrum of 21 in CD ₂ Cl ₂ at 193 K (bottom) with 4 equiv. of TFA (top)	104
34. Figure 3.33: Variable Temperature ¹ H NMR spectra of 21	106
35. Figure 3.34: ¹ H NMR spectrum of 22 in CD ₂ Cl ₂ at 193 K (bottom) with 4 equiv. of TFA (top)	107
36. Figure 3.35: Cyclic (Solid line) and Differential Pulse Voltammogram (dotted line) of 21 in CH ₂ Cl ₂ contains 0.1 M TBAPF ₆ with scan rate of 50 mV/s	108
37. Figure 3.36: NICS value for 21	109
38. Figure 3.37: NICS value for 21.4H⁺	110
39. Figure 4.1: ESI-Mass spectrum of 9	117

40. Figure 4.2: ESI-Mass spectrum of 10	118
41. Figure 4.3: ^1H NMR spectra of 9 in CDCl_3 (1mM); a) before and b) after protonation by TFA. The inset shows ^1H - ^1H COSY correlations	119
42. Figure 4.4: ^1H NMR spectrum of 9 in CDCl_3 at variable temperature	122
43. Figure 4.5: ^1H NMR spectra of 10 in CDCl_3 ; a) before b) after protonation with TFA at 298 K	121
44. Figure 4.6: Single crystal X-ray structure of 10	123
45. Figure 4.7: Single crystal X-ray structure of 9.2H⁺ . Top view (above) side view (below).	124
46. Figure 4.8: Single crystal X-ray structure of 9.2H⁺⁺ with bond length (\AA , Blue) and torsion angles ($^\circ$, Red).	125
47. Figure 4.9: Titration of dilute solution of TFA (0.1mM – 100mM) with 9 (0.01mM) in CH_2Cl_2	127
48. Figure 4.10: Electronic absorption spectra of 9 in different solvents	127
49. Figure 4.11: Titration of dilute solution of TFA (0.1mM – 100mM) with 10 (0.01mM) in CH_2Cl_2	128
50. Figure 4.12: Molecular orbital diagram of 9	129
51. Figure 4.13: Calculated MO energy diagram of 9.2H⁺	130
52. Figure 4.14: Calculated NICS values for the various positions on 9.2H⁺	131
53. Figure 4.15: AICD plots of 9.2H⁺	132
54. Figure 4.16: Femtosecond transient absorption spectra and representative decay profiles of a) 9 , b) 9.H⁺ and, c) 9.2H⁺ in toluene	133
55. Figure 4.17: Steady-state absorption spectra (black line) and TPA cross-sections (blue dot) of 9 (Top), 9.H⁺ (middle) and 9.2H⁺ (Bottom)	134
56. Figure 4.18: Cyclic voltammetry of 9 in CH_2Cl_2 (Scan rate: 50mV/s)	136
57. Figure 4.19: Cyclic voltammetry of 10 in CH_2Cl_2 (Scan rate: 50mV/s)	136
58. Figure 4.20: Electronic absorption spectrum of oxidized products (A and B) of 9	137
59. Figure 4.21: ESI-mass spectrum of 13	139

60. Figure 4.22: ESI-mass spectrum of 14	140
61. Figure 4.23: ESI-mass spectrum of 15	140
62. Figure 4.24: ESI-mass spectrum of 16	141
63. Figure 4.25: Electronic absorption spectra of 13 in CH ₂ Cl ₂ and 13.2H⁺ in CH ₂ Cl ₂ /TFA	142
64. Figure 4.26: Electronic absorption spectra of 14 in CH ₂ Cl ₂ and 14.2H⁺ in CH ₂ Cl ₂ /TFA	142
65. Figure 4.27: Electronic absorption spectra of 15 in CH ₂ Cl ₂ and 15.2H⁺ in CH ₂ Cl ₂ /TFA.	143
66. Figure 4.28: ¹ H NMR spectrum of 13 in CDCl ₃	144
67. Figure 4.29: ¹ H NMR spectrum of 13.2H⁺ in CDCl ₃	144
68. Figure 4.30: ¹ H NMR spectrum of 14 in CDCl ₃	146
69. Figure 4.31: ¹ H NMR spectrum of 14.2H⁺ in CDCl ₃	146
70. Figure 4.32: ¹ H NMR spectrum of 15 in CDCl ₃	147
71. Figure 4.33: ¹ H NMR spectrum of 15.2H⁺ in CDCl ₃	148
72. Figure 4.34: Single crystal X-ray structure of 15 a) Top view and b) side view	149
73. Figure 4.35: Cyclic Voltammogram of 13 in CH ₂ Cl ₂	150
74. Figure 36: Cyclic Voltammogram of 14 in CH ₂ Cl ₂	151
75. Figure 37: Cyclic Voltammogram of 15 in CH ₂ Cl ₂	151
76. Figure 5.1: ESI-Mass spectrum of 17	161
77. Figure 5.2: ESI-Mass spectrum of 18	162
78. Figure 5.3: ¹ H NMR spectrum of 17 in CD ₂ Cl ₂ at 298K.	162
79. Figure 5.4: Absorption spectra of 17 in acetonitrile and acetonitrile/water mixture	163
80. Figure 5.5: Emission spectra of 17 in acetonitrile/water mixtures with different fractions of water	164
81. Figure 5.6: Changes in the emission intensities of 17 with the water content in the acetonitrile/water mixtures	165

-
- | | |
|---|-----|
| 82. Figure 5.7: Temperature effect on the emission peak intensity of 17 in acetonitrile/water (1:9 v/v), ($\lambda_{\text{ex}} = 449 \text{ nm}$) | 165 |
| 83. Figure 5.8: SEM image of 17 in acetonitrile/water mixture (10:90) at 278 K | 166 |
| 84. Figure 5.9: DLS measurement of 17 ($6 \times 10^{-6} \text{ M}$) in acetonitrile/water mixture (30:70) at 278 K | 167 |
| 85. Figure 5.10: DLS measurement of 17 ($6 \times 10^{-6} \text{ M}$) in acetonitrile/water mixture (10:90) at 278 K | 167 |
| 86. Figure 5.11: Single crystal X-ray structure of 17 . (a) Top view with intramolecular hydrogen bonding interaction and (b) side view. | 168 |
| 87. Figure 5.12: One-dimensional arrays of 17 | 169 |
| 88. Figure 5.13: a) Two-dimensional arrays of 17 | 170 |
| 89. Figure 5.14: Absorption spectral changes of 17 in CH_2Cl_2 upon addition of TFA. (a) Step-wise formation of mono-, di protonated species and anion bound species; (b) Titration experiment between 17 in CH_2Cl_2 with TFA. | 172 |
| 90. Figure 5.15: Absorption spectral as well as color changes of 17 in CH_2Cl_2 upon addition of HClO_4 | 174 |
| 91. Figure 5.16: Job's plot for 17 . ClO_4^- and Benesi-Hildebrand plot for 17 . ClO_4^- . | 174 |
| 92. Figure 5.17: Absorption spectral changes of 17 upon addition of H_2SO_4 | 175 |
| 93. Figure 5.18: Job's plot for 17 . SO_4^{2-} and Benesi-Hildebrand plot for 17 . SO_4^{2-} | 175 |
| 94. Figure 5.19: Absorption spectral changes of 17 upon addition of HNO_3 | 176 |
| 95. Figure 5.20: Job's plot for 17 . NO_3^- and Benesi-Hildebrand plot for 17 . NO_3^- | 176 |
| 96. Figure 5.21: Absorption spectral changes of 17 upon addition of HCl | 177 |
| 97. Figure 5.22: Job's plot for 17 . Cl^- and Benesi-Hildebrand plot for 17 . Cl^- | 177 |
| 98. Figure 5.23: Single crystal X-ray structure of 17 . 2H^{++} (with ClO_4^- anion). (a) Top view and (b) side view with 1:2 intermolecular hydrogen bonding interaction with ClO_4^- ions. | 179 |

-
99. Figure 5.24: Single crystal X-ray structure of **17.2H⁺⁺** (with ClO₄⁻ anion). (a) Top view and (b) side view with 1:1 intermolecular hydrogen bonding interaction with ClO₄⁻ ions. 180

S. No	List of Tables	Page. No
1.	Table 4.1: HOMA and BLA values	131

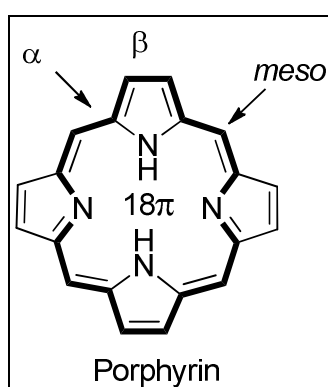
List of Abbreviations

Ar	Aryl
Calcd.	calculated
BLA	Bond length alteration
CDCl ₃	Chloroform-deutrated
COSY	Correlation Spectroscopy
DMF	N, N' Dimethyl formamide
DMSO	Dimethyl Sulphoxide
DDQ	2, 3-Dichloro-5, 6-dicyano-1, 4-benzoquinone
DTT	Dithieno[3,2-b:2',3'-d]thiophene
ESI	Electron Spray Ionization
equiv	equivalent
HOMA	Harmonic oscillator measure of aromaticity
HOMO	Highest occupied molecular orbital
LUMO	Lowest unoccupied molecular orbital
IR	Infrared
Mes	mesityl
MSA	methanesulfonic acid
NICS	nucleus independent chemical shift
NIR	Near infrared
NLO	Non Linear Optics
NMR	Nuclear Magnetic Resonance
Py	pyrrole
ppm	parts per million
<i>p</i> -TSA	<i>para</i> - Toluenesulphonicacid
Tol	tolyl
TFA	Trifluoroacetic acid
THF	Tetrahydrofuran
TLC	Thin Layer Chromatography
TMEDA	N, N, N, N, Tetramethylethylenediamine
TPA	Two Photon Absorption
UV-Vis	Ultra Violet- Visible

General Introduction

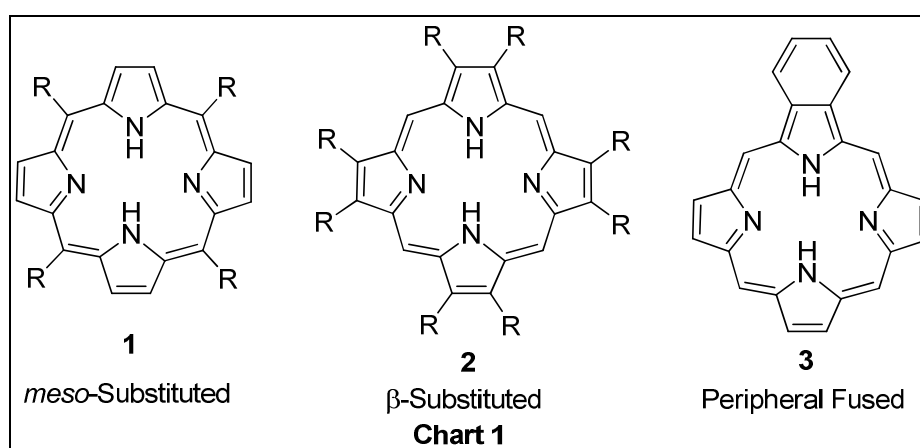
1.1 Introduction

Porphyryns are ubiquitous molecule in nature and have been referred to as “pigments of life”. These macrocyclic molecules consist of four pyrrole rings connected by four methine carbon bridges which has 18π electrons in conjugation and are considered to be a Hückel aromatic molecule. Porphyryin and its derivatives play a critical role in living systems which form the basic unit for many functionally diverse enzymes and proteins like Hemoglobin, Myoglobin, Cytochromes, Peroxidases, Coenzyme B₁₂, etc, [1,2]. These respective proteins or coenzymes are performing various important processes such as oxygen transport, oxygen storage, photosynthesis and catalysis [3,4].

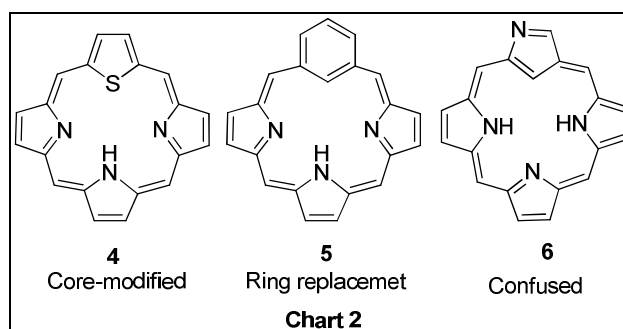


Last few decades, varieties of modified porphyrin derivatives were synthesized for an objective to mimic the biological processes and use them for diverse applications. These modifications in general can be classified in to three categories such as i) peripheral modification ii) core modification and iii) contracted / isomer / expanded porphyrins [5].

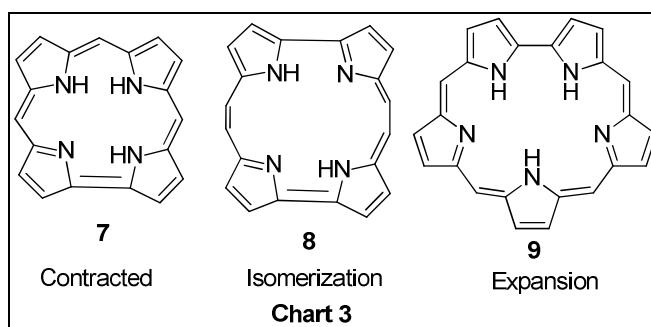
- a. **Peripheral modification:** Porphyrin *meso* position **1** and heterocyclic β - positions **2** & **3** are modified by using suitable substituents such as halogens or alkyl / aryl groups with electron donating and withdrawing behavior (Chart 1). Peripheral modification alters the global electron conjugation pathway of the macrocycle which in turn leads to change in the reactivity, aromaticity, photophysical and electrochemical properties of the macrocycle [6].



- b. **Core modification:** Normal porphyrin containing pyrrole rings in the macrocyclic skeleton, whereas in the core modified porphyrin, one or more pyrrole rings are replaced by other heterocyclic rings such as thiophene **4**, furan, selenophene, benzene, pyridine or other heterocyclic and aromatic rings **5**. Further, changing the linkage between *meso* position and pyrrole leads to core modified N-confused porphyrin **6** (Chart 2). Core modification in the porphyrin framework alters the coordination properties, electronic properties and aromaticity of the macrocycle [7].



- c. **Contracted / Isomer / Expanded porphyrins:** Contracted porphyrin containing less numbers of heterocyclic rings and/or *meso* position **7**. This can be obtained by removal of one or more *meso* and/or heterocyclic ring. Whereas isomeric porphyrins **8** can be obtained by reshuffling the pyrrole and methine bridges, which contains same number of heterocycle rings and *meso* carbon bridge as like normal porphyrin. [8]



Expanded porphyrin **9**, on the other hand, contains more number of heterocyclic rings and/or *meso* position than the normal porphyrin. These macrocycles have more than 16 non-hydrogen atoms in their innermost periphery and more than 18π electrons in its conjugation pathway [9,10]. These modification leads to change in photo-physical, electrochemical properties, aromaticity, coordination properties, anion and cation binding properties.

1.2 Expanded Porphyrins

Among all the modifications depicted above, expanded porphyrins have received much attention due to its structural diversity and versatile applications. Sessler defined the expanded porphyrins as “*macrocycle that contain pyrrole, furan, thiophene or other heterocyclic subunits linked through either directly or through spacer atoms in such a manner that the internal ring pathway contains a minimum of 17 atoms*” [11]. Expanded porphyrins possess the excellent physical and chemical properties such as large red-shifted absorption spectrum, multi-metal coordination site, ability to adopt various conformations,

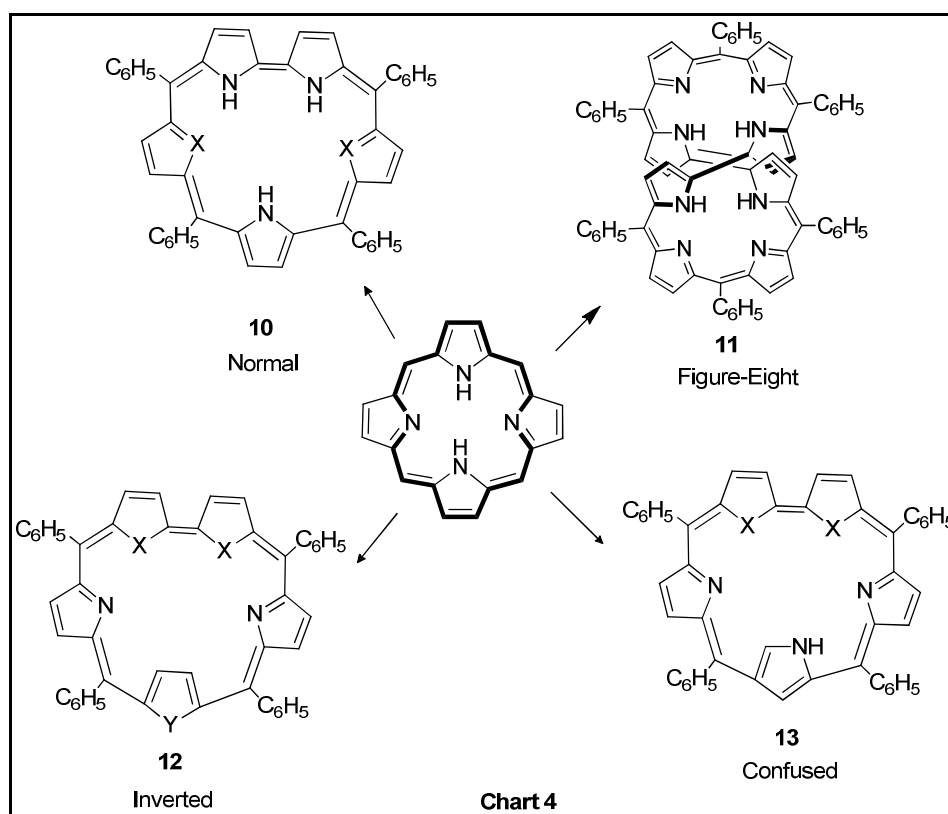
increased number of π electrons conjugation pathway. These excellent properties led this molecule to potential application as sensitizer for photodynamic therapy (PDT) [12], magnetic resonance imaging contrasting agent (MRI-CA) [13], nonlinear optical materials (NLO) [14-18], model for aromaticity in annulene family compounds [5], near infrared (NIR) dyes, anion and cation complexing agents and so on [19-20].

In 1966, Woodward and co-workers have serendipitously synthesized the first expanded porphyrin derivative sapphyrin (22π macrocycle) [21]. Even though it was synthesized long back, efforts towards the synthetic methodology in expanded porphyrin chemistry was made only in last decades mainly by the Vogel and Sessler groups. Vogel and co-workers have reported a series of octaphyrin derivatives in addition to normal porphyrin [22]. On the other hand, Sessler and co-workers mainly focused on the rational synthesis of 22π sapphyrin, 26π rubyrin, 24π rosarin, 24π amethyrin, 28π heptaphyrin, and 40π turcasarin using stable precursors in good yields [11]. They have not only reported developing efficient synthetic methods and also reported syntheses of stable building blocks, such as tripyrromethanes, dipyrromethanes, and quaterpyrroles required for the synthesis of expanded porphyrins in simple and efficient way [10].

So far, expanded porphyrins containing more than four pyrrole or heterocyclic rings were reported in literature, such as pentaphyrin (five heterocyclic rings with five *meso* carbons), sapphyrin (five heterocyclic rings with four *meso* carbons) [21], hexaphyrin (six heterocyclic rings with six *meso* carbons) [23], rubyrin (six heterocyclic rings four *meso* carbons) [24], heptaphyrin (seven heterocyclic rings with seven *meso* carbons) [25], octaphyrin (eight heterocycle) [22], nonaphyrin (nine heterocycle) [26], decaphyrin (ten heterocycle) [27] and dodecaphyrin (twelve heterocycle) [28] where in the last four derivatives the number of *meso*-carbon bridges varies depending on the size.

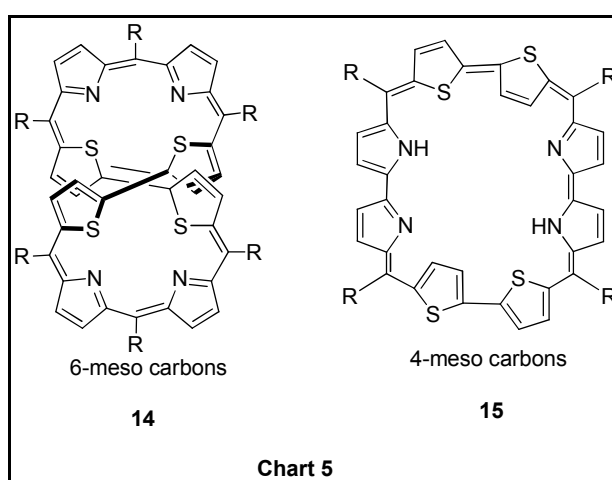
1.3 Conformation of Expanded Porphyrins

As mentioned in the previous section, the expanded porphyrins have more number of *meso* carbon bridges, hence it suffer from structural flexibility which leads to the molecule attain the various conformation in solution and solid state such as normal **10**, twisted figure-eight structure **11**, inverted heterocyclic ring structure **12**, ring confused **13** [11,29].



Surprisingly, depending on the site of substitution (either at *meso* carbons or at β -pyrrole positions) the expanded porphyrin exhibits different structural diversity. For instance, β -substituted expanded porphyrins shows normal structure where all the pyrrole rings point inward in the cavity, while the *meso*-substituted derivatives exhibit the structural diversity such as normal **10** and inverted conformations **12**. Overall in expanded porphyrins, the conformation is dependent on the nature of the linkage of the heterocyclic rings, the nature and the number of heteroatoms present in the cavity, measurement temperature and the state of protonation. However, it is also possible to change one conformation to another by varying

temperature, simple chemical modification, protonation by acids, metallation, changing the bulkiness of *meso* substitutions, varying the number of *meso* positions, modifying the heteroatom in core, etc [29-31]. For instance, octaphyrins are known to exhibit figure eight conformation due to more number of *meso* positions where the macrocycle undergoes a twist at the *meso* carbon, hence losing aromatic character. So, it was remain challenge to prepare the planar expanded porphyrin.

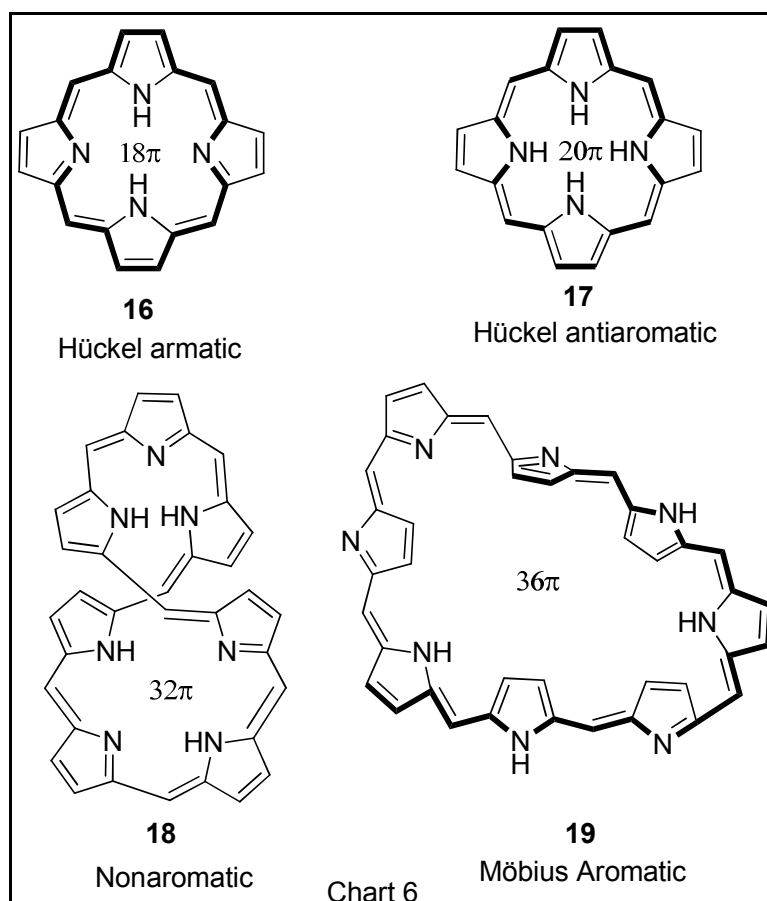


However, Chandrashekar and co-workers have synthesized two kinds of octaphyrins (Chart 5), one of them has eight *meso* positions and adopts figure-eight conformation **14** and another octaphyrin **15** has six *meso* positions and exhibits the planar structure both in solution and solid state. This study unambiguously proved that by suitable chemical modification such as decreasing the number of *meso* carbons enhancing the planarity of the macrocycle [32].

1.3 Aromaticity of expanded porphyrins

Aromaticity is one of the most important and basic concept of the organic molecules in chemistry. Because, the chemical and physical properties of the molecule fully depending on the aromatic nature of the molecules. In general, aromaticity of the molecule can be classified into three categories such as i) aromatic ii) antiaromatic and iii) nonaromatic. According to Hückel concept, aromatic molecules are defined as the molecule should possess

$(4n+2)\pi$ electrons in conjugation pathway with planar structure. Recently, continuous attempts to quantify the degree of aromaticity by various parameters, such as structural, energetic, reactivity, and spectroscopic criteria have been made [5,11].

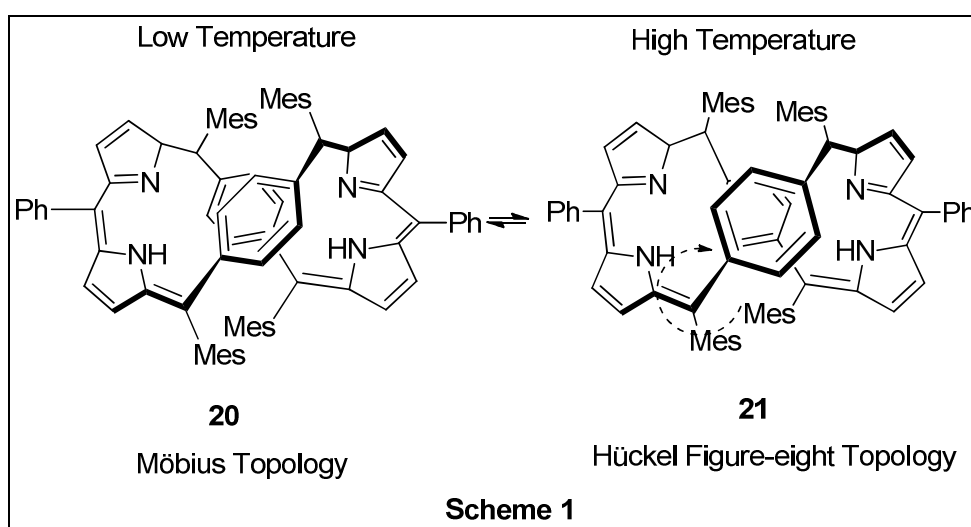


Normal porphyrins possess 18π electrons in conjugation, so it is considered to be a $(4n+2)\pi$ Hückel aromatic molecule. Expanded porphyrins, on the other hand, exhibit versatile aromatic properties such as $(4n+2)\pi$ Hückel aromatic **16**, $(4n)\pi$ Hückel antiaromatic **17** and nonaromatic **18** (Chart 6). The expanded porphyrin derivatives containing 22π , 26π , 30π and 34π electron in its conjugation frame work exhibits Hückel aromatic character [29]. Aromaticity of the porphyrin unit can be easily predicated from the NMR chemical shifts of inner and outer protons. An aromatic compound shows the diatropic ring current (the peripheral protons resonate in the downfield region while inside protons resonate in the up

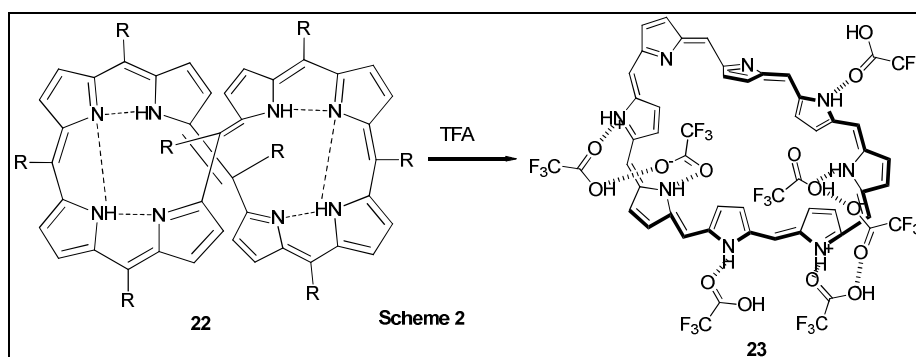
field region) whereas antiaromatic shows paratropic ring current (the peripheral protons resonate in the up-field region while inside protons resonate in the downfield region). However, expanded porphyrins with more than six heterocyclic rings have flexibility and attain figure-eight conformation. Hence, it loses planarity and attains nonaromatic behavior [11]. Further, there have been continuous efforts to synthesize antiaromatic porphyrins. For instance, the $[4n]\pi$ -electronic freebase [20]isophlorin would be expected as antiaromatic on the basis of Hückel's $[4n]$ electronic configuration but turned out to be nonaromatic as a consequence of its non-planar saddle structure [33]. However, there are other approaches which describe the syntheses of stable antiaromatic porphyrins. [34]

Recently expanded porphyrins attracted attention of researchers for its ability to form Möbius aromatic molecules **19**. The concept was first proposed by Heilbronner in 1964, predicts an electronically delocalized aromatic circuit for a $[4n]$ annulene when lying on a single-sided, non-orientable Möbius strip [35]. However, the concept was extensively challenged from both the theoretical and experimental viewpoints, as it is theoretically simple and difficult to make such a compound in practice. The first stable neutral Möbius aromatic molecule was reported by Herges and co-workers in 2003, in which the correct combination of a normal conjugated system and a belt-shaped conjugated system were employed to enforce a twist in the molecule, however, the reported $[16]$ annulene of Möbius topology shows weak aromaticity as inferred from the ring current and NICS values [36]. Recently, by using the expanded porphyrins Latos–Grazyński and co-workers reported the temperature-dependent topology change between Möbius conformations **20** and Hückel **21** in di-*p*-benzi[28]hexaphyrin(1.1.1.1.1.1) (Scheme 1). [37]

After that, Osuka and co-workers have introduced series of Möbius aromatic molecules. Initially they have described the facile metalation of a series of *meso*-aryl substituted expanded porphyrins led to conformationally rigid, single sided twisted structures with distinct Möbius aromaticity. Moreover, it has fast equilibrium between different Möbius conformers of freebase [28]hexaphyrins(1.1.1.1.1.1), which was frozen on the NMR time scale at 173K.[38,39]



The same group have also reported 36π octaphyrin with a twisted figure-eight conformation **22** in its freebase form changes into an open extended Möbius structure upon protonation **23** (Scheme 2).



The driving force for such a structural change is attributed to breaking intramolecular hydrogen-bonds in freebase form and formation of intermolecular hydrogen-bonds with TFA in the dicationic form. Detailed photophysical studies revealed increase in excited singlet and triplet state lifetimes which are attributable to the rigidity of the macrocycle in the dicationic form. Further, two-photon absorption (TPA) values increases more than four times in the dicationic form proved that the macrocycle attaining Möbius aromatic character of with open extended structure [40].

1.4 Photophysical properties of expanded porphyrins:

Porphyrins have unique absorption characteristic in UV-Vis spectrum which exhibits the strong intense Soret band in higher energy region and very weak Q-bands in lower energy region. Expanded porphyrins on the other hand, have extended π -electron conjugation pathway hence the electronic structures of expanded porphyrins give rise to considerably red-shifted absorption bands relative to those of normal porphyrins [11,41]. The π -conjugation pathways become longer and longer going from porphyrin to expanded porphyrin, hence the HOMO–LUMO energy gap becomes smaller. However, on increasing the number of heterocyclic rings in the macrocycle (e.g. hexaphyrin and/or higher analogue) deviation from planarity is observed due to the intrinsic conformational distortion in the *meso* positions. Upon non-planar conformations due to the flexibility of their molecular frameworks, they exhibit (i) only broad Soret band without Q-like bands, (ii) no emission intensity, (iii) short singlet and triplet excited (π, π^*) state lifetimes, and low triplet state quantum yields and (iv) small TPA values. This clearly indicates that there is a close relationship between the photophysical properties and geometrical structure of expanded porphyrins. Further, aromatic, nonaromatic and antiaromatic characters of the expanded porphyrin also have effect on photophysical properties. For instance, the aromatic derivatives have relatively long

singlet excited (π , π^*) state lifetimes and large σ^2 values. However, the antiaromatic and nonaromatic derivatives have the broad Soret band, low excited state lifetime and TPA values. [41,42]

The materials with high TPA values are found suitable for commercial NLO applications. Among these, porphyrins with 18π -electrons are quite promising, but high TPA performance has only been achieved when the π -electron networks have been considerably enlarged by conjugation with peripheral substituents and/or by covalent and non-covalent assembling, because normal porphyrin monomers only exhibit small TPA values of less than 100 GM. In this aspect, expanded porphyrins can be good candidates as new NLO materials with large TPA values, because expanded porphyrins possess a greater number of π -electrons along the extended π -conjugation pathway [14,17]. In the next section we would like to highlight such materials and their brief mechanical background.

1.4.1 Nonlinear Optical Materials (NLO)

Nonlinear optics deals with the *interactions of applied electromagnetic fields with materials to generate new electromagnetic field altered in phase, frequency, amplitude or other physical properties* [43]. NLO processes can be viewed as dielectric phenomena. Electrons that are bound to the nearby nuclei in the medium gets slightly perturbed by the external applied electromagnetic field and begin oscillating at the applied frequency. The magnitude of such an induced polarization (P) at modest field strengths will be proportional to the applied field and expressed as

$$P = \chi^{(1)} E \dots\dots\dots(1.1)$$

Where E is the magnitude of the applied electric field and $\chi^{(1)}$ is the polarizability of the material.

The NLO phenomena occur at sufficiently intense fields. As the applied field strength increases (e.g., lasers) the polarization response of the medium is no longer linear as shown by the eq (1.1). The induced polarization (P) becomes a function of the applied field and given by the equation,

$$P = \chi^{(1)} E + \chi^{(2)} E^2 + \chi^{(3)} E^3 + \dots \dots \dots (1.2)$$

Where the $\chi^{(2)}$ and $\chi^{(3)}$ coefficients represent the second and third order susceptibilities of the medium respectively.

At the molecular level eq. 1.2 is expressed as

$$P = \sum \alpha_{ij} E + \sum \beta_{ijk} E^2 + \sum \gamma_{ijkl} E^3 + \dots \dots \dots (1.3)$$

$$i < j < k < l$$

Where α_{ij} = Polarizability

β_{ijk} = First hyperpolarizability (second order effects)

γ_{ijkl} = Second hyperpolarizability (third order effects)

i, j, k, l = corresponds to the molecular coordinates.

A medium exhibiting such a NLO response might consist of a crystal composed of molecules with symmetric charge distribution, which are known as second order NLO materials. However, if the medium (or molecule) is centrosymmetric, then first order hyperpolarizability (β) is zero, indicating that centrosymmetric media do not show second harmonic generation. This can be explained as follows, if a field +E is applied to the medium, eq (1.3) predicts the first nonlinear term as $+\beta E^2$. If a field -E is applied, the polarization is still predicted to be $+\beta E^2$. Yet if the medium is centro-symmetric the polarization should be $-\beta E^2$. Thus the centro-symmetric medium has zero β -value. In the case of third order NLO susceptibility, if +E field produces polarization $+\gamma E^3$ and -E field produces $-\gamma E^3$, so the

second order hyperpolarizability (γ) is the first nonzero nonlinear term in centrosymmetric media. These materials are known as 3rd order NLO materials.

The value of 3rd order nonlinear coefficient is measured in terms of σ^2 known as the two photon absorption coefficient.

$$\sigma^2 = \frac{4\pi^2 \hbar \omega L^4 \text{Im}(\gamma)}{n^2 c^2} \dots\dots\dots (1.4)$$

1.4.2 Materials for Non-Linear Optics

Currently, inorganic solids such as LiNbO₃, KH₂PO₄ and semiconductors are the most popular NLO materials for commercial applications. These are ionic bulk materials where the optical nonlinearity is a bulk effect. However, the rigidity of these systems, their high cost and their poor response time to the electromagnetic radiation had been a hurdle in the further development of these materials and has limited their applications. Moreover, phase matching is not satisfied for these inorganic crystals. [14]

On the contrary, organic materials are emerging as an alternative to inorganic materials because of their low cost, ease of fabrication and integration into devices, and intrinsic tailorability which allows one to fine tune the chemical structure and properties for a given NLO process. Conjugated polymers, polyacetylenes, polythiophenes were considered to be a good candidates for NLO applications but these systems showed a very low γ value (3rd order) to replace the inorganic materials commercially. [44]

However, in the last few years, expanded porphyrins have turned out to be excellent candidates for this purpose. These systems can be easily tailored to obtain highly π conjugated systems and also show a drastic change in the properties on metallation. Recently, our groups synthesized series of expanded porphyrins ranging from 22π – 50π and

demonstrated the aromaticity, coordination properties of these derivatives and also used them as a potential commercial material for NLO applications. [45-46]

1.5 Topologically controlled expanded porphyrins

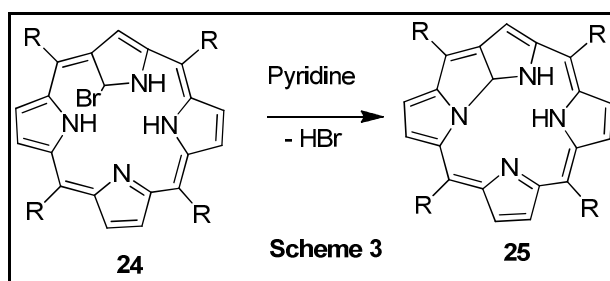
Merits and applications of expanded porphyrins are as a result of enlarged π electron conjugation. However, structural distortion in expanded porphyrins leads to disturbed delocalization of π -electrons along the molecular framework. Thus, while the absorption bands of a series of representative planar expanded porphyrins show a continuous red-shifted absorption spectrum, but some of the larger expanded porphyrins with distorted topologies exhibit (i) broad and ill-defined Soret banded absorption spectra without Q bands or very weak bands (ii) low singlet and triplet life time and (iii) low NLO coefficient. Considering these demerits, the overall molecular structure is an important factor to determine the electronic structures of expanded porphyrins for understanding the molecular structure–property relationship in expanded porphyrins. [11,15,47]

It is obvious that topology control is become the one of important solution for maintain the planarity and aromaticity in expanded porphyrin. So far, various attempts has been made to rigidify the expanded porphyrins such as metal coordination, temperature control, solvent change, protonation with appropriate acids, and functional group modifications [48]. Fused and bridged strategies to control the topology become an interesting topic which does not alter the porphyrin intrinsic properties.

1.5.1 Fused porphyrins

In 2000, Furuta and co-workers have reported the first N-fused porphyrin (NFP) **25** where the new fusion bond is formed between the pyrrole nitrogen and β -CH of another pyrrole. The **25** was synthesized from the self-condensation reaction of α -bromo substituted

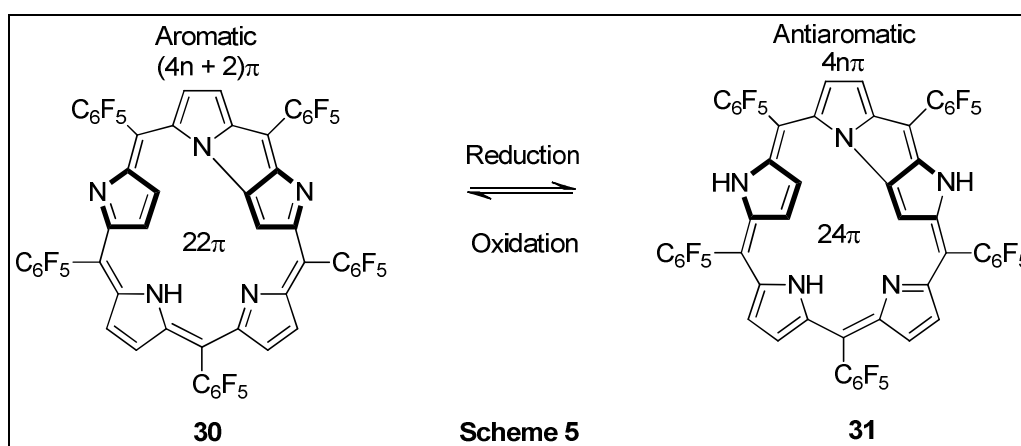
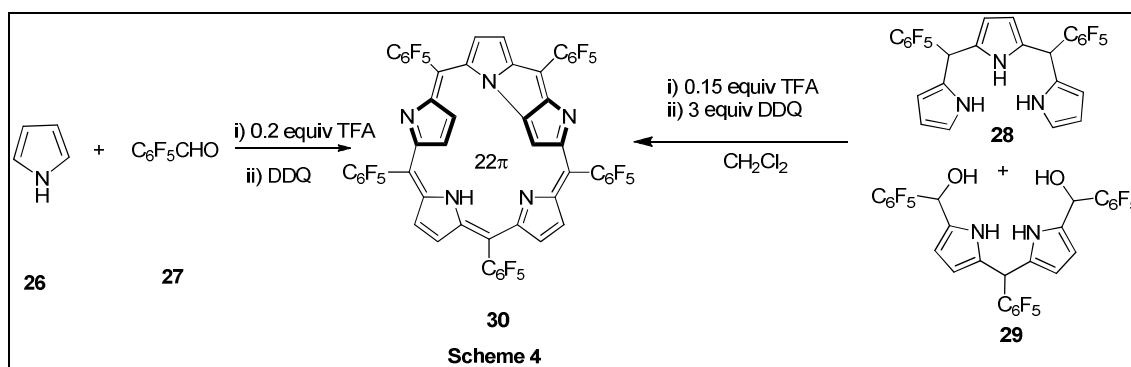
N-confused tetraaryl porphyrin **24** in presence of base, pyridine solution at room temperature. From the mechanistic point of view, the reaction has been initiated by the inversion of the confused pyrrole ring, followed by the nucleophilic attack of the adjacent pyrrole and HBr elimination. The X-ray diffraction analyses clearly shows that the porphyrinoid like core containing a fused tri-pentacyclic ring, the whole molecule is completely flat in nature. This unique structure of fused tri-pentacyclic ring in the macrocyclic core leads the molecule to show unusual long wavelength absorption near 1000 nm. [49]



The next higher homologue of fused porphyrin, N-fused pentaphyrin (NFP₅) **30** was reported by Furuta, Osuka and co-workers, where the pentaphyrin ring contains a fused tri-pentacyclic ring in the macrocyclic framework. The **30** was synthesized through two different strategies. In the first case, they have performed the Rothmund type condensation reaction, where the pyrrole and pentafluorobenzaldehyde reacted in the presence of Lewis acid (BF₃.OEt₂) followed by DDQ oxidation afforded normal porphyrin and **30** along with series of expanded porphyrins. In the second strategies, they have also adopted step-wise synthesis, where [2+3] acid-catalyzed condensation of tripyrromethane **28** and dipyrromethane dicarbinol **29** afforded **30** (Scheme 4). [50]

In both the synthetic methodology, they observed both oxidized (**30-R**, R represents for Red color solution) and reduced form (**30-Y**, Y represents for Yellow color solution) of **30**. Depending on the amount of oxidizing agent used, the yield varies accordingly. Further, they have also demonstrated that the CH₂Cl₂ solution of **30** was treated with DDQ, the yellow

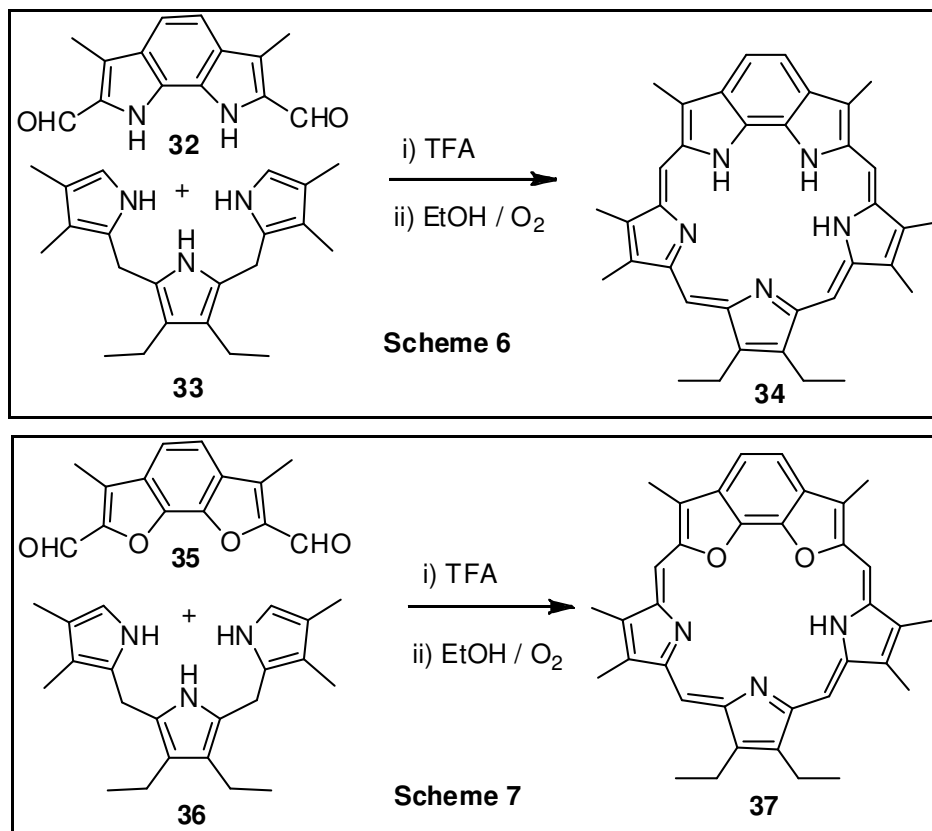
solution changed to red color and afforded the quantitative conversion into oxidized form. Similarly, the obtained oxidized form is quantitatively converted into reduced form in the presence of reducing agent, such as NaBH_4 (Scheme 5).



1.5.2 Fused precursor approach for Fused Porphyrins

The fused tripentacyclic ring was formed through step-wise strategies in the synthetic scheme-3 has the control over the reaction, however, in the second methodology (scheme 4), there is no control for the formation of fused tripentacyclic ring formation. In addition, in the later methodology, the overall yield of the fused derivative reduced drastically and also the site of fusion is not specific. In order to overcome these problems, C. H. Lee and co-workers synthesized the benzobipyrrole based fused sapphyrin **34**. The [3+2] acid-catalyzed condensation of diformyl benzodipyrrole **32** and tripyrromethane **33** followed by aerial oxidation afforded **34** in 18% yield, respectively (Scheme 6) [51]. Similarly, Sessler and co-

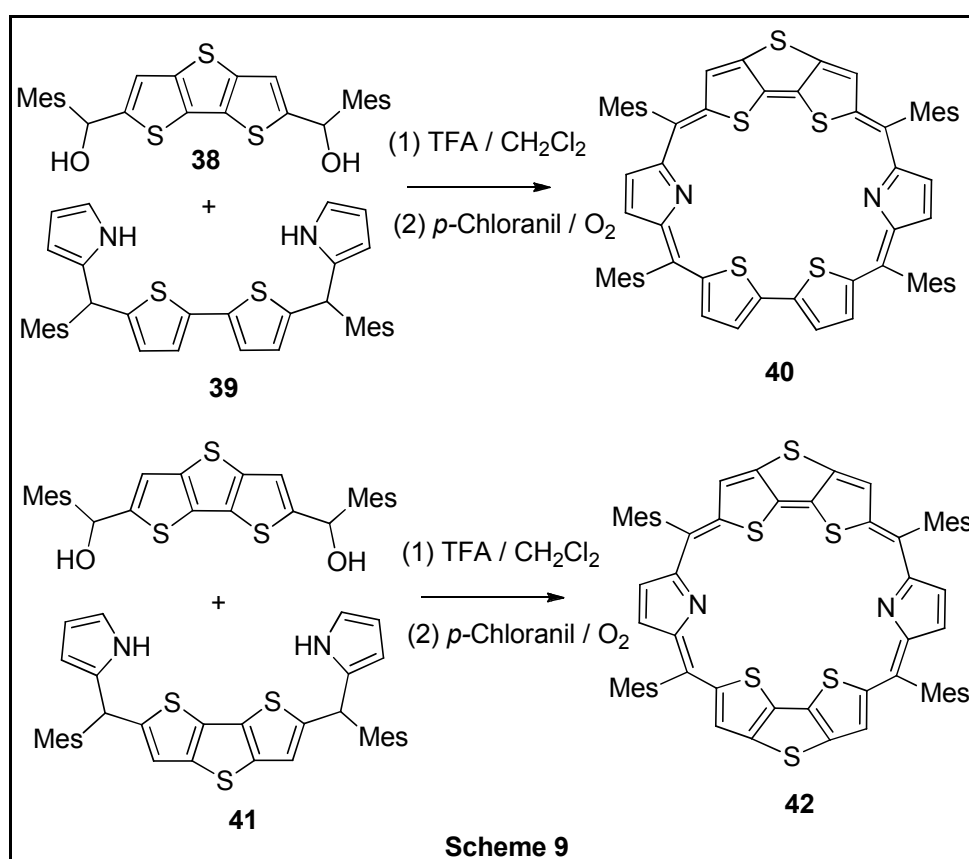
workers have synthesized the benzodifuran **37** macrocycle by condensation reaction of **35** and **36** (Scheme 7) [52]. The effect of fusion led to; (a) red-shifted Soret band absorption and (b) extended π -conjugation and aromaticity as compared to non-fused sapphyrin. The single crystal X-ray analysis of salt of **34** and **37** confirmed the planar structure in the solid state.



In 2010, our group has reported the dithienothiophene modified singly **40** and doubly fused rubyrin **42**. The [4+2] Mac-Donald type condensation of DTT-diol **38** with modified tetrapyrans **39** or **41** in the presence of 1 equiv of trifluoroacetic acid (TFA) as a catalyst followed by oxidation with *p*-chloranil in air afforded singly fused **40** and doubly fused rubyrins **42** in good yield as single product (Scheme 8). [53]

The single crystal X-ray analysis of both **40** and **42** revealed the planar structure defined by four *meso* carbon atoms. However, two or more heterocyclic units were tilted in the case of non-fused rubyrin derivatives (all aza and core-modified) reported earlier. The

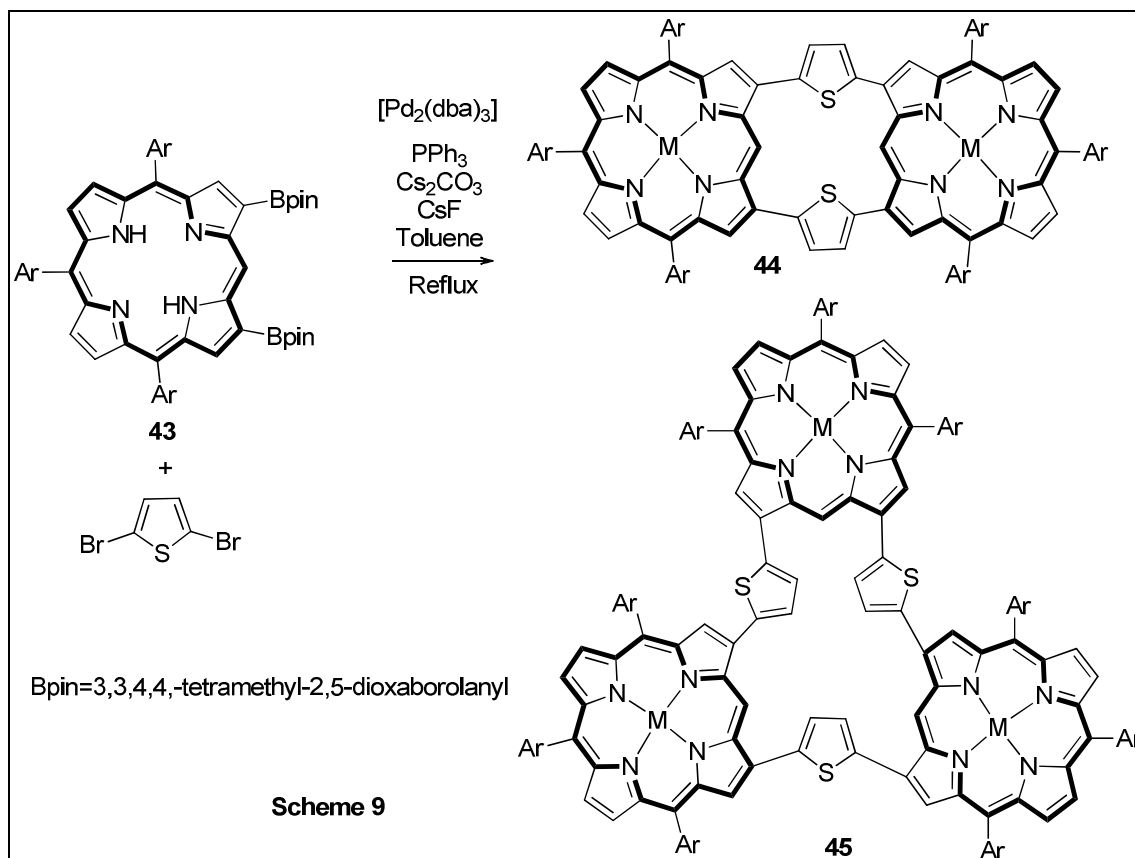
effect of conformational restriction was further reflected by electronic spectral analysis which inferred the following physical characteristics; (i) the red shifted Soret band absorption; (ii) the increase in the molar extinction coefficient by four times upon fusion; (iii) enhanced aromaticity, probably due to the planar structure. The introduction of fusion in the macrocyclic framework resulted in conformational restriction, where the inversion was avoided in the singly and doubly fused rubyrin.



1.5.3 Bridged porphyrins

There are several reports described the syntheses and characterization of porphyrin dimers, trimers and etc, by bridging spacer groups [54]. Recently, Osuka and co-workers demonstrated the syntheses of highly conjugated porphyrin arrays such as β -to- β 2,5-thienylene-bridged porphyrin dimer **44**, a triangular trimer **45**, and a ladder like trimer. The β,β' -diborylporphyrin was cross-coupled with 2,5-dibromothiophene under Suzuki–Miyaura

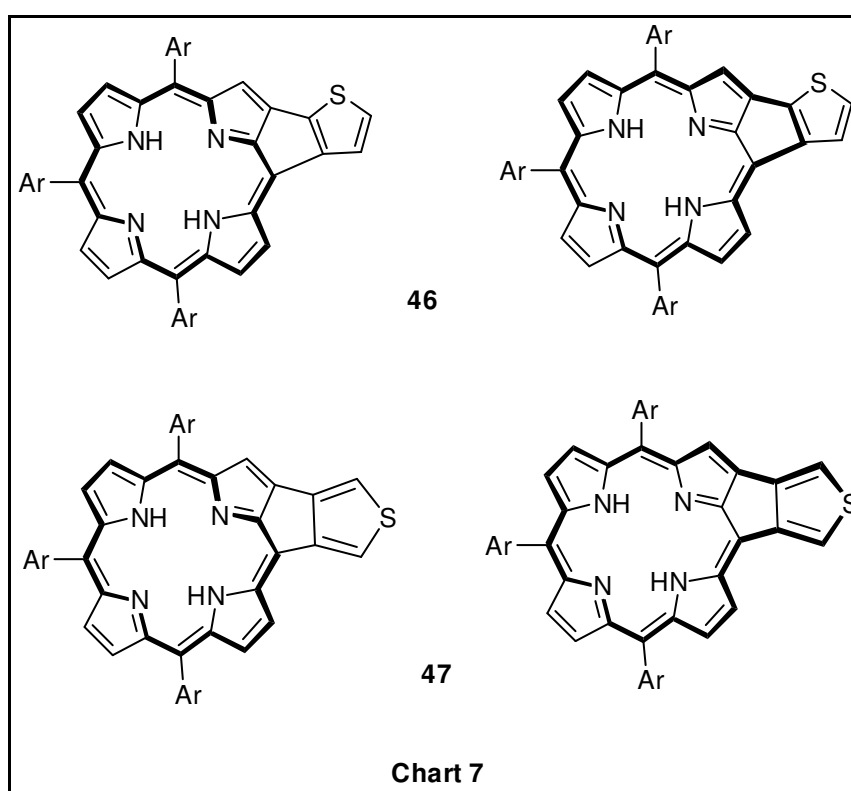
coupling conditions resulted doubly 2,5-thienylene-bridged diporphyrin was obtained in 29% yield. [55]



The π -conjugation through thienylene linkages was quite effective because of their relatively strong aromaticity as well as their small rotational barriers. Although several thienylene-bridged porphyrin systems have been reported, the doubly linked diporphyrin (**44**) showed a large TPA cross-section values. However, the respective values are not significant in the cyclic trimer system. On the other hand, the ladder like trimer showed a very large TPA cross-section value. The effective electronic delocalization through the thienyl bridge to porphyrin array led to large TPA cross-section value.

In 2012, Dongho Kim and co-workers have synthesized two types of thieno-bridged porphyrins **46** & **47** incorporating a thiophene group across the *meso* and β -positions with different directions of the thiophene ring to investigate the aromaticity of these porphyrins

with extended π -systems. The 2,3-thieno bridged porphyrin **46** showed a larger antiaromatic contribution than the 3,4-thieno-bridged porphyrin **47**. The antiaromatic contribution in **46** was based on a 20π -electron conjugated circuit. In addition to regular spectral and structural analysis, the two thieno-bridged porphyrins were further analyzed by electrochemical studies, time resolved excited state analysis, TPA cross-section measurements and also theoretically calculated the NICS value and the AICD plot. [56]



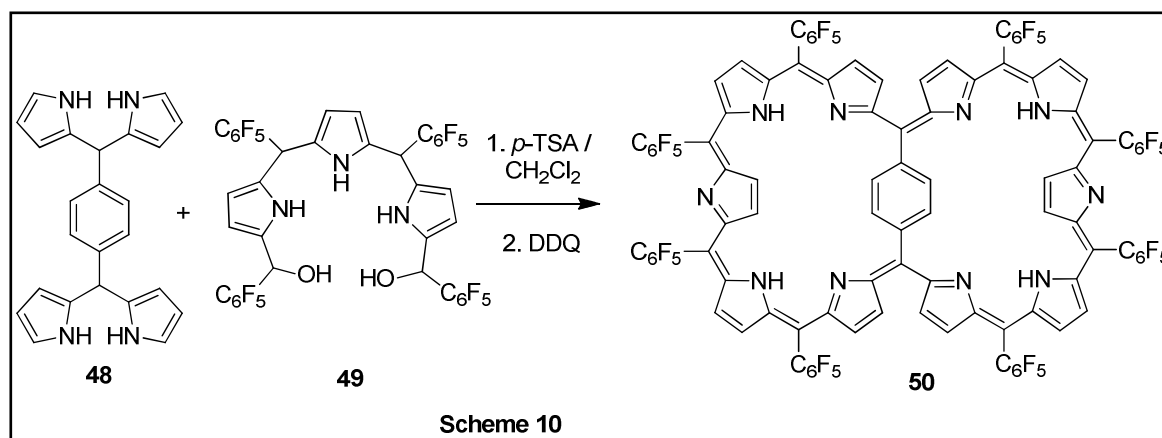
Nucleus independent chemical shift (NICS), which has been successfully used as a measure of aromaticity. At the five-membered ring between the porphyrin and thiophene moieties, the NICS(0) values for both **46** and **47** are positive (+30.5 and +13.1 ppm, respectively). The large positive NICS(0) value for **46** indicates a large contribution from the antiaromatic 20π circuit. A smaller contribution from the antiaromatic 24π circuit of **47** is also possible, judging from the positive value at the five membered rings between the porphyrin and thiophene moieties of **47**. The NICS(0) values at the porphyrin macrocycle of

46 are more positive (−10.1 to −13.6 ppm) than those of **47** (−14.6 to −16.1 ppm; suggesting that the antiaromatic network makes a larger contribution to the overall electronic structure in **46** than in **47**.

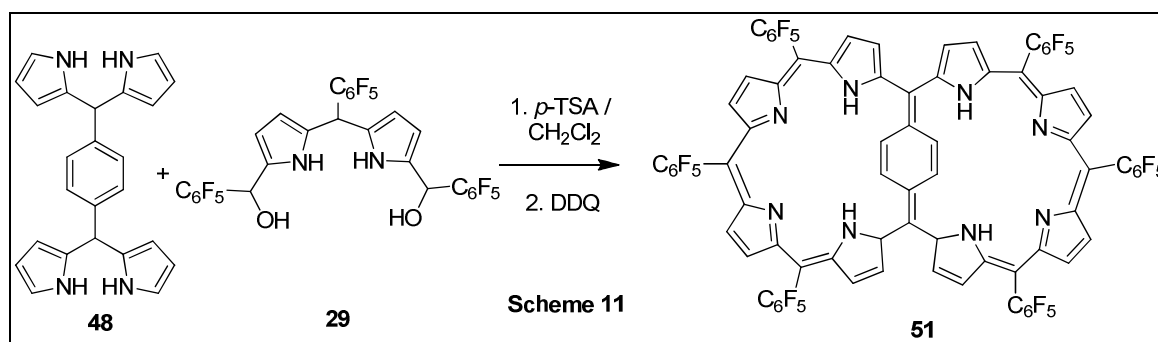
1.5.4 Internally Bridged porphyrins

Although several reports describe the synthesis of dimer porphyrin by spatial bridging group, only three reports in the literature discussed the synthesis of internally bridged porphyrins. Osuka and co-workers synthesized the internally 1,4-phenylene bridged octaphyrin **51** and decaphyrin **50**. The main objective of this bridged system was to maintain the planarity. [57]

A solution of one mole equiv of 1,4-phenylene-bridged bis(dipyrromethane) **48** and two mole equiv of tripyrromethane diol **49** in CH₂Cl₂ in the presence of *p*-TSA followed by oxidation with DDQ afforded **50** in 10 % yield (Scheme 10).

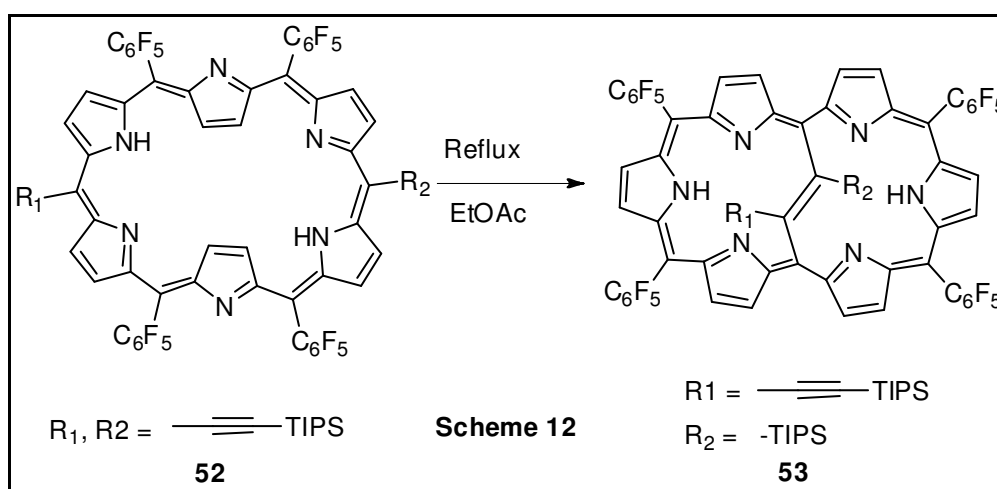


They have also demonstrated the reversible redox inter-conversion between [46]decaphyrin and [44]decaphyrin by simple oxidation and reduction. Treatment of [46] decaphyrin with 10 equiv of DDQ resulted in quantitative conversion into [44]decaphyrin, with a color change from dark red to dark green. Similarly, it was reduced quantitatively with NaBH₄.



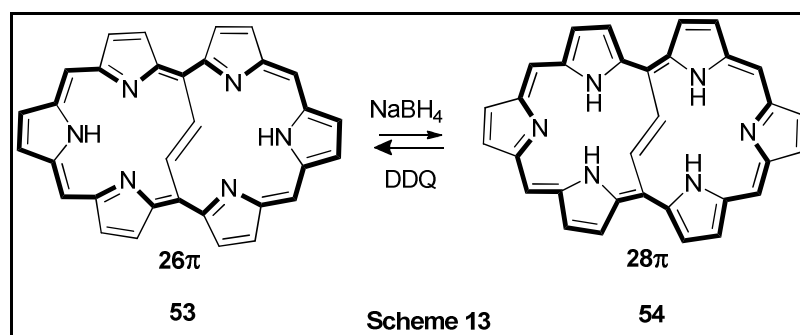
Both [46]decaphyrin and [44]decaphyrin were confirmed by single crystal X-ray diffraction analysis. Decaphyrin showed C_2 -symmetric nonplanar, but not a figure-eight structure in which the two twisted pentapyrrolic subunits were interconnected by the central 1,4-phenylene bridge. Each pentapyrrolic arm, has dipyrromethene and a tripyrrodimethene unit, maintained the near planar structure.

The same group also reported the vinylene bridged hexaphyrin **53**. Cross-bridging reaction of 5,20-diethynyl substituted [26]hexaphyrins (1.1.1.1.1.1) **52** under reflux condition in ethylacetate for 36h resulted in a quantitative conversion to trans-vinylene bridged [26]hexaphyrins(1.1.1.1.1.1) with vivid color change from indigo blue to magenta purple (Scheme 12) [58].



The electronic absorption and emission spectral analyses of **52** and **53** showed remarkable differences where the bridged compound exhibited unique features: (i) relatively broad and weak Soret-like bands in the 400-600 nm region; (ii) smeared Q-like bands in the 620-850 nm region; (iii) an extremely weak and broad NIR absorption band in the 900-1800 nm region; and (iv) a lack of emission in the NIR region [59].

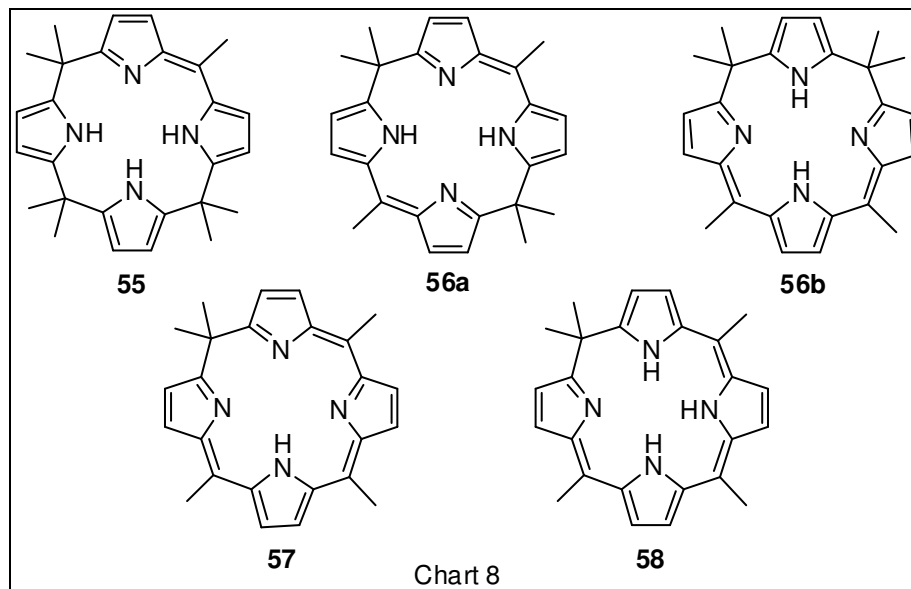
As observed in the case of **30** and **45**, the compound **53** was also shown to be interconvertible into its reduced form **54** by using NaBH_4 and oxidized back to **53** by using DDQ (Scheme 13). Single crystal X-ray analysis confirmed the trans-vinylene-bridged [28] π hexaphyrin. The overall conjugated electronic systems of **53** and **54** were characterized as 26- and 28- π circuits respectively, while a resonance form that contributes to **53** was regarded as [16]diazannuleno[16]diazannulene. However, this contribution should be lower due to the perpendicular arrangement of the central vinylene bridge. This [16]annuleno[16]annulene was regarded as [4n]annuleneo[4n]annulene which consists of two annulated antiaromatic[4n]annulenes with a total of $(4n+2)\pi$ -electrons have been extensively studied to examine a possibility that such conjugated molecular systems could possess overall aromaticity.



1.6. Calixphyrins

The definition of calix[4]phyrins comprise systems with one, two, and three sp^2 -hybridized bridging *meso* carbons in the macrocycle. They are divided into three types;

porphomethenes, porphodimethenes, and porphotrimethenes, based on the number of sp^2 hybridized *meso* carbon (Chart 8). [60]



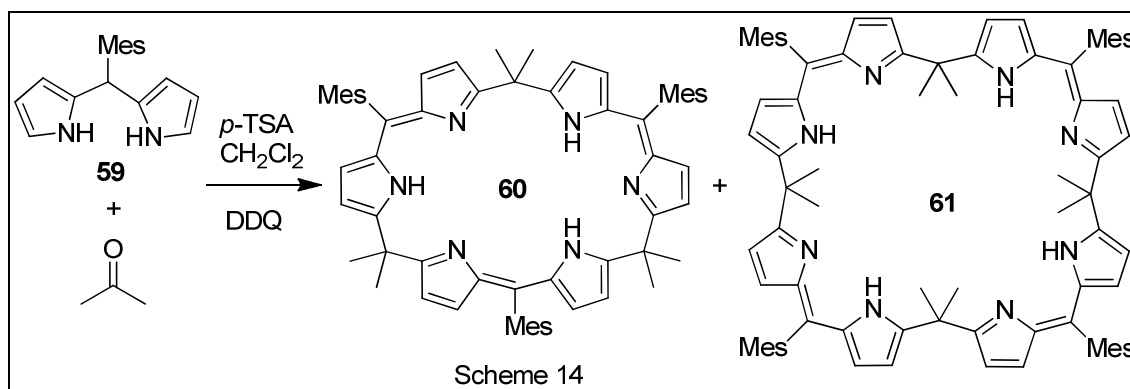
Porphomethenes **55** contain only one sp^2 hybridized *meso* carbon atom and are named as calix[4]pyrins-(1.1.1.1) (The numbering system refers as follows: bold numbers refer to sp^2 *meso* centers, and italicized numbers refer to sp^3 *meso* centers [60]). Porphodimethenes are containing two sp^2 -hybridized *meso* carbon atoms. There are two types of porphodimethenes; 5,15-porphodimethene type calix[4]pyrin-(1.1.1.1) **56a** and 5,10-porphodimethene type calix[4]pyrin-(1.1.1.1) **56b**. Porphotrimethenes are containing three sp^2 hybridized *meso* carbon bridges. They are further divided into two, based on the number of –NH protons; isoporphyrins **57** (one NH hydrogen atom) and Phlorins **58** (three NH hydrogen atoms). [61]

Porphyrins are long well known as cation coordinating ligands, while calixpyrroles have emerged as anionic receptors. The introduction of both sp^2 and sp^3 -hybridized *meso* carbon bridges in calixpyrin leads to partial interruptions in the conjugation pathway of the molecule and hence introducing novel structural features and anion and cation recognition properties. Today, the field of calix[*n*]pyrin chemistry is growing rapidly and is opening up

new opportunities in the porphyrin analogue area. Recently, the step-wise synthesis and binding process of calixphyrins are exploited by Sessler and co-workers. [60-62]

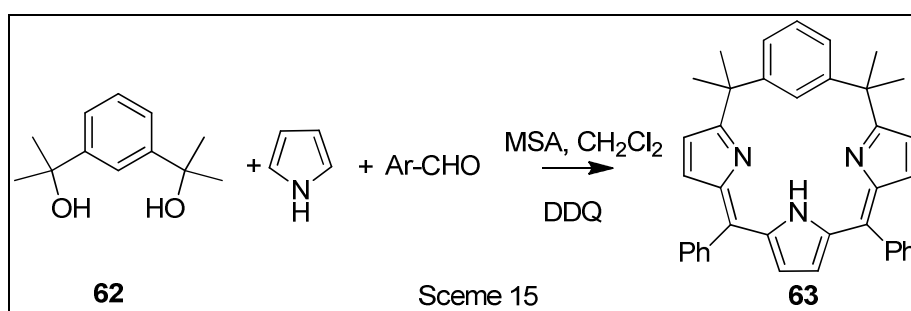
1.7. Expanded and core-modified calixphyrins

Sessler and co-workers have demonstrated the synthesis of first expanded calixphyrin. The acid-catalyzed condensation of mesityl dipyrromethane **59** with acetone followed by oxidation with DDQ, along with normal calixphyrins, such as diaryl tetraalkyl porphodimethenes, affords higher order homologues **60** and **61** in 13% and 08% yield, (Scheme 14) respectively. [63]

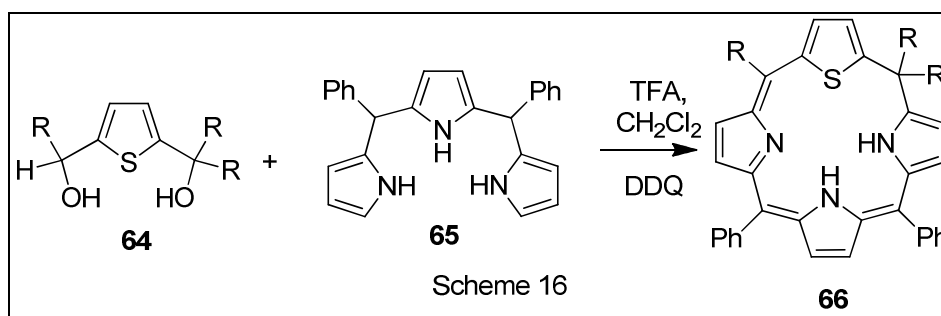


In 2004, Latos Grażyński and co-workers described the synthesis of core modified calixphyrin, thus, they introduced benzene ring in the macrocyclic framework. The acid-catalyzed condensation of 1,5-bis(diphenylhydroxymethyl)benzene, pyrrole and *p*-nitrobenzaldehyde followed by oxidation afforded benziporphodimethene in 14% yield. The coordination chemistry was further performed by using divalent metal complexes such as Ni(II), Zn(II) and Cd(II), where the NMR spectral analyses of Ni(II) complex reflected the paramagnetic nature of the complex and single crystal X-ray analysis showed the weak agostic metal-arene interactions. [64]

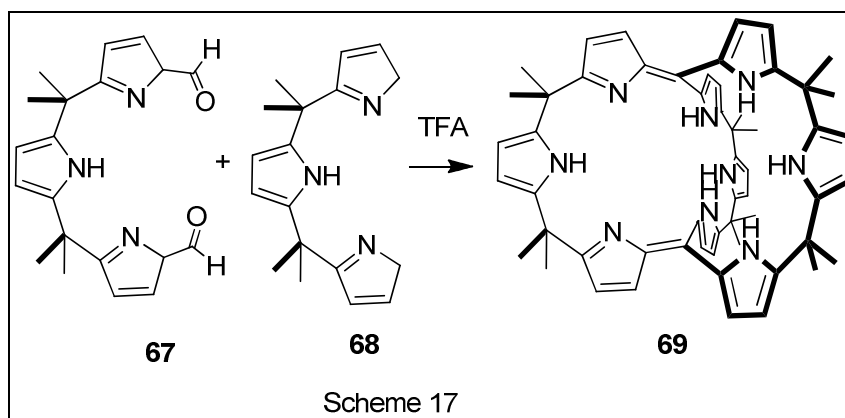
In 2007, C. H. Hung et.al have also reported similar type of porphodimethenes, where the acid-catalyzed condensation of 1,5-bis(dimethylhydroxymethyl)benzene **62** with pyrrole and aryl aldehyde gave **63** in 27% yield (Scheme 15). The Zn^{2+} complex of **63** showed the long wavelength absorption and also the turn-on fluorescent emission at 672 nm with the quantum yield of 0.34 reflects the chemosensor properties of **63**. [65]



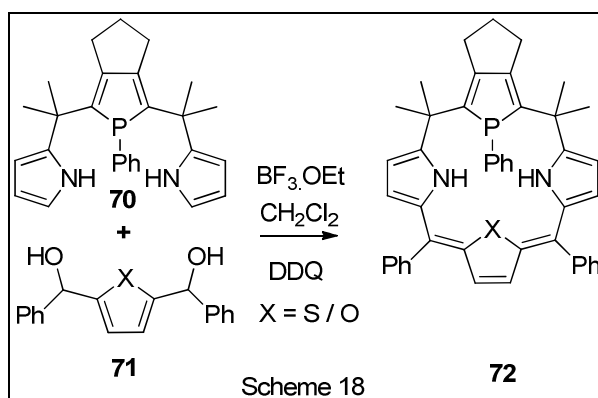
Recently, Ravikanth and co-workers have also synthesized thia-analogue of calix[4]phyrin-(1.1.1.1) **66** starting from 2,5-bis(diphenylhydroxymethyl)thiophene **64** with tripyrromethane **65** afforded in 15% yield (scheme 16). [66]



Interestingly, in 2003, Sessler and co-workers have synthesized the cryptand like three dimensional calixphyrin **69** from diformyl tripyrromethane **67** and tripyrromethane **68** precursors, in the presence of acid-catalyst followed by oxidation afforded in 08% yield, respectively (Scheme 17). The single crystal X-ray analysis confirmed the proposed novel calixphyrin like three dimensional structure for **69**. Also, revealed the presence of H_2O molecule inside the cavity, which supported that such system could have a role to play in the area of substrate specific molecular recognition. [67]



In the year 2006, Matano and co-workers demonstrated the phosphole-containing hybrids which exhibited characteristic coordination behavior derived from both the phosphole ring and the π -conjugated pyrrole-heterole-pyrrole (N-X-N) subunits. The synthesis of phosphole-containing hybrid calixphyrin was done by treatment of 2,5-bis[pyrrol-2-yl)methyl]phosphole **70** and 2,5-bis[phenylhydroxymethyl]thiophene **71** in the presence of acid-catalyst such as $\text{BF}_3 \cdot \text{OEt}_2$ followed by oxidation with DDQ afforded **72** in 15% yield (Scheme 18), respectively. Further, they introduced the new class of calixphyrin transition metal catalysts by synthesizing a Pd(II) complex and was found to catalyze the Heck reaction with high efficiency. The coordination number and the oxidation state at the metal center are controllable by the flexible calixphyrin framework. Similarly, they reported the thiophene analogue of calixphyrin as well (Scheme 19). [68,69]



1.8. Molecular Receptors

Molecular receptors are host molecules which specifically and selectively recognize certain guest molecules and ions such as anions, cations and neutral substrates. Interactions between host and guest can be donor-acceptor interaction, hydrogen-bonding, dipole-dipole interaction, electrostatic interaction. The size and shape of the ions play a major role where cations are normally spherical in shape and anion of different shapes like CO_3^{2-} has a planar shape, SO_4^{2-} has a tetrahedral shape, N_3^- has a linear shape while F^- and Cl^- are spherical in shape. For cation recognition, the size of the cation has to be considered. However, for the anion receptor both size and shape has to be considered when designing the receptor for the anions. Some of the examples of molecular receptors are crown ethers, cryptands, cyclodextrins, calixpyrroles, calixarenes and expanded porphyrins. [70]

1.9. Anion Binding

Anions play an important role in biological, medical, chemical and environmental processes. Hence, the anion recognition and sensing continue to attract the researchers because of its challenges in the mentioned areas. Therefore the ability to detect and quantify such anions is of particular importance [70]. While designing molecular receptors, should have the significant binding affinities and selectivity like by naturally occurring biological anion receptors such as proteins, so that it can be used for real world applications. These systems possesses multiple balancing hydrogen-bonding interactions to bind their target guest anions within complicated three-dimensional cavities buried deep below the surfaces of the proteins [71,72].

Recently, Sessler and co-workers proved that calixpyrroles are best suited for selective binding of anions in sensing mode or for purification/removal of anions from mixtures when bound to solid supports [60]. However, compared to calixpyrroles,

calixphyrins are less explored for anion binding studies. This may be explained by the fact that the more reduced calixphyrins have less N–H bonds to interact via electrostatic hydrogen bonds with anions [61-63]. However, protonation of the basic di or oligopyrrin units in the macrocycle significantly increases the anion binding. An advantage of calixphyrins is that they (and certainly their protonated forms) contain a strong chromophore which helps to visualize the binding experiments by simple analytical techniques such as Uv-Vis spectroscopy and photometry. Initial reports on calix[n]phyrins, Sessler et al. demonstrated the synthesis of three calixphyrins and performed the receptor properties by using various anions and monitored the binding event by electronic spectral analysis. The “deep cavity” calix[6]phyrin was not bind with anions unless it was protonated. The single crystal X-ray analysis confirmed that the chloride was firmly located in the cavity [60,63]. Recent years various calixphyrins with expanded, core-modified and functional group attached were reported for anion binding studies, such details, which we have discussed further in the respective chapter.

1.10. Aggregation Induced Enhanced Emission

Recent years, the design and synthesis of potential luminophores is an attractive research topic in the field of molecular imaging technology, photonics and electronic devices, as fluorescent probes in molecular biology, photosensitizers in dye-sensitized solar cells and dye lasers, and many more. In general, many fluorophores are emissive when it is in solution state. However, when they are fabricated into solid state or films for device applications, which undergo the well-known effect of aggregation caused quenching (ACQ) [73,74]. Planar luminophores tend to aggregate in solid state or in film or in a higher concentrated solution like as discs pile up due to strong π - π stacking interaction as shown in the below

Figure 1.1, which commonly turns non-emissive because these stacking often induces non-radiative energy transfer [75].

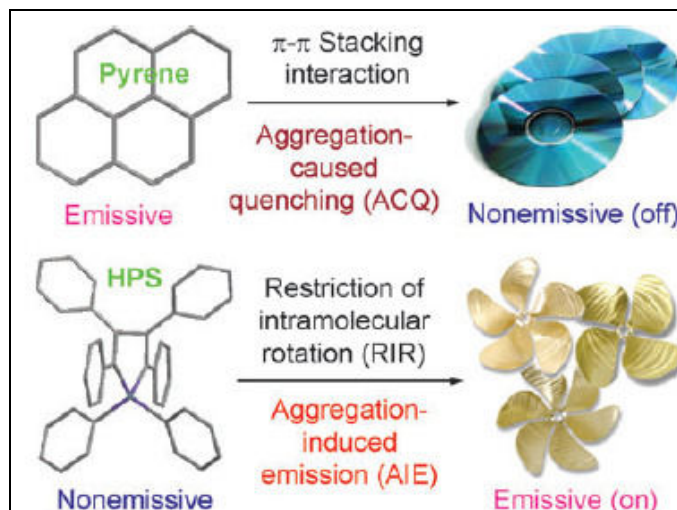


Figure 1.1: Aggregation mode of π stacking molecules

This ACQ effect is the hurdle for luminophores to use them for real world applications. Moreover, as we know, most of our biological system deal with water is major component, and since water is not a good solvent for almost all organic fluorophores. So, the molecules get aggregated due to which they can not act as a good and effective sensors in biological system. However, there are molecules, which are weakly emissive or nonemissive in dilute solution but when they are in aggregated state, they show intense emission. This phenomena is known as aggregation induced enhanced emission (AIEE) or aggregation induced emission (AIE) respectively. [74,76]

Tang and co-workers and other researchers proposed the following effects need to be taken into consideration with respect to the luminophore moiety in the aggregated states: [74]

- (i) Conformational planarization
- (ii) Prevention of close intermolecular interaction that leads to emission quenching
- (iii) Restriction of intramolecular rotation (RIR).

Scope of the present thesis:

In light of the extensive literature discussion covering the chemistry of fused and bridged expanded porphyrins and also the receptor properties of expanded calixphyrins, it is clear that the synthesis of new bridged and fused variants has been a growing area of highly interdisciplinary research over the last decade. In the present thesis, an attempt has been made to carry out a simple novel precursor in order to maintain the planarity and aromaticity of the expanded derivatives, which are difficult to maintain for more than six heterocyclic rings present in the expanded porphyrins framework. The main content of the thesis includes synthesis, spectral, structural and photodynamic studies of such novel expanded porphyrins. The goal, therefore, is to provide easy and simple synthetic methodologies to prepare fused, bridged expanded porphyrins and expanded calixphyrins.

In the second chapter, the synthesis of novel dithienothiophene precursor (DTT) is discussed, which is the important building block for the synthesis of bridged and fused expanded porphyrin. The other precursors required for the synthesis of expanded porphyrin and calixphyrin such as heterocyclic diol and tripyrromethane are also discussed in this chapter.

In the third chapter, we have demonstrated the synthesis of core-modified analogues of internally bridged expanded porphyrins with dual aromatic character. The synthetic methodology adopted here is simple and straight-forward. Interestingly, depending on the heteroatom present in the core such as Sulfur or Selenium atom, the participation of bridging thiophene ring in the π electron conjugation pathway are different and exhibit hybrid aromatic character revealed by spectroscopic studies. The structural analyses further confirm that the hexaphyrin macrocycle is planar and aromatic and that the internal bridging thiophene ring deviates from the mean plane of *meso* carbon atoms. The spectral data of these

bridged hexaphyrins are more planar, thus facilitating better a π conjugation pathway and therefore increasing the aromaticity, as compared to its core-modified congeners. The preliminary photophysical studies reveal an increase of singlet lifetime by two times upon introduction of bridge, which is presumably due to increased rigidity of the macrocycle.

The fourth chapter describes the synthesis, spectral, structural and photophysical characterization of fused derivative of expanded porphyrin such as doubly fused octaphyrins. These are synthesized by simple acid-catalyzed condensation of appropriate precursors followed by oxidation with DDQ. The single-crystal X-ray structure shows a figure-eight twisted conformation. Spectroscopic and quantum mechanical calculations reveal that both the octaphyrin conform to a $[4n]\pi$ nonaromatic electronic structure. Protonation of the pyrrole nitrogen atoms results in dramatic structural change from twisted figure-eight to extended open structure. The spectral analysis, photodynamic studies, NICS values and AICD plot reveal the paratropic ring-currents with $[4n]\pi$ Hückel antiaromatic and further confirm by single-crystal X-ray structural analysis. The second part of this chapter discusses the synthesis and structural characterization of mono-fused sapphyrins and antiaromatic heptaphyrins.

Fifth chapter demonstrates the core-modified expanded calixphyrin synthesis and their important properties such as aggregation induced enhanced emission (AIEE) and anion receptor properties. The presence of *meso* phenyl substitution on the sp^3 carbons not only restricts the intramolecular rotations and inducing AIEE. Further, it also forces the macrocycle to adopt a distorted chair like conformation in the solid state. Furthermore, the anion binding properties reported here suggest that macrocycle has stronger affinity for tetrahedral ions.

General Experimental Methods and Technique

The detailed experimental procedure for synthesis of precursors and their important characterization technique used for analyze in the course of investigation are described in this chapter. Further, this chapter discusses the materials and methods employed for synthesis and characterization.

2.1 Chemicals for syntheses

All anhydrous solvents used for the reactions and analyses were purified and dried by standard purification procedure [77,78]. Pyrrole, thiophene and furan were purchased from Sigma-Aldrich and were distilled before use. Selenophene, Tolualdehyde, Mesitaldehyde, *p*-Chloroanil, DDQ, 2,2'-bithiophene, *n*-butyllithium, Trifluoroacetic acid, *p*-Toluenesulphonic acid, methane sulphonic acid and deuterated solvents for NMR measurement were used as received from Sigma-Aldrich. Aluminium oxide and silica gel for column chromatography were purchased from Merck. *N,N,N,N*-Tetramethylethylenediamine was procured from Sigma-Aldrich and distilled over KOH before use [77]. Tetrabutylammonium hexafluorophosphate was procured from Sigma-Aldrich and vacuum dried in desiccator for more than 2h before use.

2.2 Physico-chemical techniques:

ESI-Mass analysis: Masses of the compounds were recorded by electron spray ionization-mass spectra-Time of flight (ESI-MS-TOF) instrument of Bruker, micrOTOF-QII mass spectrometer.

NMR measurements: NMR spectra were recorded on a Bruker (400 MHz) spectrometer. The NMR protonation titration experiments were carried out with TFA solution quantitatively dissolved in deuterated solvent. Chemical shifts are expressed in parts per million (ppm) relative to TMS, unless otherwise specified.

Spectrophotometer analysis: Steady-state absorption measurement, electronic absorption spectra were recorded with Perkin Elmer – Lambda 750 UV-Visible spectrophotometer and data analyses were done using the UV-winlab software package. Fluorescence spectra were recorded on a Perkin Elmer LS55 Fluorescence spectrometer. Fluorescence quantum yields in solution state were determined using fluorescein in 0.1M NaOH ($\Phi_f = 0.95$) as a reference.

Femto-second Transient Absorption Measurement: The femtosecond time-resolved transient absorption (TA) spectrometer consist of a homemade noncollinear optical parametric amplifier (NOPA) pumped by a Ti:sapphire regenerative amplifier system (Quantronix, Integra-C) operating at 1 kHz repetition rate and an optical detection system. The generated visible NOPA pulses had a pulse width of ~100 fs and an average power of 1mW in the range 500-700 nm which was used as pump pulses. White light continuum (WLC) probe pulses were generated using a sapphire window (3mm of thickness) by focusing of small portion of the fundamental 800 nm pulses which was picked off by a quartz plate before entering to the NOPA. The time delay between pump and probe beams was controlled by making the pump beam travel along a variable optical delay (Newport, ILS250). Intensities of the spectrally dispersed WLC probe pulses are monitored by miniature spectrograph (OceanOptics, USB2000+). The polarization angle between pump and probe beam was set at the magic angle (54.7°) in order to prevent polarization-dependent signals. Cross-correlation fwhm in pump-probe experiments was less than 200 fs and chirp of WLC

probe pulses was measured to be 800 fs in the 400-800 nm region. To minimize chirp, all reflection optics in probe beam path and 2 mm path length of quartz cell were used.

Two-photon Absorption Measurement: The TPA measurements were performed using the open-aperture Z-scan method with 130 fs pulses from an optical parametric amplifier (Light Conversion, TOPAS) operating at a 2 kHz repetition rate using a Ti:sapphire regenerative amplifier system (Spectra-Physics, Hurricane X). After passing through a $f=10$ cm lens, the laser beam was focused to 1 mm-quartz cell. As the position of the sample cell was varied along the laser-beam direction (z-axis), the transmitted laser beam from the sample cell was then probed using a Ge/PN photodiode (New Focus, 2033) as used for reference monitoring.

Quantum Mechanical Calculations: All calculations were carried out using the Gaussian 09 program. Initial geometries were obtained from X-ray structures. All structures were fully optimized without any symmetry restriction. The calculations were performed by the density functional theory (DFT) method with restricted B3LYP (Becke's three-parameter hybrid exchange functionals and the Lee-Yang-Parr correlation functional) level, employing a basis set 6-311G (d,p). The nucleus independent chemical shift (NICS) values were obtained with the GIAO method at the B3LYP/6-311G (d,p) level. The global ring centers for the NICS values were designated at the non-weighted means of the carbon and sulfur coordinates on the peripheral positions of macrocycles. In addition, NICS values were also calculated on centre of other local cyclic structures [79-82].

X-ray Diffraction Analysis: The single crystals for the X-ray analysis were grown by appropriate solvents. X-ray data were recorded on a BRUKER-APEX X-ray diffractometer equipped with a large area CCD detector in 100 K. The structures were solved by Patterson synthesis and refined with the SHELX-97 programs [83]. These data can be obtained free of charge from the Cambridge crystallographic data centre via www.ccdc.cam.ac.uk/data_request.cif.

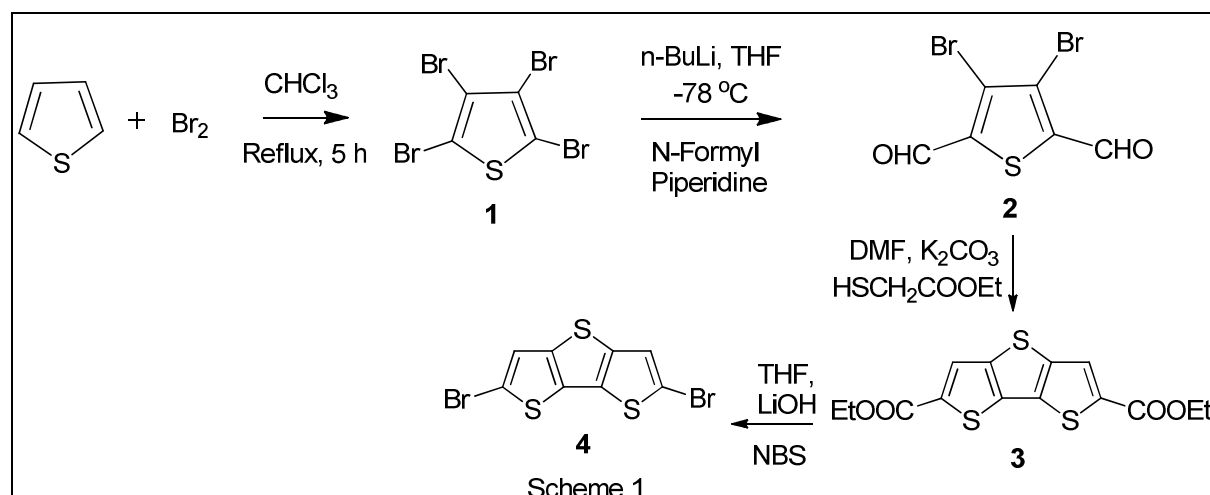
Dynamic light scattering: DLS analyses were carried out with a Zeta sizer Nano from Malvern Instruments at 25°C.

Scanning electron microscope: SEM analysis was carried out using Zeiss Carl instrument.

Voltammetry: Cyclic voltammetry and differential pulse voltammetry (CV & DPV) experiments were done on CHI model 620B, CH-instruments Inc., interfaced to computer. Three electrode system was used which consist of glassy carbon working electrode, platinum counter electrode and Ag/AgNO₃ reference electrode.

2.3 Experimental Procedure:

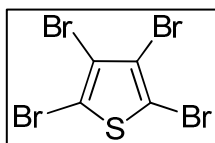
The essential precursors required for the synthesis of core-modified macrocycles described in this thesis such as bridged & fused expanded porphyrin [84-87] and expanded calixphyrin [88,89] are described in Scheme 1-7.



Tetrabromothiophene (1):

22 ml (0.431mol) Br₂ was slowly added into the mixture of 8 mL (8.4 g, 0.1 mol) thiophene and 3 mL CHCl₃ in 2h on ice bath. The reaction mixture was refluxed for 5h, then, cooled to ambient temperature. To the reaction mixture 5 mL of 2N NaOH was added and

vigorously stirred for 30 min. The solid product was separated, washed with water and crystallized over hot CHCl_3 . The white crystals of **1** were obtained in

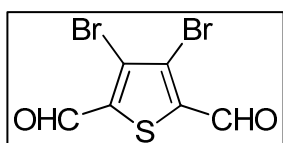


75 % yield (16.0 g)

^{13}C NMR (100 MHz, CDCl_3 , 298 K): δ (ppm): 117.10, 110.44

3,4-dibromo-2,5-diformylthiophene (**2**):

An oven-dried, three-necked round-bottomed flask (1L) was equipped with a magnetic stir bar, a low temperature thermometer, a rubber septum and a three-way stopcock. Under a gentle flow of argon, the flask is added with tetrabromothiophene (16.0 g, 40.0 mmol) and freshly-distilled tetrahydrofuran (200 mL). The solution was cooled in a methanol/2-propanol bath with an internal temperature of less than $-65\text{ }^\circ\text{C}$ and a solution of *n*-butyllithium (50 mL, 1.6 M in hexane, 80 mmol) was added via syringe. The addition proceeds at a rate that keeps the internal temperature below $-60\text{ }^\circ\text{C}$, usually taking 15 min. When the addition was complete, the brown solution was stirred at about $-65\text{ }^\circ\text{C}$ for 30 min., anhyd. *N*-formylpiperidine (10 mL, 90 mmol) was added quickly by syringe to the reaction mixture, which was then allowed to warm slowly to ambient temperature overnight. The reaction mixture was cooled to $0\text{ }^\circ\text{C}$ in an ice-water bath, and hydrochloric acid (100 mL, 6 M) was added slowly to the reaction mixture, causing a yellow precipitate to form. The mixture was stirred at $0\text{ }^\circ\text{C}$ for 45 min then filtered immediately under vacuum through a sintered-glass funnel. The solid was washed with water (150 mL) and dried in the funnel under vacuum for 30 min before being dried further in a vacuum desiccator (25 mmHg,



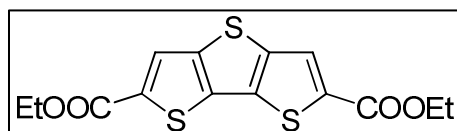
overnight, silica gel desiccant with moisture indicator) to give **2** in

70% yield (8.8 g).

^1H NMR (400 MHz, CDCl_3 , 298 K): δ (ppm): 10.12 (s, 2H)

Dithieno[3,2-b:2',3'-d]thiophene-2,6-dicarboxylic acid diethyl ester (3):

In an oven-dried 500-mL, two-necked round-bottomed flask equipped with a magnetic stir bar, nitrogen inlet and rubber septum, **2** (8.0 g, 26.9 mmol) was suspended in anhydrous N,N-dimethylformamide (250 mL), anhydrous potassium carbonate (9.65 g, 69.8 mmol) and ethyl 2-mercaptoacetate (6 mL, 55 mmol) were added to the slurry, causing a slight exotherm, and the reaction mixture was stirred under nitrogen at ambient temperature for three days. The dark solution was poured into a beaker containing 500 mL of water stirred with a magnetic stir bar, and a yellow precipitate forms. The aqueous suspension was extracted with CH₂Cl₂ (3 × 250 mL). The red organic extracts were combined, washed with brine (4 × 500 mL) and dried over anhydrous magnesium Sulphate. After filtration through fluted filter paper, the solvent was evaporated on a rotary evaporator and a yellow solid begins to form. When the volume of solvent remain about 100 mL, yellow color solid formed and it was filtered under vacuum on a Büchner funnel, washed with water (100 mL) and dried in a vacuum desiccator overnight (7–8 mm Hg, silica gel desiccant with moisture indicator) to give the crude diester. Yield: 6.5 g, 74%

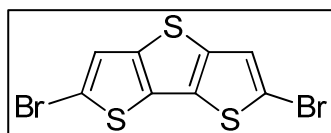


¹H NMR (400 MHz, CDCl₃, 298 K): δ (ppm): 8.03 (s, 2H); 4.44 (q, 4H); 1.42 (t, 6H)

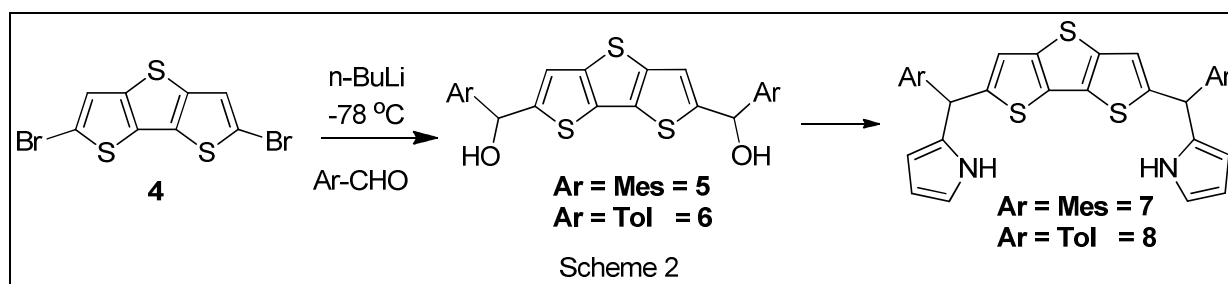
Synthesis of 2,6-dibromo dithieno[3,2-b;2',3'-d]thiophene (4):

To a suspension of DTT-diester **3** (2.5g, 7.3mmol) 40 mL of 1M aqueous solution of LiOH was added. The reaction mixture was refluxed for 3h and water was added to give a clear brownish yellow solution. Excess N-bromosuccinimide (6.28g, 35.3mmol) was then added and the reaction mixture was stirred overnight at ambient temperature. The reaction mixture was then extracted with CH₂Cl₂. The organic layers were washed with saturated NaHCO₃ water and brine, and dried with anhydrous sodium sulphate. After the solvent was

removed under reduced pressure, the residue was precipitated with ethanol and then filtered to give a white solid (1.7g, 85%). The melting point was recorded to be 164° C. (lit m.p. 162-163° C).



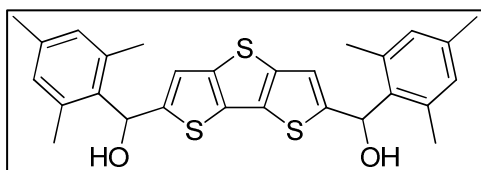
$^1\text{H NMR}$ (400 MHz, CDCl_3 , 298 K): δ (ppm): 7.279 (s, 2H)



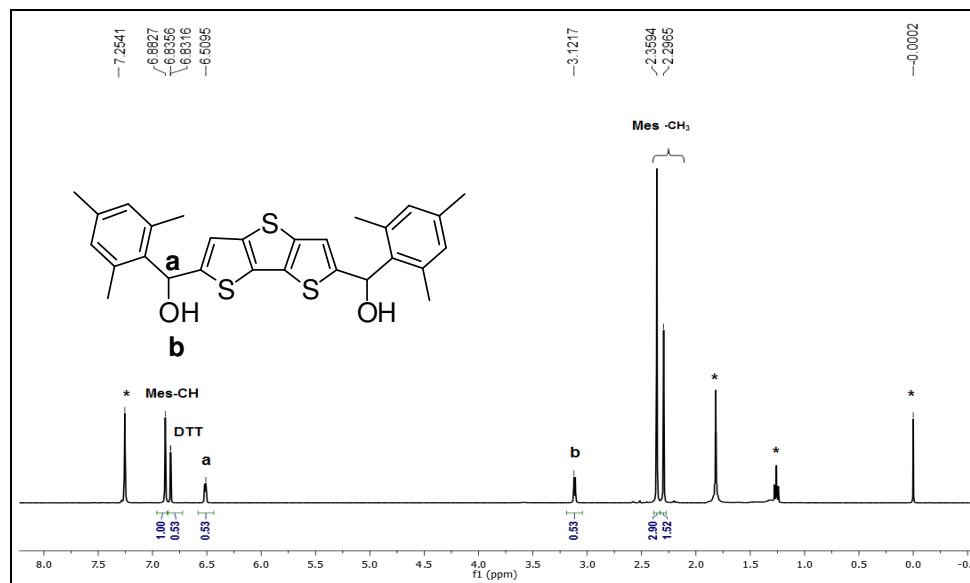
5,5'-Bis-(mesitylhydroxymethyl)-dithienothiophene–(DTT diol) (5) :

To a solution of **4** (0.7 g, 3.5 mmol) in 50 ml THF, n-Butyllithium (5 ml 1.6 M, 7.8 mmol) was added slowly at -78°C under inert atmosphere. It was allowed to stir for 1h. Mesitylaldehyde (1.154 g, 7.8 mmol) in 30 ml of THF was added drop wise at 273 K. The mixture was allowed to warm to room temperature and stirred further for 1h. To the reaction mixture 75 ml of saturated ammonium chloride solution was added and extracted with diethyl ether. The organic layers were combined, washed with brine and dried over sodium sulphate. After evaporation, the crude was subjected to silica gel column (100-200 mesh) chromatography with ethyl acetate: Hexane (1:5) afforded **5** in 63% yield.

$^1\text{H NMR}$ (400 MHz, CDCl_3 , 298 K) δ (ppm): 6.88 (s, 4H), 6.78 (s, 2H), 6.51 (s, 2H), 2.35 (s,

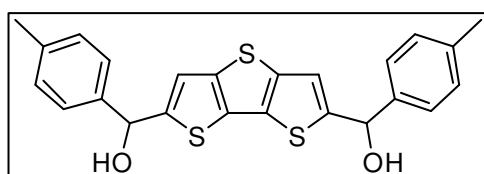


12H), 2.29 (s, 6H); ESI-MS: m/z : 492.36 $[\text{M}]^+$, Calcd for $\text{C}_{28}\text{H}_{28}\text{O}_2\text{S}_3$: 492.13



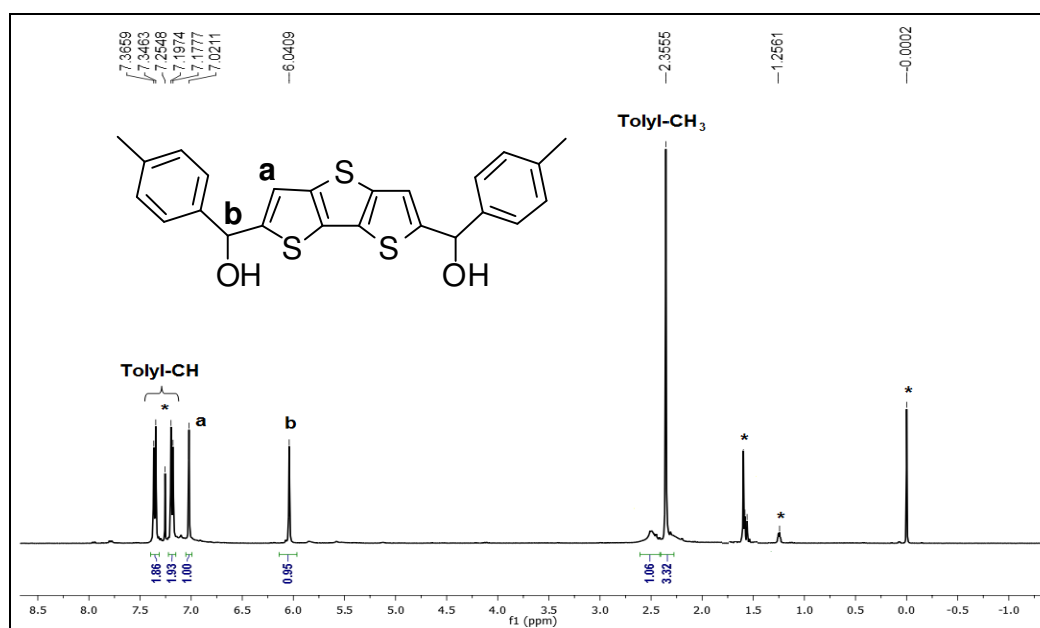
5,5'-Bis-(tolylhydroxymethyl)-dithienothiophene-DTT diol (6):

Following the procedure of **5**, diol **6** was prepared by using tolualdehyde instead of mesitaldehyde.



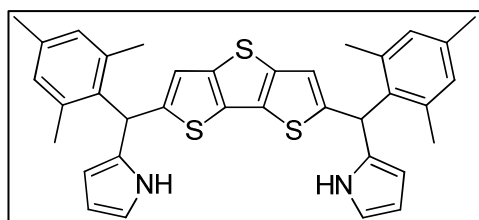
^1H NMR (400 MHz, CDCl_3 , 298 K) δ (ppm) : 7.3 (d, 4H), 7.22 (d, 2H), 7.02 (s, 2H), 6.04 (s, 2H), 7.36 (d, $^3J=8\text{Hz}$, 2H), 7.19 (d, $^3J=8\text{Hz}$, 2H) 6.51 (s, 2H), 2.32

(s, 6H); ESI-MS: m/z : 436.24 (54%) $[\text{M}]^+$, Calcd for $\text{C}_{24}\text{H}_{20}\text{O}_2\text{S}_3$: 436.16



DTT-Mes-dipyrane (7)

5, 5'-bis-(mesitylhydroxylmethyl)dithienothiophene (DTT-mes-diol) **5** (0.5g, 1.01mmol), pyrrole (3.66 ml, 56.5mmol) was added and the mixture was degassed by bubbling nitrogen gas. To this solution TFA (0.03, 0.38mmol) was added and the reaction mixture was stirred for about 30 min at room temperature. After completion of the reaction, CH_2Cl_2 (100 ml) was added and the reaction mixture was neutralized with 0.1M NaOH solution. The organic layer was separated and washed two times with water (50 ml) then dried over sodium sulphate. The solvent and excess pyrrole was removed by vacuum. The crude product obtained was purified by silica gel (100-200 mesh) column chromatography

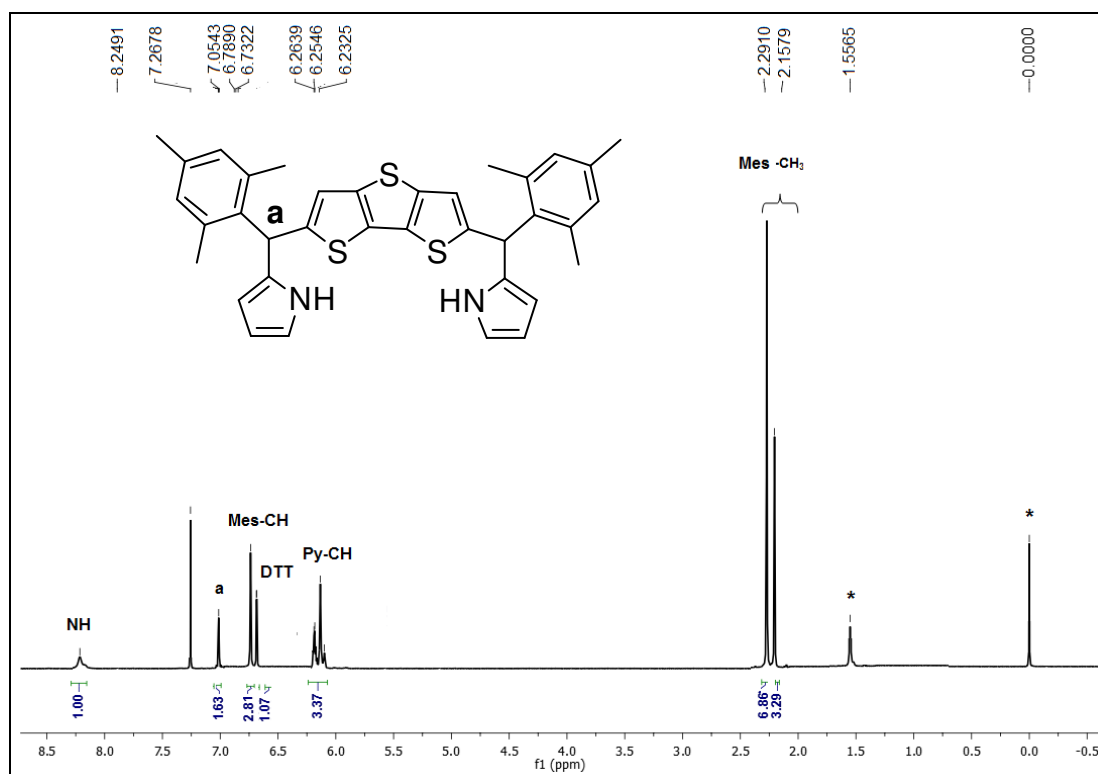


with ethyl acetate/hexane (8:92, vol/vol) **7** was obtained as yellow semi-solid. Yield:85%.

ESI-MS: m/z (%): calcd for $\text{C}_{36}\text{H}_{34}\text{N}_2\text{S}_3+\text{H}^+$:

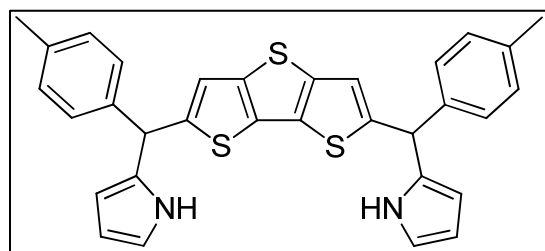
590.1884; found: 590.1127; ^1H NMR (400 MHz, CDCl_3 , 298 K), δ [ppm]: 8.24 (brs, 2H),

7.05 (s, 2H), 6.79 (s, 4H), 6.73 (s, 2H), 6.26-6.23 (m, 6H), 2.29 (s, 12H), 2.16 (s, 6H).



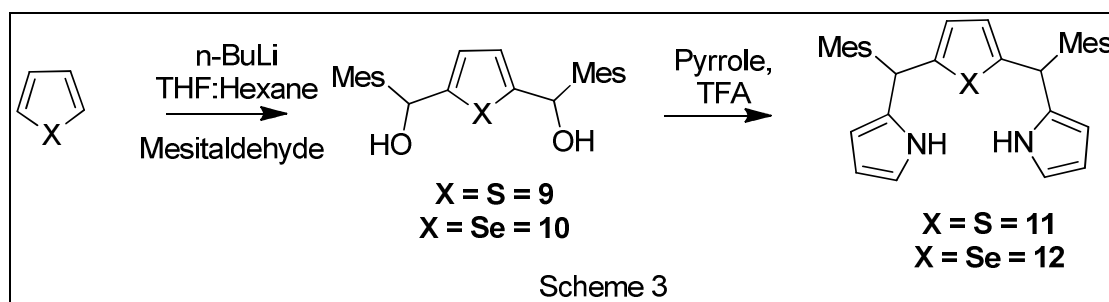
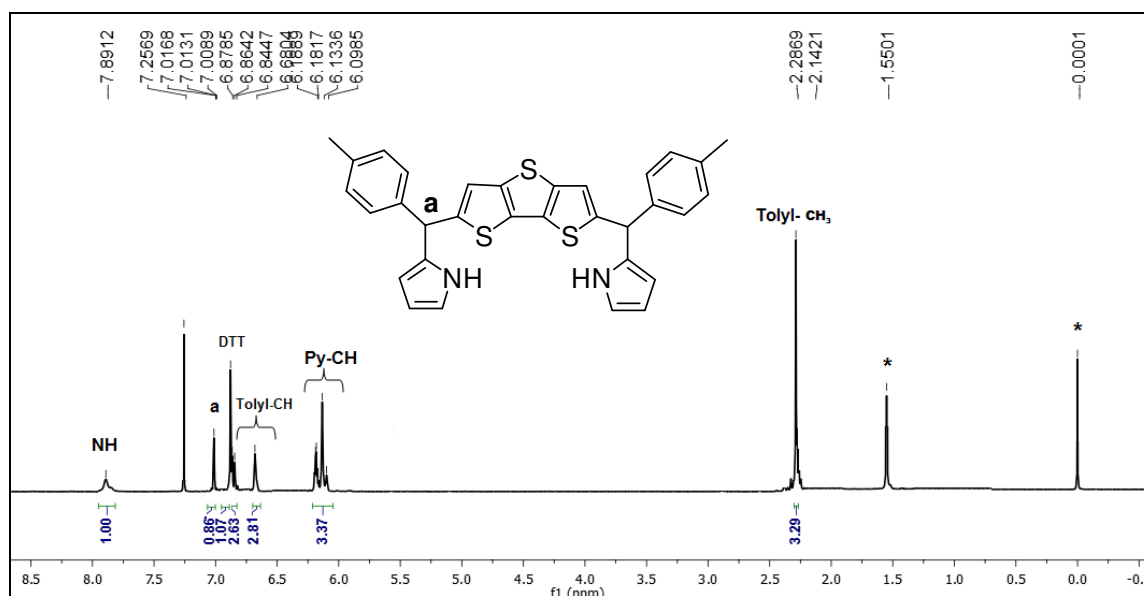
DTT-Tol-dipyrane (8)

The above procedure was used with 5, 5'-bis-(tolylhydroxymethyl)dithienothiophene (DTT-tolyl-diol) (0.5g, 1.15mmol). The crude product obtained was purified by silica gel (100-200 mesh) column chromatography with ethyl acetate/hexane (8:92, vol/vol) **8** was obtained as yellow semi-solid. Yield:82%.



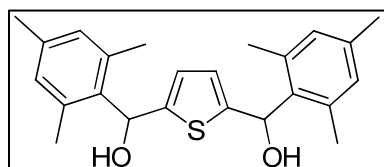
8: ESI-MS: m/z (%): m/z calcd for $C_{32}H_{26}N_2S_3+H^+$: 534.1258; found: 534.1378; 1H NMR (400 MHz, $CDCl_3$, 298 K), δ [ppm]: 7.89 (brs, 2H), 7.01 (s, 2H), 7.00 (s, 2H), 6.87 (s, 2H),

6.85 (d, $^3J=8\text{Hz}$, 4H), 6.68 (d, $^3J=8\text{Hz}$, 4H), 6.18-6.09 (m, 6H) 2.28 (s, 6H).



2, 5 bis-(mesitylhydroxymethyl)thiophene (9):

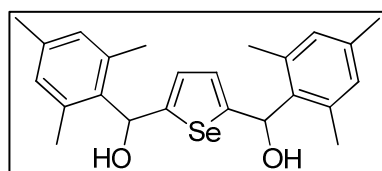
To a solution of N,N,N',N'-tetramethylethylene diamine (4.03 mL, 26.75 mmol) in dry n-hexane (80 mL), n-butyllithium (1.6 M hexane, 17.8 mL, 26.75 mmol) was added followed by thiophene (0.72 mL, 8.9 mmol) under argon atmosphere. The reaction mixture was stirred at room temperature for an hour and later heated under reflux for 1h. The reaction mixture was then allowed to attain the room temperature. Then, it was ice cooled and a solution of Mesityldehyde (3.28 mL, 22.28 mmol) in dry THF (12.5 mL) was added drop wise to it under continuous stirring. After the addition was over, the reaction mixture was allowed to attain room temperature and saturated ammonium chloride solution was added and it was then extracted with ether solvent. The organic layers were combined and washed with brine (60 mL) and dried over anhydrous sodium sulphate. The crude product obtained on evaporation of the solvent was purified by silica gel chromatography (100-200 mesh) with ethyl acetate: hexane (20:80), **9** was obtained as white solid. Yield: 55%.



$^1\text{H NMR}$ (400 MHz, CDCl_3 , 298 K): δ (ppm) = 1.65 (brs, 2H), 2.27 (s, 6H), 2.32 (s, 12H), 6.37- 6.41 (m, 4H), 6.84 (s, 4H)

Synthesis of 2,5 bis-(mesitylhydroxymethyl)selenophene (10) :

Following the procedure of **9**, **10** was synthesized by using selenophene in 48% yield.

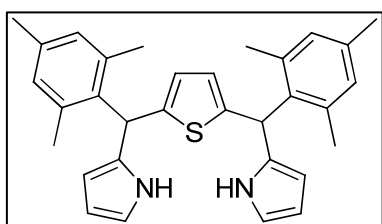


$^1\text{H NMR}$ (400 MHz, CDCl_3 , 298 K): δ (ppm): 1.62 (brs, 2H), 2.25 (s, 6H), 2.31 (s, 12H), 6.34 (s, 1H), 6.35 (s, 1H), 6.50 (s, 1H), 6.52 (s, 1H), 6.82 (s, 4H)

Synthesis of 5,10 dimesityl-16-thiatripyrrane (11):

A mixture of **9** (1g, 2.63 mmol) and pyrrole (7.3 mL, 105.28 mmol) was degassed by bubbling nitrogen gas. Trifluoroacetic acid (TFA) (0.06 mL, 0.79 mmol) was added to this solution and the mixture was stirred for about 30 min at room temperature. After completion

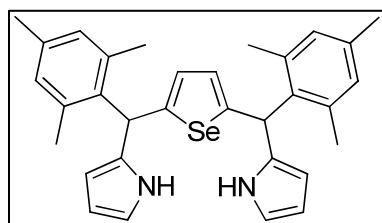
of the reaction, CH_2Cl_2 (100 mL) was added and the reaction mixture was neutralized with 0.1M NaOH solution. The organic layer was separated and washed two times with water before drying over sodium sulphate. The solvent and excess pyrrole was removed by vacuum. The crude product was purified by silica gel column chromatography (100-200 mesh) with ethyl acetate and petroleum ether (3:97) gave the desired tripyrrane **11** as a yellow band in 90% yield.



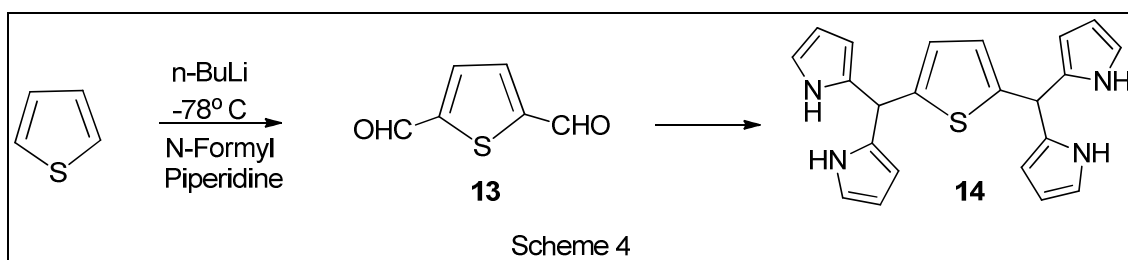
$^1\text{H NMR}$ (400 MHz, CDCl_3 , 298 K): δ (ppm): 2.11 (s, 12H), 2.26 (s, 6H), 5.98-6.02 (m, 4H), 6.13-6.156 (m, 2H), 6.60-6.64 (m, 4H), 6.84 (s, 2H), 7.84 (brs, 2H)

Synthesis of 5,10-dimesityl-16-selenatripyrrane [12]:

2,5-bis(mesityl hydroxymethyl)selenophene **10** (1 g, 2.34 mmol), pyrrole (5 ml, 93.6 mol) and TFA (0.018 ml, 0.235 mmol) under similar reaction conditions as mentioned above gave dark yellow semi solid identified as **12** in 90% yield.



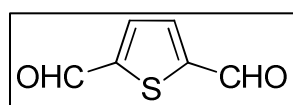
$^1\text{H NMR}$ (400 MHz, CDCl_3 , 298 K): δ (ppm): 2.12 (s, 12H), 2.24 (s, 6H), 6.0 (s, 2H), 6.05 (s, 2H), 6.12-6.16 (m, 2H), 6.61 (m, 2H), 6.79 (s, 2H), 6.83 (s, 4H), 7.84 (brs, 2H)



Synthesis of 2,5-thiophene dicarboxaldehyde (13):

A suspension of 2,5-dilithiothiophene was prepared by the addition of n-butyllithium (18.6 mL, 30 mmol) at room temperature to a mixture of N,N,N',N'-tetramethylethylenediamine (TMEDA (4.5 ml, 30 mmol), thiophene (1 g, 11.9 mmol) and n-

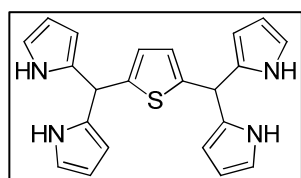
hexane (30ml). The temperature of thus obtained yellow suspension was raised to 40° C and the conversion was completed by refluxing for 30 min. Then 15 mL of THF was added, the solution was cooled to -40° C and excess DMF (2.3 mL, 32 mmol) was added over a period of 10 min. The temperature of the mixture was gradually raised to room temperature and stirring was continued for 30 min. The suspension was then poured into a mixture of 30% HCl and H₂O at -20 to -50 °C under vigorous stirring. Saturated NaHCO₃ solution was added until the aqueous layer pH becomes 6. The organic layer was separated and the aqueous layer was extracted with diethyl ether. The organic solution was evaporated by a rotavapour. The crude product thus obtained was purified by silica gel (100-200 mesh) chromatography; an orange band eluted with ethylacetate/hexane (20:80) identified as **13** 51% yield.



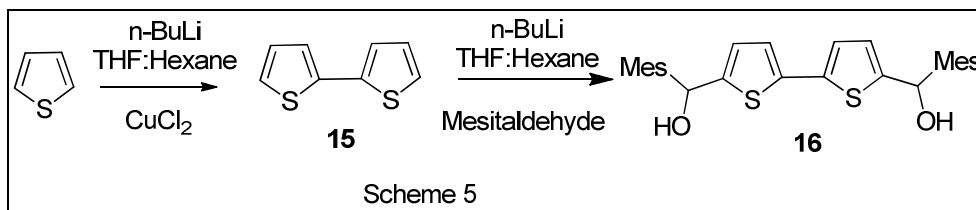
¹H NMR (400 MHz, CDCl₃, 298 K): δ (ppm): 7.85 (s, 2H); 10.05 (s, 2H)

Synthesis of 2,5-bis(dipyrrolylmethyl)thiophene (**14**):

A mixture of **13** (0.05 g, 3.6 mmol) and pyrrole (9.14 g, 143 mmol) was stirred under argon atmosphere for 5 min. To this solution trifluoroacetic acid (TFA) (0.1 mL, 0.86 mmol) was added and stirring was continued for 30 min. The reaction was quenched by adding 30 mL of CH₂Cl₂ and 20 mL of 0.1N NaOH. The organic layer was separated and washed with water. The excess pyrrole and solvent was removed by vacuum distillation. The residue was purified by chromatography on silica gel column (100-200) with ethyl acetate/petroleum ether (1:4) gave an orange band eluted of **14** in 47% yield.

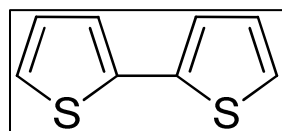


¹H NMR (400 MHz, CDCl₃, 298 K), δ (ppm): 7.98 (br, 4H), 6.72 (s, 2H), 6.68 (m, 4H), 6.14 (m, 4H) 6.02 (m, 4H), 5.64 (s, 2H).



Synthesis of Bithiophene (15):

To a solution of thiophene (1 g, 12 mmol) in 1:1 mixture of dry ether (20 mL) and dry THF (20 mL), n-BuLi (8.4 mL, 13 mmol) was added at -70 °C and allowed to stir for 2h at same temperature. After 2h CuCl₂ (2.88 g, 21 mmol) was added to the above mixture and it was quenched with saturated NH₄Cl (25 mL) solution at 0 °C. The reaction mixture was then extracted with ethyl acetate. The organic layers were combined and washed with brine. The crude product obtained on evaporation was purified by silica gel column chromatography (100-200 mesh). A colorless fraction eluted with petroleum afforded **15** as a white solid in 30% yield.

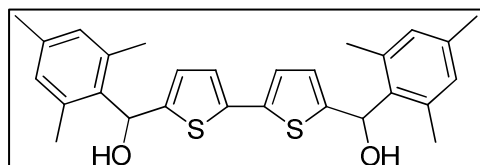


¹H NMR (400 MHz, CDCl₃, RT): δ (ppm): 7.21 (d, ³J = 1.2 Hz, 1H); 7.20 (d, ³J = 1.2 Hz, 1H); 7.18 (dd, 2H), 7.03 (dd, 2H)

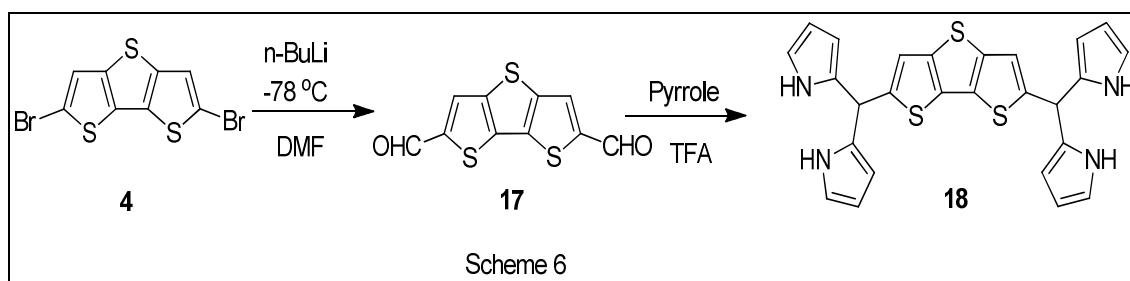
Synthesis of 5,5'-bis-(mesitylhydroxymethyl)-2,2'-bithiophene(16):

To a solution of N, N, N',N'-tetramethylethylenediamine (TMEDA) (2.7 mL, 18 mmol) in dry THF (40 ml), n-butyllithium (11 ml, 18 mmol) was added followed by 2,2'-bithiophene (1 g, 6 mmol) under nitrogen atmosphere. The reaction mixture was stirred at room temperature for 1h and later heated under reflux for 1h. The reaction mixture was then allowed to attain 25 °C. Mesitaldehyde (2.2 mL, 15 mmol) in dry THF was added drop wise to the reaction mixture at 0 °C. After addition was over, the reaction mixture was allowed to attain room temperature and saturated ammonium chloride (100 ml) was added to quench the reaction. The reaction mixture was extracted with diethylether. The organic layers were

combined and washed with brine and dried over anhydrous sodium sulphate. The crude product obtained on evaporation of solvent was purified by silica gel column chromatography (100-200 mesh). A yellow band eluted with ethyl acetate/petroleum ether (1:5) afforded the diol **3** as pale solid. Yield: 1.5 g, 54%

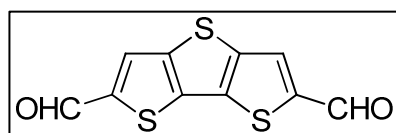


$^1\text{H NMR}$ (400 MHz, CDCl_3 , 298 K): δ (ppm): 6.91 (d, $J = 3.6$ Hz, 2H), 6.86 (s, 4H), 6.51 (m, 2H), 6.39 (d, $J = 3.6$ Hz, 2H), 2.33 (s, 12H), 2.28 (s, 6H), 1.57 (s, 2H).



Synthesis of dithieno[3,2-b;2',3'd]thiophene-2,5-dicarbaldehyde (**17**):

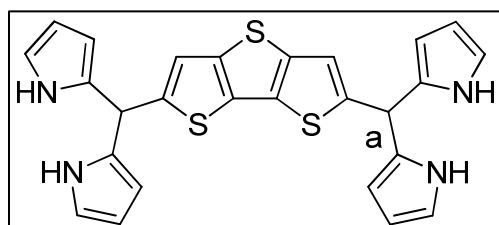
To a solution of **4** (0.5 g, 1.41 mmol) in 50 ml THF at -78 °C, n- Butyllithium (1.6 M in Hexane), (4.4 ml, 5.64 mmol) was added drop wise. After keeping the same temperature for 3 h, N,N'-dimethylformamide (DMF) (0.3 ml, 4.23 mmol) was added. The reaction mixture was warmed up slowly to room temperature and stirred for about 1h. After quenching with water, 5% citric acid was used to keep the pH at 5. The reaction mixture was extracted with CHCl_3 . Organic layers were combined and washed with NaHCO_3 and brine and dried over anhydrous sodium sulphate The crude product thus obtained was purified by silica gel column chromatography (100-200 mesh) with ethyl acetate/petroleum ether (1:4) in 25% yield.



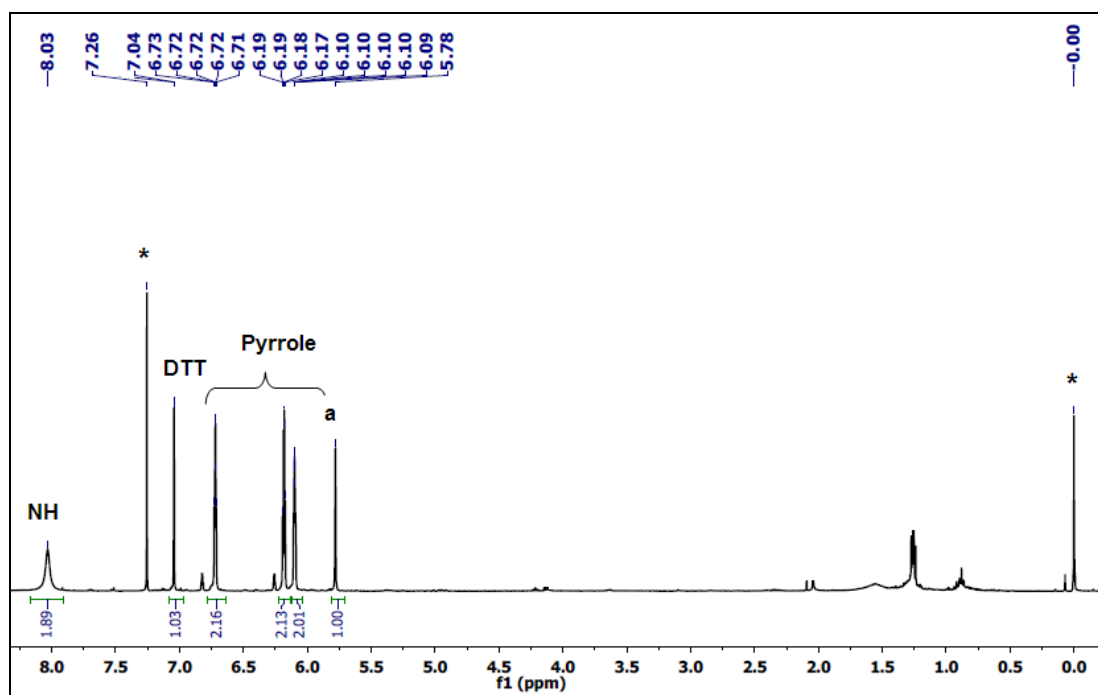
$^1\text{H NMR}$ (400 MHz, DMSO-d_6 , 298K): δ (ppm): 8.53 (s, 2H); 10.05 (s, 2H)

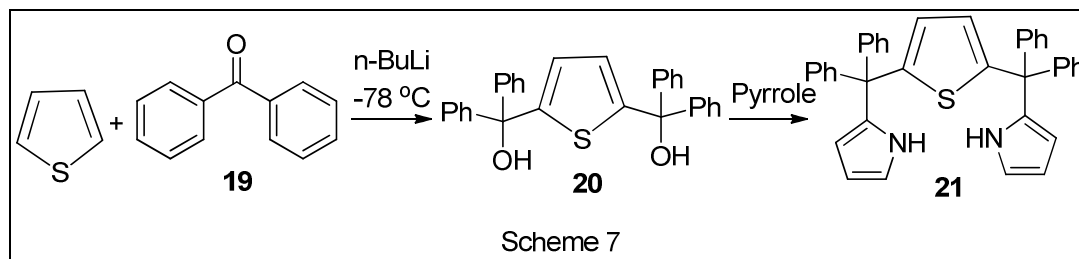
Synthesis of 2,5-bis(dipyrromethyl)dithienothiophene (18):

A mixture of **17** (0.2 g, 0.8 mmol) and pyrrole (2.14g, 32 mmol) were stirred under inert atmosphere for 5 minutes. Trifluoroacetic acid (0.015 ml, 0.2 mmol) was added and the stirring was continued for 3h. The reaction was quenched by adding 30 mL of CH₂Cl₂ and 20 mL of 0.1N NaOH. The organic layers were separated and washed with brine and water and solvent was removed under reduced pressure. The residue was purified by silica gel column chromatography (100-200 mesh). A pink band eluted with ethyl acetate and hexane (15:85) gave a reddish- brown solid which was identified as **18** in 41% yield.



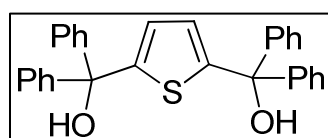
¹H NMR (400 MHz, CDCl₃, 298 K): δ (ppm): 8.03 (brs, 4H) 7.04 (s, 2H), 6.72 (m, 4H), 6.18 (m, 4H), 6.10 (m, 4H), 5.78 (s, 2H).



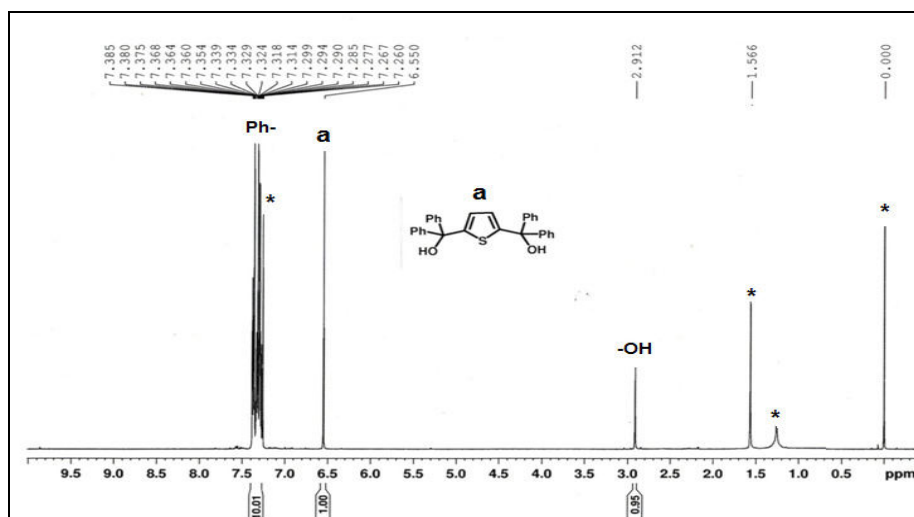


2,5-bis(diphenylhydroxymethyl)thiophene (20):

N,N,N',N'-tetramethylethylenediamine (1.6ml, 2.5mmol) was dissolved in dry hexane under argon atmosphere. *n*-Butyllithium (1.875ml, 3mmol) was added drop wise and followed by addition of thiophene (0.79ml, 1mmol) and allowed to stir at ambient temperature for 1h and refluxed for 2h. The mixture was brought back to room temperature. Finally, the mixture was kept in an ice-bath and then benzophenone (0.432g, 2.3mmol) in dry hexane was added drop wise to the above reaction mixture and allowed to stir for 2h. The work up was done using water and saturated brine solution. The organic layer was then extracted with CH₂Cl₂ and dried over anhydrous sodium sulphate. The solvent was removed by using rotary evaporator. The crude product was purified by silica gel column chromatography (100-200 mesh) and eluted with petroleum ether: ethyl acetate (17:3) afforded 65% yield.

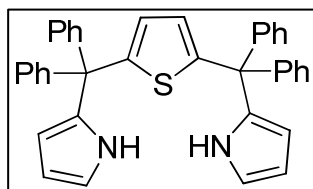


¹H NMR (400 MHz, CDCl₃, 298 K) δ (ppm): 7.38-7.26 (m, 20H), 6.55 (s, 2H), 2.91 (s, 2H).



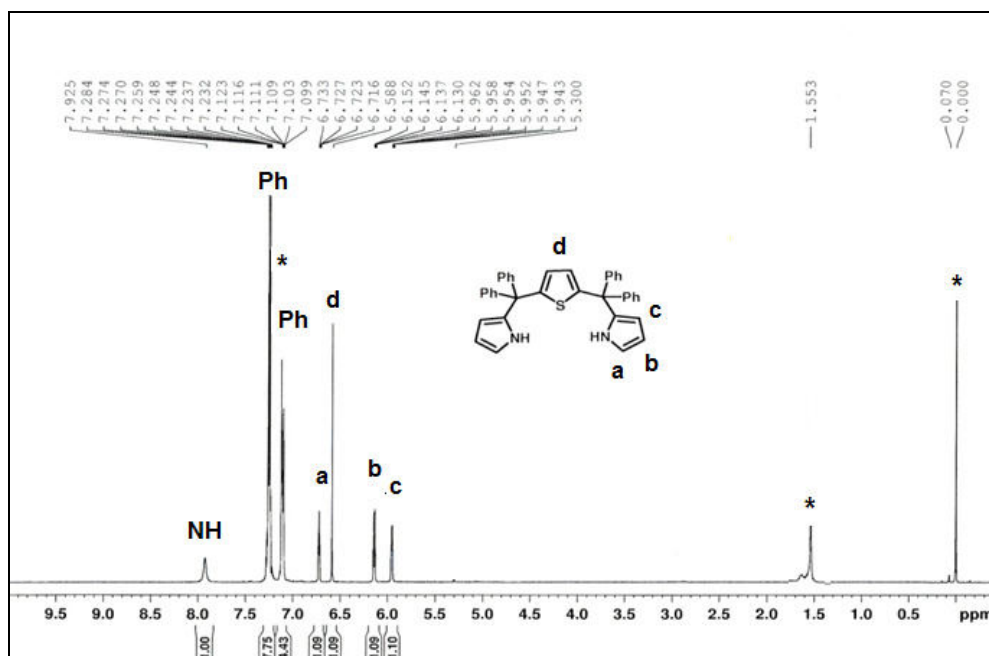
2,5-bis(diphenylpyrrolylmethyl)thiophene (21):

2,5-bis(diphenylhydroxymethyl)thiophene **20** (1 g, 2.23 mmol) was added to pyrrole (7.73 ml, 111.5 mmol) under argon atmosphere and after 10 min TFA (0.053 ml, 0.69 mmol) was added and stirred for 30 min in ambient temperature. CH_2Cl_2 (30 ml) and KOH were added to quench and neutralize the acid respectively. The organic layer was then extracted with CH_2Cl_2 and dried over anhydrous sodium sulphate. The solvent was removed by rotary evaporator. The crude product was purified by silica gel column chromatography (100–200 mesh) with petroleum ether/ethyl acetate (95:5) gave yellow color semi-solid in 45% yield.



ESI-MS: m/z calcd for $\text{C}_{38}\text{H}_{30}\text{N}_2\text{S}$: 546.2130; found: 546.2143; ^1H

NMR (400 MHz, CDCl_3 , 298 K) δ ppm: 7.92 (brs, 2H), 7.28-7.09 (m, 20H), 6.73-6.71 (m, 2H), 6.58 (s, 2H), 6.15-6.13 (m, 2H), 5.96-5.95 (m, 2H).

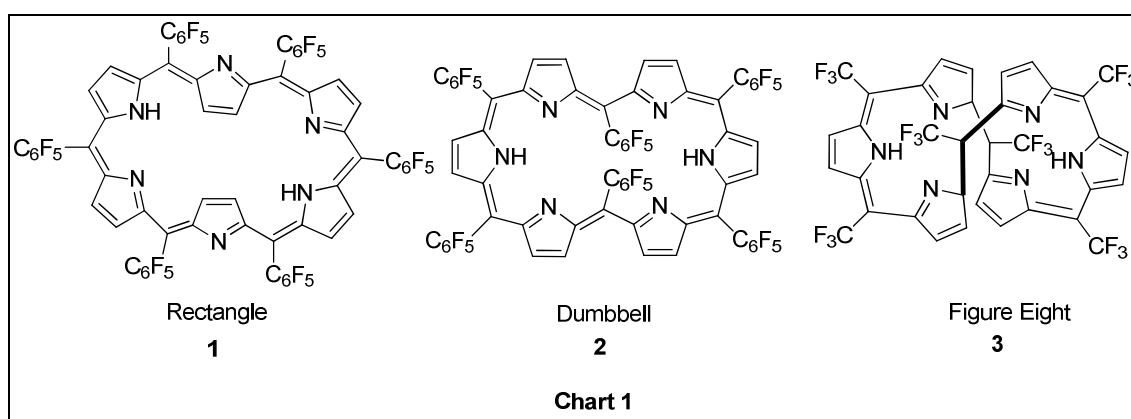


Core-Modified Bridged Expanded porphyrins

3.1 Introduction

The optical, electronic and coordination properties of expanded porphyrins varies depending upon their conformation in solution and solid state [11]. Hence, control over their conformations is foremost important and is subject to many factors such as nature of β -substitution, linkage, number of *meso* positions, bulkiness of substitution on *meso* position, etc., [29]. Porphyrins and pentapyrrolic systems such as sapphyrin or pentaphyrins exhibit inherent planar conformation in solution and solid state. However, starting from hexaphyrins, expanded porphyrins become conformational dependence system where more number of *meso* carbons and heterocyclic rings leads to conformational flexibility. For instance, Hexaphyrins (1.1.1.1.1.1) exhibit two major conformations (Chart 1), namely rectangular **1** and dumbbell shaped conformation **2** [23,90]. Mostly, *meso* aryl substituted [26]hexaphyrins adopt the rectangular conformations **1**, in which two pyrrole rings are inverted, while the remaining four pyrrole rings are in normal form in order to have an effective intramolecular hydrogen-bonding between amine and imine pyrroles. These rectangular conformations maintains the strong 26π aromaticity and are planar, however the planarity is lower than normal porphyrin. On the other hand, a dumbbell shaped conformation also adopts by the hexaphyrins, however, it is not favored because of the steric repulsion between the inward facing *meso*-substituents. Figure-eight conformations **3** are relatively rare in [26]hexaphyrins(1.1.1.1.1.1) but are observed for those that bear less bulky substituents at the *meso* positions, such as *meso*-CF₃ substituted [26]hexaphyrin. Recently, it is found that

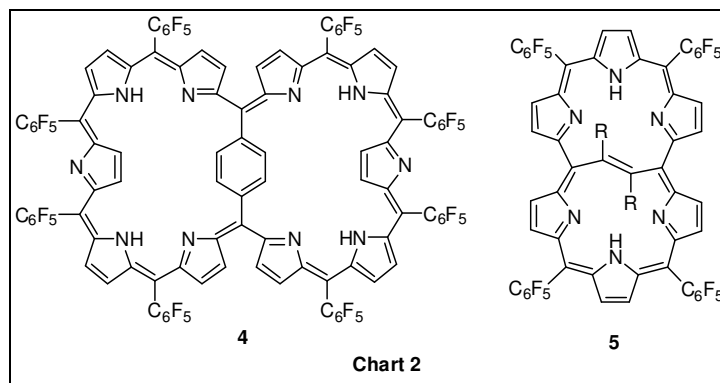
[28]hexaphyrins has the dynamic equilibrium between different conformation such as figure-eight, planar and Möbius band and these are depending on the *meso* substitution, solvent polarity and temperature. For instance, in low temperature (183K) and polar solvents Möbius aromaticity predominates while high temperature (343K) and non-polar solvent favors twisted non-aromatic conformation [39].



In expanded porphyrins, as the number of pyrrole rings and *meso* carbon pyrrole rings and *meso* carbon increases, the conformational flexibility also increases, which results in non-planar twisted structures [29,91]. Various synthetic approaches has been tried to avoid twisting in various expanded porphyrin derivatives such as decreasing the number of *meso* substitution and increasing the bulkiness of the *meso* substitution, etc, leading to planar aromatic 30π , 34π systems [32,92]. However these approaches were limited to some extend of expanded porphyrin and further it was not applicable to higher derivatives.

In order to avoid twisting, recently, Osuka and co-workers introduced an internal bridging group by linking the *meso* carbons. Using this approach, they have synthesized the decaphyrin **4** by bridging two *meso* carbons with 1,4-phenylene group (Chart 2). This bridged decaphyrin **4** exhibit near planar structure in solid state which was confirmed by single crystal X-ray structure. The diatropic ring current in NMR analysis further support the aromatic planar rigid molecular structure of the decaphyrins [57].

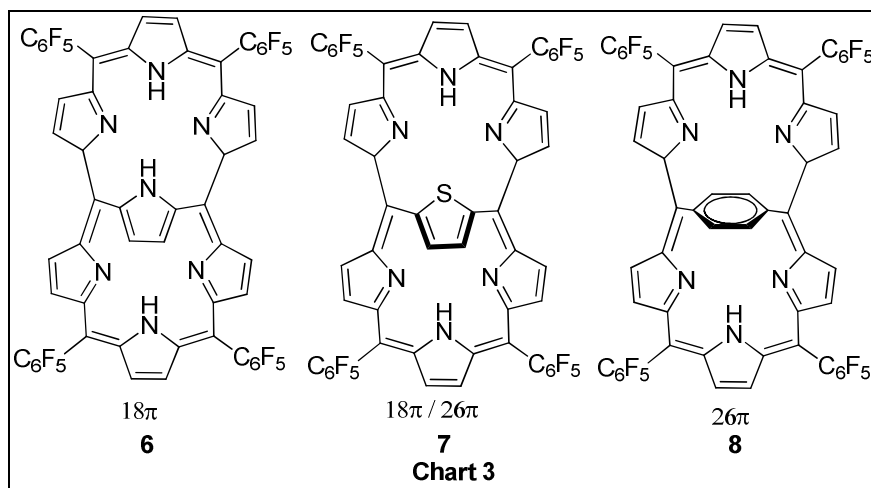
Later, the same group was also synthesized planar hexaphyrin **5** using an internal vinylene bridge, and these molecules showed interesting electronic properties [11, 5b]. This derivatives exhibits a switch over between 26π aromatic to 28π antiaromatic by oxidation and reduction and also without changing the conformation of the macrocycle owing to the rigid molecular structure imposed by vinylene-bridge [58].



The magnetic and structural characteristics of vinylene-bridged [26]hexaphyrin and [28]hexaphyrin exhibits Hückel aromatic and antiaromatic behavior, respectively. All the characteristics of [28]hexaphyrins are in line with antiaromatic properties such as broad featureless absorption spectra, an optically dark NIR absorption band, lack of fluorescence and short lowest-excited-state lifetimes. On the other hand [26]hexaphyrins has sharp Soret absorption band, distinct Q-bands and fluorescence. [59]

Very recently, the same group has synthesized three hexaphyrins in which *meso* position were bridged by pyrrole **6**, thiophene **7** and phenylene **8** moieties as shown in Chart 3. These bridged moieties have different orientation with respect to mean *meso* plane of macrocycle. Phenylene bridge in hexaphyrin **8** is perpendicular orientation with respect to macrocycle and hence adopts $[26\pi]$ electronic conjugation pathway. The thiophene bridged hexaphyrin **7** exhibits dual $[18\pi]$ and $[26\pi]$ conjugation pathway due to bridging thiophene units is 49° tilted from the mean plan. The pyrrole bridged hexaphyrin **6** has a predominant

contribution of $[18\pi]$ porphyrin network due to its coplanar conformation with macrocycle plane. [93]



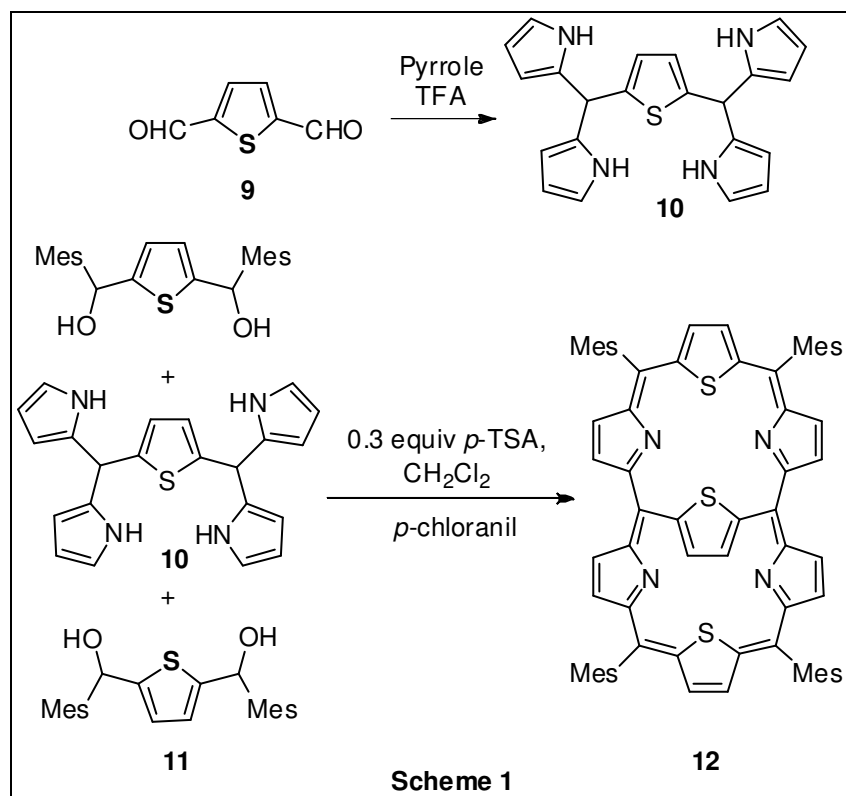
3.2 Core modified internally bridged Expanded Porphyrins:

This first part of this chapter describes the synthesis of core modified hexaphyrins with an internal thiophene bridge following a simple and efficient synthetic approach. Spectroscopic and structural studies revealed that hexaphyrin macrocycle was planar and aromatic and internal bridging ring was deviated from the mean plane of *meso* carbons. Preliminary photo-physical studies indicate increase in excited state lifetime and two photon absorption cross section values for the bridged systems.

3.2.1 Synthesis of Thiophene bridged Hexaphyrins

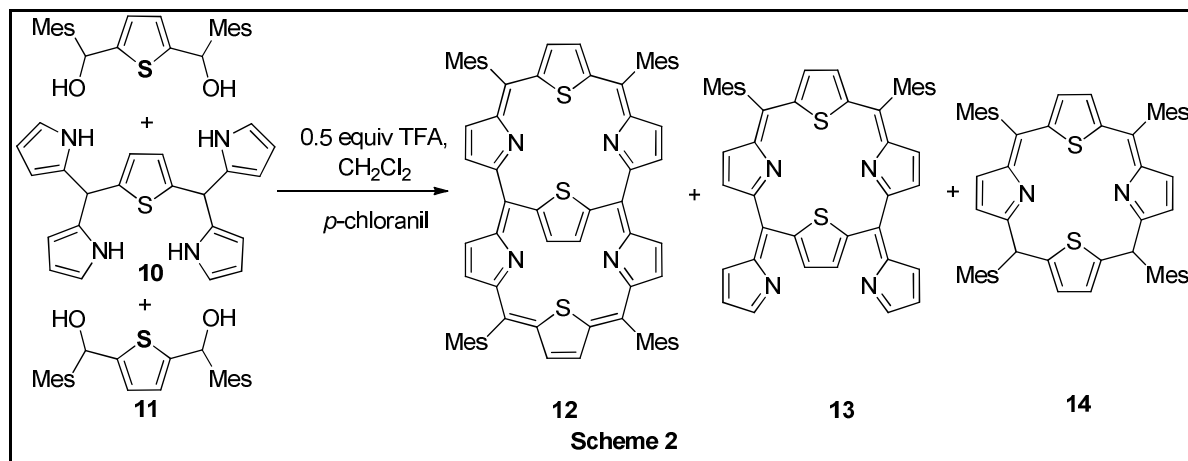
For the synthesis of thiophene bridged hexaphyrins, we have adopted two synthetic methodologies. In method-I, we have followed similar synthetic route as reported by Osuka and co-workers which is shown in Scheme 1. The required 2,5–thienylbis(dipyrromethane) **10** was synthesized by condensing 2,5–thiophenedicarboxaldehyde **9** with pyrrole in the presence of TFA as catalyst to afford **10** in 45% yield. **10** was further condensed with 2,5–bis(mesitylhydroxymethyl) thiophene **11** in the presence of 0.5 equiv of TFA and later oxidized with *p*-chloranil to afford **12** in 4% yield along with two side products, mono–

condensed porphyrin (5,10-dimesityl 15,20-dipyrrolyl dithiaporphyrin) **13** and tetramesityldithiaporphyrin **14**. The formation of dithiaporphyrin **14** might be due to acidolysis of 2,5-bis(dipyrrolylmethyl)thiophene **10**.

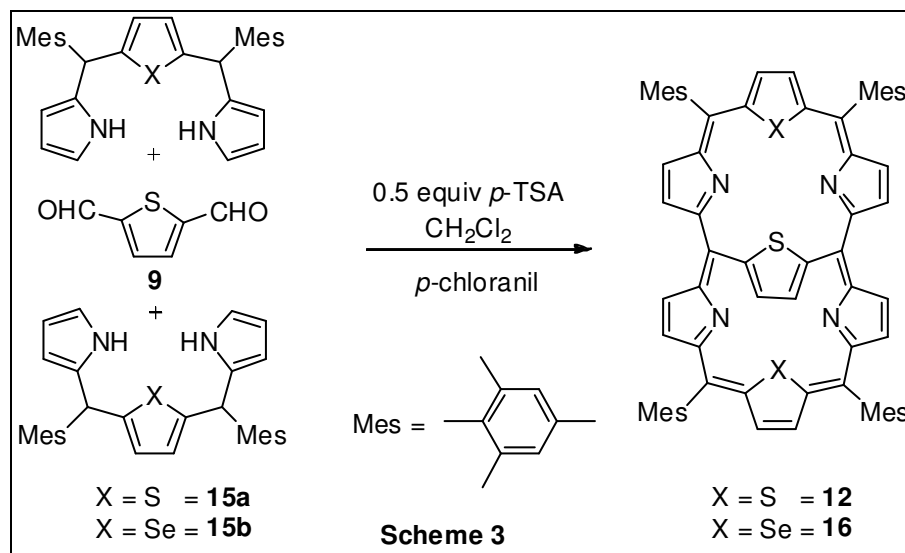


Scheme 1. Syntheses of internally thiophene bridged *meso*-aryl hexaphyrins (method 1)

Increasing the acid concentration led to more acidolysis product and reduced yield of **12**, while decreasing the acid concentration led to more mono-condensed product. By changing the acid catalyst to *p*-Toluenesulphonic acid (*p*-TSA), no drastic change in the yield of **12** was observed. However, the amount of acidolysis product was reduced. By using this synthetic route, varying the acid and its concentration, a maximum 6% yield of **12** was observed at 0.3 equiv of *p*-TSA (Method-I) with trace amount of side products.



Scheme 2. Plausible side product formation during the synthesis of internally thiophene bridged *meso*-aryl hexaphyrin **12**.



Scheme 3. Syntheses of internally thiophene bridged *meso*-aryl hexaphyrins (Method-II)

In order to avoid the side product formation, we adopted the modified synthetic methodology as mentioned in Scheme 3 (Method-II). The core-modified tripyrromethane **15a** or **15b** was condensed with **9** in the presence of 0.5 equiv of *p*-TSA followed by oxidation with *p*-chloranil to give the hexaphyrins **12** or **16** in 8–15% yields. Since tripyrranes are less prone to acidolysis no other side products were detected.

3.3 Spectral Characterization:

3.3.1 Mass Spectral Analysis

The ESI-mass spectral analyses show parent ion peaks at m/z 1051.7947 [$M; H^+$] for **12** (Figure 3.1) and 1146.8234 [M^+] for **16** (Figure 3.2) confirming a composition that is consistent with the expected macrocycles. Similarly, the side products such as mono-condensed porphyrin **13** and dithiaporphyrin **14** are also characterized by mass spectral analyses and showed the exact molecular ion signal for the respective macrocycle (Figure 3.3 and 3.4).

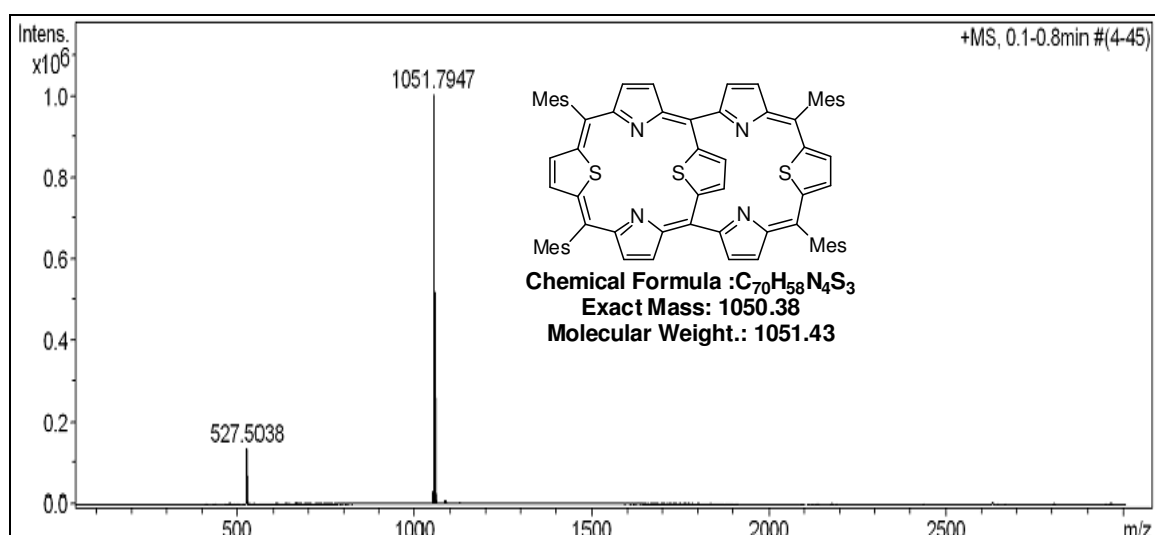


Figure 3.1: ESI-Mass spectrum of **12**

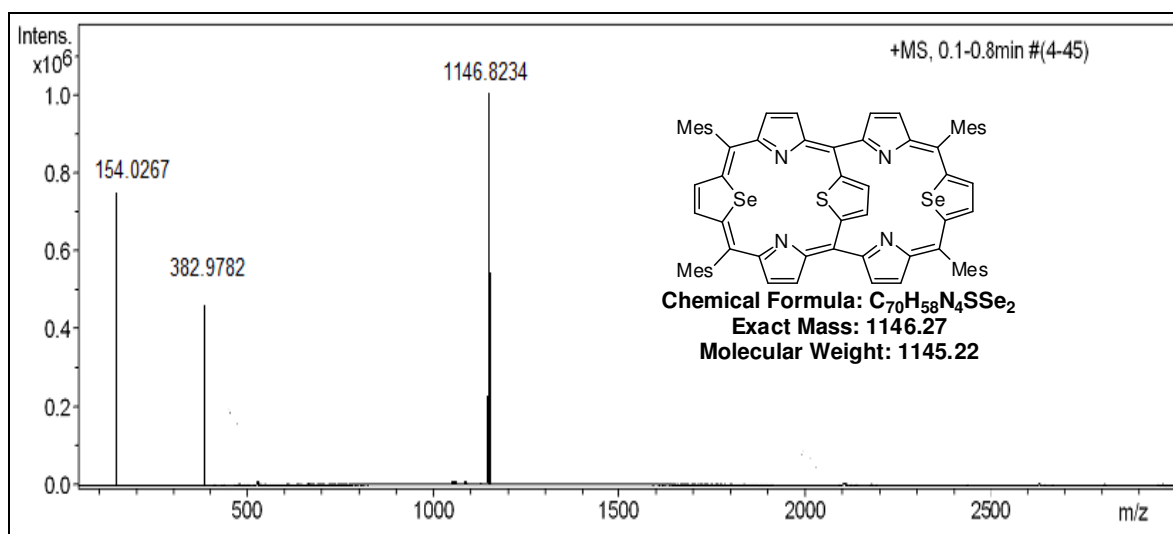
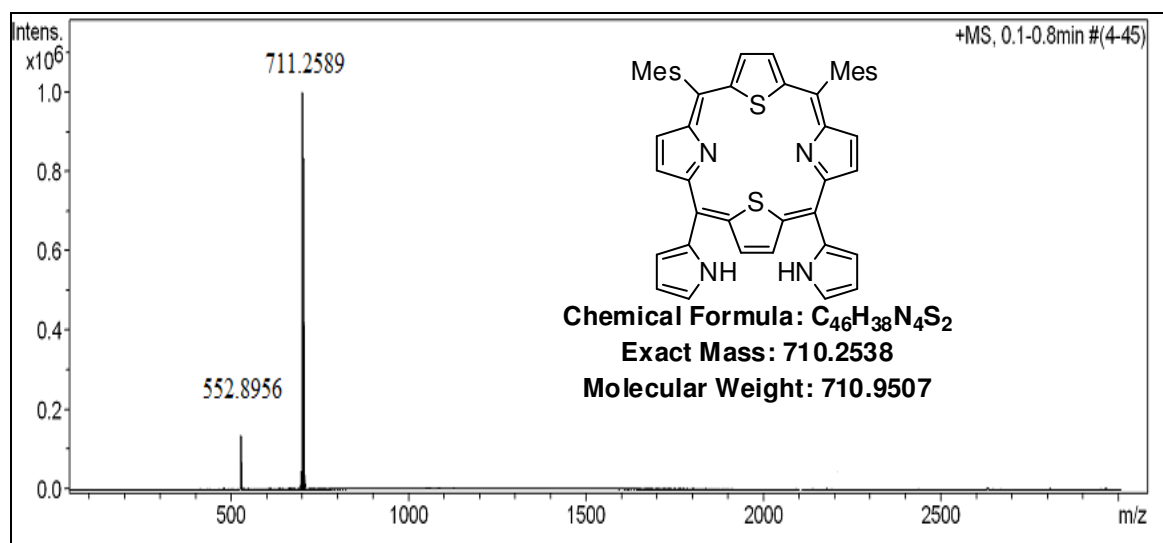
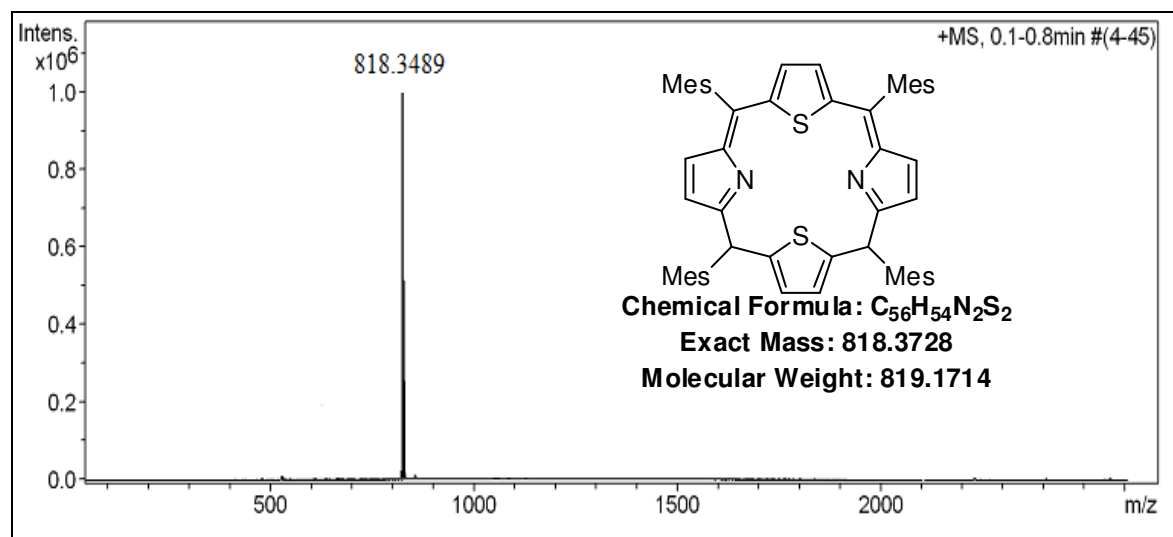


Figure 3.2: ESI-Mass spectrum of **16**

Figure 3.3: ESI-Mass spectrum of mono-condensed porphyrin **13**Figure 3.4: ESI-Mass spectrum of Dithiaporphyrin **14**

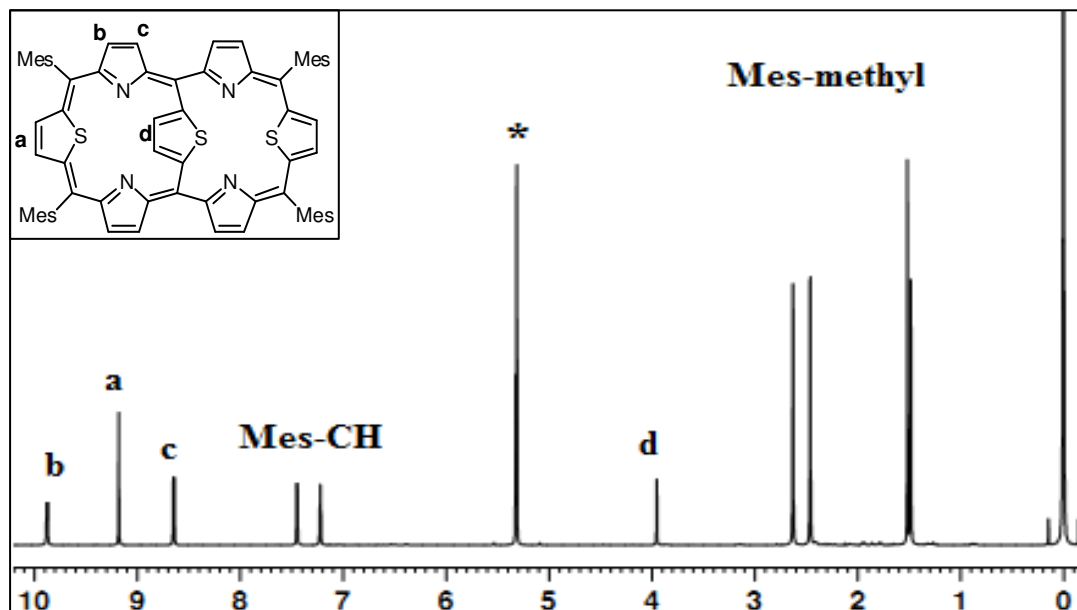
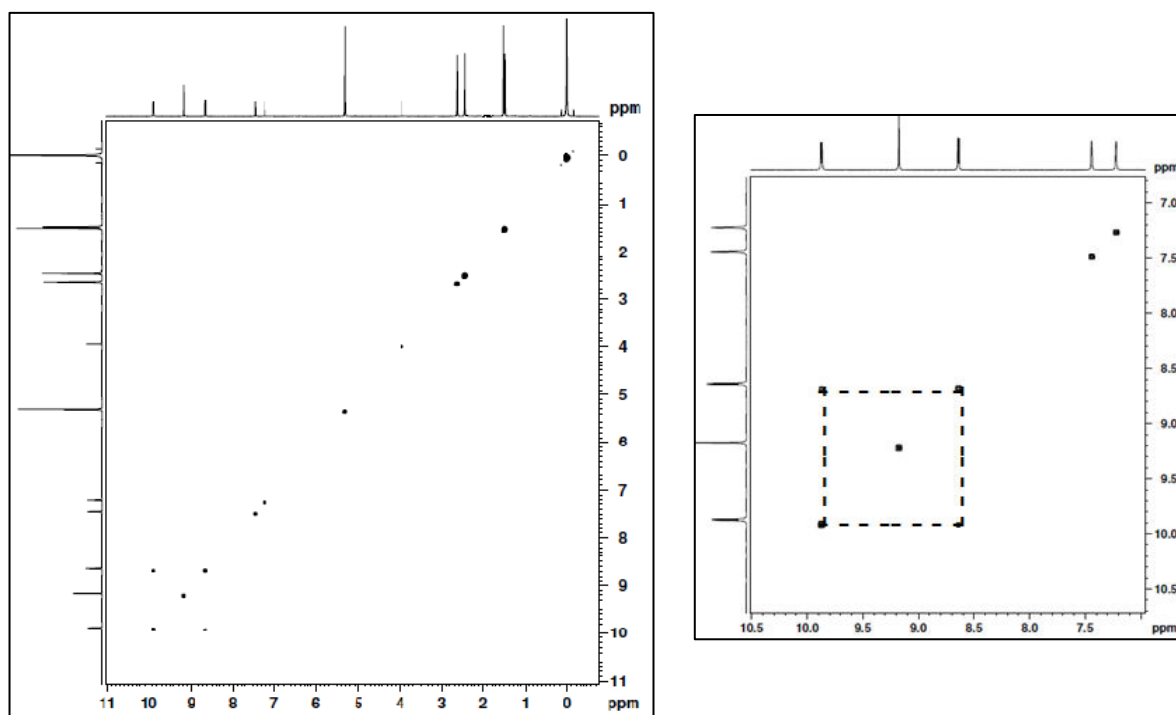
3.3.2 NMR characterization

The ^1H NMR spectrum of **12** in CD_2Cl_2 at 298K is shown in Figure 3.5. In the down field region two doublets and three singlets with equal intensities are observed. The doublets (b and c) at 9.8 and 8.6 ppm are assigned to four pyrrolic β -CH protons. This was further confirmed by 2D homonuclear correlation spectroscopy (COSY) (Figure 3.6). The β -CH protons of two thiophene rings in the core resonate as singlet (a) at 9.17 ppm. The remaining

two singlets (Mes-CH) at 7.4 and 7.2 ppm are assigned to the phenyl protons of the mesityl group. The methyl protons of mesityl resonate as three singlets (Mes-methyl) at 2.6, 2.4 and 1.49 ppm respectively. The spectrum also contains singlet (d) at 3.95 ppm which is assigned to the bridging thiophene β -CH protons. The $\Delta\delta$ (the shift difference between the bridged thiophene and the macrocyclic core thiophene β -CH protons) value of the 5.22 ppm shows that the bridging thiophene unit is experiencing an aromatic ring current effect from core porphyrin ring suggesting that the bridging thiophene unit was not completely orthogonal with respect to the plane of macrocycle.

Further, protonation of **12** using TFA in CDCl_3 leads to small downfield shift in the pyrrole and thiophene β -CH protons in the ^1H NMR spectrum. On the contrary, the β -CH protons of bridging thiophene experience shielding of 1.2 ppm upon addition of 2 equiv of TFA. However, excess addition of TFA (4 equiv) leads to deshielding of the β -CH protons and they appear at 4.2 ppm (Figure 3.7). These observations clearly suggest that the conformation of the bridging thiophene group is sensitive to protonation and significant changes occur in the conformation upon protonation.

The protonated inner NH peaks were observed only at low temperature (183K) by protonation of **12** using TFA in CDCl_3 . On adding 2 equiv of TFA, five different NH peaks were observed in the range of -1 to -7 ppm, suggesting the presence of different tautomers which are chemically as well as magnetically in-equivalent. On adding 4 equiv of TFA, a single peak at -4.7 ppm was observed which indicates the saturation of protonation centers (Figure 3.8). Additionally, a splitting in the peaks of methyl and pyrrole β -CH protons was observed which is presumably due to interaction of mesityl methyl protons and pyrrole β -CH protons.

Figure 3.5: ^1H spectrum of **12** in CD_2Cl_2 at 298KFigure 3.6: ^1H - ^1H COSY spectrum of **12** in CD_2Cl_2 at 298K

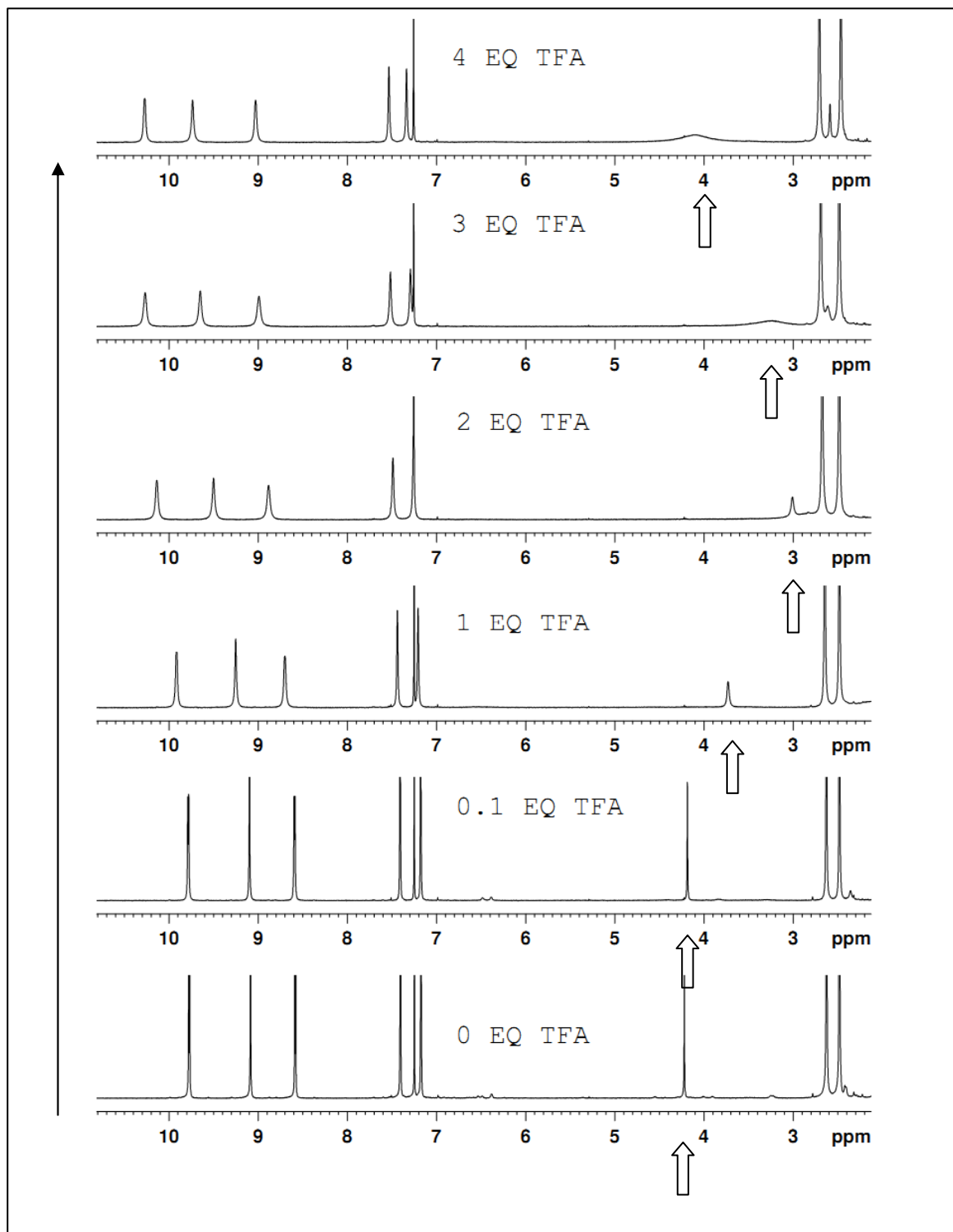


Figure 3.7: ^1H NMR spectral changes of **12** in CDCl_3 at 298K with 0.1, 1.0, 2.0, 3.0, 4.0 equiv of TFA

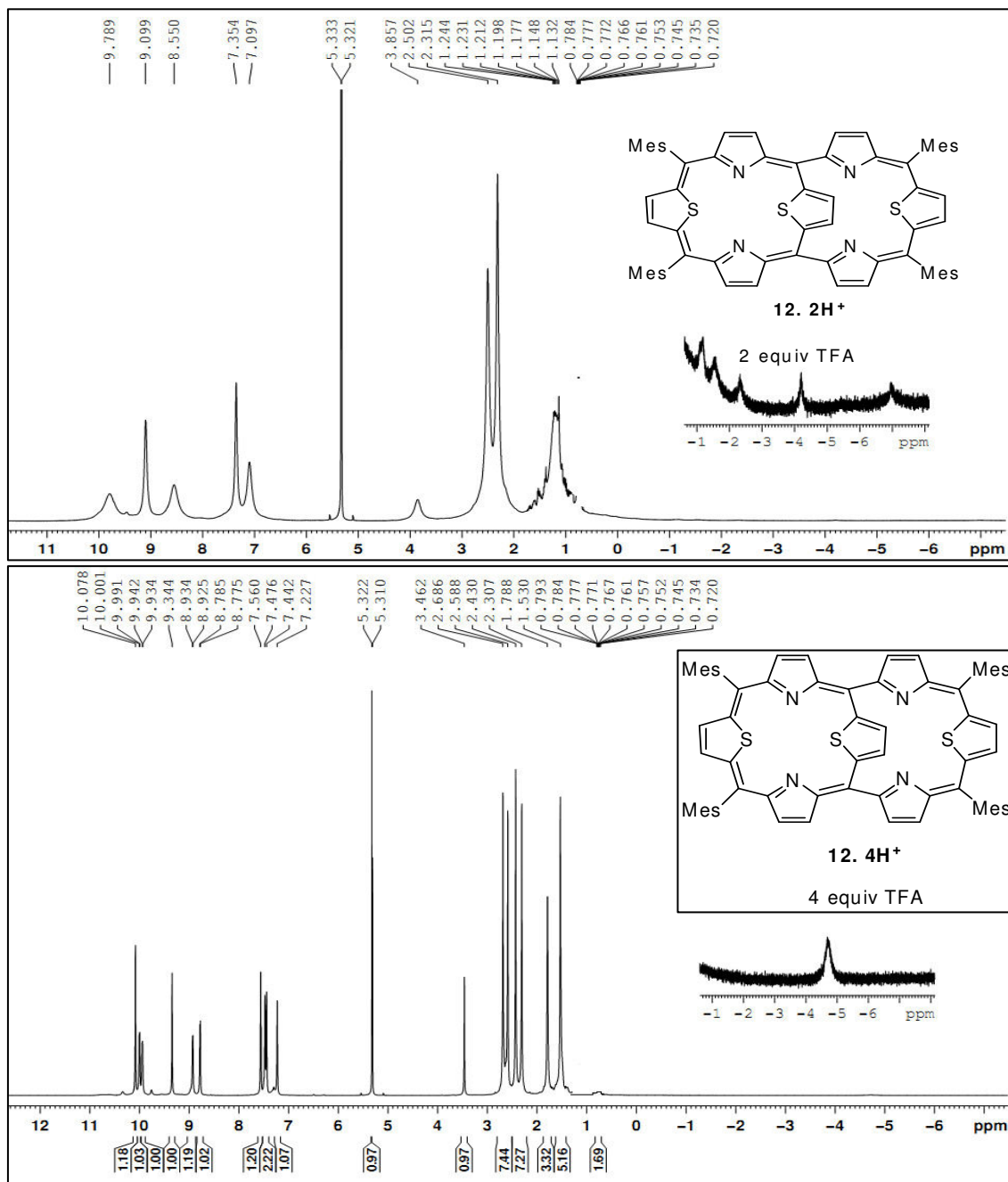


Figure 3.8: ^1H NMR spectrum of **12** in CD_2Cl_2 at 183K with 2 (top) and 4 (bottom) equiv of TFA

The ^1H NMR spectrum of **16** at 298K shows the similar pattern as that of **12**. The β -CH protons of the bridging thiophene in **16** are more shielded relative to **12** and resonate at 1.35 ppm (Figure 3.9).

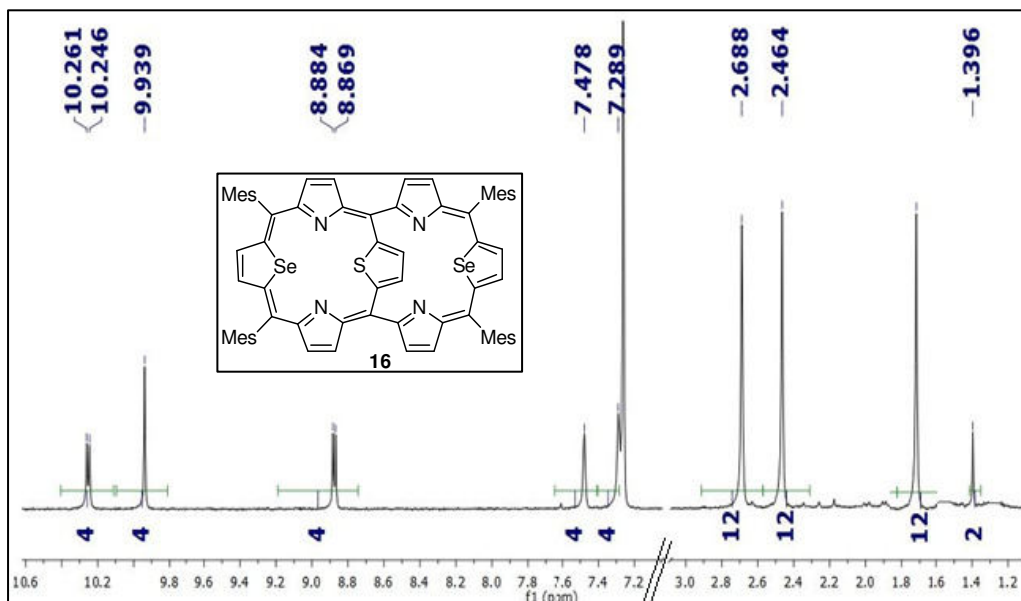


Figure 3.9: ^1H NMR spectrum of **16** in CDCl_3 at 298K

3.3.3 Electronic absorption spectral characterization

The electronic absorption spectra of **12** and **16** were characterized by typical strong Soret band and weak low energy Q-bands (Figure 3.10). In the Soret region **12** exhibits two bands (433 nm and 531 nm).

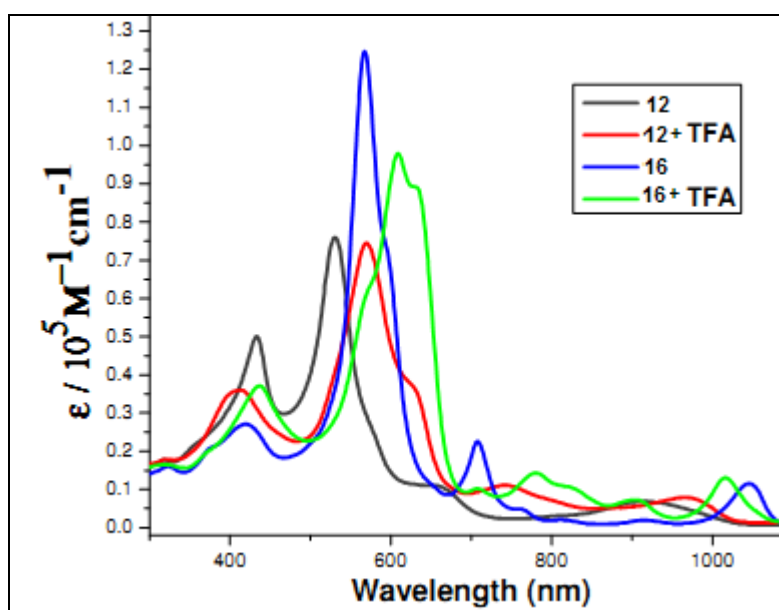


Figure 3.10: Electronic absorption spectra of **12**, **16** and their protonated forms

The position of higher energy band was similar to that found in dithiaporphyrin [94] while band at 531 nm has similar features as in hexaphyrin [95]. However, **16** has only one Soret band at 567 nm and was found to be 1.6 times more intense than observed for **12**. The position of low energy Q-bands were typical of hexaphyrins. Upon protonation, the band at 531 nm in **12** is red shifted to 570 nm with a shift value of 39 nm, while the band at 567 nm in **16** is red shifted to 609 nm with a shift value of 42 nm indicating an extension of conjugation.

3.3.4. MO diagram

In an effort to understand these characteristics in the absorption spectra, we have calculated molecular orbitals (MO) based on X-ray crystal structures and transition energies by TD-DFT method using Becke's three-parameter hybrid exchange functional and the Lee–Yang–Parr correlation functional (B3LYP) employing the 6–31G basis set for **12** (Figure 3.11, left) [79,80].

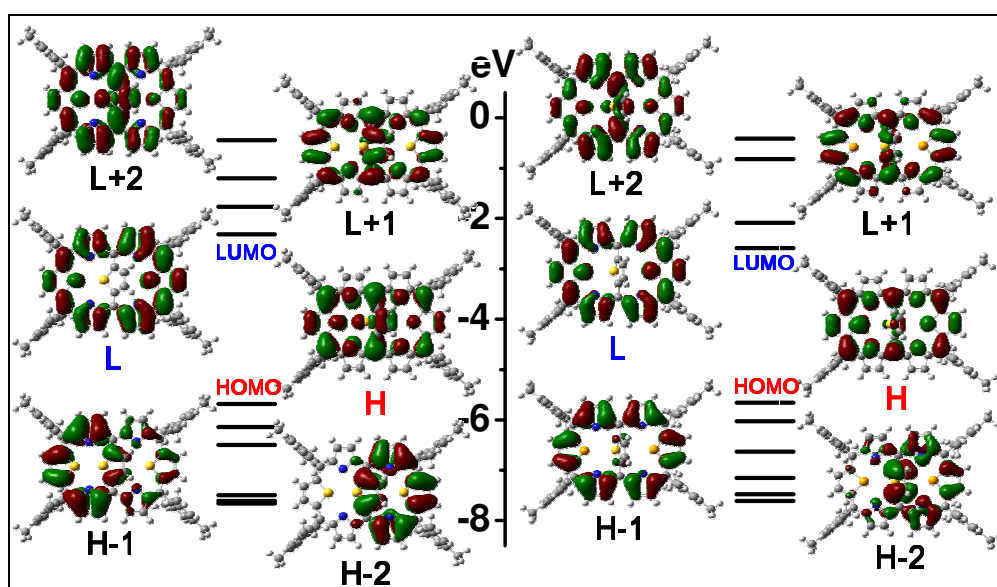


Figure 3.11: MO energy diagram of **12** (left) and **16** (right)

According to the frontier orbital diagram, we could recognize that the MOs of bridged hexaphyrin consists of the summation of the MOs in which electron density

distribution is localized on porphyrin (H-1, H-2) and the MOs in which electron density distribution is localized on hexaphyrins (LUMO). The MOs where electron density distribution of **12** is localized on porphyrin give rise to porphyrin-like transition at 433 nm. Furthermore, the MOs where electron density distribution is localized on porphyrin moiety also affect hexaphyrin-like transition at 917 nm. From these data, we could assume that the hybrid character of bridged hexaphyrin cause two transitions; one is porphyrin-like transition while the other is hexaphyrin-like transition. Based on a comparison of the absorption spectra with the calculated results, we could assume that the peak at 433 nm is originated from porphyrin, that around at 531 nm region is mixed with hexaphyrin and porphyrin, and one at 917 nm is caused by hexaphyrin.

This hybrid character of **12** is also supported by the AICD plots which shows the 3D image of delocalized electron densities with a scalar field and illustrates the paramagnetic term of the induced current density; aromatic molecules show clockwise current density and antiaromatic species show counter-clockwise current density (Figure 3.12). The AICD plot shows that the ring currents flow along not only the hexaphyrin frame but also the bridged thiophene. On the other hand AICD plot for **16** shows that the conjugation pathway mainly pass through the hexaphyrin framework. [96]

From this result, we could assume that the overall ring current density consist of the ring current flows which are mainly localized on hexaphyrin and partially localized on porphyrin. On the other hand, MO picture for **16** (Figure 3.11, Right) indicate that the electron density distribution is mainly localized on the 26π hexaphyrin skeleton and an intense Soret like band observed at 567 nm is consistent with this conclusion.

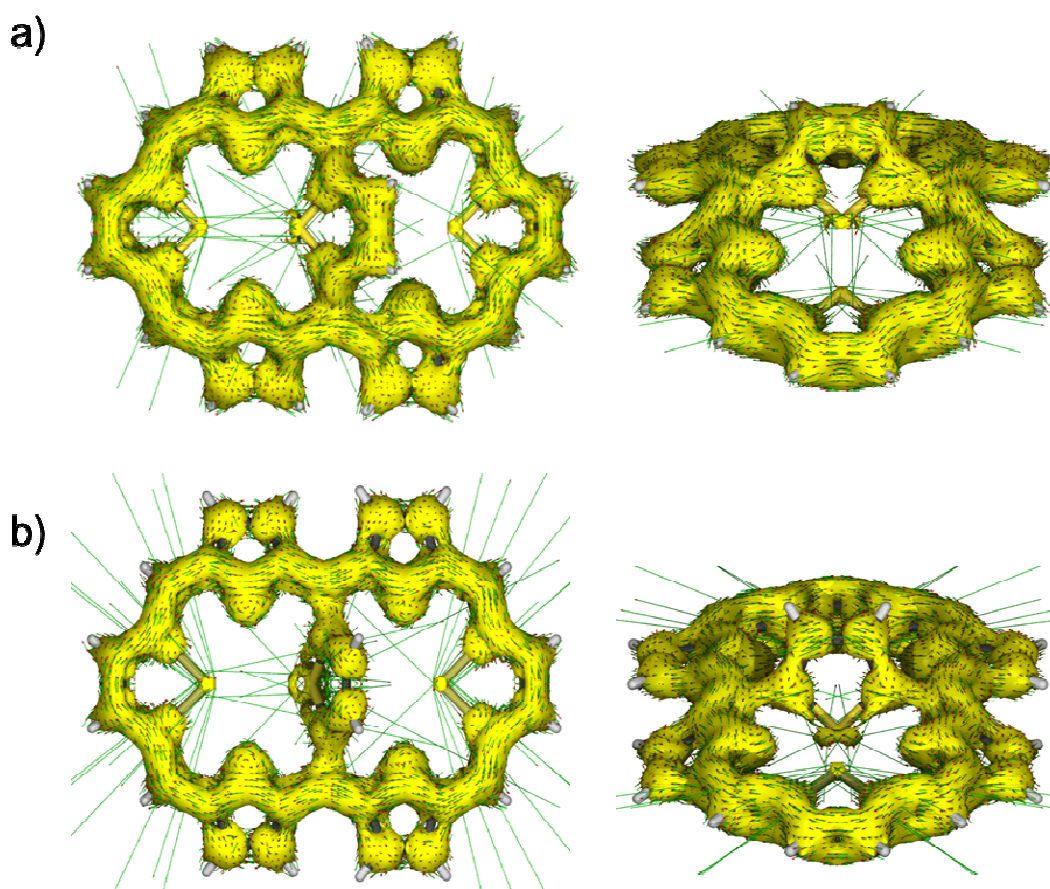


Figure 3.12: AICD plots for bridged core-modified hexaphyrins **12** (a) and **16** (b). The direction of external magnetic field is perpendicular to the hexaphyrin macrocycle

3.3.5 NICS calculation

For the evaluation of aromaticity, we have calculated the NICS(0) values both within the inner porphyrin cavities and outside (Figure 3.13). To avoid the local aromatic effect from the bridging thiophene ring, we chose to calculate the NICS values at the centres of two porphyrin like cavities rather than at the center of the hexaphyrin skeleton. The highly negative NICS(0) values observed (for **12**, -14.0 and -13.3 ppm, for **16**, -18.3 and -17.9 ppm) at the inner cavities and positive values outside strongly suggest the aromatic nature of the bridging hexaphyrins. [97]

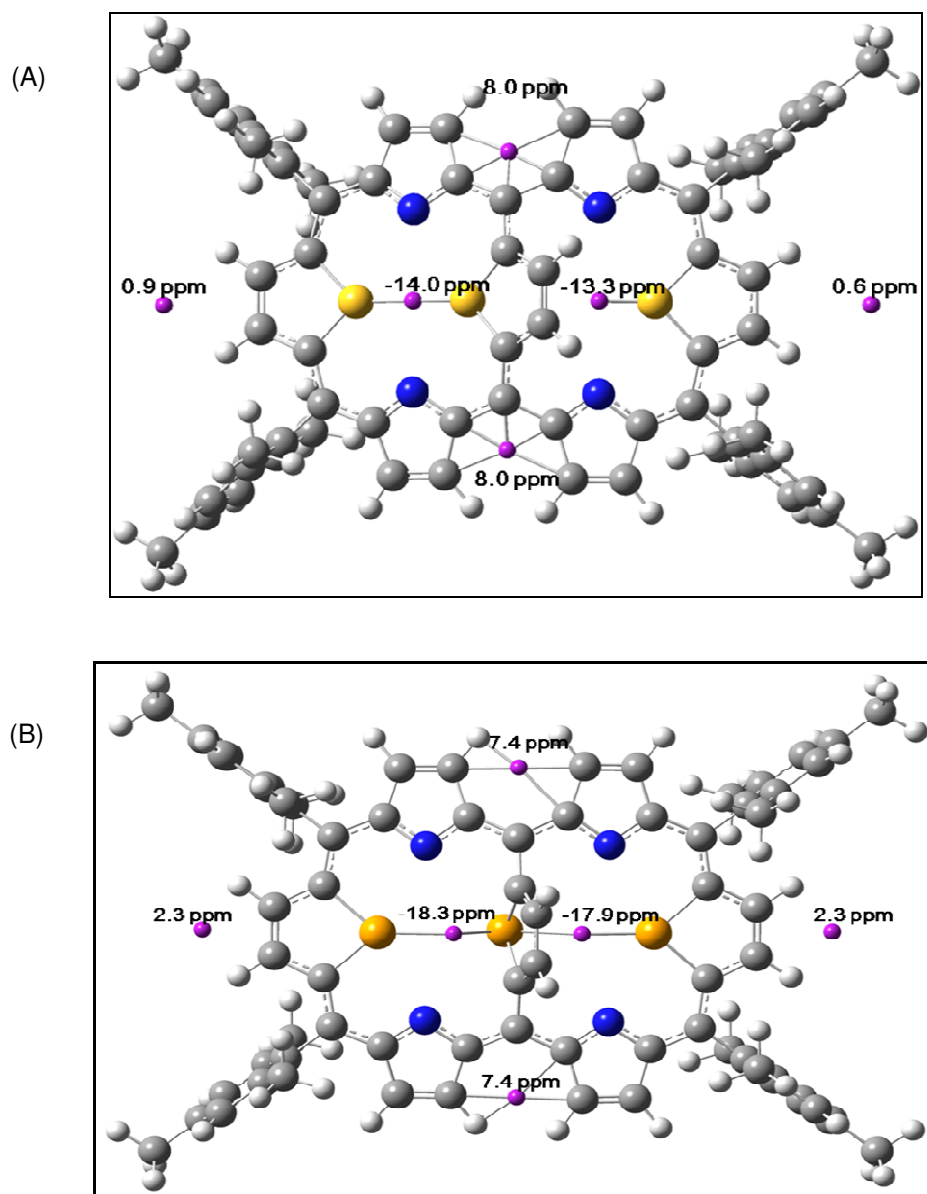


Figure 3.13: The NICS (0) values of **12** (A) and **16** (B) calculated within inner and outside cavities. The purple points indicates the point at which NICS(0) values have been calculated

3.3.6 Single Crystal X-ray Structure and Analyses of **12** and **16**:

The final confirmation of structures of **12** and **16** came from the single crystal X-ray structural analyses (Figure 3.14). In both **12** and **16**, the molecule is located on a crystallographic two fold axis. As predicted from the spectral analyses, **12** contains two thiatripyrrin units, while **16** consists of two selenatripyrrin units and both the units are individually bridged by a thiophene moiety and the remaining four *meso* positions are

occupied by the mesityl groups. The bridged thiophene in **12** and **16** is in positional disorder, where two of the thiophene units overlap each other. Analysis of the crystal structure reveals that the thiatripyrrin units in **12** (N1–S1–N2) are slightly deviated from the mean plane with the deviations of 10.2°, 3.3° and 5.7°, where the selenatripyrrin in **16** (N1–Se1–N2) units are hardly deviated from the plane.

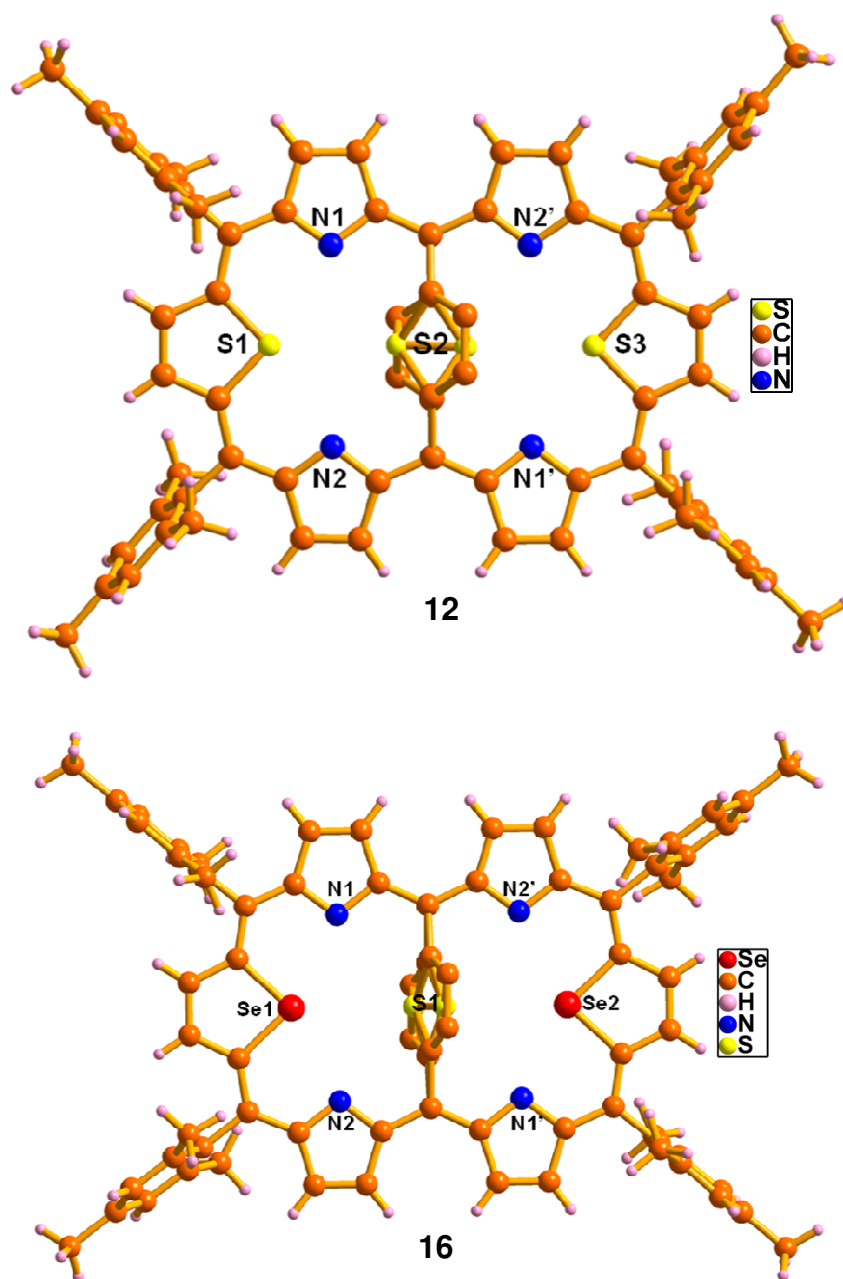


Figure 3.14: Single crystal X-ray structures of **12** and **16** with disorder

However, the bridged thiophene unit in **12** and **16** are deviated by 49° and 73° , respectively (Figure 3.15 and 3.17, side view), while the *meso*-mesityl rings in **12** and **16** are almost perpendicular (89.3° ; 81.5° for **12** and 83.4° ; 78.1° for **16**) to the mean macrocyclic plane.

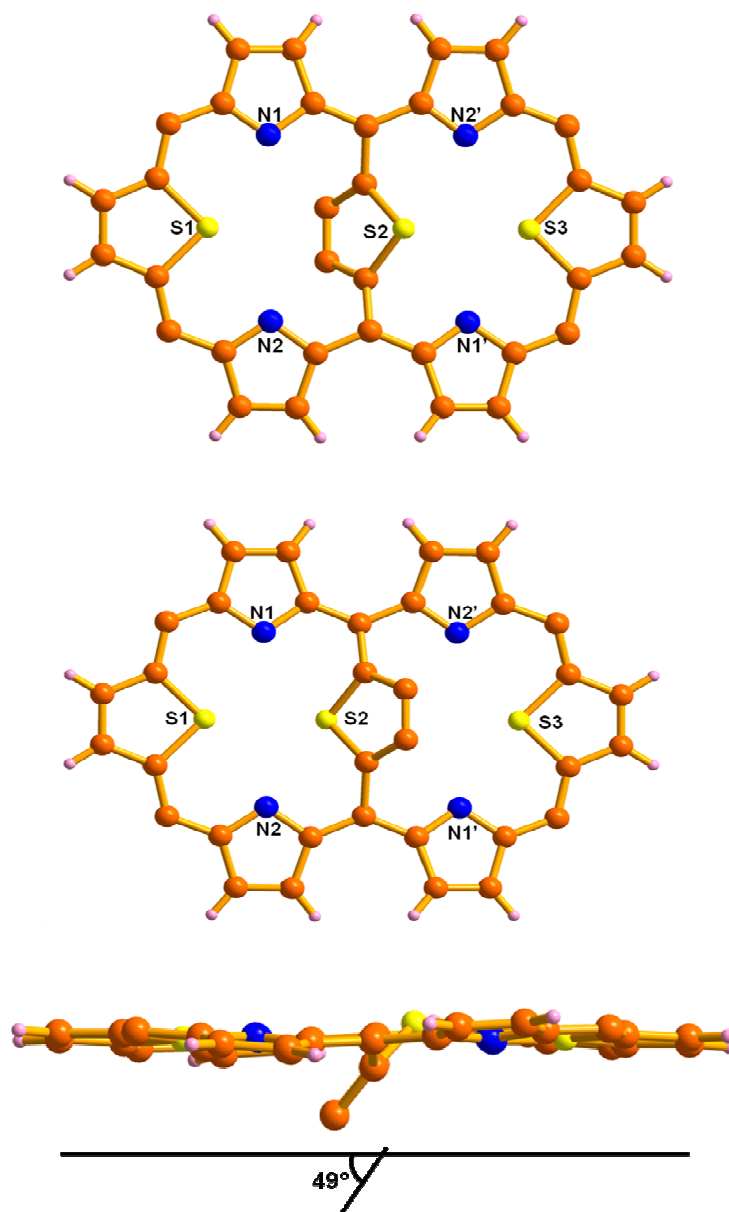


Figure 3.15: Single crystal X-ray structure of **12**, Top view and side view. *meso*-Mesityl units are omitted for clarity

Further, one of the *meso*-mesityl CHs is in intermolecular hydrogen bonding interaction with *meso*-mesityl π -cloud (C23–H23b...Mes(π)) of the adjacent molecule which was used to

generate the one-dimensional supramolecular array in the solid state with the distance and angle of 3.17Å and 144° respectively (Figure 3.16).

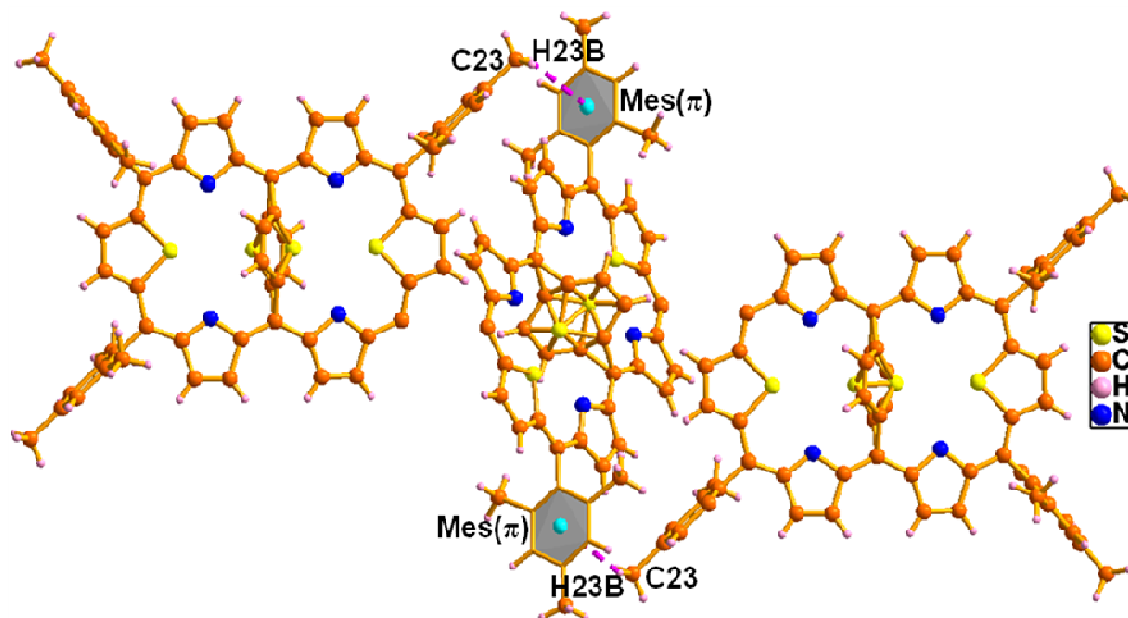


Figure 3.16: One dimensional array of **12**. The C-H... π interactions are generated between one of the *meso*-mesityl CHs and adjacent molecule *meso*-mesityl π -cloud (C23-H23c...Mes(π)) with the distance and angle of 3.17Å and 144° respectively

The participation of bridging thiophene ring in the π electron conjugation pathway and the hybrid character observed for **12** can be rationalized in terms of a smaller tilt angle of 49° of the bridging thiophene ring with respect to mean plane of hexaphyrin skeleton. The observation of 433 nm Soret band (typical of 18 π dithiaporphyrin) also supports such a conclusion. However, a near orthogonal tilt angle of 73° of the bridging thiophene group in **16** does not facilitate conjugation through bridging thiophene ring and thus **16**, exhibits a 26 π electron conjugation pathway, typical of hexaphyrins.

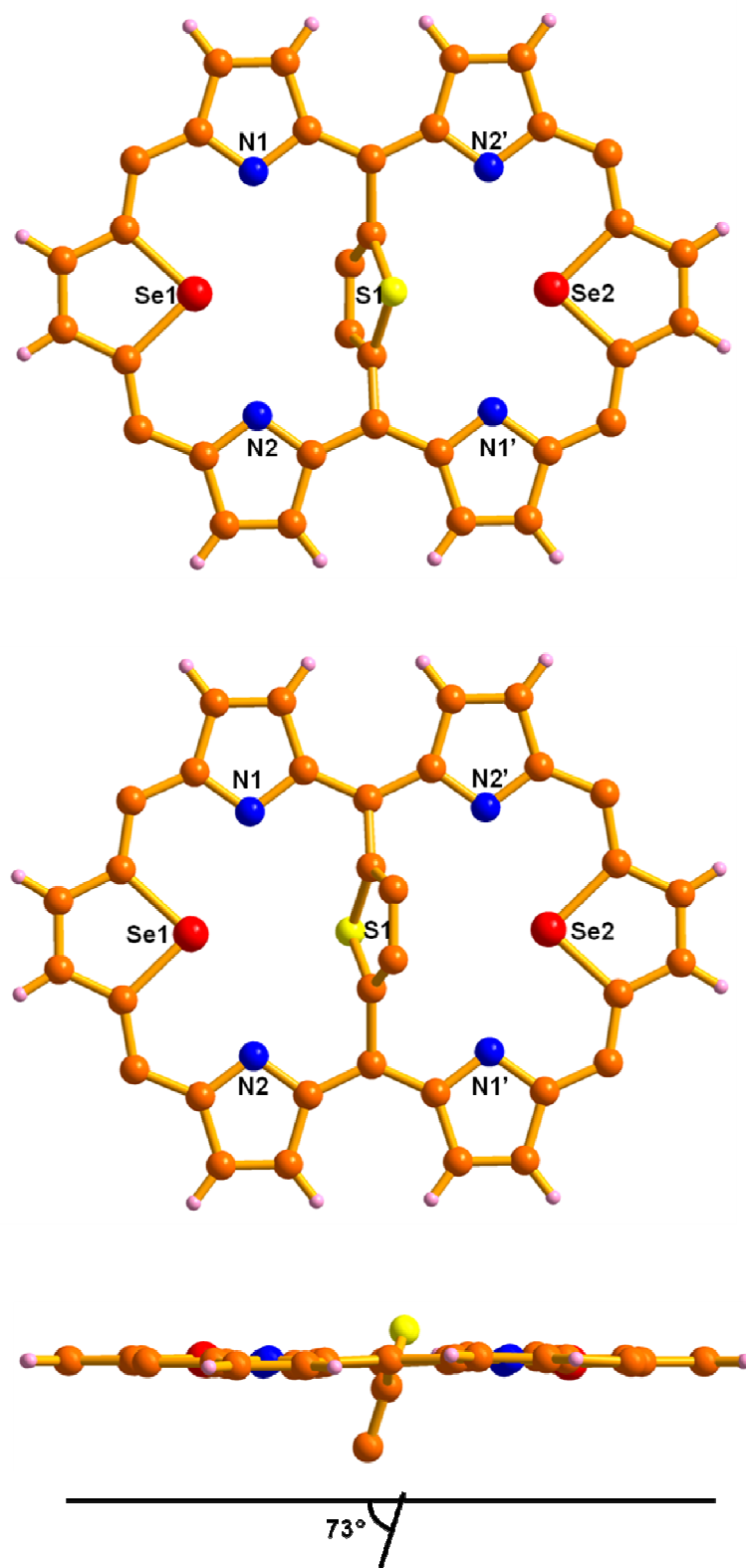
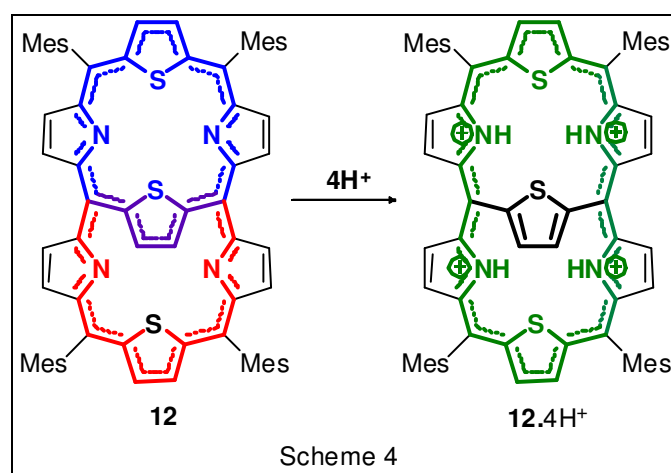


Figure 3.17: Single crystal X-ray structure of 16, Top view and side view. *meso*-Mesityl units are omitted for clarity

A schematic representation of proposed conjugation pathway for **12** before and after protonation is shown below (Scheme 4). Red-shifted absorption from the electronic spectral analysis and significant changes occur in the conformation of the bridging thiophene unit upon protonation further substantiate the extension in π -electron conjugation pathway.



Scheme 4. Proposed conjugation pathway of **12** and its protonated form.

3.3.7. Electrochemistry of **12** and **16**:

In an effort to understand the redox behavior of **12** and **16**, the cyclic voltammetry and differential pulse voltammetry analysis has been carried out in spectral CH_2Cl_2 solution. Electrochemical analysis was carried out in three electrode cell system; Glassy carbon working electrode, platinum wire counter electrode and Ag/Ag^+ reference electrode. Both the bridged hexaphyrin **12** and **16** exhibit the reversible/quasi-reversible redox behaviour which is consistent with aromatic porphyrinoids. The ΔE value for the **12** and **16** are 0.9 and 0.85V respectively which clearly explain the observed red-shift in the UV-Vis absorption spectroscopy.

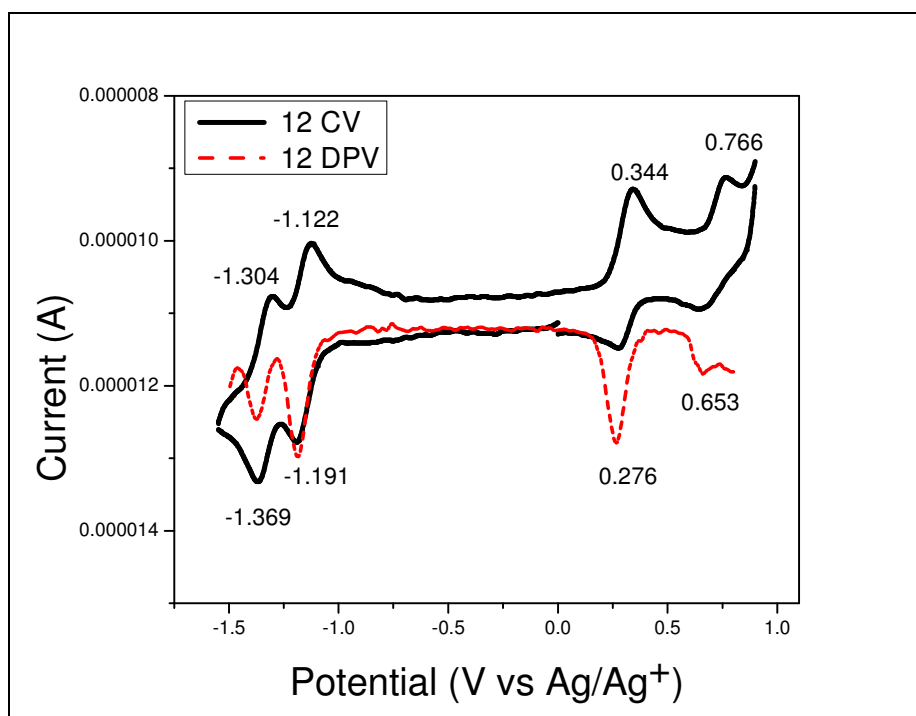


Figure 3.18: Cyclic Voltammogram (solid line) and Differential Pulse Voltammogram (dotted line) of **12** in CH₂Cl₂, containing 0.1 M TBAPF₆ with scan rate 50 mV/s.

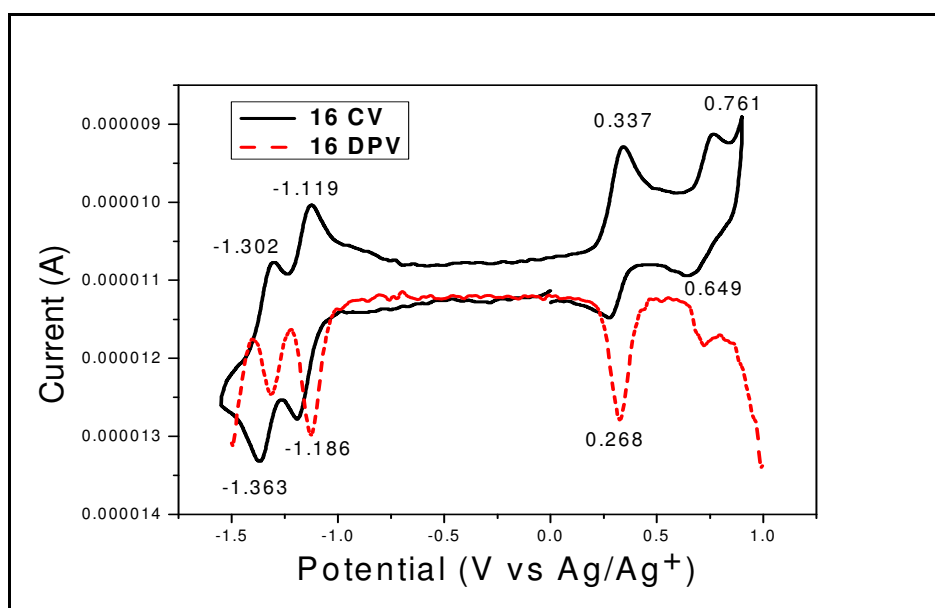
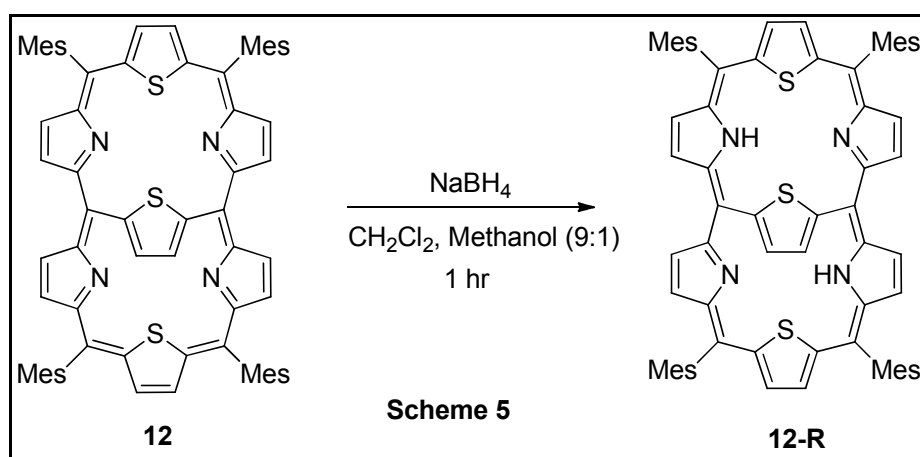


Figure 3.19: Cyclic Voltammogram (solid line) and Differential Pulse Voltammogram (dotted line) of **16** in CH₂Cl₂, containing 0.1 M TBAPF₆ with scan rate 50 mV/s.

3.3.8 Chemical Reduction of **12**:

Chemical reduction of the bridged hexapyrin was carried out to observe the similar behavior was carried out in order to find out similar behavior as observed in vinylene bridged

hexaphyrin [58]. In brief, anhydrous methanol was added to a suspension of **12** and excess NaBH_4 in CH_2Cl_2 , and it was stirred for 1h in argon atmosphere. The reaction mixture was quenched with water. The organic phase was successively washed with water and brine, and then dried over Na_2SO_4 . The solvent was removed by vacuum. The reduced product shows the ESI-MS peak at 1052.3998 which is consistent with the expected reduced product **12-R** (Figure 3.21). Electronic absorption spectra exhibit the broad peak as expected for the antiaromatic expanded porphyrin. However, the compound was unstable to purify by column chromatography.



Scheme 5: Chemical reduction of **12**.

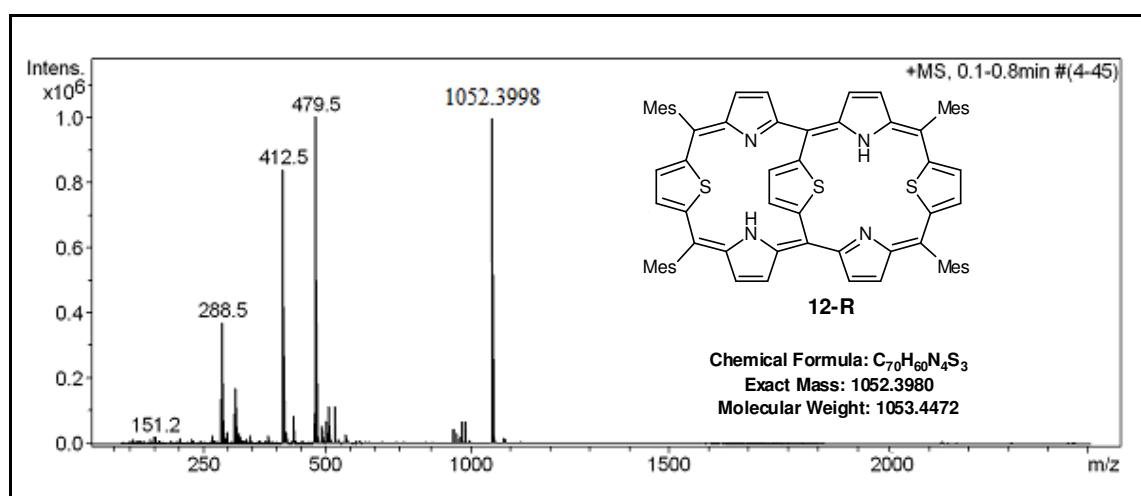


Figure 3.20: ESI-Mass spectrum of **12-R**

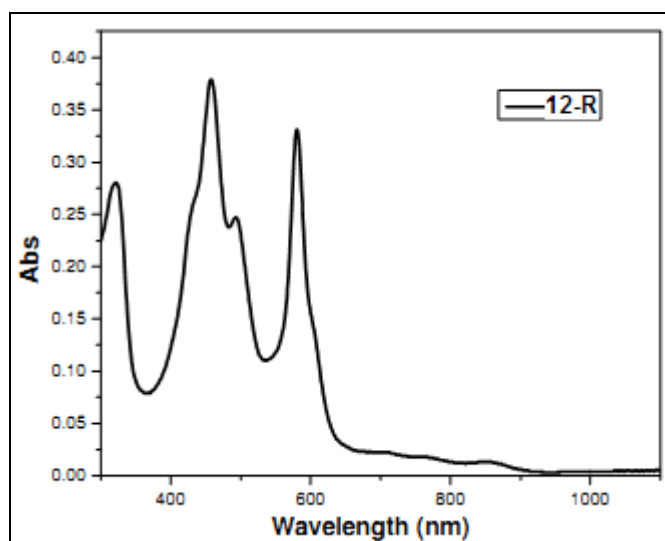


Figure 3.21: Electronic absorption spectrum of **12-R** in CH_2Cl_2

3.4 Photodynamic Study:

To explore the conjugation behaviour and resulting photophysical properties, we have investigated femtosecond transient absorption dynamics of core-modified hexaphyrins (Figure 3.22). The ultrafast excited state dynamics of normal [26]hexaphyrin show excited state lifetime of ~ 100 ps which has planar and rectangular conformation [98]. However, in the cases of the thiophene-bridged core-modified hexaphyrins which have planar conformation with enhanced molecular rigidity and symmetry, we have observed relatively long excited state decay profiles. Transient absorption signals of the bridged thiophene hexaphyrin **12** were analysed with the time constant of 217 ps and residual species which may be contributed by the triplet excited state. In the case of the bridged selenophene-hexaphyrin **16**, as a result of heavier selenium atom substitution, the transient species show more prominent signal of long-lived component after fast decay process with a time component of 57 ps [98]. Along with the fact that the relative fluorescence intensity of **16** is weaker than **12**, this feature supports that the introduction of the heavier selenium atom

increases the relative rate of intersystem crossing (S_1 - T_1) compared to sulfur substituted hexaphyrin.

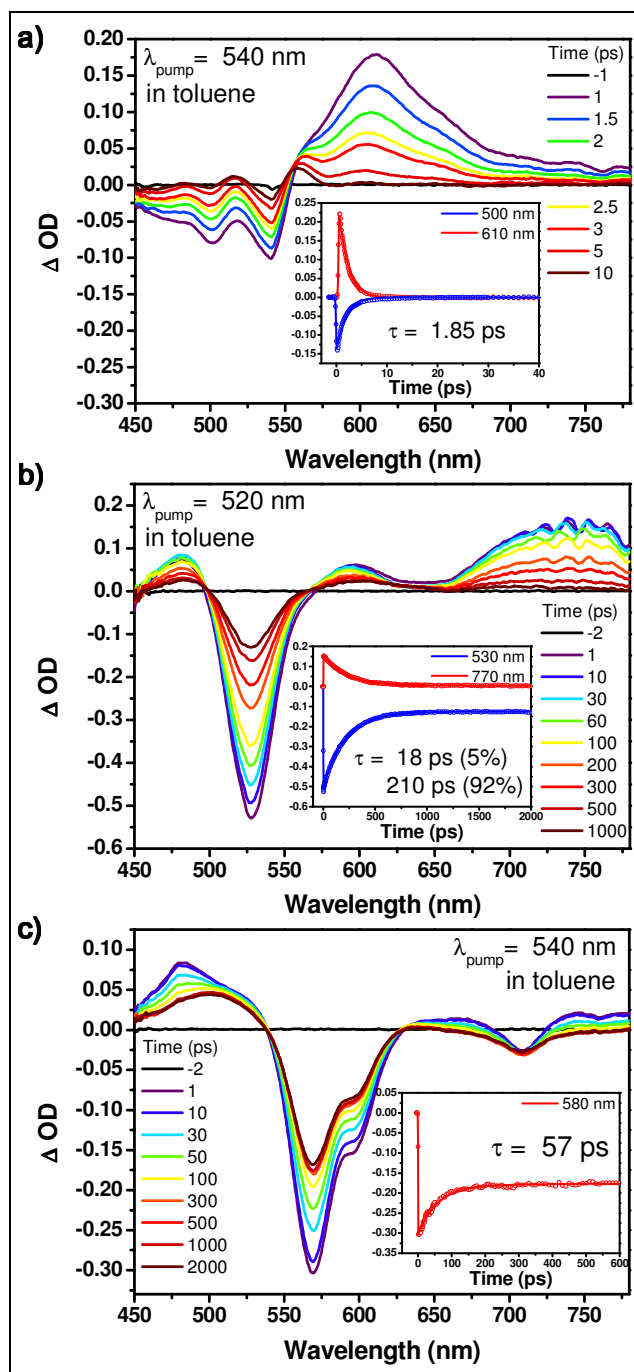


Figure 3.22: Femtosecond transient absorption spectra and decay profiles of a) thiophene-substituted [26]hexaphyrin (without thiophene bridge), b) **12**, and c) **16**

Further, preliminary nonlinear optical properties of thiophene-bridged hexaphyrins reveal that the TPA value for **12** is 2.6 times higher (1000 GM for dithiahexaphyrin and 2600 GM for **12**) the non-bridged congener, which proves that this class of molecules are promising candidate for NLO applications.

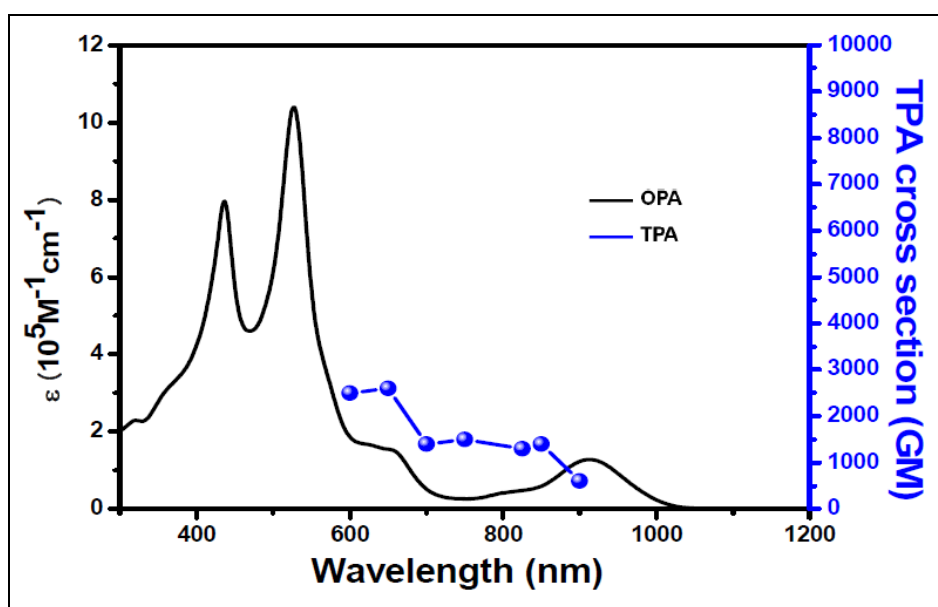


Figure 3.23: one photon (OPA) and two photon absorption (TPA) spectra of **12**

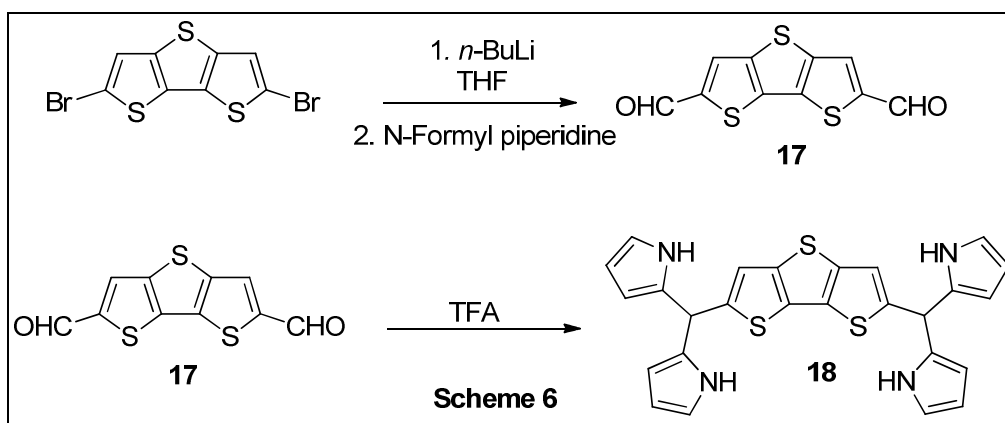
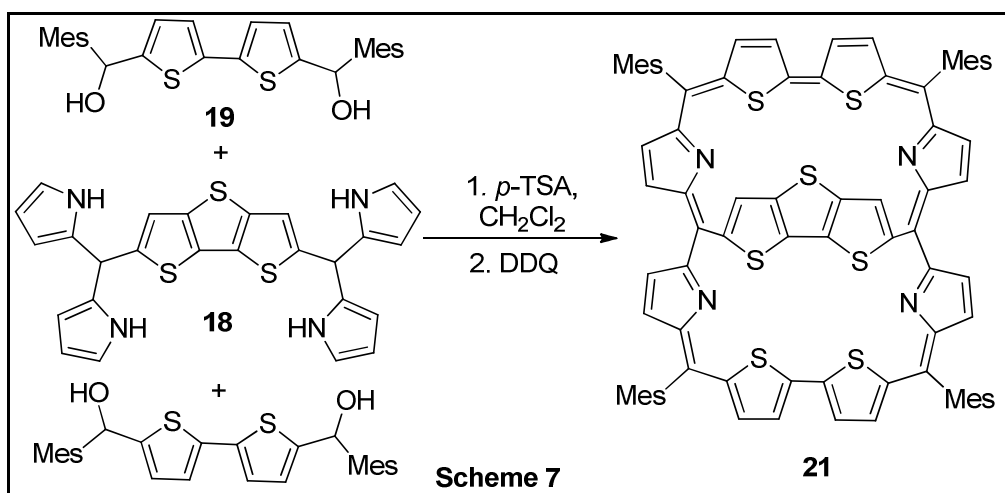
3.5 Inter-*meso* Dithienothiophene (DTT) Bridged Expanded Porphyrins

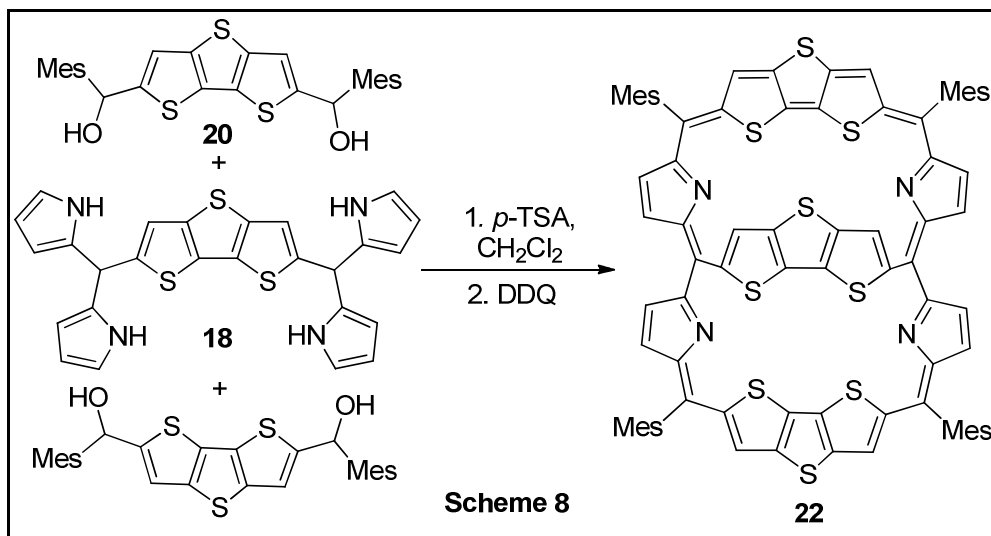
In order to validate the bridging approach for maintain the planarity in expanded porphyrin, the higher homologue of expanded bridged octaphyrins **21** and **22** were synthesized by using DTT as the bridging group.

3.5.1 Synthesis:

For the synthesis of dithienothiophene bridged octaphyrins, we have adopted the methodology similar to one used for the synthesis of thiophene bridged hexaphyrin **12**. The required 2,5-dithienothiophene bis(dipyrromethane) was synthesized by condensing 2,5-dithienothiophenedicarboxaldehyde **17** with pyrrole in the presence of TFA as catalyst to afford **18** in 45% yield (Scheme 6). **17** was synthesized from lithiated 5,5'-dibromo-DTT

followed by reaction with N-formyl piperidine. **18** was further condensed with 5,5'-bis(mesitylhydroxymethyl)-2,2'-bithiophene **19** in the presence of 0.5 equiv of *p*-TSA as an acid-catalyst followed by oxidation with *p*-chloranil to afford **21** in 6% yield along with two trace amount of side products, rubyrin and heptaphyrin (heptaphyrin). The formation of rubyrin and heptaphyrin are might be due to acidolysis of 2,5-bis(dipyrrolylmethyl)dithienothiophene **18**. We have also adopted the similar methodology for the synthesis of **22** by using 2,5-bis(mesitylhydroxy methyl)dithienothiophene **20** (Scheme 8).

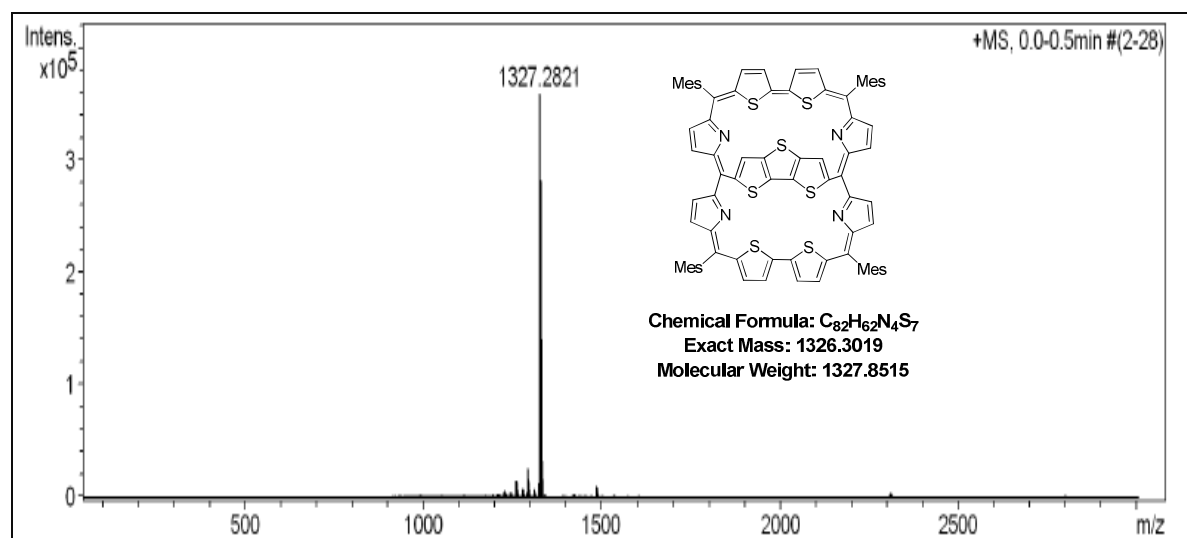
Scheme 6: Synthesis of **18**Scheme 7: Synthesis of **21**

Scheme 8: Synthesis of **22**

3.6 Results and Discussion

3.6.1 Mass spectral analysis

The targeted macrocycles **21**, **22** and side products were confirmed by mass spectral analysis. **21** shows the parent ion peak at 1327.2821 (M: H⁺) while **22** at 1387.226 (M: H⁺) with exact composition (Figure 3.24 and 3.25). The side products rubyrin and heptaphyrin show parent ion peak at 981.3334 (M; H⁺) and 1046.3589 (M; H⁺) (Figure 3.26 and 3.27) respectively.

Figure 3.24: ESI-Mass Spectrum of octaphyrin **21**

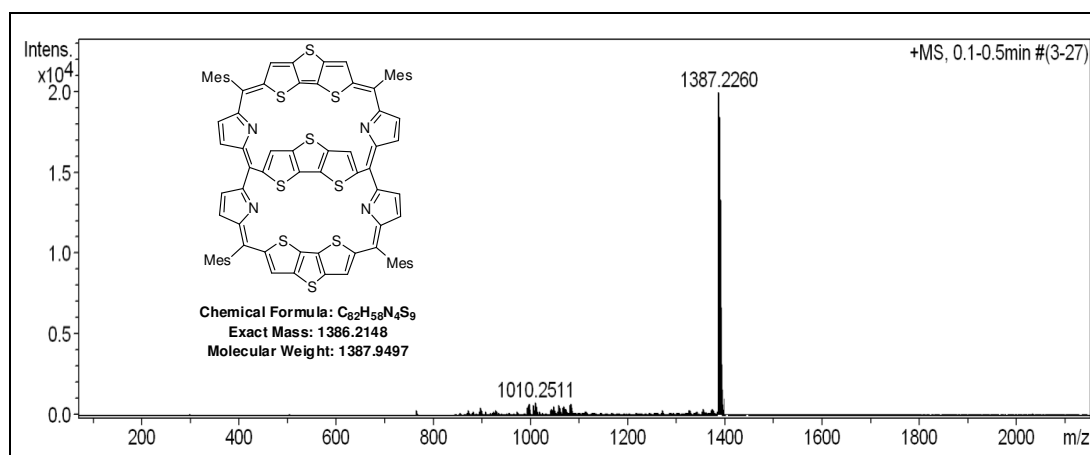
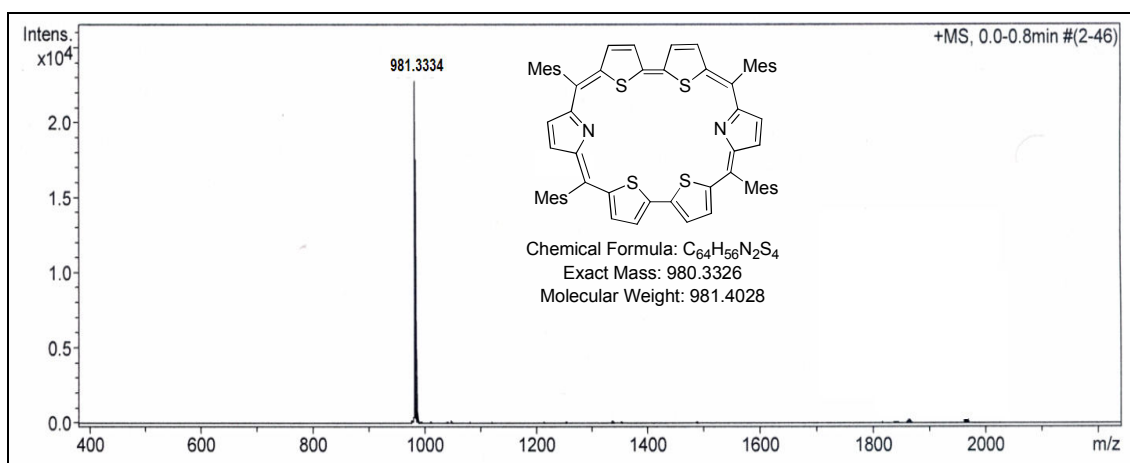
Figure 3.25: ESI-Mass Spectrum of octaphyrin **22**

Figure 3.26: Mass Spectra of rubyrin

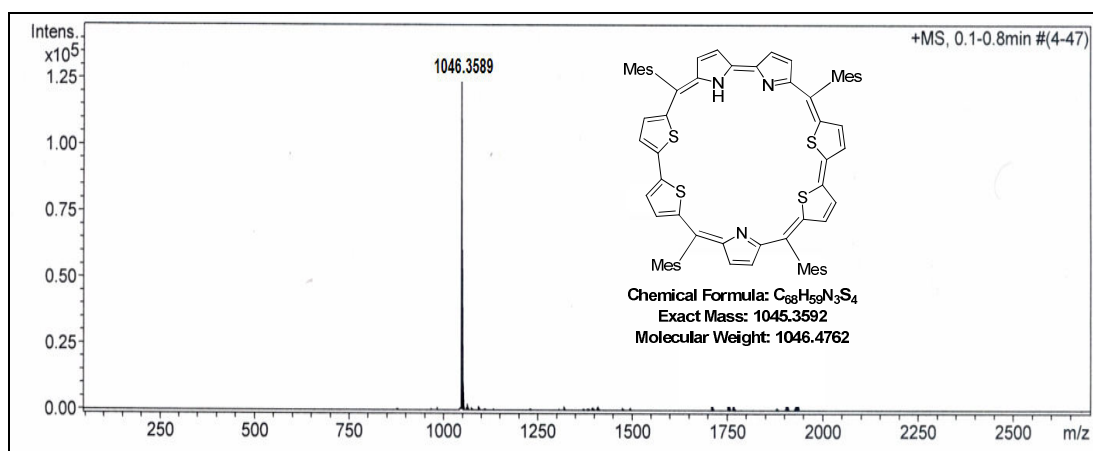


Figure 3.27: ESI-Mass Spectra of heptaphyrin

3.6.2 UV-Vis Absorption Spectral Analysis

The UV-Vis-NIR spectrum of freebase and the protonated form of **21** in CH_2Cl_2 is shown in Figure 3.28, which shows split Soret bands at 502 and 605 nm and two weak Q-bands at 827 and 1004 nm. The peak at 502 nm resembles the singly fused $[26\pi]$ rubyrin conjugation pathway and the peak observed at 605 nm corresponds to the extended conjugation of expanded macrocycle, thus, combination of $[26\pi]$ rubyrin and $[34\pi]$ octaphyrin conjugation pathways. Hence, freebase spectrum indicates that macrocycle **21** has dual conjugation pathways of singly fused rubyrin and singly fused rubyrin and bridged-octaphyrin which follows similar trend as observed in the case of thiophene bridged hexaphyrin **16** [52, 99].

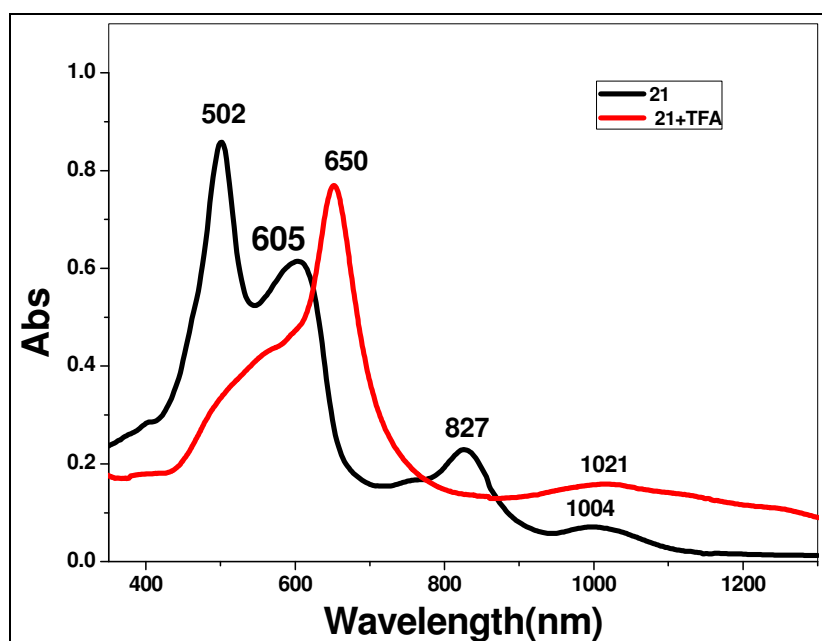


Figure 3.28: Electronic absorption spectrum of **21** and its protonated form

Upon protonation of **21** with TFA in CH_2Cl_2 , the bands observed at 502 and 605 nm merged together and shifted to 650 nm. The weak Q-bands were also further shifted to 1021 nm. The intensity of both the bands is slightly reduced as compared to freebase. The red-shifted bands upon protonation clearly reflect the previous observation of dual conjugation as observed in the case of thiophene bridged hexaphyrin **12**. Similar trend was observed in the

electronic absorption spectral analysis of **22** which is shown in Figure 3.29. The band observed at 498 nm in its freebase form is shifted to 654 nm upon protonation reflects the similar structural conformation as observed in **21**.

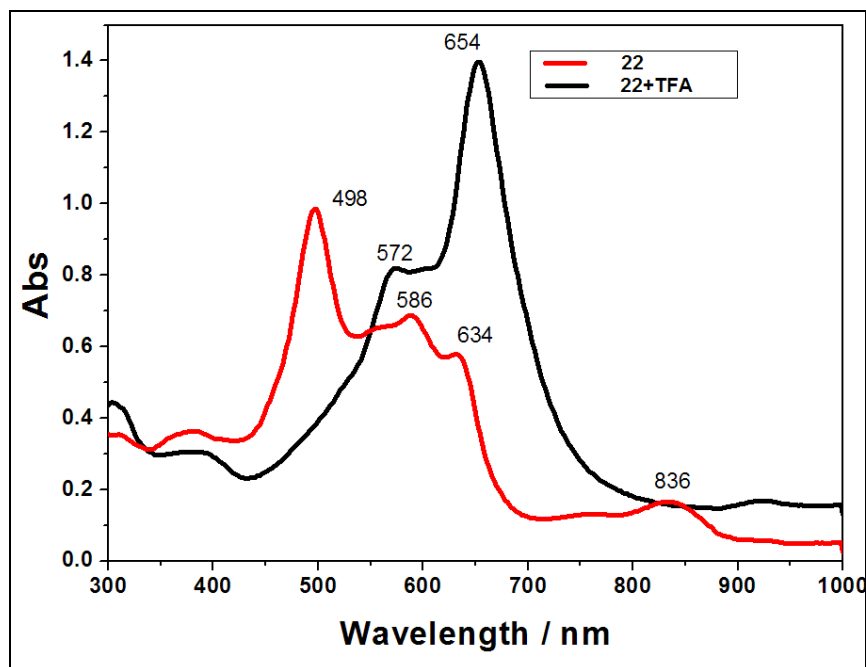
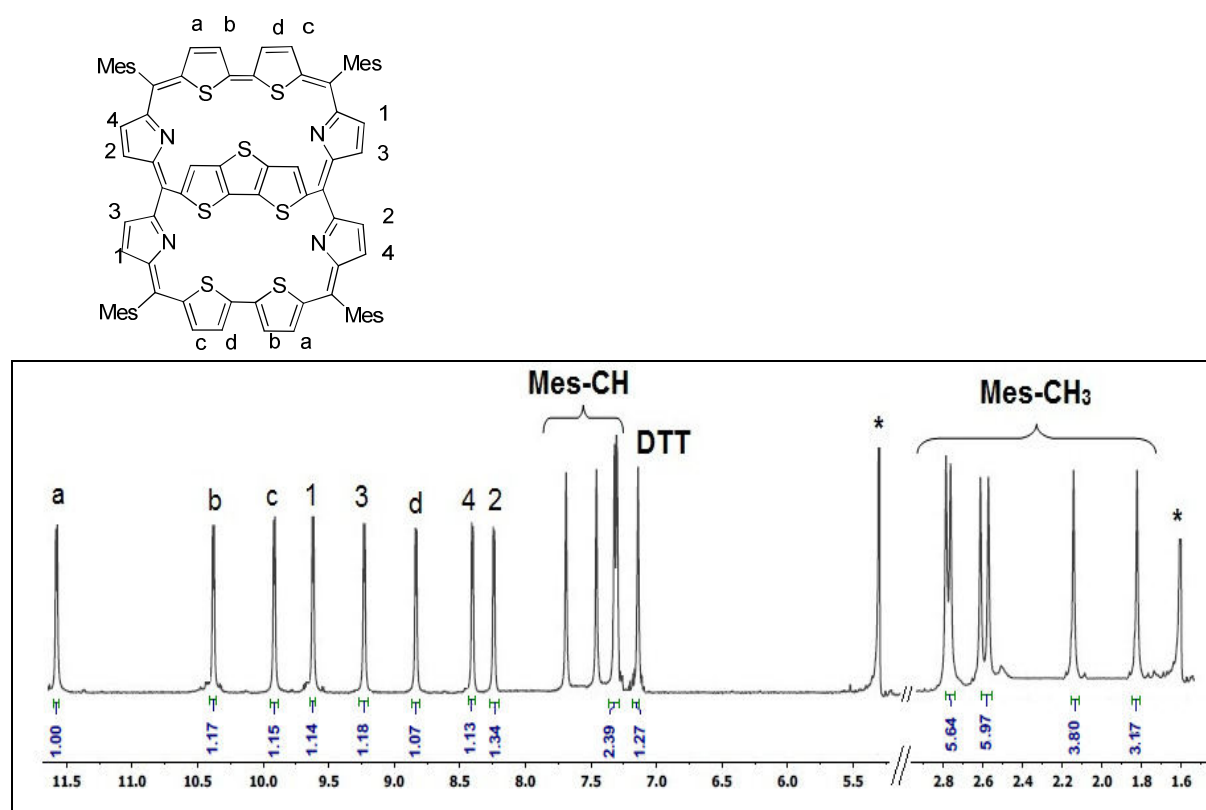
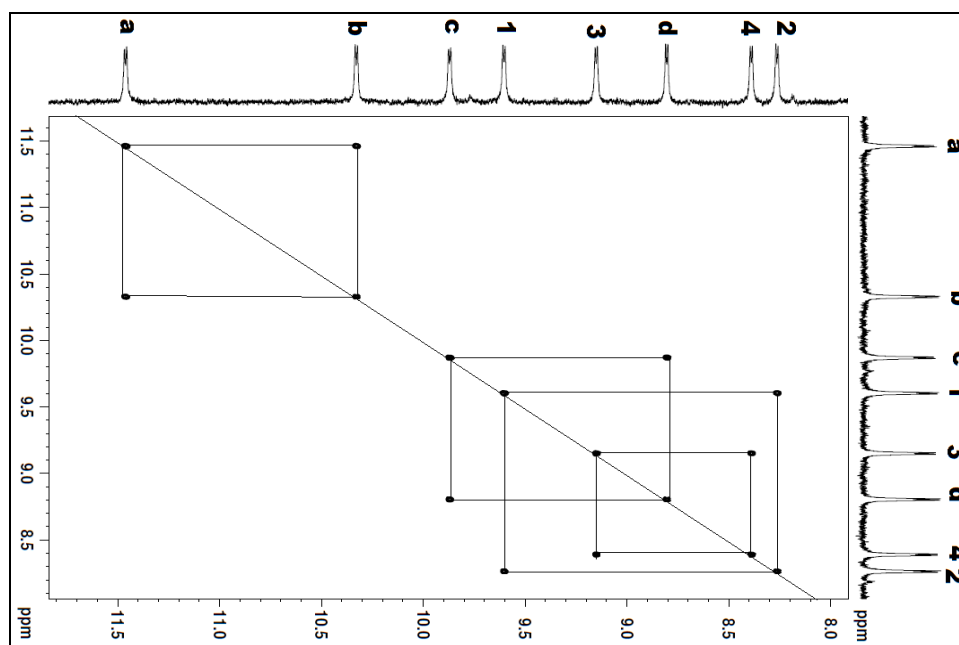


Figure 3.29: Electronic absorption spectrum of **22** and its protonated form

3.6.3 NMR analysis

The ^1H NMR spectrum of **21** has been recorded in CDCl_3 and shown in Figure 3.30. There are eight doublet signals appeared in the downfield region between 8-12ppm which indicates the β -CH protons of pyrrole and bithiophene. The singlet at 7.20 can be assigned to DTT-CH protons. The eight CH singals from four mesityl groups are resonated as two singlets between 7.40 to 7.64 ppm. The mesityl- CH_3 protons are observed at aliphatic region around 2.5 -2.9 ppm. The doublet observed for pyrrolic and bithiophene β -CH protons clearly indicate that all the protons are in-equivalent and hence the molecule is distorted. This was further confirmed by ^1H - ^1H correlation spectroscopy (COSY), where the a-d peaks correspond to β -CH protons of bithiophene unit and 1-4 peaks correspond to pyrrolic β -CH protons as shown in the Figure 3.31.

Figure 3.30: ^1H NMR spectrum of **21** in CD_2Cl_2 at 273KFigure 3.31: ^1H - ^1H COSY spectrum of **21** in CD_2Cl_2 at 273K

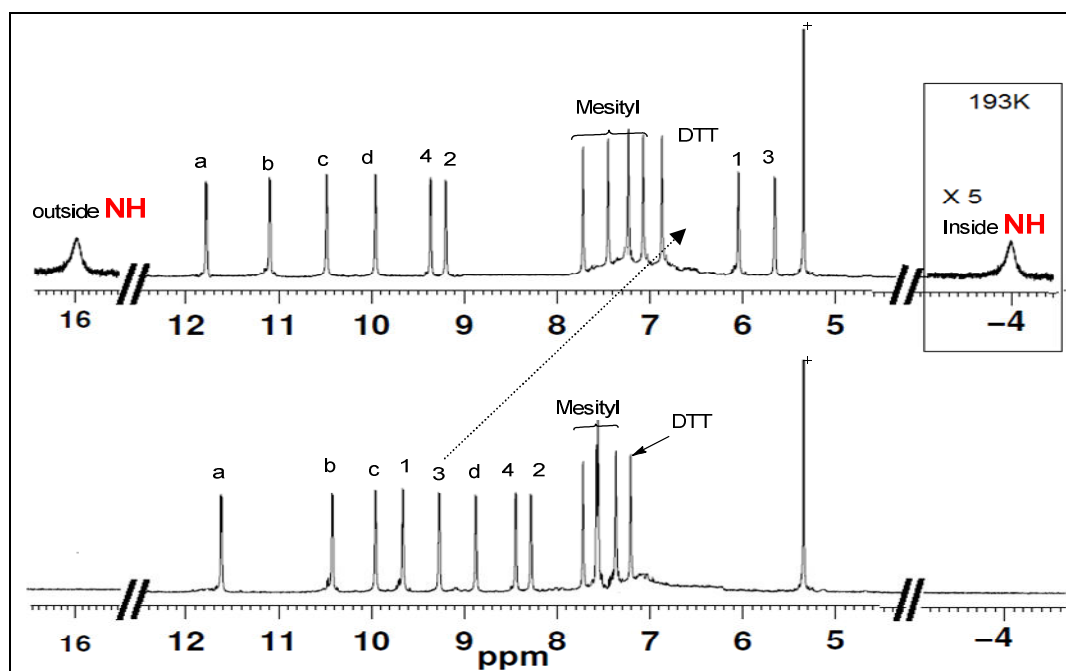
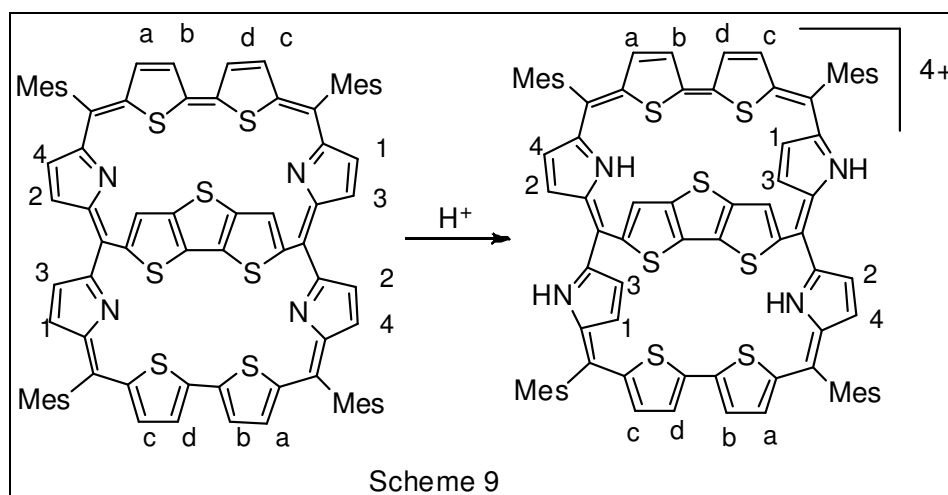


Figure 3.32: ^1H NMR spectrum of **21** in CD_2Cl_2 at 193 K (bottom) with 4 equiv of TFA (top)

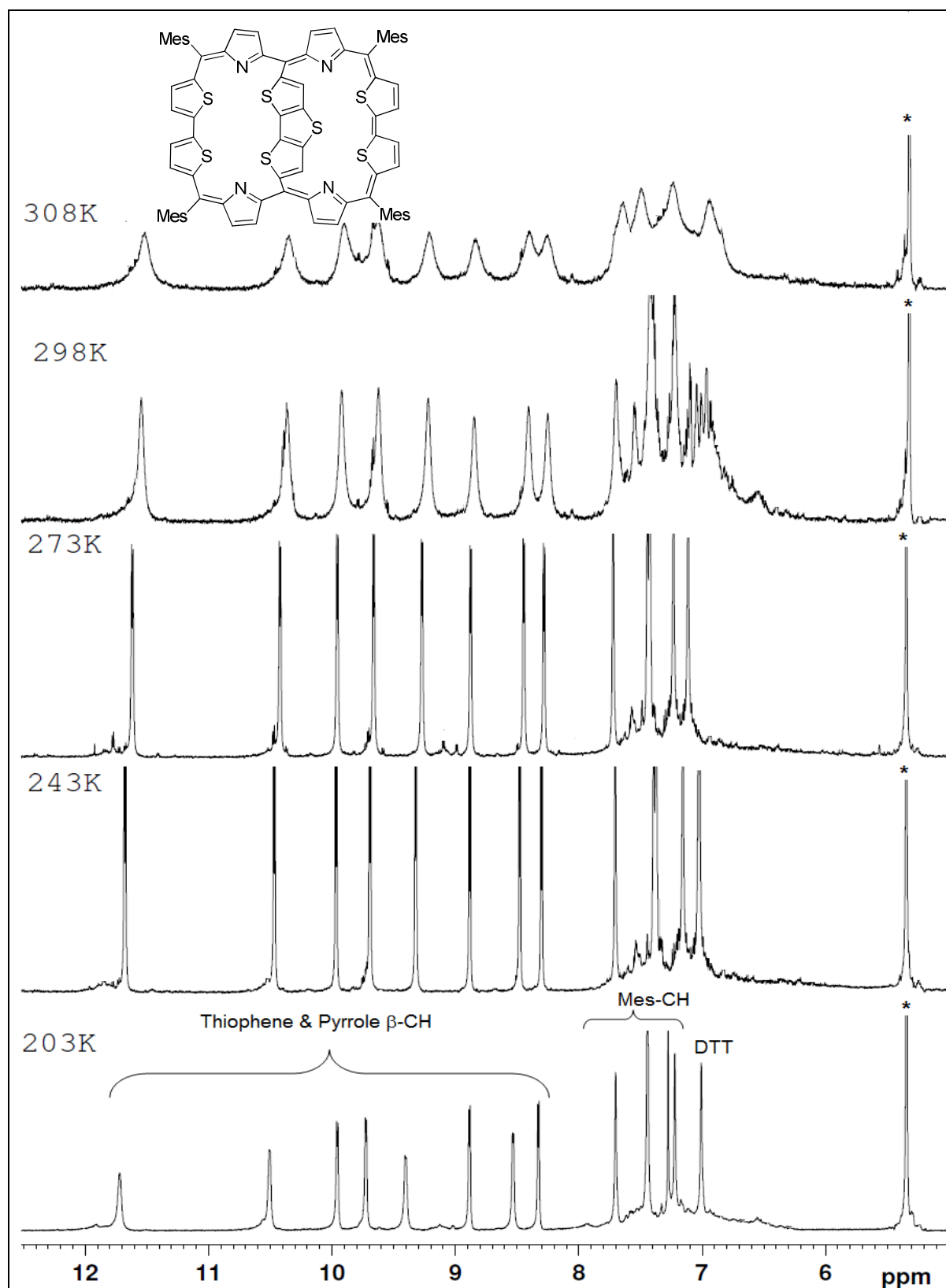
The protonation of **21** using TFA in CD_2Cl_2 leads to small downfield shift in the a, b and slightly upfield shift in the c, d signals of bithiophene β -CH protons in the ^1H NMR spectrum. On the contrary, out of eight pyrrolic β -CH protons 2,4-protons are slightly downfield shifted, while the 1,3-protons are drastically upfield shifted from 9.5 ppm to 5.8 ppm reflects that these two β -CH protons are inverted and experience the aromatic ring current effect with $\Delta\delta$ (chemical shift difference between the outer and inner β -CH signals) value of 3.7 ppm. At 4 equiv. of TFA, **21** become fully protonated, the two different NH signals are observed at low temperature. The inverted pyrrolic NHs which are in the periphery observed at 16 ppm, while the inner NH which is experiencing the aromatic ring current effect observed at -4.00 ppm. The result reflects that the ring inversion occur upon protonation (Scheme 9).

Variable temperature NMR of **21** exhibits no chemical shift upon lowering or increasing the temperature which support the molecular rigidity imposed by the DTT bridge (Figure 3.33).



Scheme 9: Proposed structural change of **21** upon protonation of TFA

The ^1H NMR spectrum of **22** in CD_2Cl_2 at 193 K is shown in Figure 3.34 (bottom). There are two doublets at 11.00 and 11.80 ppm (b,c) which indicate the pyrrolic β -CH protons. The peripheral DTT- β -CH protons are resonated as singlet at 11.50 ppm, however, the bridged DTT- β -CH protons are appeared as a singlet at 7.20 ppm. The half of the proton signals observed for pyrrolic and DTT- β -CH protons clearly reflects the macrocycle has centrosymmetry. The two singlets observed at 7.50 and 7.60 ppm are assigned to eight protons of four mesityl-CH signals. The mesityl- CH_3 protons are observed at aliphatic region around 2.5 -2.9 ppm. The DTT protons are not affected by ring current effect as observed in the case of thiophene bridged hexaphyrin **12**. Equivalent doublets of pyrrole clearly indicate a symmetric molecule which is significantly undistorted.

Figure 3.33: Variable Temperature ¹H NMR spectra of **21**

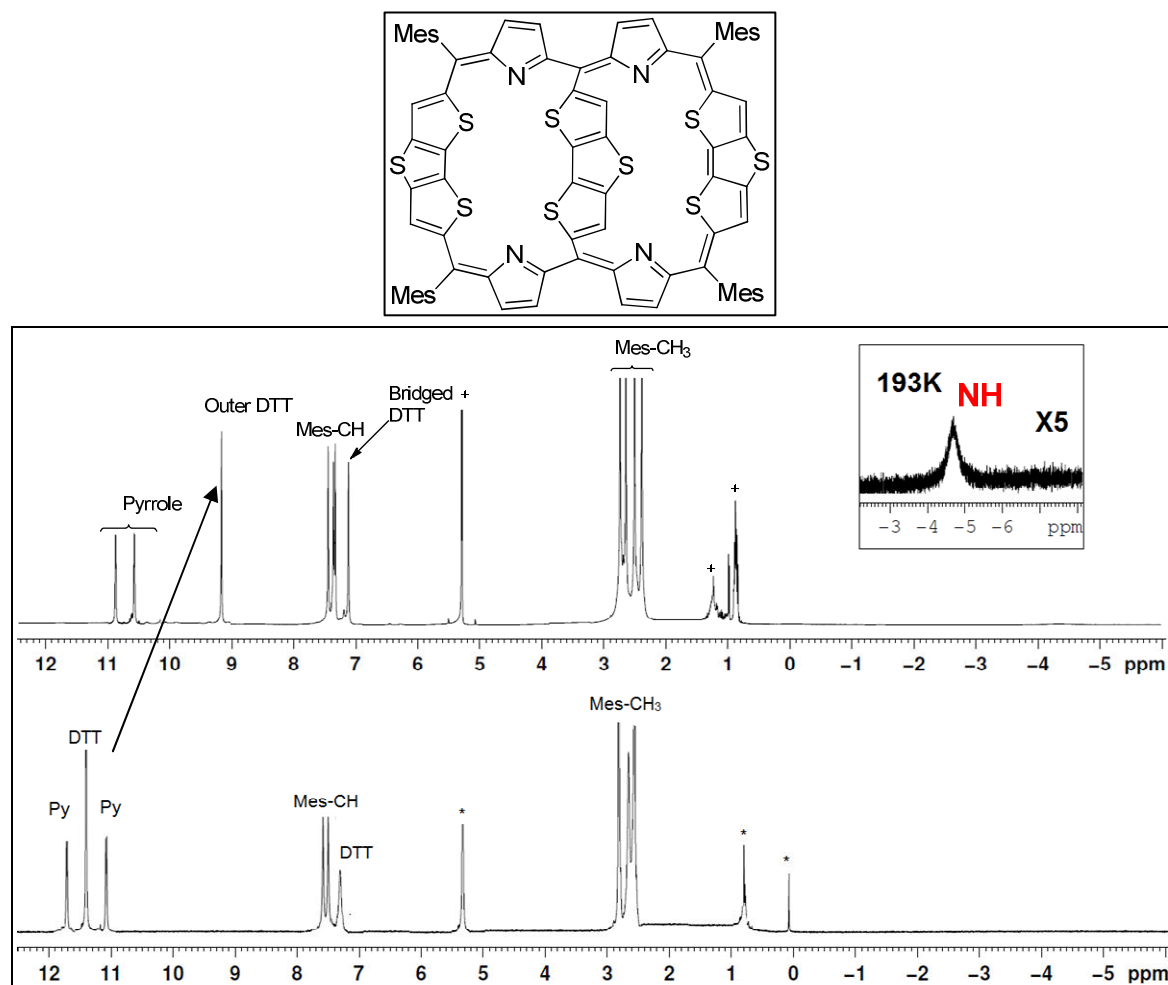


Figure 3.34: ¹H NMR spectrum of **22** in CD₂Cl₂ at 193 K (bottom) with 4 equiv. of TFA (top)

Upon addition 4 equiv of TFA, the macrocycle was fully protonated. All the β-CH (pyrrolic, peripheral DTT and bridged DTT) protons are slightly upfield shifted. The pyrrolic β-CH protons are centered at 10.80 ppm, while the peripheral DTT-β-CH protons, which is observed at 11.5 ppm in the free base is now shifted to 9.1 ppm with the up-field shift difference of 2.4 ppm. However, the bridged DTT β-CH protons are resonated at 7.1 ppm. The NH signal corresponds to the protonated imine nitrogen was observed at -4.5 ppm (Figure inset).

Overall, there is no ring inversion in the case of pyrrolic β-CH protons upon protonation and no chemical shift difference of bridged DTT-β-CH protons upon lowering the temperature in the presence of TFA clearly reflects the molecular rigidity imposed by the

bridged DTT moiety and peripheral DTT.

3.6.4 Voltammetry

The cyclic voltammetry and differential pulse voltammetry of the DTT-bridged-octaphyrin **21** was carried out in anhydrous CH_2Cl_2 and Tetrabutylammoniumhexafluorophosphate as supporting electrolyte as shown in Figure 3.36. Electrochemical analysis was carried out in three electrode cell system; Glassy carbon working electrode, platinum wire counter electrode and Ag/Ag^+ reference electrode.

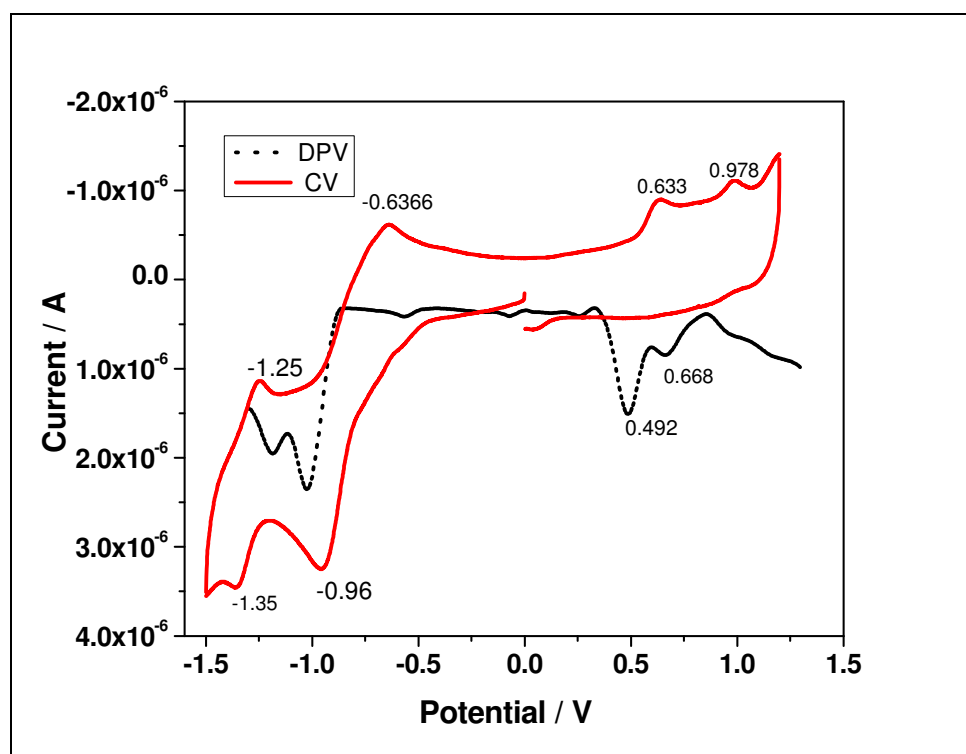


Figure 3.35: Cyclic (Solid line) and Differential Pulse Voltammogram (dotted line) of **21** in CH_2Cl_2 contains 0.1 M TBAPF6 with scan rate of 50 mV/s

21 shows two quasi-reversible oxidation and reduction waves and redox process was further confirmed by differential pulse voltammetry. The ΔE_{redox} (potential difference between first oxidation and reduction) was found to be 1.59 which clearly indicates the reduction in the HOMO-LUMO value reflects the extended π -conjugation and further supports the red shift in the electronic absorption spectra, where the ΔE_{redox} value of

porphyrin is: 2.25 V [99]. **22** also exhibit the similar redox behavior with ΔE_{redox} value of 1.57 V.

3.6.5 Nucleus Independent Chemical Shift:

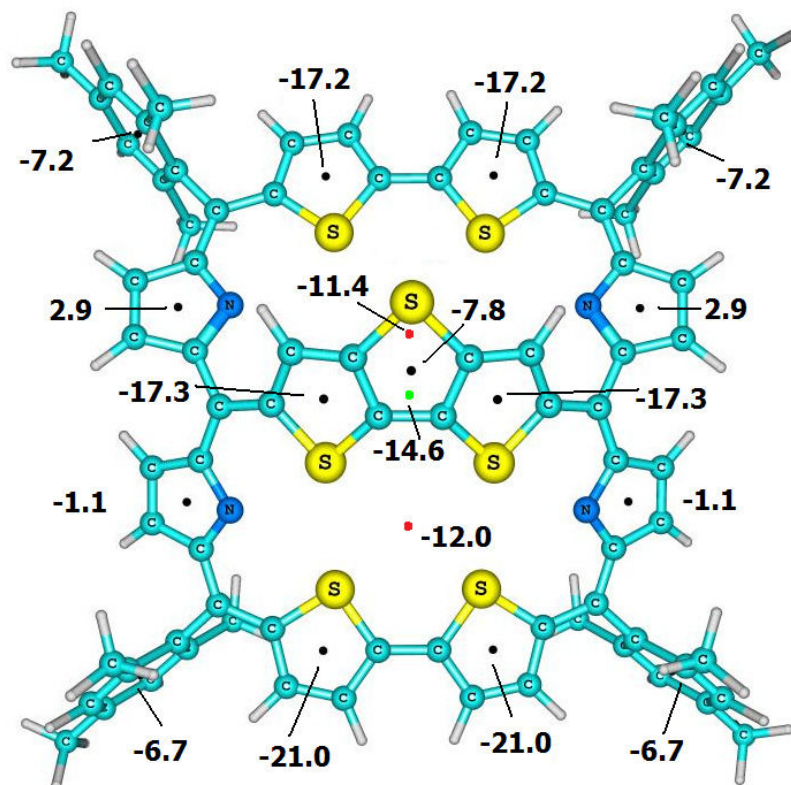


Figure 3.36: NICS value for **21**

NICS value at the center of **21** is -14.6 (green dot) while that for the circular portion at the bottom and top regions are -12.0 and -11.4 (red dots), respectively. This indicates that the global aromaticity of **21** is very high. A free thiophene has NICS value -13.4 while all the thiophene rings except the central one of the bridging dithieno[3,2-b:2',3'-d]thiophene in **21** show significantly larger negative NICS values (black dots) and among them the rings at the bottom is more aromatic than those at the top. NICS of the central ring of dithieno[3,2-b:2',3'-d]thiophene moiety is less negative than free thiophene by 5.6 ppm. Among the pyrrole rings, NICS values suggest that rings at the bottom region possess slight aromatic character while those at the top region possess some amount of antiaromatic character.

NICS value of $\mathbf{21.4H}^+$ at the top and bottom end are showed significantly less negative value than $\mathbf{21}$ (red dots). Also, the NICS value at the centre of $\mathbf{21.4H}^+$ is -3.0 (green dot) which is more than 10 ppm less negative than $\mathbf{21}$. The result clearly indicates that the global aromaticity of $\mathbf{21.4H}^+$ is decreased as compared to $\mathbf{21}$ and $\mathbf{21.2H}^+$ (Figure 3.37). In general thiophene rings show significant aromatic character than free thiophene while the individual NICS values except the central one of the bridging dithieno[3,2-b:2',3'-d]thiophene are more or less similar to $\mathbf{21}$ (black dots). NICS of the central ring of dithieno[3,2-b:2',3'-d]thiophene moiety is less negative than free thiophene by 1.4 units but more negative than the corresponding ring of $\mathbf{21}$ by 4.2 units. Protonation gives high aromatic character to all the pyrrole rings.

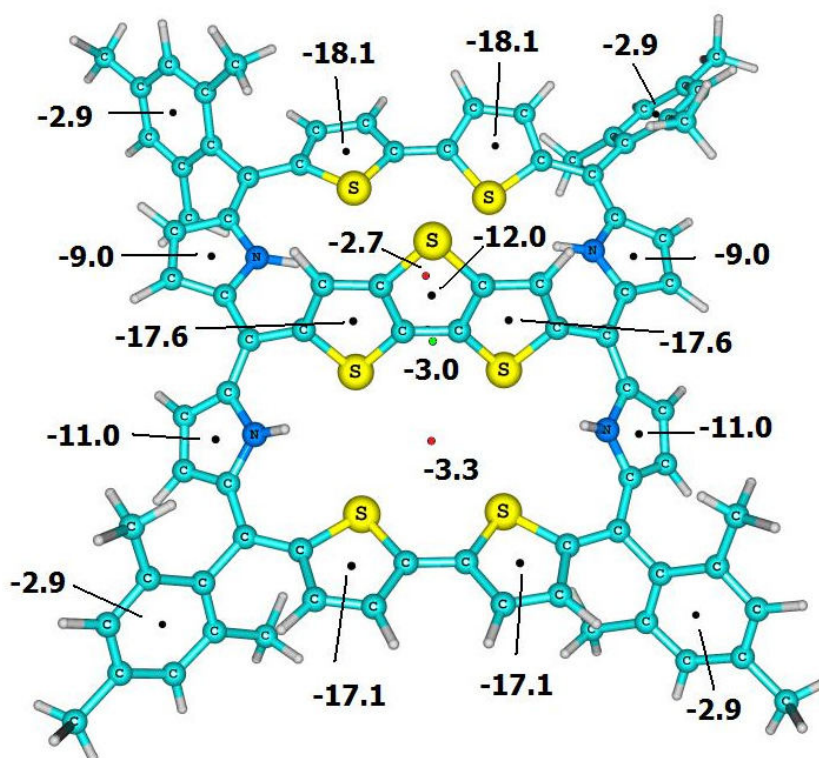


Figure 3.37: NICS value for $\mathbf{21.4H}^+$

NICS value of benzene is -9.7. The NICS of *meso* mesityl substituents in $\mathbf{21}$ is -7.2 and -6.7 and upon double protonation, NICS negative character decreases to -6.2 and -5.7 in

21+2H⁺. Further, with tetra protonation, a drastic decrease in the negative character of the NICS of *meso* substituent (-2.9) is observed for **21+4H⁺**. Reduction in the aromatic character of *meso* substituent in **21+4H⁺** may contribute to the overall reduction of the global aromatic character of **21+4H⁺** compared to **21**.

3.7 Conclusion:

We have demonstrated the syntheses of two new inter *meso* thiophene bridged core modified hexaphyrins and DTT bridged octaphyrins by a simple and efficient methodology. Spectroscopic and structural data reveals the aromatic nature of both the hexaphyrins and octaphyrins. A comparison of structures of bridged hexaphyrins with the corresponding hexaphyrins without internal bridge reveal the following; (a) introduction of internal bridging group makes the hexahyrin skeleton rigid thus preventing ring inversion of heterocyclic ring; (b) the hexaphyrin skeleton in the bridged structure are more planar facilitating better π conjugation pathway thus increasing the aromaticity. Such structural changes lead to changes in the electronic structure which are important from the point of view of their application as nonlinear optical materials and model compounds for aromaticity in higher annulene compounds.

3.8 Experimental Procedure:

3.8.1 Synthesis of 12: (method 1)

A mixture of 2,5-bis(dipyrrolylmethyl)thiophene **10** (0.3 g, 0.81 mmol) and 2,5-bis(mesitylhydroxymethyl)thiophene **11** (0.62g, 1.62mmol) were dissolved in anhydrous CH₂Cl₂ (200 mL) and stirred under argon atmosphere for 10 min. *p*-Toluenesulphonic acid (*p*-TSA) (0.076 g, 0.4 mmol) was added and the stirring was continued for 90 min. *p*-Chloranil (0.590 g, 2.4 mmol) was added and the reaction mixture was refluxed for another 90 minutes under aerobic condition. The solvent was evaporated under vacuum. The residue

was purified by column chromatography on basic alumina. A pink color band eluted with CH₂Cl₂/petroleum ether (1:3) gave **12** as green crystals in 6% yield.

ESI-MS: m/z(%): 1051.7947 (100) [M; H⁺]; UV/Vis (CH₂Cl₂): λ_{max}[nm] (ε [10⁵M⁻¹cm⁻¹]): 433 (0.309), 530 (0.460), 655 (0.061), 914 (0.036); (CH₂Cl₂/TFA) λ_{max}[nm] (ε [10⁵M⁻¹cm⁻¹]): 388 (0.160), 570 (0.557), 766 (0.0521), 921 (0.101); ¹H NMR (400MHz, CD₂Cl₂, 25° C, TMS) δ[ppm] : 9.8 (d, 4H, ³J=4.8 Hz), 9.17 (s, 4H), 8.6 (d, 4H, ³J=4.8 Hz), 7.4 (s, 4H), 7.2 (s, 4H), 3.95 (s, 2H) 2.6 (s, 12H), 2.4 (s, 12H) 1.58 (s,12H).

3.8.2 Synthesis of 12: (Method 2)

To a solution of tripyrrane **15a** (0.48 g, 1 mmol) and 2,5-bisthiophene carboxaldehyde **9** (0.07 g, 0.5 mmol) in 200mL dry CH₂Cl₂ in argon atmosphere, *p*-toluenesulfonic acid (0.047 g, 0.25 mmol) was added and the mixture was stirred for 90 min, followed by oxidation with *p*-chloranil (0.740 g, 3 mmol) by refluxing for 90 min under aerobic condition. The solvent was evaporated in vacuum. The residue was purified by column chromatography on basic alumina. A pink color band eluted with CH₂Cl₂/hexane (1:3) gave bridged hexaphyrin **12** as green crystals in 12% yield.

3.8.3 Synthesis of 16:

The compound **16** was prepared by same procedure as that of **12**, selenophene tripyrrane **15b** was used instead of thiophene tripyrrane **15a**.

ESI-MS: m/z(%): 1146.8234 (100) [M+2⁺]; UV/Vis (CH₂Cl₂): λ_{max}[nm] (ε [10⁵M⁻¹cm⁻¹]): 415 (0.136), 564 (0.736), 702 (0.138), 932 (0.036); (CH₂Cl₂/TFA) λ_{max} [nm] (ε [10⁴M⁻¹cm⁻¹]): 422 (0.163), 598 (0.475), 677 (0.267), 969 (0.104); ¹H NMR (400MHz, CDCl₃, 25° C, TMS) δ[ppm]: 10.24 (d, 4H, ³J= 5 Hz), 9.93 (s, 4H), 8.87 (d, 4H, ³J= 5 Hz), 7.48 (s, 4H), 7.28 (s, 4H), 2.28 (s, 12H), 2.46 (s, 12H) 1.48 (s,12H), 1.35 (s, 2H).

3.8.4 Synthesis of 21:

A mixture of **18** (150mg, 0.31mmol) and **19** (300 mg, 0.65 mmol) were dissolved dry CH₂Cl₂ (200 ml) and stirred under N₂ atmosphere for 5 min. *p*-Toluene sulphonic acid (29.4 mg, 0.15 mmol) was added and the stirring was continued for 90 min. DDQ (2.5 eq) was added to the reaction mixture and allowed to stir for 4 hrs. The solvent was then evaporated at reduced pressure. The residue was purified on a basic alumina column which gave three bands; blue, pink and dark blue in color. The third band was identified as **21**. **21** was further purified by neutral alumina column to give a brown color solid in 6% yield.

ESI-MS: m/z (%): 1327.2821 (100) [M; H⁺];

Uv/Vis (CH₂Cl₂): λ_{max}[nm] (ε [10⁴M⁻¹cm⁻¹]): 501 (1.7), 605 (4.8), 827 (1.7), 999 (0.5);

TFA/CH₂Cl₂): λ_{max}[nm] (ε [10⁴M⁻¹cm⁻¹]): 650 (0.79), 1010 (0.162), 1380 (0.17)

¹H NMR (400MHz, CD₂Cl₂, 25°C, TMS) δ[ppm]: 11.61 (d, 2H), 10.41 (d, 2H), 9.95 (d, 2H), 9.65 (d, 8H), 9.26 (d, 8H), 8.87 (d, 2H), 8.43 (d, 2H), 8.27 (d, 2H), 7.20 (s, 2H), 7.44 (s, 2H), 7.42 (s, 4H), 7.23 (s, 2H), 2.79 (s, 6H), 2.78 (s, 6H), 2.61 (s, 6H), 2.59 (s, 6H), 2.15 (s, 6H), 1.81 (s, 6H).

3.8.4 Synthesis of **22**:

A mixture of **8** (150 mg, 0.31 mmol) and **20** (305 mg, 0.62 mmol) were dissolved in anhydrous CH₂Cl₂ (200ml) and stirred under N₂ atmosphere for 5 minutes. *p*-Toluenesulphonic acid (29.4 mg, 0.15 mmol) was added and the stirring was continued for 2 hrs. *p*-Chloranil (2 equiv.) was added to the reaction mixture and refluxed under stirring condition for 2hrs. The solvent was then evaporated at reduced pressure. The residue was purified on a basic alumina column which gave three bands; blue and dark blue in color. The second blue band was identified as **22**. This band was further purified by neutral alumina column to give a dark violet color solid in 3% yield.

ESI-MS: m/z (%): 1387.2260 (100) [M; H⁺];

UV/Vis (CH₂Cl₂): λ_{\max} [nm] (ϵ [$10^5\text{M}^{-1}\text{cm}^{-1}$]): 498 (1.02), 486 (0.72), 634 (0.63), 836 (0.21);

TFA/CH₂Cl₂): λ_{\max} [nm] (ϵ [$10^4\text{M}^{-1}\text{cm}^{-1}$]): 572 (0.83), 654 (1.42), 930 (0.22)

¹H NMR (400 MHz, CD₂Cl₂, 25° C, TMS) δ [ppm]: 10.89 (s, 4H), 10.55 (s, 4H), 9.21 (s, 4H),

7.45 (s, 4H), 7.40 (s, 4H), 7.11 (s, 2H), 2.75 (s, 6H), 2.63 (s, 6H), 2.54 (s, 3H), 2.32 (s, 3H).

3.9.1 Crystal data for 12 and 16

Parameters	12	16
Solvent of crystallization	CHCl ₃ / Hexane	CH ₃ Cl / Pentane
Empirical formula	C ₇₀ H ₅₈ N ₄ S ₃	C ₇₁ H ₅₇ Cl ₃ N ₄ S ₂ Se ₂
M_w	1051.38	1262.54
T [K]	100(2)K	296(2)K
λ [Å]	0.71073	0.71073
Crystal system	monoclinic	monoclinic
Space group	P21/n	P21/n
a [Å]	13.9067(4)	14.6576(7)
b [Å]	15.8085(4)	12.8656(6)
c [Å]	15.0187(4)	17.6237(8)
α [°]	90.00°	90.00°
β [°]	111.7020° (10)	101.350 (2)°
γ [°]	90.00°	90.00°
V [Å ³]	3067.74(14) Å ³	3258.5(3) Å ³
Z, ρ_{calcd} [Mg m ⁻³]	1.138	1.287 mg/m ³
μ (MoK α) [mm ⁻¹]	0.164	0.133
$F(000)$	3384	1292
Crystal size [mm]	0.2 × 0.1 × 0.05	0.11 × 0.09 × 0.07
θ range for data collection [°]	1.94 to 26.49	1.97 to 25.40
Reflections collected	42997	33036
Refinement method	Full-matrix least-squares on F^2	Full-matrix least-squares on F^2
Data / restraints / parameters	8281 / 0 / 377	5985 / 169 / 426
Goodness-of-fit on F^2	1.108	1.181 { $I > 2\sigma(I)$ }
Final R indices [$I > 2\sigma(I)$]	$R_1 = 0.0684$	$R_1 = 0.0910$ $wR_2 = 0.1137$
R indices (all data)	$wR_2 = 0.1932$	$R_1 = 0.0509$, $wR_2 = 0.2694$

Core-Modified Fused Expanded Porphyrins

4.1 Introduction

In the previous chapter attention has been focused on the syntheses, spectral and structural characterization of bridged expanded porphyrins. In order to avoid twist in the expanded porphyrins, we adopted the bridging strategies. As expected, the bridged expanded porphyrins such as thiophene bridged hexaphyrins and dithienothiophene bridged octaphyrins maintained planar structure. To maintain planarity, in addition to bridging strategies in this chapter, we have focused on another strategy, called fusion. There are series of fused expanded porphyrins are known in the literature [51-53, 101-104] and such a macrocycles were briefly discussed in the first chapter.

There are two strategies adopted so far in the literature for the synthesis of fused expanded porphyrinoids. In the first strategy, the fused ring is generated during the final condensation or synthesized after macrocyclic formation **1** (Chart 1). In this case, there is no control for the fused ring formation. In the second strategy, the fusion is introduced in the starting material itself. For example, Lee and co-workers reported the benzodipyrrole sapphyrin **2** [51] and Sessler and co-workers synthesized the dioxobenzosapphyrin **3** [52]. Recently, our group also has demonstrated the synthesis of electron rich core dithienothiophene modified singly and doubly fused **4** rbyrins [53].

In fused expanded porphyrins, both the rigid and flexible parts can coexist in one molecule at a time, which is known to be a critical factor for synthesizing molecule with

Hückel and/or Möbius aromatic character and also monitor their structural transformation from Möbius to Hückel topology or vice versa [105]. Further, the ring fusion reaction has received much attention because it allows one to investigate thoroughly the intrinsic photophysical properties and aromaticity [106].

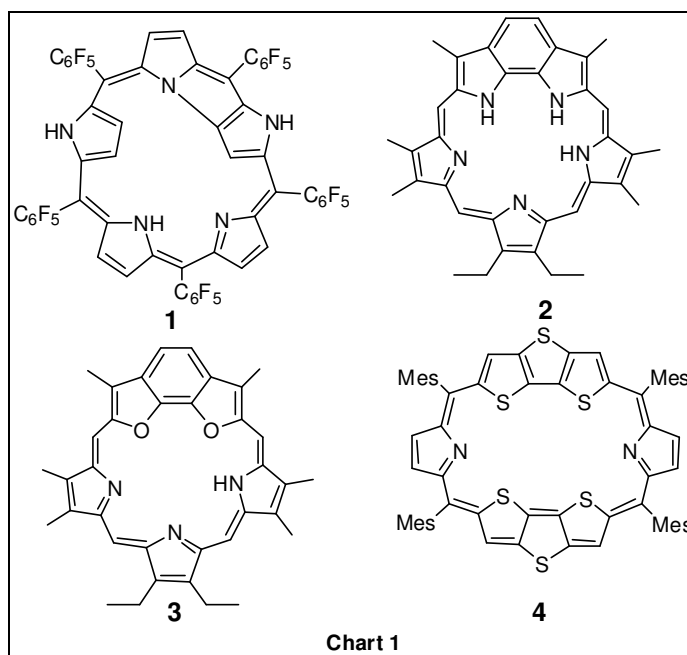
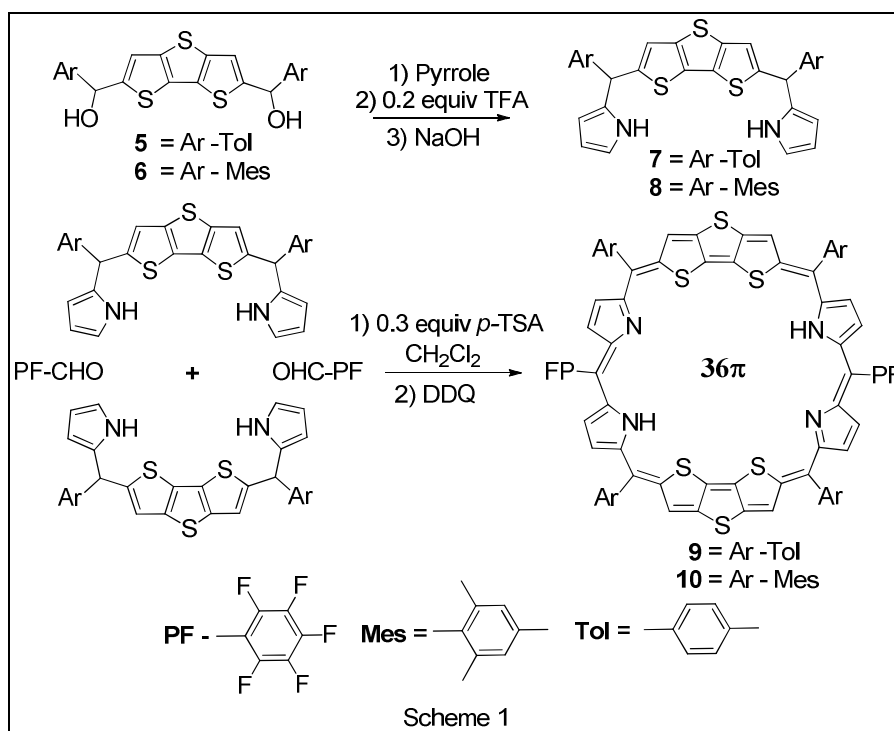


Chart 1. Fused expanded porphyrins

4.2 Core modified doubly fused octaphyrins: Syntheses

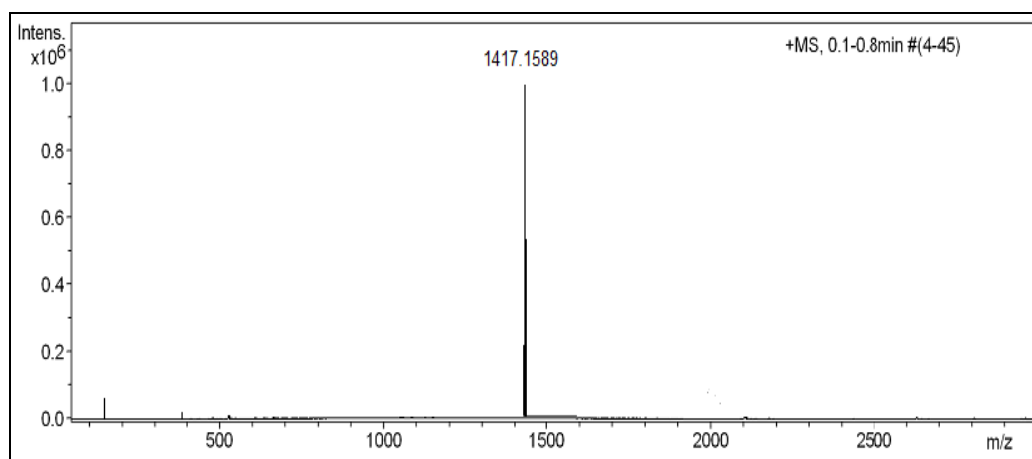
The fused DTT-diol (**5** or **6**) was reacted with pyrrole in presence of 0.2 equiv of trifluoroacetic acid (TFA) to get fused DTT-dipyrane (**7** or **8**) in 85% yield (Scheme 1). Further acid-catalyzed condensation of **7** or **8** with equal amount of pentafluorobenzaldehyde in presence of 0.3 equiv of *p*-toluenesulfonic acid (*p*-TSA) followed by oxidation with 2,3-dichloro-5,6-dicyano-1,4-benzoquinone (DDQ) gave the crude product. Repeated purification by column chromatography over basic alumina followed by silica gel (100-200 mesh) with CH₂Cl₂-hexane (30:70) gave a pink fraction which was identified as the doubly fused octaphyrins **9** or **10**. After evaporation of solvent a green color solid was isolated in 7-10 % yield.



Scheme 1: Syntheses of doubly fused octaphyrins.

4.3 Result and Discussion:

4.3.1 Mass spectral analysis

Figure 4.1: ESI-Mass spectrum of **9**

The ESI-mass spectral analysis of **9** and **10** were shown in Figure 4.1 and 4.2. The molecular ion peaks of **9** and **10** were observed at 1417.1589 (M+ H⁺) and 1529.287 (M+H⁺), which confirm the exact composition of the macrocycles.

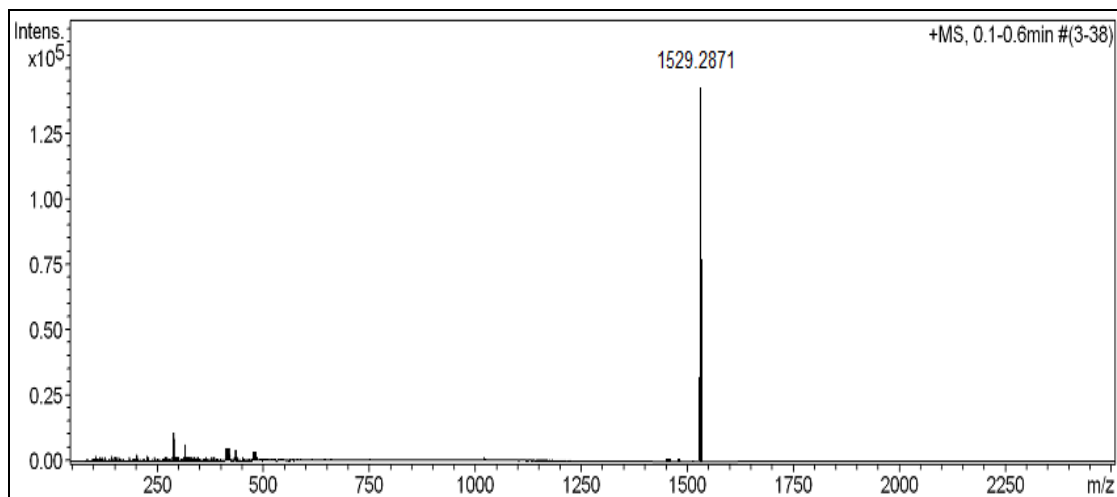


Figure 4.2: ESI-Mass spectrum of **10**

4.3.2 NMR characterization

The ^1H NMR spectra of **9** and its diprotonated derivative **9.2H⁺** along with the assignments are shown in Figure 4.3. The two inner-NH protons of pyrrole ring in **9** resonates as singlet in the deshielded region at 15.48 ppm and this assignment was confirmed by D_2O exchange experiment. Two multiplets centered at 6.32 and 5.87 ppm are assigned to four pyrrole β -CH protons and this assignment was confirmed by ^1H - ^1H correlation spectroscopy (COSY) experiment (Inset in Figure 4.3).

The *meso* tolyl -CH protons appear as doublet of doublet at 7.25 ppm and 7.41 ppm (confirmed by ^1H - ^1H COSY spectrum, Inset). Four DTT ring protons appear as two sharp singlets at 9.38 ppm and 6.85 ppm and NOESY experiment confirms the presence of long range correlation between these protons. Four *meso*-Tolyl- CH_3 protons resonate as two singlets at 2.48 and 2.45 ppm. Furthermore, the ^1H NMR spectrum of **9** did not show any major changes in chemical shift on varying the temperature from 298 – 178 K except that the spectrum was resolved better at 178 K. This observation suggests that there is no change in the structure of the macrocycle upon temperature variation. However, at 343 K the spectrum became broad (Figure 4.4). The ^1H NMR data, on comparison with the data reported for other

expanded porphyrins suggest that **9** in its freebase form conform to the 36π twisted figure-eight structure and is nonaromatic. [107]

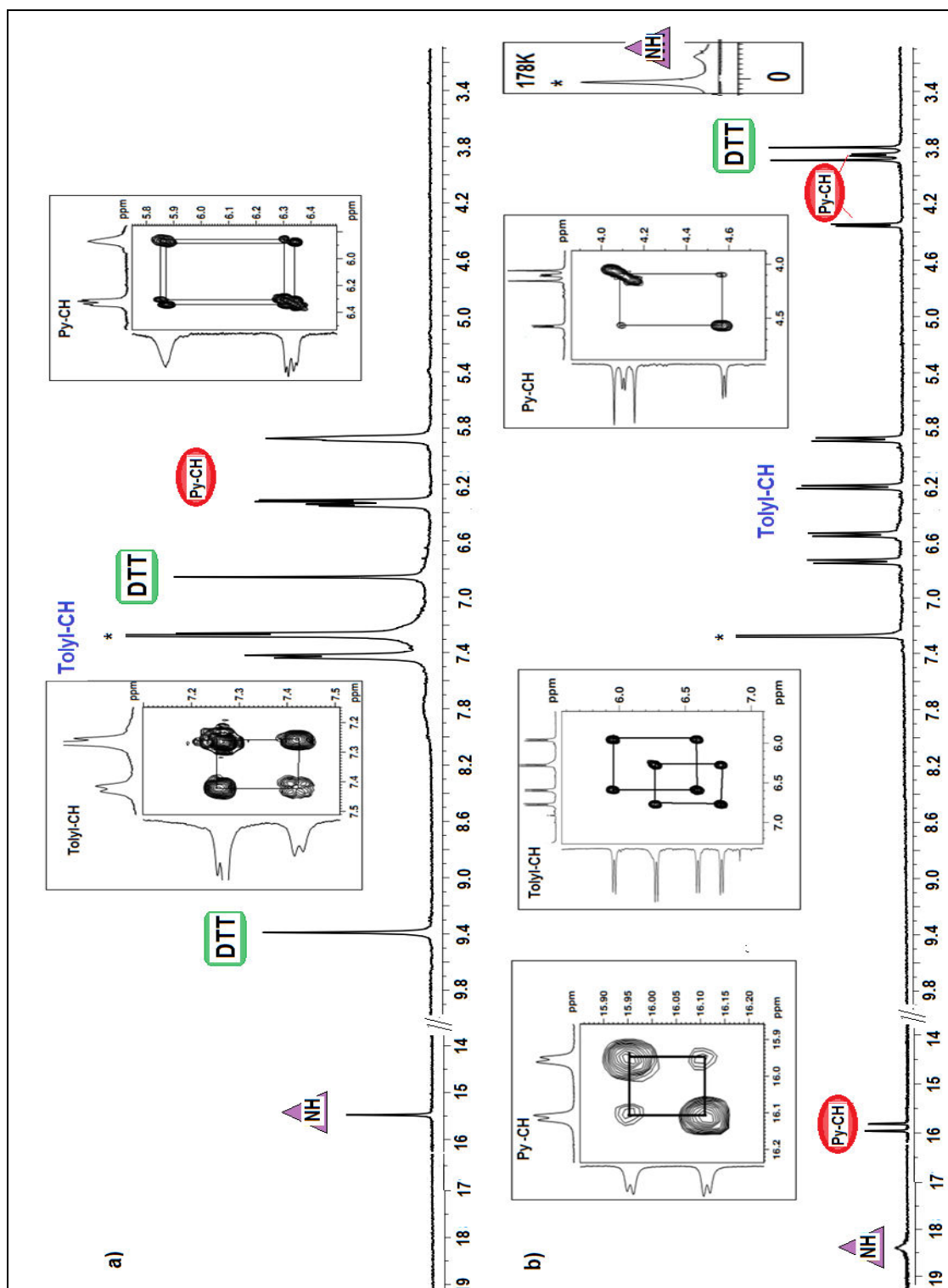
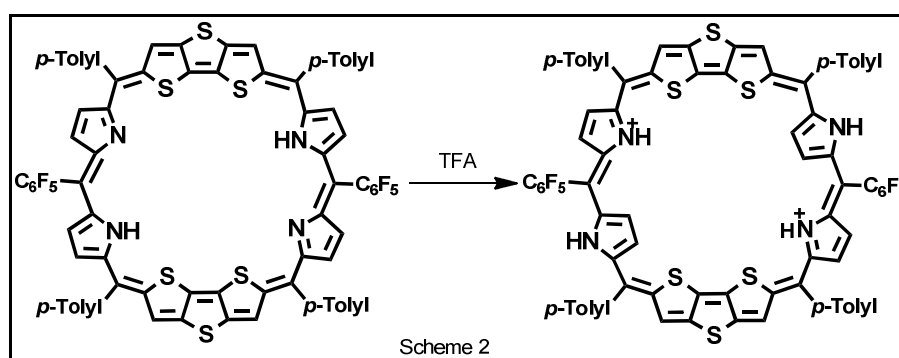


Figure 4.3: ^1H NMR spectra of **9** in CDCl_3 (1mM); a) before and b) after protonation by TFA. The inset shows ^1H - ^1H COSY correlations

Major changes were observed in ^1H NMR spectrum on protonation of **9** by TFA in CDCl_3 solution at 298 K. The changes are; a) two broad NH signals were observed at 18.7 ppm and -0.1 ppm (-0.1 ppm peak was observed only at 178 K), b) Two sets of pyrrole β -CH resonances; a doublet of doublet centered at 15.91 ppm ($^3J = 5.2$ Hz) and other at 4.36 ppm ($^3J = 5.2$ Hz) (assignment confirmed by ^1H - ^1H COSY spectrum, Inset in Figure 4.3), c) the tolyl-CH protons are shielded and appear as four doublets in the region 5.97-6.78 ppm and d) the DTT protons are shielded relative to freebase form and appear as two sharp singlets at 4.17 and 4.08 ppm. These results suggest a major structural change upon protonation.



Scheme 2: Ring inversion of pyrrole rings on protonation for **9**.

The appearance of two sets of pyrrolic β -CH protons in shielded and deshielded region is attributed to ring inversions where one pyrrole ring of each dipyrin subunits undergoes an 180° rotation (Scheme 2) which are common in core-modified expanded porphyrins.[6] This interpretation also accounts for observations of two separate NH signals in shielded and deshielded region. Pyrrole ring inversion upon protonation of **9** led us to have two possible ways of interpretation of the ring current effect (paratropic vs diatropic) in the macrocycle,

- a) If the protonated derivatives are aromatic ($[4n]\pi$ Möbius), one would expect a large diatropic ring current which is reflected in the chemical shifts of β -CH and -NH protons for *normal* and *inverted* pyrrole rings: In such a scenario, the following assignments

holds; *Normal* pyrrole ring: (β -CH: 15.91 ppm and NH: -0.1ppm), *Inverted* pyrrole ring: (β -CH: 4.36 ppm and -NH: 18.7 ppm). Hence, the corresponding $\Delta\delta$ values are 16.1 and 14.34 ppm for normal and inverted pyrrole rings respectively.

- b) If the protonated derivatives are antiaromatic ($[4n]\pi$ Hückel), one would expect a large paratropic ring current. In such a case, the following assignment holds; *Normal* pyrrole ring: (β -CH: 4.36 ppm and -NH: 18.7 ppm), *Inverted* pyrrole ring: (β -CH: 15.91 ppm and -NH: -0.1 ppm)

However, other spectroscopic data and theoretical calculations support the later assignment. Thus, **9** exhibit the antiaromatic character with extension of π -conjugation upon protonation. The observed up-field shift of DTT protons upon protonation also supports such a conclusion. Similar spectral trend was observed in **10** and shown in Figure 4.5.

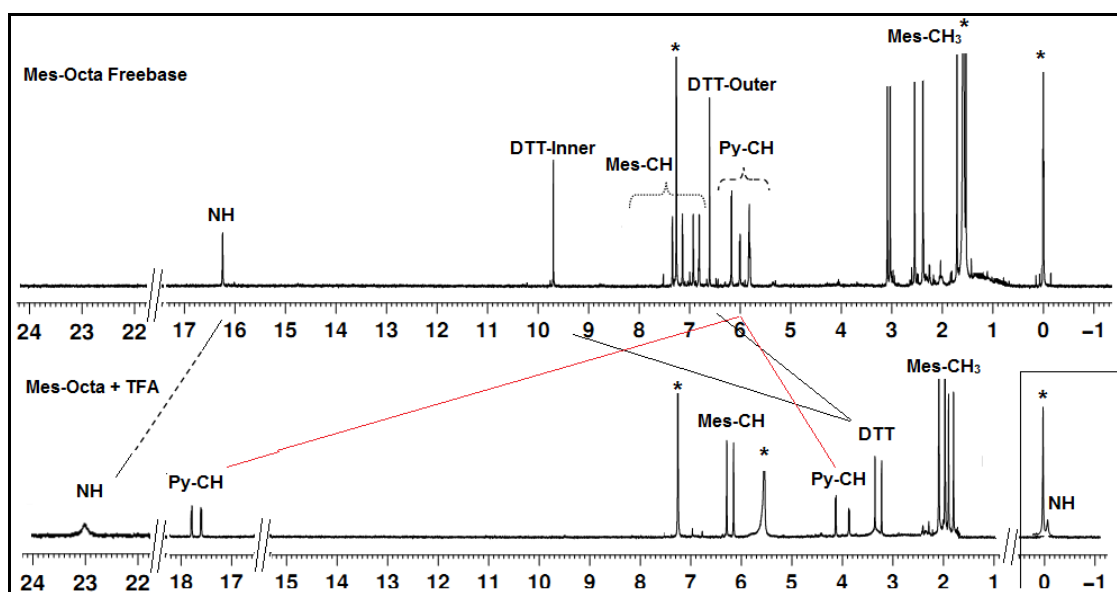


Figure 4.5: ¹H NMR spectra of **10** in CDCl₃; (Top) before (bottom) after protonation with TFA at 298 K

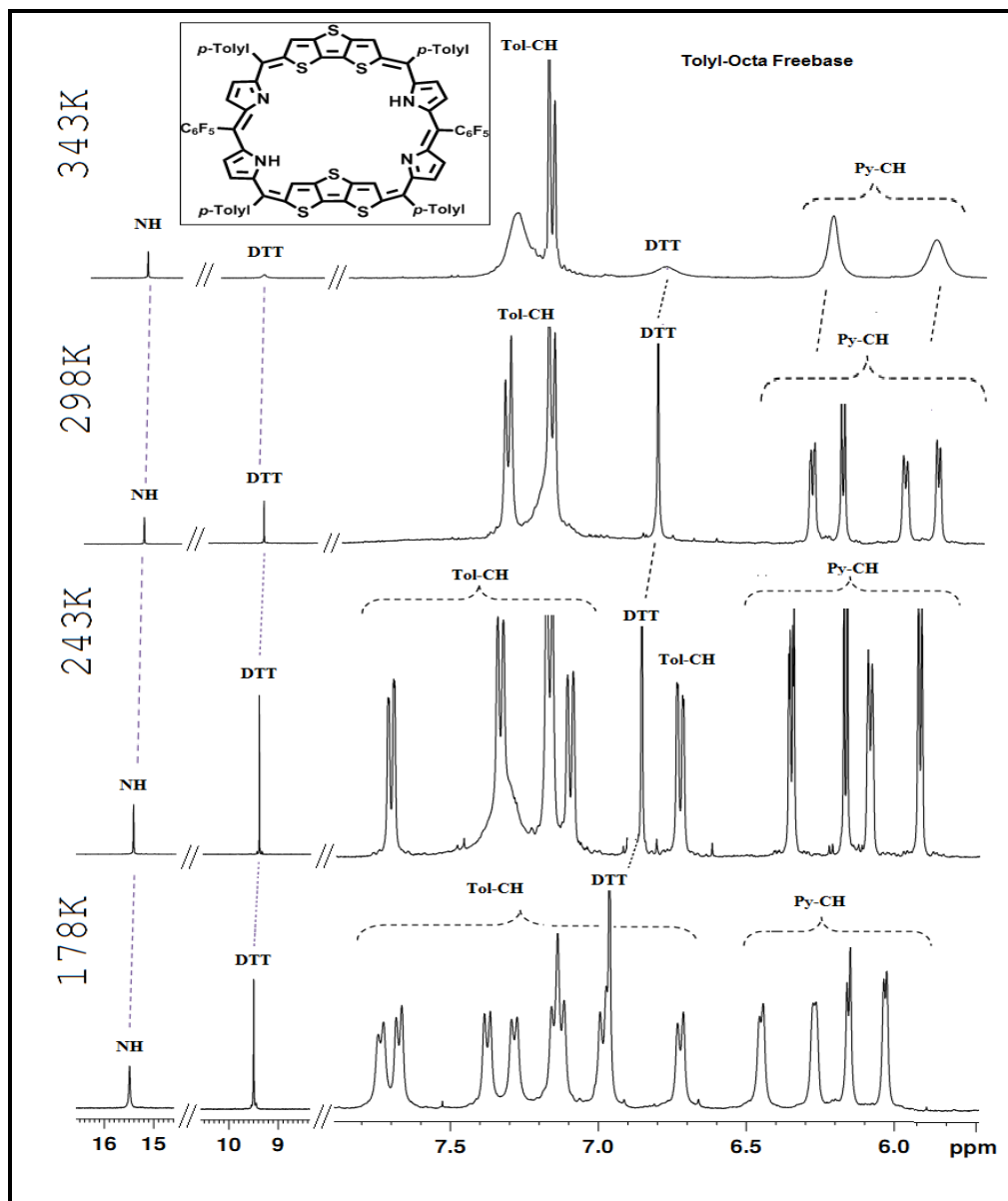


Figure 4.4: ^1H NMR spectrum of **9** in THF-D_8 at variable temperature

4.3.3 Single crystal X-ray analysis

The explicit structure of **10** was unambiguously confirmed by single crystal X-ray diffraction analysis where the macrocycle crystallizes in monoclinic system with $P2_1/n$ space group which is shown in Figure 4.6. As predicted from the NMR spectral analysis, the structure adopts figure-eight conformation in the solid state with 36π electron circuit. There are two dipyrin moieties and two DTT units which are connected through the six *meso*-

carbon bridges by mesityl and pentafluorophenyl units, where all the pyrrolic nitrogens point inwards. The amino (N2-H2A and N3-H3) and imino (N1 and N4) nitrogens which are in the dipyrin moieties are in strong intramolecular hydrogen bonding interactions (N2-H2A...N1 and N3-H3...N4) with distances of 2.13, 2.20 Å and angles of 124°, respectively. Both the DTT moieties are staggered and appended one over the other with the π cloud distance of 3.70 Å. This observation is consistent with the large chemical shift difference for DTT protons found in ^1H NMR of **10**. The macrocyclic conjugation is nicely preserved since the pyrrole rings and DTT rings are in the same plane as that of the six *meso* carbon atoms making dihedral angle almost zero in conformation with twisted double sided Hückel topology [107].

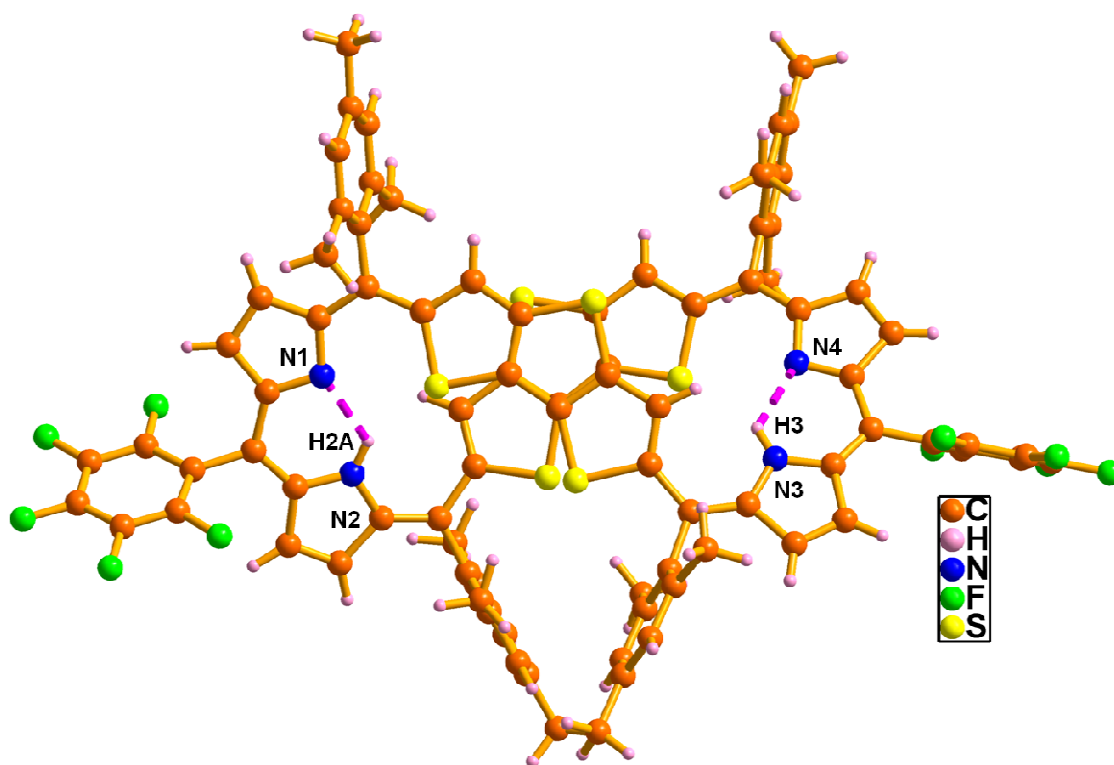


Figure 4.6: Single crystal X-ray structure of **10**

The octaphyrin **9.2H⁺** (with TFA anion) crystallizes in the triclinic system with P-1 space group and the structure is shown in Figure 4.7. The doubly twisted figure-eight conformation of freebase was dramatically changed to an open conformation upon

protonation. All the intramolecular hydrogen bonds observed in free-base are replaced by intermolecular hydrogen bonds with TFA counter anion. One pyrrole ring of each dipyrin unit is inverted as reflected in the ^1H NMR analysis upon protonation. The distances between the two heterocyclic rings S6 & N3 and S3 & N1 are 7.28 Å and 7.36 Å, respectively, which is sufficient enough to accommodate two pyrrole β -CH protons inside the macrocyclic ring.

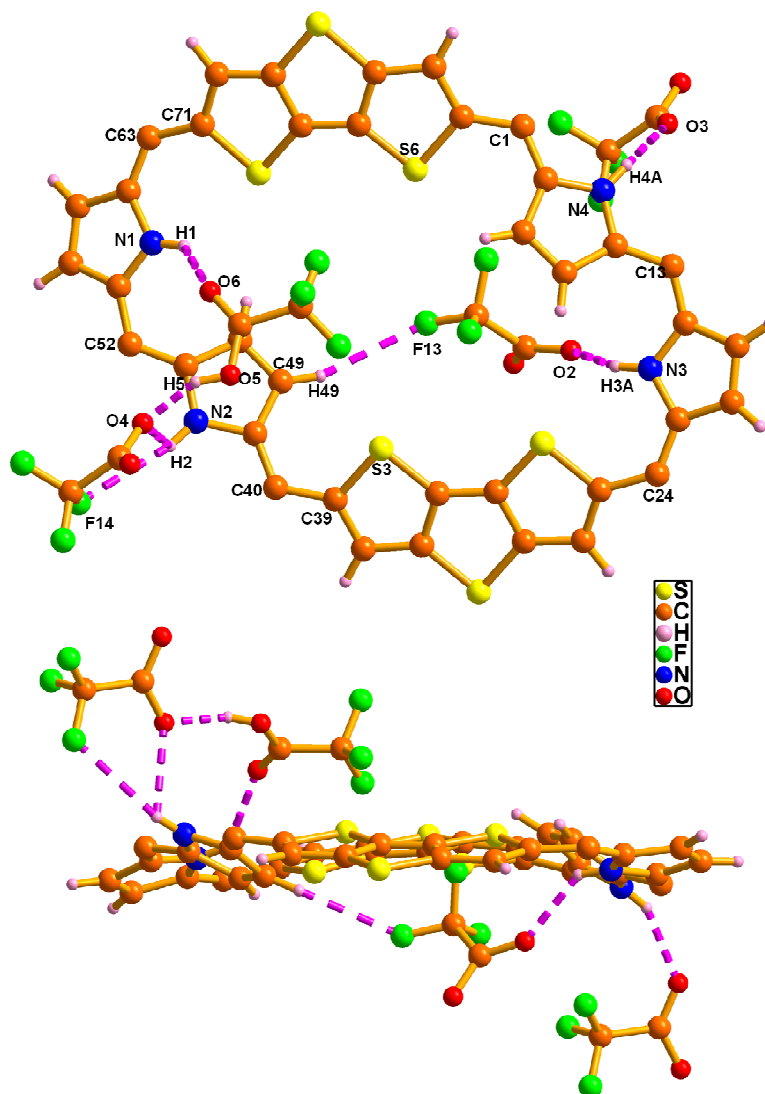


Figure 4.7: Single crystal X-ray structure of **9.2H⁺**. Top view (above) side view (below). *meso*-aryl groups are omitted in the top and side views for clarity

There are four TFA molecules (O6, O4, O2 and O3) which are directly bound with the four pyrrolic NHs (N1-H1, N2-H2, N3-H3A and N4-H4A) through intermolecular hydrogen bonding interactions (N1- H1...O6; N2-H2...O4; N3-H3A...O2 and N4-H4A...O3)

with the distance and angle of 2.33 Å, 2.51 Å, 2.21 Å, 2.10 Å and 135°, 106°, 140°, 152°, respectively.

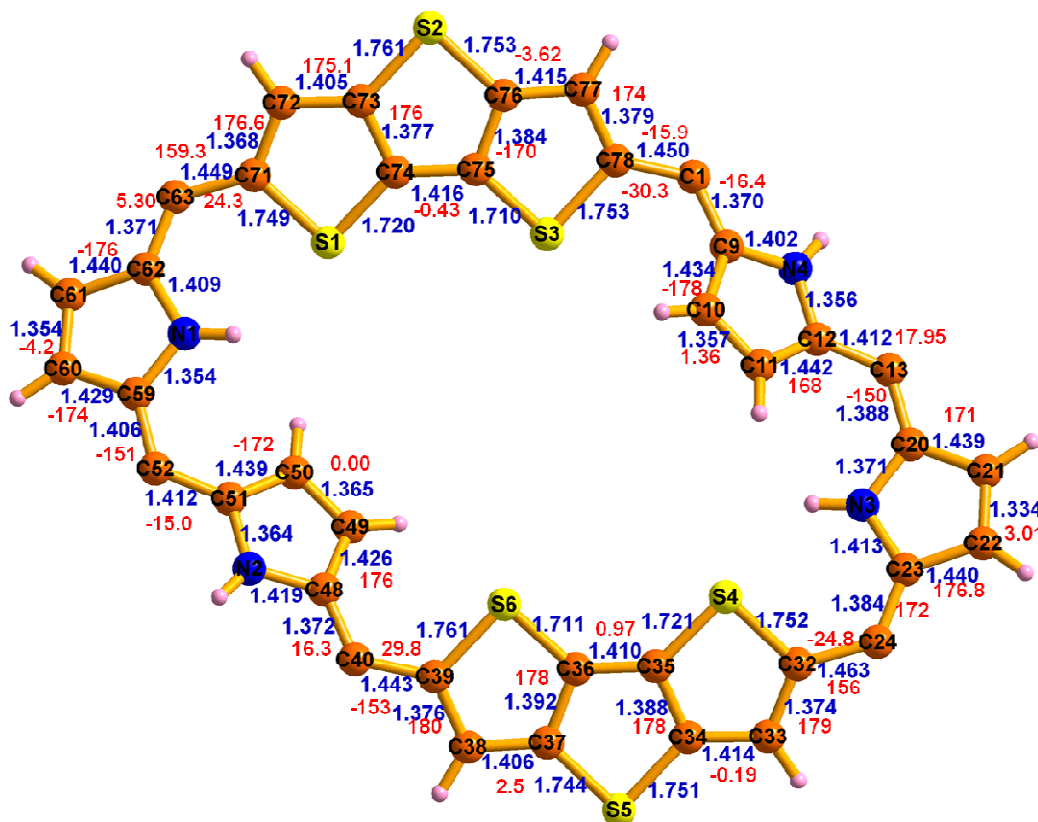


Figure 4.8: Single crystal X-ray structure of **9.2H⁺⁺** with bond length (Å, Blue) and torsion angles (°, Red). *Meso*-aryl groups and the TFA molecules are omitted for clarity

In addition, the N2 pyrrolic NH (N2-H2) and one of its β -CH protons (C49-H49) are in intermolecular interaction with TFA fluorine atoms (F14 and F13) with the distance and angles of N2-H2...F14 and C49-H49...F13 are 2.85 Å, 2.83 Å and 164°, 162°. Out of the four TFA molecules, two TFA units are above and two are below the mean macrocyclic plane defined by six *meso*-carbons (C1, C13, C24, C40, C52, C63) with the distances of 3.02, 2.21, 2.04, and 2.44 Å, respectively. On the other hand, the inverted pyrrolic units (N4, N2) are more deviated from the plane with respect to the normal (N3, N1) counterparts with the dihedral angles of 31.15°, 24.16° and 13.28°, 20.60°. However, the comparison of dihedral angles of *meso*-tolyl groups in free-base form (76° to 88°) and protonated derivative (50.34°

to 39.7°) indicates a decrease in the protonated derivative suggesting the extension of conjugation. The observed torsion angles of 29.8° (C39-C40) and 24.3°(C63-C71) are within 30° and this allows π electron conjugation in the extended structure of protonated derivative (Figure 4.8).[107,108]

4.3.4 Electronic absorption spectral studies:

The electronic absorption spectra of **9** (Figure 4.9) in CH₂Cl₂ are broad, ill-defined with three major bands at 368, 524 and 724 nm without any distinct Q-bands. This is in contrast with the absorption spectra of dithienothiophene modified doubly fused rubyrin **4** which exhibit intense split Soret band in the region of 500-550 nm and weak Q-bands in the region of 600-900 nm. Doubly fused rubyrins are known to be highly aromatic. [53] Furthermore, the absorption spectra of **9** remain unaltered upon changing the polarity of the solvent (Figure 4.10). These observations taken together suggest nonaromatic nature of **9** and the conformation of **9** remains intact upon changing the solvent polarity.

The absorption spectra of **9** upon stepwise protonation using a dilute solution of TFA reveal definite spectral changes (Figure 4.9). Interestingly, broad absorption bands change to intense sharp ones with an increase in molar absorption coefficient accompanied by significant red shifts. Specifically, monoprotonated **9** shows Soret like band appearing at 568 and 696 nm with additional bands at 816 and 1136 nm. Further protonation leads to diprotonation resulting in further shift of bands to 416, 632, 701 and 992 nm. These observations reveal that a major structural change has taken place upon protonation. Similar spectral changes were observed in **10** and shown in Figure 4.11.

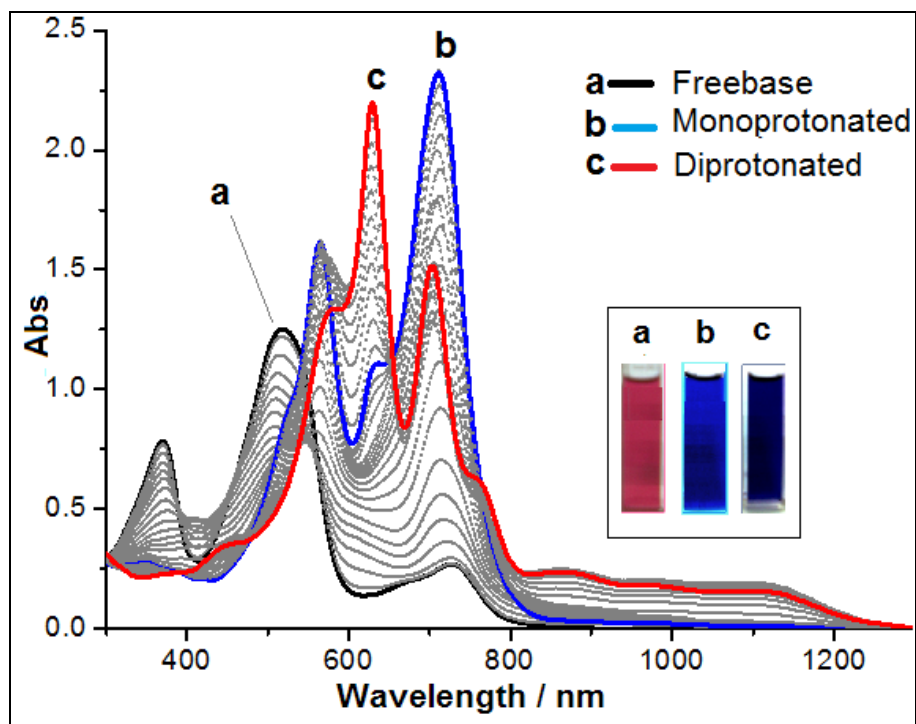


Figure 4.9: Titration of dilute solution of TFA (0.1mM – 100mM) with **9** (0.01m M) in CH_2Cl_2

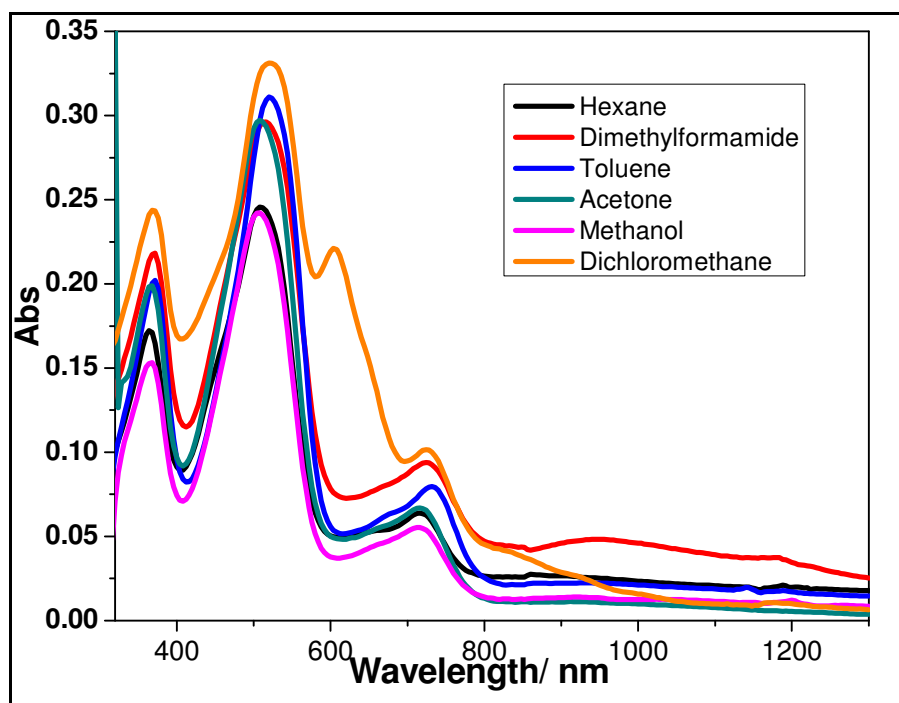


Figure 4.10: Electronic absorption spectra of **9** in different solvents

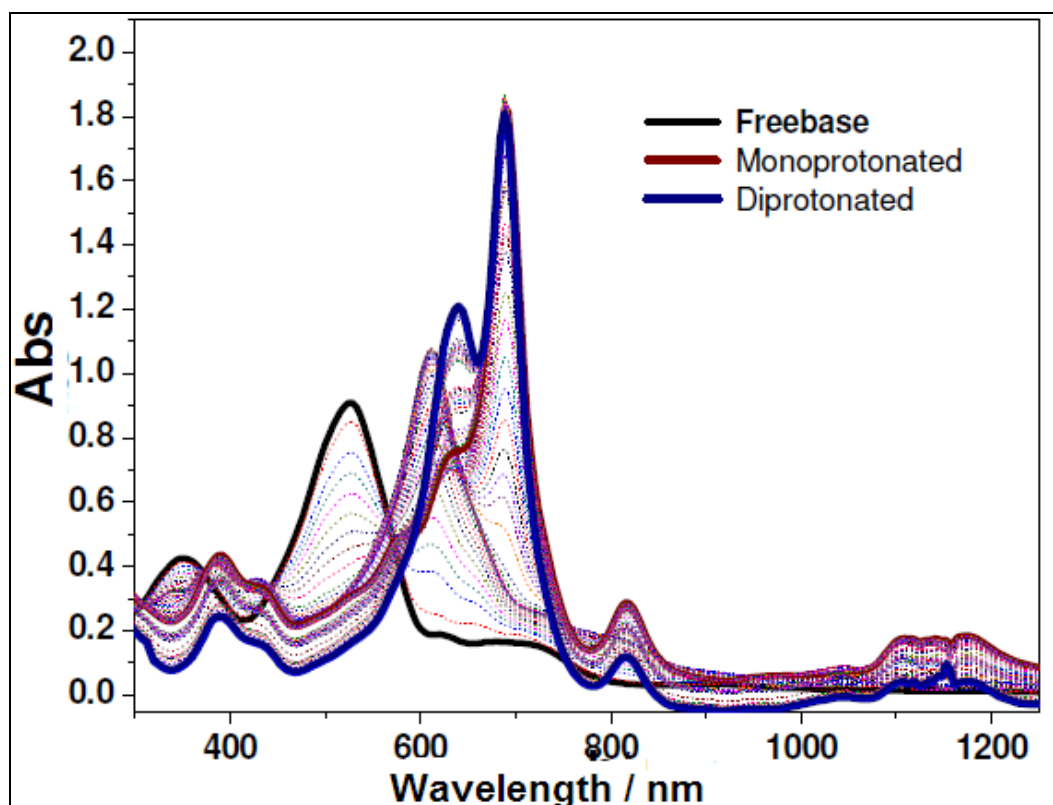


Figure 4.11: Titration of dilute solution of TFA (0.1mM – 100mM) with **10** (0.01m M) in CH_2Cl_2

4.4 MO calculation

The first look at changes in the absorption characteristics probably suggests that **9** and **10** might be aromatic in nature upon protonation. [107,109] However, theoretical calculations and the MO diagram does not support the presence of aromaticity in the diprotonated form (*vide infra*). We have performed TD-DFT calculations on the doubly fused rubyrin **4** which is known to be aromatic. Keeping this as the reference, calculations were done on both freebase and diprotonated forms of **9** and **10**. For **4**, from MO diagram we confirmed the aromatic porphyrins like features following typical Gouterman's four orbital model [110]. These calculations revealed nearly degenerate HOMO/HOMO-1 and LUMO/LUMO-1 for **4** which are characteristic of aromatic expanded porphyrins. A calculation of oscillator strength for the major transition of **4** reveals 96.58% for transition from HOMO-1 to LUMO. On the other

hand, the MO energy level diagram of **9** shows a broken degeneracy for HOMO/HOMO-1, LUMO/LUMO+1 orbital (Figure 4.12). The oscillator strength for the major transition is only 14% from HOMO-1 to LUMO+1 confirming the nonaromatic nature of the doubly fused octaphyrins in freebase form.

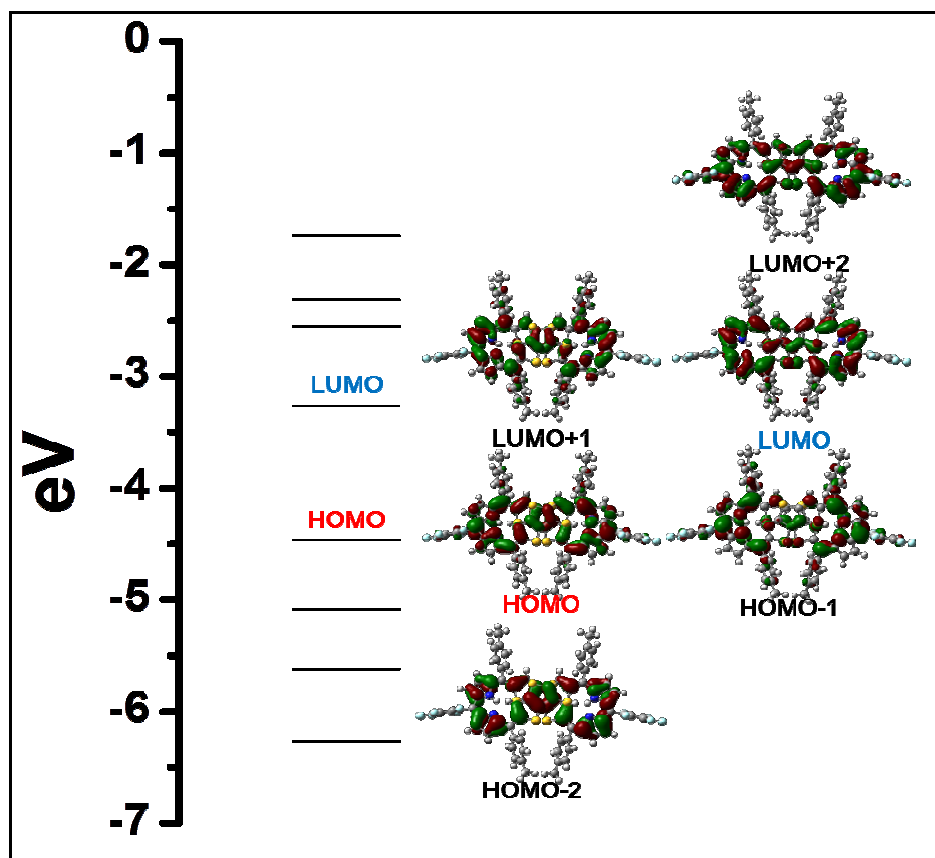


Figure 4.12: Molecular orbital diagram of **9**

The MO diagram calculated for the diprotonated derivative **9.2H⁺** reveals; (a) the perturbed degeneracy of HOMO/HOMO-1 and LUMO/LUMO+1; (b) relatively small HOMO-LUMO gap and (c) same number of nodes for the frontier orbitals. These observations clearly suggest the antiaromatic nature of macrocycle in the diprotonated state (Figure 4.13).

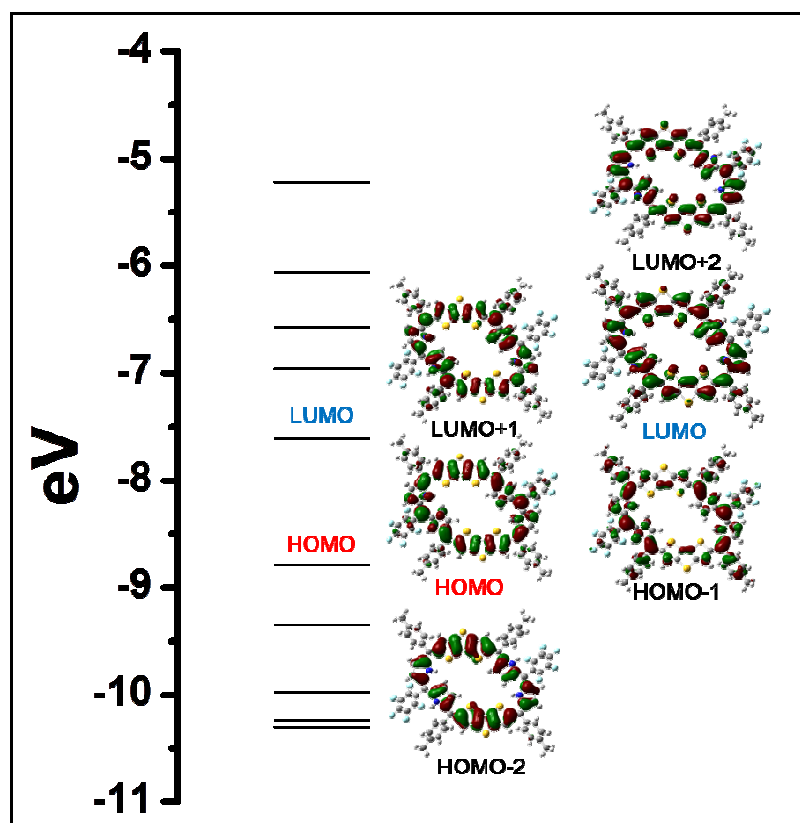


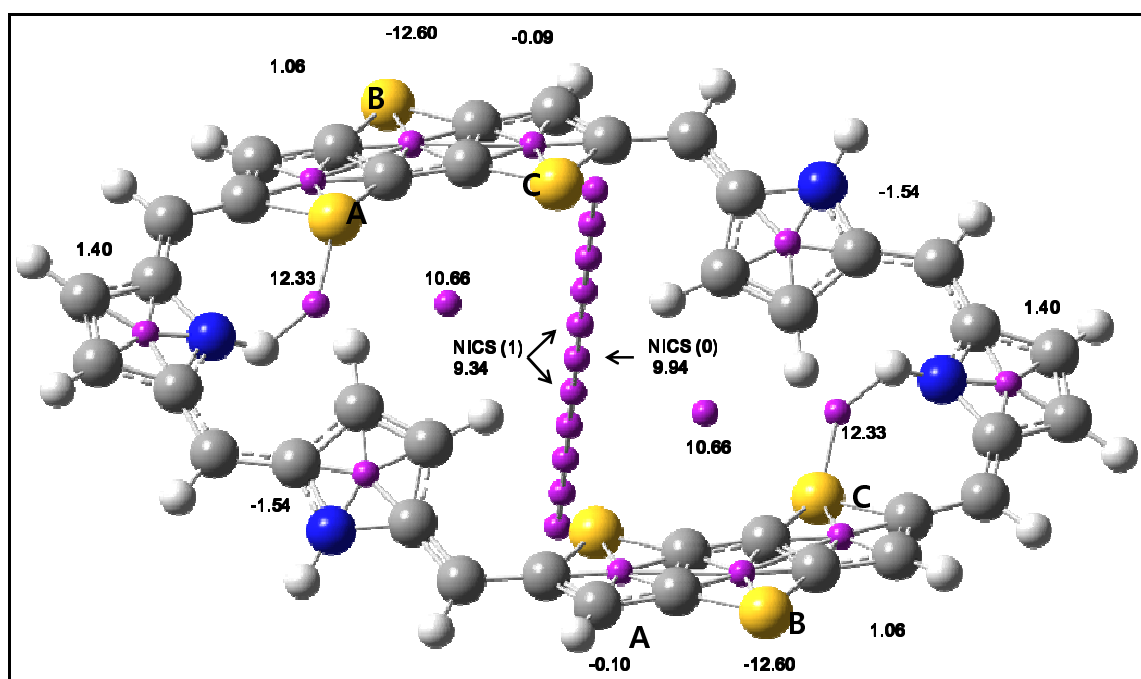
Figure 4.13: Calculated MO energy diagram of $9.2H^+$

4.5 Theoretical Calculations

We have calculated the optimized structures (B3LYP/6-311G(d,p)) [79,80] for neutral and diprotonated octaphyrins using the coordinates obtained by crystal structures of **10** and $9.2H^+$. Compared to the highly distorted conformation of neutral form, diprotonated octaphyrin reveals quite planar structures with distortions of pyrrole rings. Based on both X-ray crystal and optimized structures, we have estimated HOMA (Harmonic Oscillator Model of Aromaticity) and BLA (Bond Length Alternation) values (Table 4.1). While the HOMA value increases, the BLA value decreases upon protonation. These features indicate that not only conformational changes but also an extension of π -conjugation is achieved upon protonation [107,108].

Table 4.1: HOMA and BLA values

Structure		HOMA	BLA
Neutral	X-ray	0.454	0.150
Neutral	Optimized	0.570	0.068
Protonated	X-ray	0.557	0.133
Protonated	Optimized	0.587	0.058

Figure 4.14: Calculated NICS values for the various positions on $9.2H^+$

To verify aromatic/antiaromatic characteristics in the extended protonated octaphyrins, we have adopted the nucleus independent chemical shift (NICS) and anisotropy induced current density (AICD) methods which are known to be a good index for the aromaticity [97,111]. Large positive NICS values were calculated at various geometrical positions (Figure 4.14) of diprotonated form (e.g. NICS(0) = 9.94 and NICS(1) = 9.34). And the NICS values at the central positions of pyrrole (-1.54 ~ +1.40 ppm) and thiophene rings

of DTT (-12.60 ppm) indicate its main conjugation pathway of 36π electronic system. In addition, we have also attempted the direct visualization of the induced ring current by using AICD method which describes the 3D image of delocalized electron densities with a scalar field. Since the AICD method illustrates the paramagnetic term of the induced current density, the aromatic molecules show clockwise current density and the antiaromatic species show counter-clockwise current density (Figure 4.15).

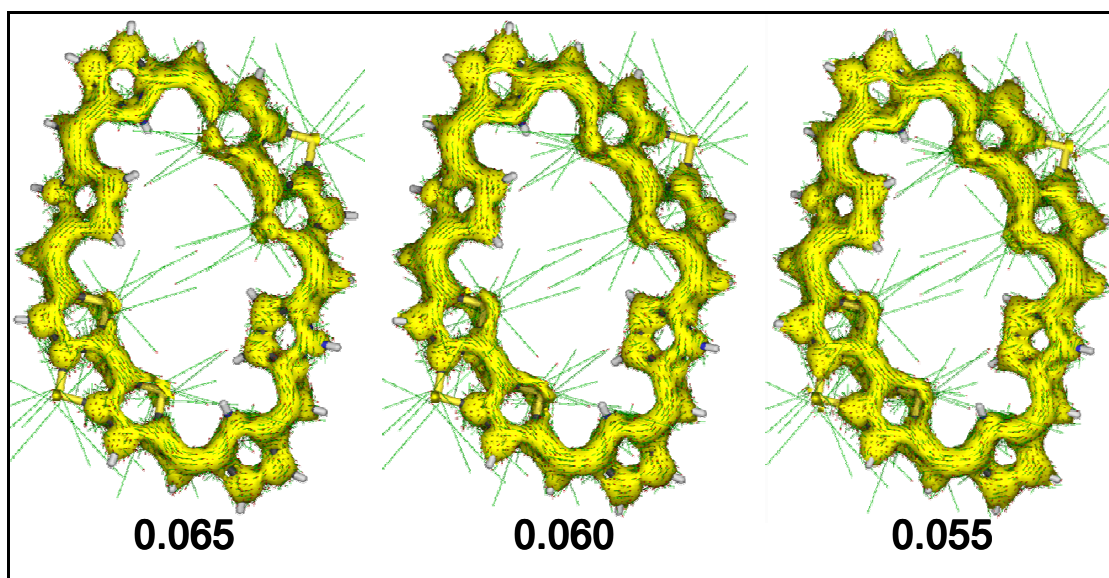


Figure 4.15: AICD plots of 9.2H^+ at isosurface values 0.055, 0.060 and 0.065, respectively. The current density vectors plotted onto the isosurfaces and the direction of the external magnetic field is out of plane. The counter clockwise current density vectors indicate an antiaromatic character.

The AICD plot of diprotonated octaphyrin reveals clear counter-clockwise current-density vectors, thus indicating a paramagnetic ring current. These results demonstrate that protonated octaphyrin has a Hückel antiaromatic character with continuous and paramagnetic current density in its extended conformation.

4.6 Excited state dynamics and optical nonlinear properties:

We have investigated excited state dynamics of neutral and protonated forms of octaphyrins by utilizing femtosecond transient absorption measurements (Figure 4.16).

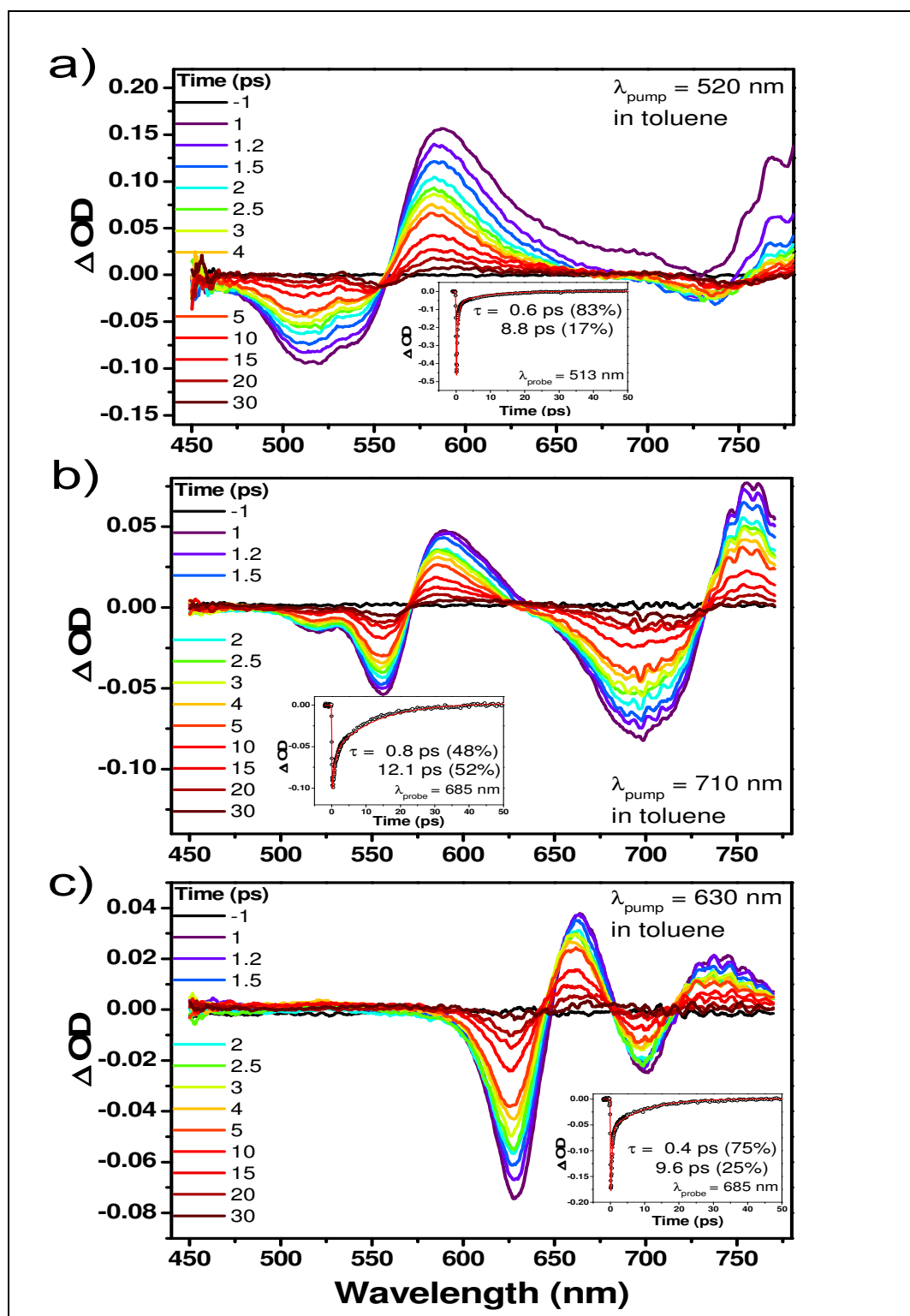


Figure 4.16: Femtosecond transient absorption spectra and representative decay profiles of a) **9**, b) **9.H⁺** and, c) **9.2H⁺** in toluene

The transient species of neutral and protonated octaphyrins exhibit prominent excited state absorption (ESA) and ground state bleaching (GSB) signals corresponding to their steady-state absorption features [98].

The highly distorted neutral octaphyrin shows broad GSB and ESA signals in the entire spectral region. And the excited-state lifetime is estimated to be 0.6 (83%) and 8.8 ps (17%). We can assign the decay time component of shorter than 1 ps as an energy relaxation processes from higher to lowest excited state such as a relaxation process from S_2 to S_1 state [98]. However, despite of spectral changes upon protonation, the transient species of protonated octaphyrins exhibit reasonably fast excited-state lifetime. Also the small increase in lifetime observed for protonated derivatives reveals the rigidity of the macrocycle arising from the intermolecular hydrogen bonding interactions. [106, 107]

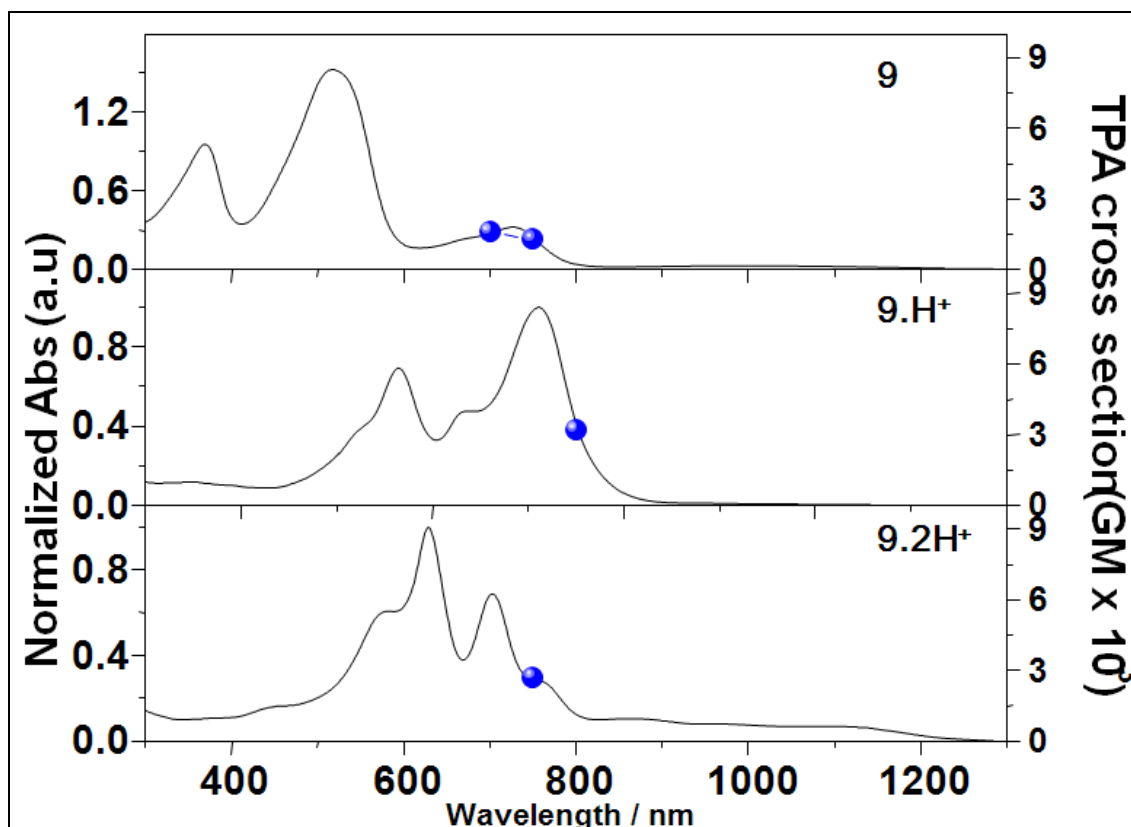


Figure 4.17: Steady-state absorption spectra (black line) and TPA cross-sections (blue dot) of **9**(Top), **9.H⁺** (middle) and **9.2H⁺** (Bottom)

We have also measured the TPA cross section (σ^2) values for **9** and its protonated derivative by using femtosecond Z-scan technique (Figure 4.17). Normal figure-eight octaphyrins without any fused ring show a TPA value of 870 GM.[112] Compared to this, **9** reveals increased TPA cross-section value of 1600 GM upon excitation at 1400 nm exhibiting the rigid fused moieties. And, upon protonation, TPA cross-section values increased to 3200 and 2700 GM for mono and diprotonated forms. TPA value in expanded porphyrin systems are known to depend on planarity, aromaticity and the number of π -electrons in conjugation. Our group and others have recently shown that an increase in aromaticity of the macrocycle results in a significant increase in the TPA values [18,45]. TPA values are also known to increase upon changing the topology from Hückel antiaromatic to Möbius aromatic one [107,113]. The moderate increase in TPA values upon protonation in doubly fused octaphyrin is attributed to the structural change from figure-eight to an open extended conjugated structure. The planarity of the DTT rings in the extended structure allows extension of π -conjugation [114]. Changes in the polarization of π -electrons upon interaction with intense laser light are effective in extended structure relative to the twisted figure-eight conformation leading to a moderate increase in the TPA values. [115]

4.7 Electrochemistry of Fused Octaphyrins:

In order to probe the redox properties of octaphyrins, cyclic voltammetry analysis has been done. Electrochemical analysis was carried out in three electrode cell system; Glassy carbon working electrode, platinum wire counter electrode and Ag/Ag⁺ reference electrode containing 0.1M Tetrabutylammonium perchlorate as supporting electrolyte (Figure 4.18 and 4.19).

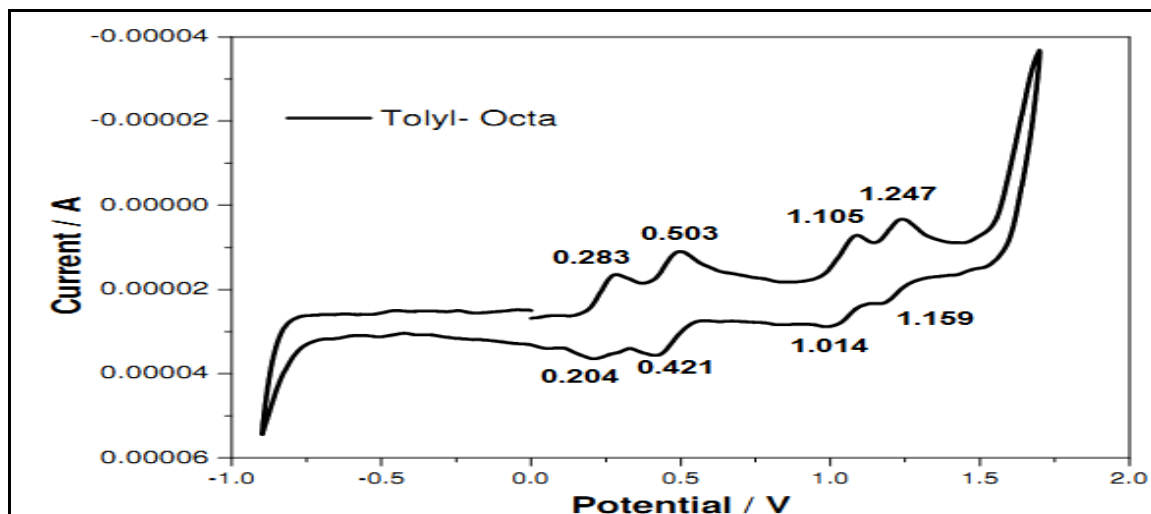


Figure 4.18: Cyclic voltammetry of **9** in CH_2Cl_2 (Scan rate: 50mV/s)

In cyclic voltammetry, **9** and **10** shows two quasi-reversible oxidation (+1.11 V, +1.25 V) and two quasi-reversible reduction (+0.421 V, +0.204 V) peaks against Ag/AgNO₃ reference electrode in dry CH_2Cl_2 . This voltammetric behavior encouraged us to try chemical oxidation and reduction of **9**. Oxidation with MnO₂ in dichloromethane resulted in the ring opening of macrocycle giving two products with m/z 741.2 and m/z 1049.8 (Scheme 3). Chemical reduction with NaBH₄ results in decomposition of the macrocycle.

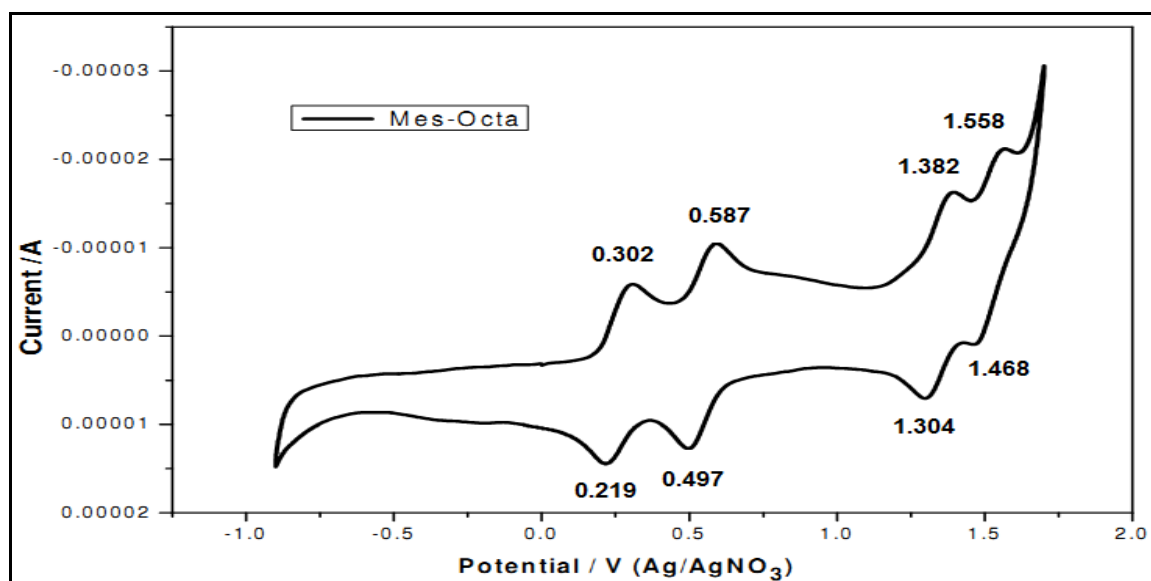
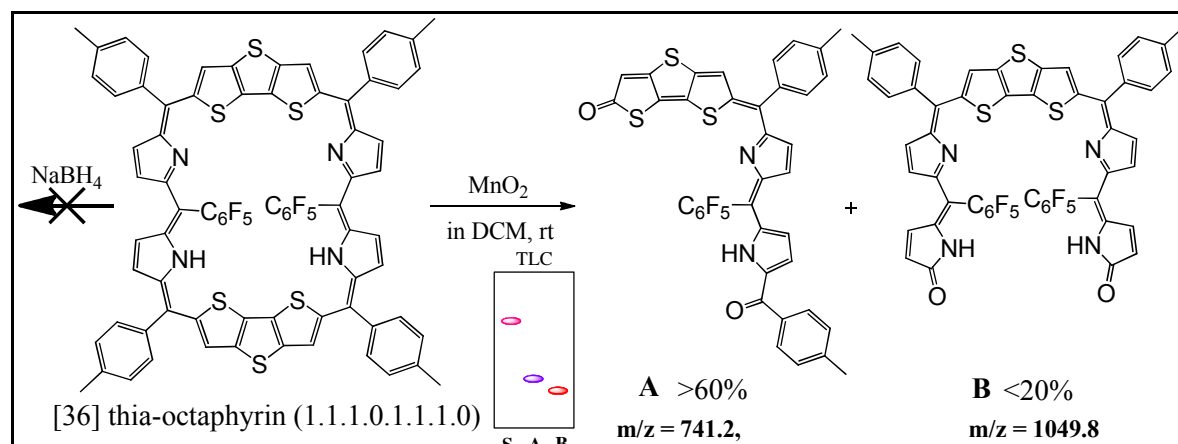
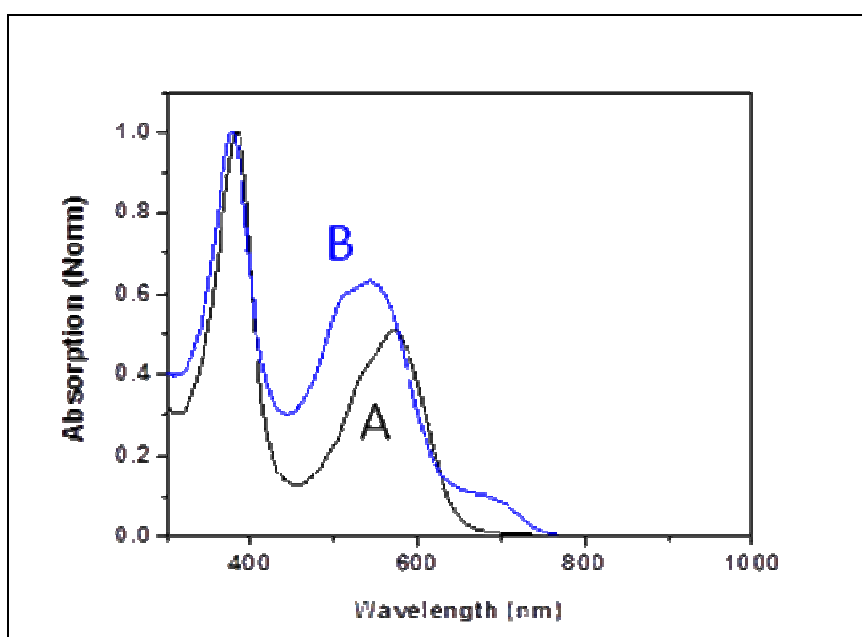


Figure 4.19: Cyclic voltammetry of **10** in CH_2Cl_2 (Scan rate: 50mV/s)

Scheme 3: Chemical reduction of **9**Figure 4.20: Electronic absorption spectrum of oxidized products (**A** and **B**) of **9**

4.8 Fused Sapphyrin and Heptaphyrin

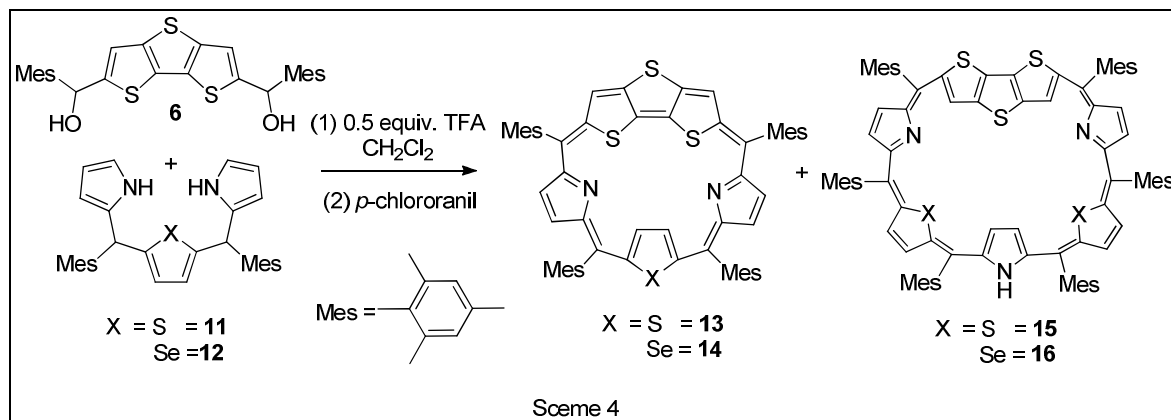
So far we have successfully demonstrated the synthesis, spectral, structural and photophysical properties of doubly fused octaphyrins. Herein, we explore the synthesis, spectral characterization of mono fused sapphyrin. The fused core-modified sapphyrin was

reported by C. H. Lee and co-workers and dioxobenzosapphyrin by Sessler and co-workers. In this section, we mainly focus on the synthesis of DTT fused core-modified sapphyrins with sulfur and selenium as core atom. Surprisingly, we have also isolated the core-modified fused heptaphyrin in the reaction along with sapphyrin.

4.8.1 Synthesis of Sapphyrin and Heptaphyrin

To synthesize the mono-fused sapphyrins, we have adopted [2+3] acid-catalyzed condensation reaction. In a typical synthetic procedure, equal molar amounts of DTT-diol **6** and thiatripyrrane **11** in CH₂Cl₂ were stirred for 1h by using 0.5 equiv of TFA as an acid-catalyst (Scheme 4). After oxidation with 2,3,5,6-tetrachloro-*p*-benzoquinone (*p*-chloranil), repeated column chromatographic purification over basic alumina followed by neutral alumina, a greenish brown color fraction was eluted with CH₂Cl₂ and hexane (10:90) which was identified as sapphyrin **13** in 10% yield. The second blue color fraction was eluted with CH₂Cl₂ and hexane (15:85) and identified as heptaphyrin **15** in 6% yield. By using similar synthetic methodology, fused sapphyrin **14** and fused heptaphyrin **16** were prepared in 8% and trace amount (Only identified by mass spectral analysis), respectively.

Formation of heptaphyrin in [3+2] condensation reaction can be explained by the well-known pyrrole acidolysis mechanism. For instance, tripyrrane undergoes an acid catalyzed pyrrole acidolysis which lead to the formation of heptaphyrin by [2+2+3] condensation. Increasing the acid concentration led to more acidolysis product and reduced the yields of sapphyrin and heptaphyrin, while decreasing the acid concentration led to more sapphyrin product. By changing the acid catalyst to *p*-toluenesulphonic acid (*p*-TSA), no drastic change in the yield distribution was observed [116].

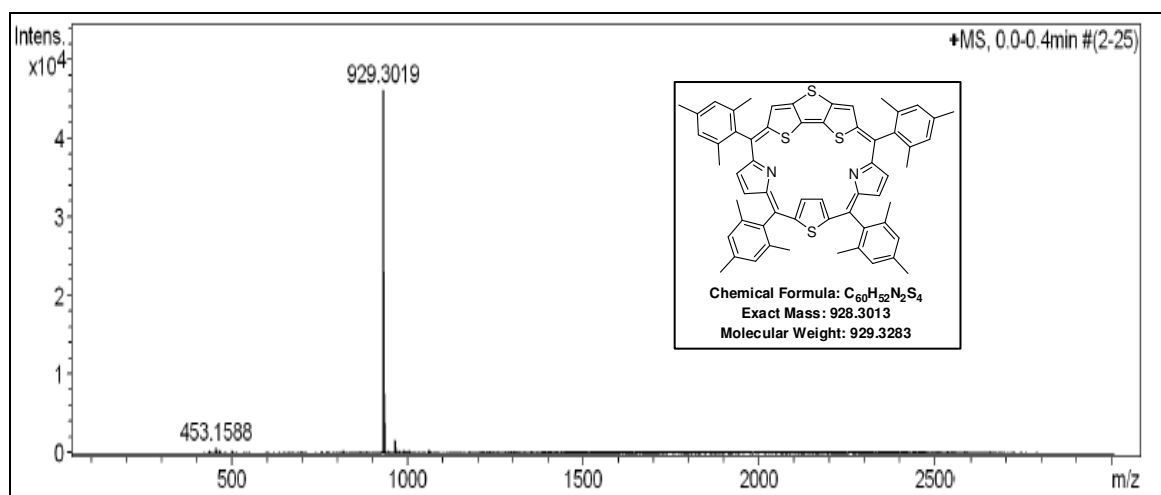


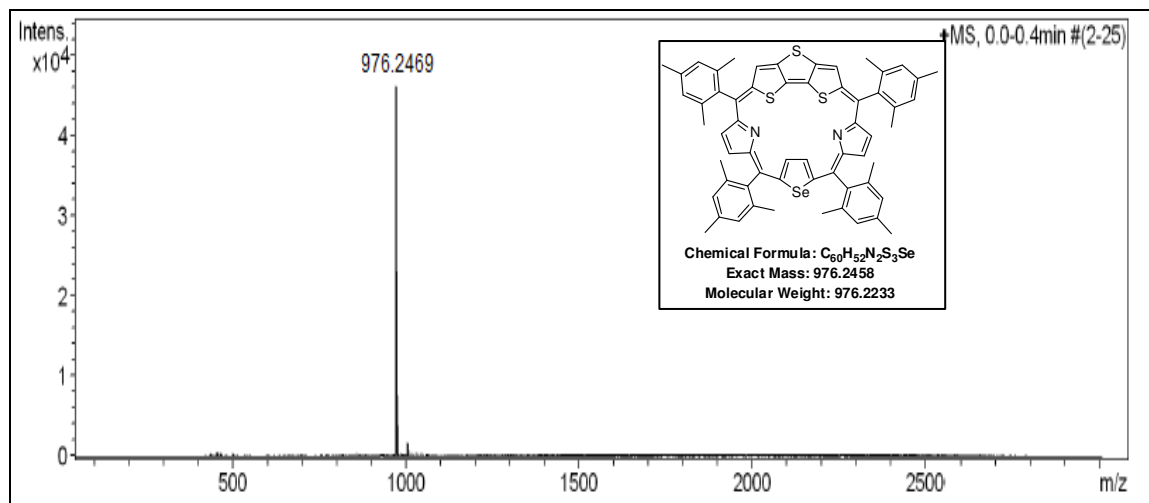
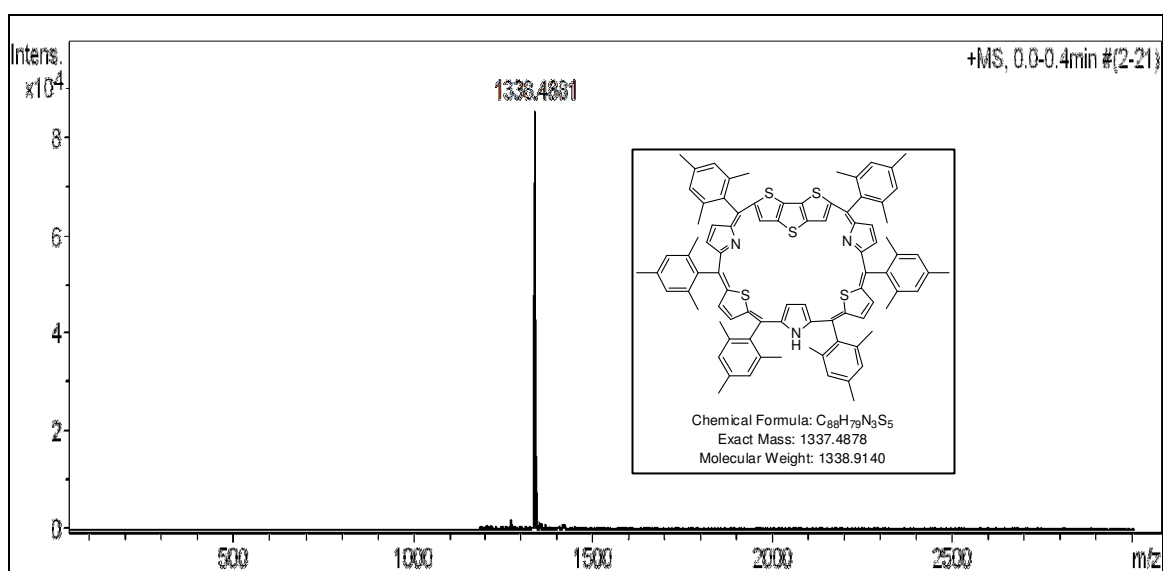
Scheme 4: Synthesis of fused sapphyrins and heptaphyrins

4.9 Result and discussion:

4.9.1 Mass spectral analysis

The spectral analyses of 13-16 are shown in Figure 4.21-4.24. The molecular ion peak for fused sapphyrin **13** and **14** are 929.3019 and 976.2810, while the respective peaks for fused heptaphyrins are at 1338.4887 and 1435.3769, respectively. The molecular ion signals confirm the exact composition of the macrocycle.

Figure 4.21: ESI-mass spectrum of **13**

Figure 4.22: ESI-mass spectrum of **14**Figure 4.23: ESI-mass spectrum of **15**

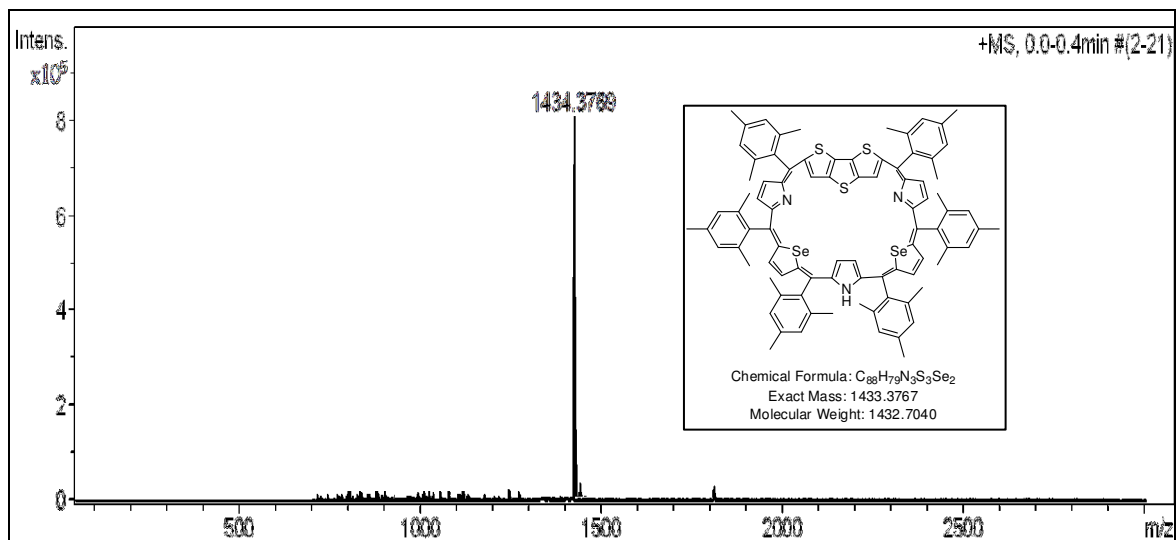


Figure 4.24: ESI-mass spectrum of **16**

4.9.2 Electronic absorption spectral analysis:

The electronic absorption spectral analysis of fused saphyrin **13** and **14** in CH_2Cl_2 are shown in Figure 4.25 and 4.26. Both show sharp Soret like band and weak Q-like bands. The higher energy band in **13** and **14** are observed at 495 nm and 501 nm and the weak energy bands are between 600 to 800 nm. Upon protonation by dilute TFA solution in CH_2Cl_2 , the band observed at 495 nm in **13** is 25 nm red-shifted and showed a new Soret band at 520 nm, which indicate the extension in π -electron conjugation in the macrocycle. Similar spectral features were observed in the case of **14** upon protonation. The molar extinction coefficients of $13.2H^+$ or $14.2H^+$ are two times higher as compared to respective freebase.

On the other hand, the electronic absorption spectrum of **15** in CH_2Cl_2 has broad and ill-defined bands from 500 to 600 nm. This is in contrast with fused saphyrin **13** which is aromatic. The observation of absorption spectral characteristic of **15** clearly reflects the antiaromatic nature. [117]

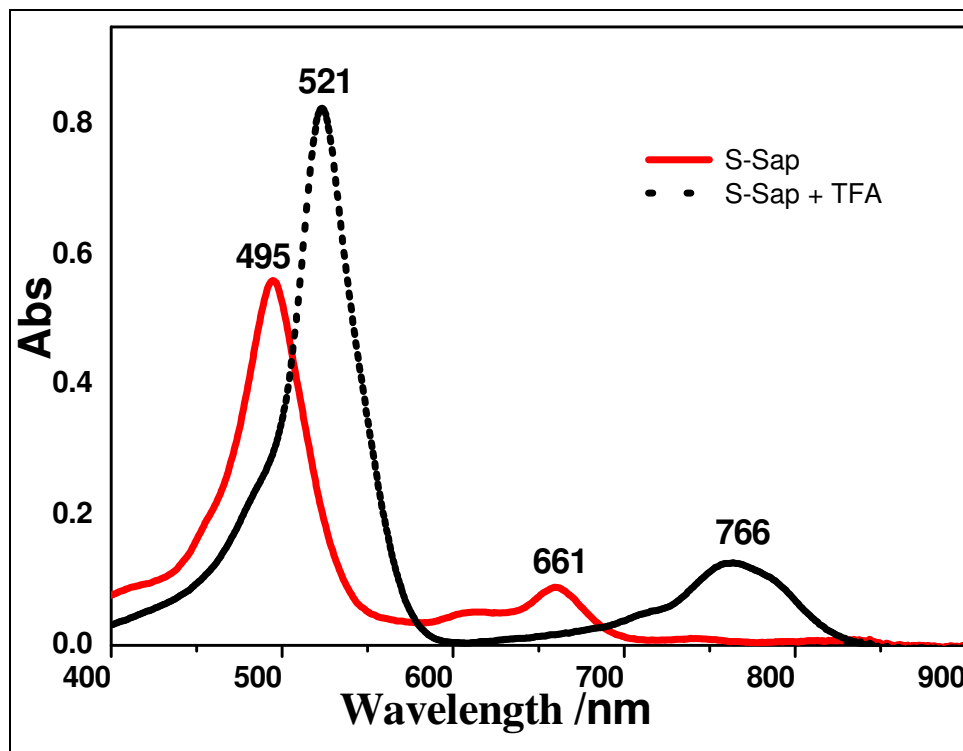


Figure 4.25: Electronic absorption spectra of **13** in CH_2Cl_2 and **13.2H⁺** in $\text{CH}_2\text{Cl}_2/\text{TFA}$

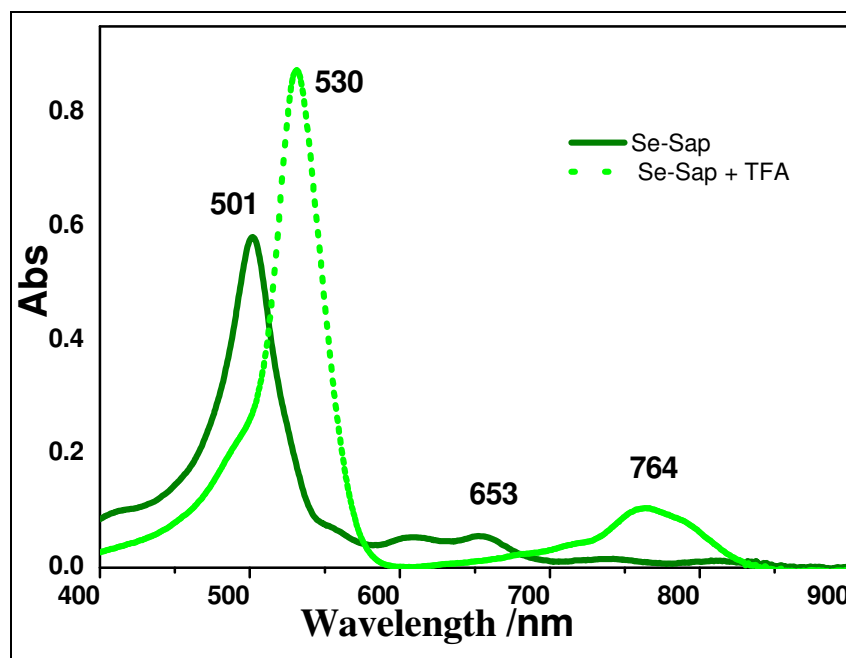


Figure 4.26: Electronic absorption spectra of **14** in CH_2Cl_2 and **14.2H⁺** in $\text{CH}_2\text{Cl}_2/\text{TFA}$

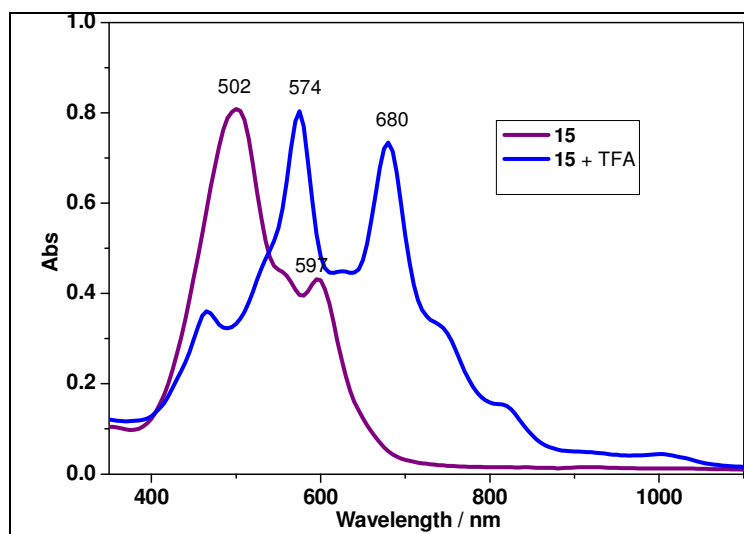
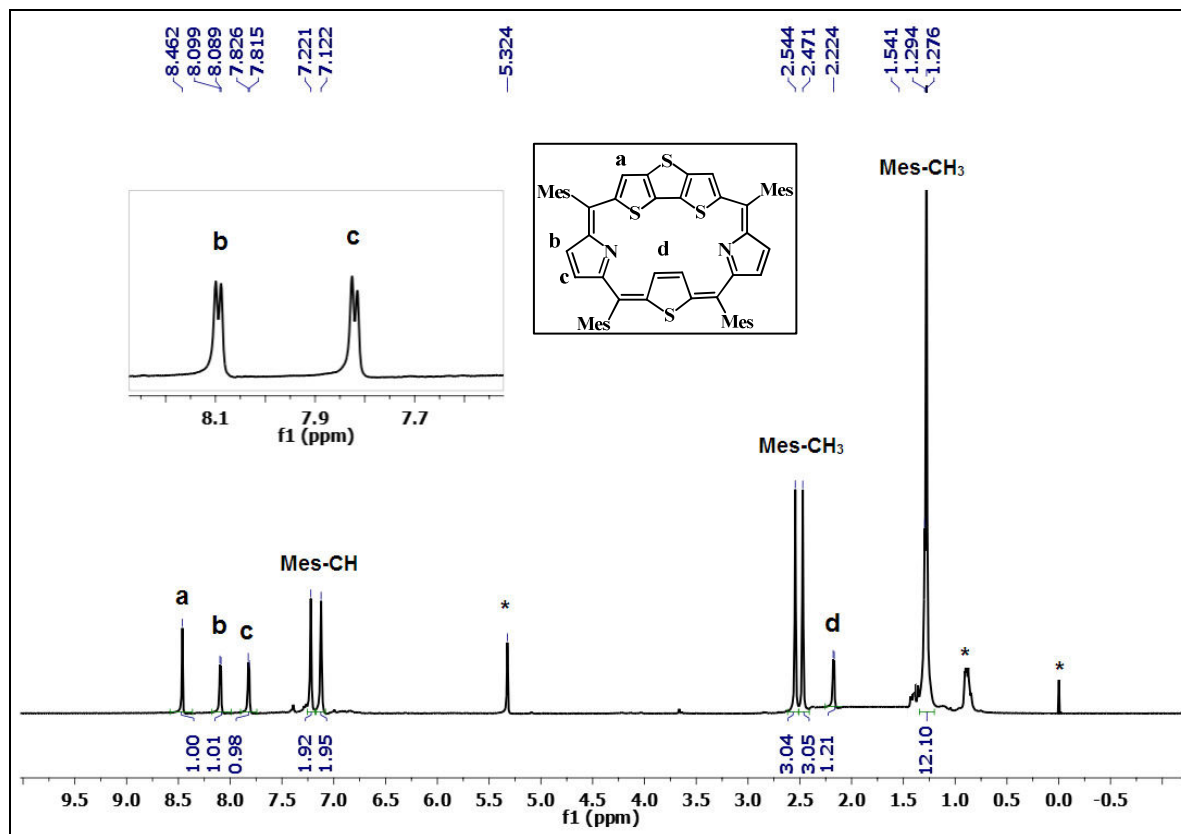
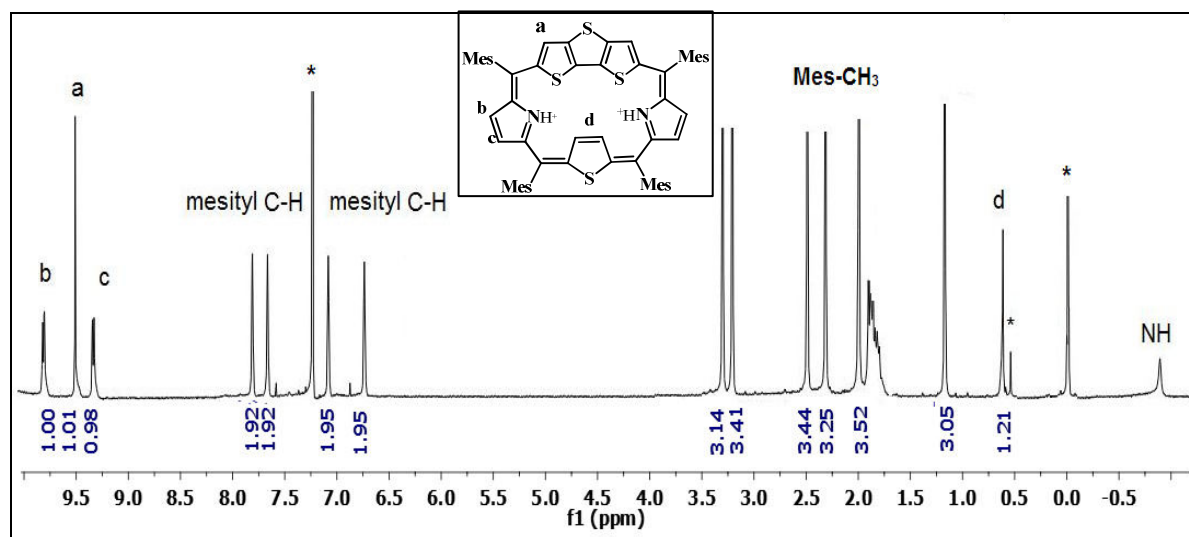


Figure 4.27: Electronic absorption spectra of **15** in CH_2Cl_2 and **15.2H⁺** in $\text{CH}_2\text{Cl}_2/\text{TFA}$.

4.9.3 NMR spectral analysis

The ^1H NMR spectrum of **13** in CD_2Cl_2 is shown in Figure 4.28, where the peaks at 8.4 ppm corresponds to two DTT-CH protons. The pyrrolic β -CH protons are resonated as doublet of doublet centered at 8.08 and 7.81 pm, which is further confirmed by ^1H - ^1H COSY spectral analysis. Two sets of mesityl-CH protons are observed as singlets at 7.22 and 7.12 ppm. The mesityl- CH_3 protons are in the aliphatic region. There is a peak at 2.15 ppm reflected the thiophene β -CH protons, which is inverted and respective protons are experiencing the aromatic ring current effect.

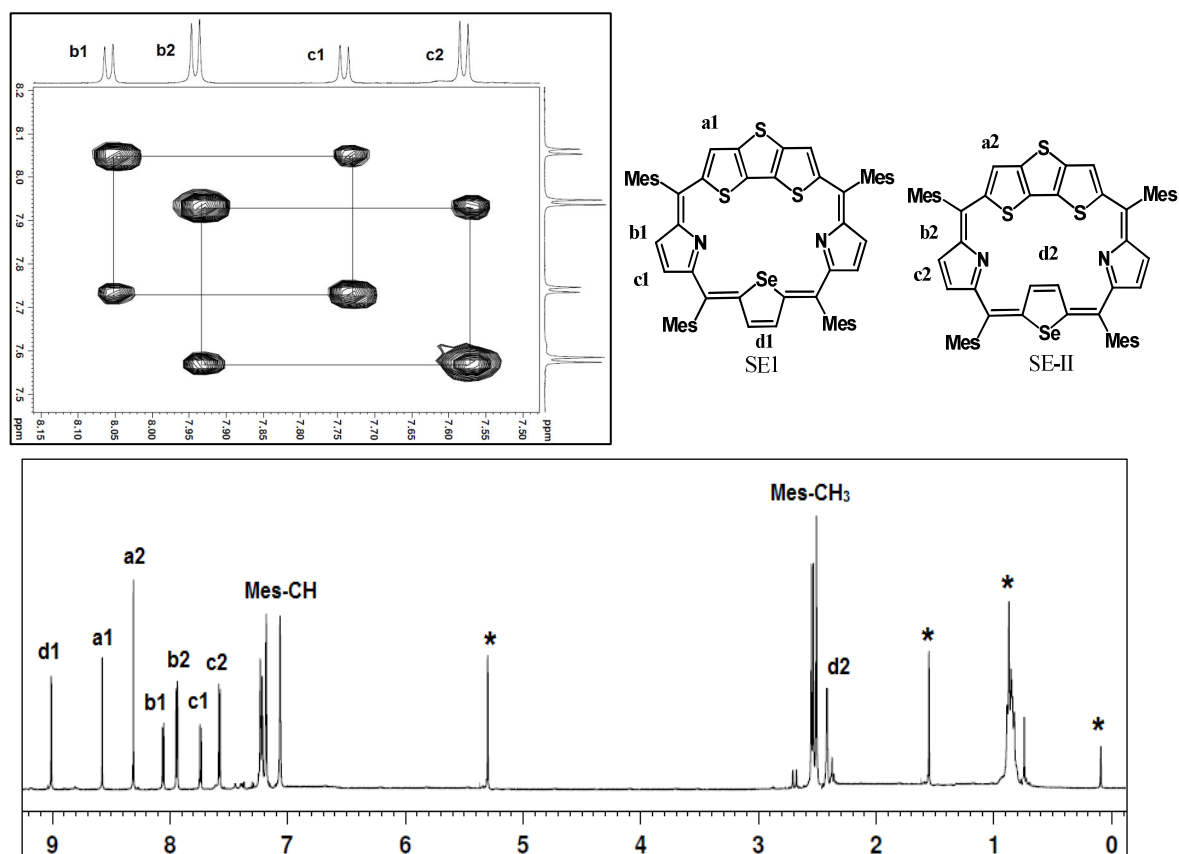
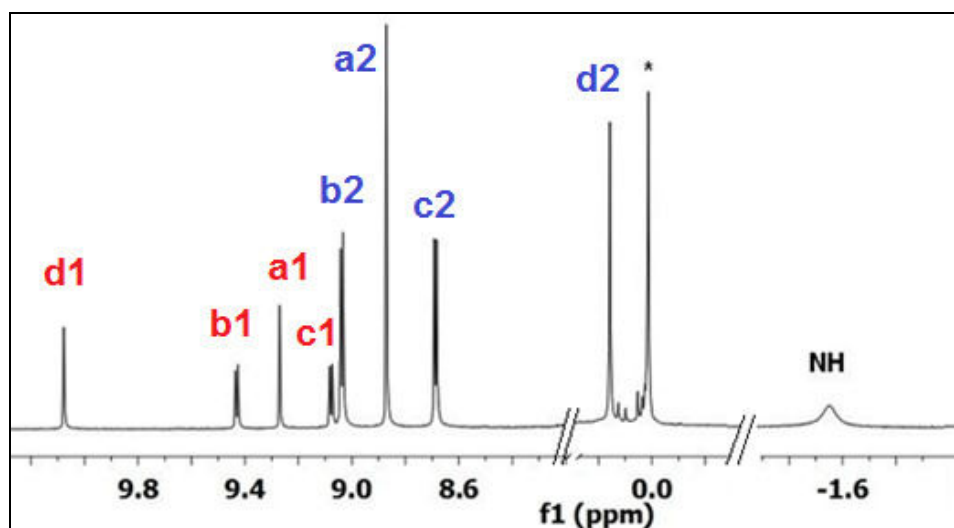
Upon protonation with TFA, the pyrrole β -CH and DTT-CH protons are 1.1 and 0.7 ppm shifted downfield as compared to the freebase. On the other hand, the inverted thiophene β -CH protons are 0.2 ppm shifted upfield and experiencing the more ring current effect. The protonated inner $-\text{NH}$ protons are observed at -3 ppm. All the mesityl-CH protons are resonated as four singlets between 6.5 to 8.0 ppm, clearly reflects that the respective protons are in-equivalent chemical environment.

Figure 4.28: ¹H NMR spectrum of **13** in CDCl₃Figure 4.29: ¹H NMR spectrum of **13.2H⁺** in CDCl₃

The ¹H NMR spectrum of Se-sapphyrin **14** in CD₂Cl₂ at 298 K is shown in Figure 4.30. Interestingly, the spectrum contains double the number of peaks than expected for Se-

sapphyrin. Careful analysis of NMR based on relative peak intensities and correlation reveal that two kind of conformer for **14**. In one of the conformer selenophene ring is normal (SE-I) and another one another one is inverted (SE-II). In normal SE-I the selenophene β -CH protons are resonated at 8.94ppm (d1) where as in the case of SE-II the selenophene protons resonate at 2.14ppm (d2) due to ring current effect. The β -CH protons of DTT are at 8.51 (a1) and 8.25ppm (a2) for SE-I and SE-II respectively. The two doublets with higher intensities at 7.99 (b1) and 7.67ppm (c1) which has correlation in the COSY spectrum have been assigned to the pyrrole β -CH protons of SE-I (b1 and c1 in Figure 4.30). The two doublets with lesser intensity at 7.87 and 7.51 ppm have been assigned to pyrrole protons of SE-II. Similarly two sets of mesityl phenyl CH and methyl protons were observed.

Upon protonation with TFA, the β -CH protons of the DTT and pyrrolic units of both the conformers SE-I and SE-II are downfield shifted as compared to freebase. In the case of SE-I, the respective protons are observed at 9.3 ppm and 9.1 to 9.4 ppm, which are 0.79 and 1.42 ppm downfield shifted. On the other hand, in SE-II, the respective e protons are resonated at 8.9 and 8.7 to 9.0 ppm, which are 0.75 and 1.15 ppm downfield shifted. The normal selenophene ring b-CH protons in SE-I is also downfield shifted and resonated at 10.01 ppm with a shift difference of 1.06 ppm. However, the inverted selenophene ring b-CH protons in SE-II are further upfield shifted and resonated at 0.2 ppm. The protonated NH signal is observed at -1.55 ppm, respectively. Overall, both the freebase and the protonated species are existing as two different conformers at room temperature (Figure 4.31).

Figure 4.30: ^1H NMR spectrum of **14** in CDCl_3 Figure 4.31: ^1H NMR spectrum of **14.2H⁺** in CDCl_3

The ^1H NMR spectrum of **15** in CDCl_3 is shown in Figure 4.32, where the DTT unit and the pyrrolic unit which is opposite to the DTT moiety are inverted and the respective β -

CH protons are observed at 15.67 (a) and 12.86 (b) ppm and the pyrrolic NH is at 4.47 ppm. The D₂O exchange experiment further confirms the NH signal. The remaining two pyrroles and thiophene β -CH protons are resonated between 7.12 to 7.14 ppm (c,c') and 7.35 to 7.37 ppm (d,d'). These signals are further confirmed by ¹H-¹H COSY spectral analysis. The meso-mesityl-CHs are observed as three singlets between 6.35 to 6.68 ppm, while the mesityl-CH₃ signals are appeared in the aliphatic region.

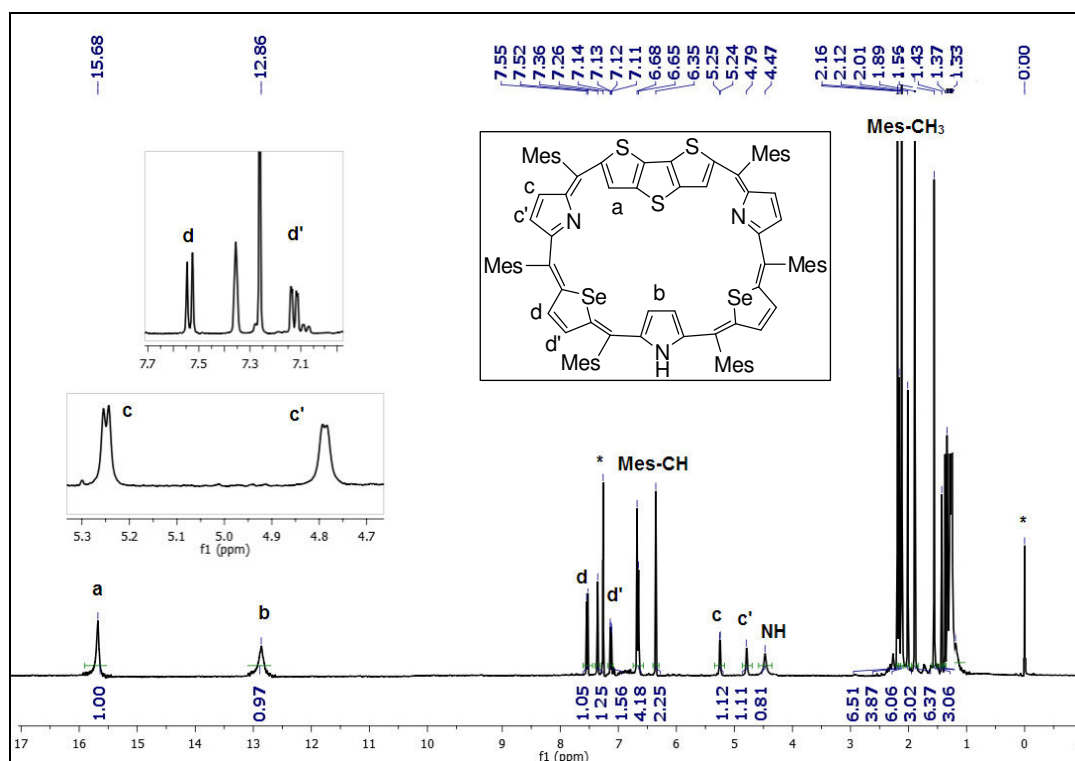


Figure 4.32: ¹H NMR spectrum of **15** in CDCl₃

Upon protonation with TFA in CDCl₃, the inverted β -CH (a) of DTT and pyrrolic (b) moiety is now upfield shifted and thus becomes normal (Figure 4.33). The pyrrolic NH proton is now appeared in the down field region and respective signals are at 7.42 (a) , 7.40 (b) and 9.35 ppm (b, NH) with the $\Delta\delta$ shift difference of 8.25, 5.46 and 4.88 respectively. On the other hand, the pyrrolic units which are along with the DTT moieties are inverted and the protonated NH appeared in the upfield region at -0.81 ppm and the β -CH protons are at 7.12

and 7.14 ppm respectively, with $\Delta\delta$ shift difference of 2.13. However, the thiophene β -CHs are slightly downfield shifted and appeared at 7.35 to 7.37 ppm. Overall, upon protonation, there is a drastic structural changes observed, however retains the anti-aromatic character. [117-118]

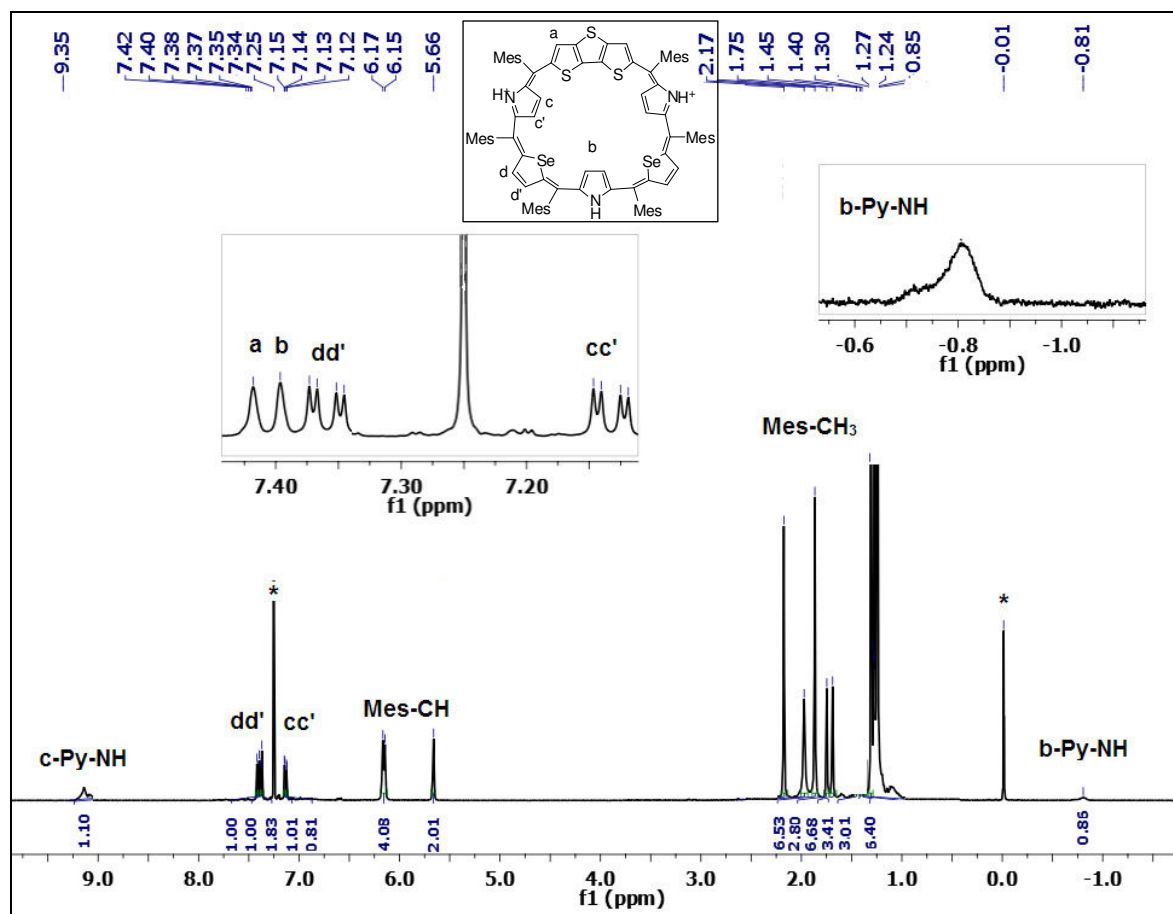


Figure 4.33: ^1H NMR spectrum of $\mathbf{15.2H}^+$ in CDCl_3

4.9.4 Single Crystal X-ray analysis:

The final confirmation of structures of **15** came from the single crystal X-ray structural analysis (Figure 4.34). As predicted from the spectral analyses, **15** contains a DTT unit, three pyrrole and two thiophene units which are connected through the six *meso*-carbon bridges by mesityl units. The DTT moiety and the pyrrole unit which is opposite to the DTT unit are inverted as predicted by the NMR analysis. The DTT unit is in positional disorder

where two of the DTT units are overlap each other. Analysis of the crystal structure reveals that the DTT unit in **15** is deviated by 28° , while the *meso*-mesityl rings are almost perpendicular to the mean macrocyclic plane, where the other units such as thiophene and pyrrole units in **15** are hardly deviated from the mean plane.

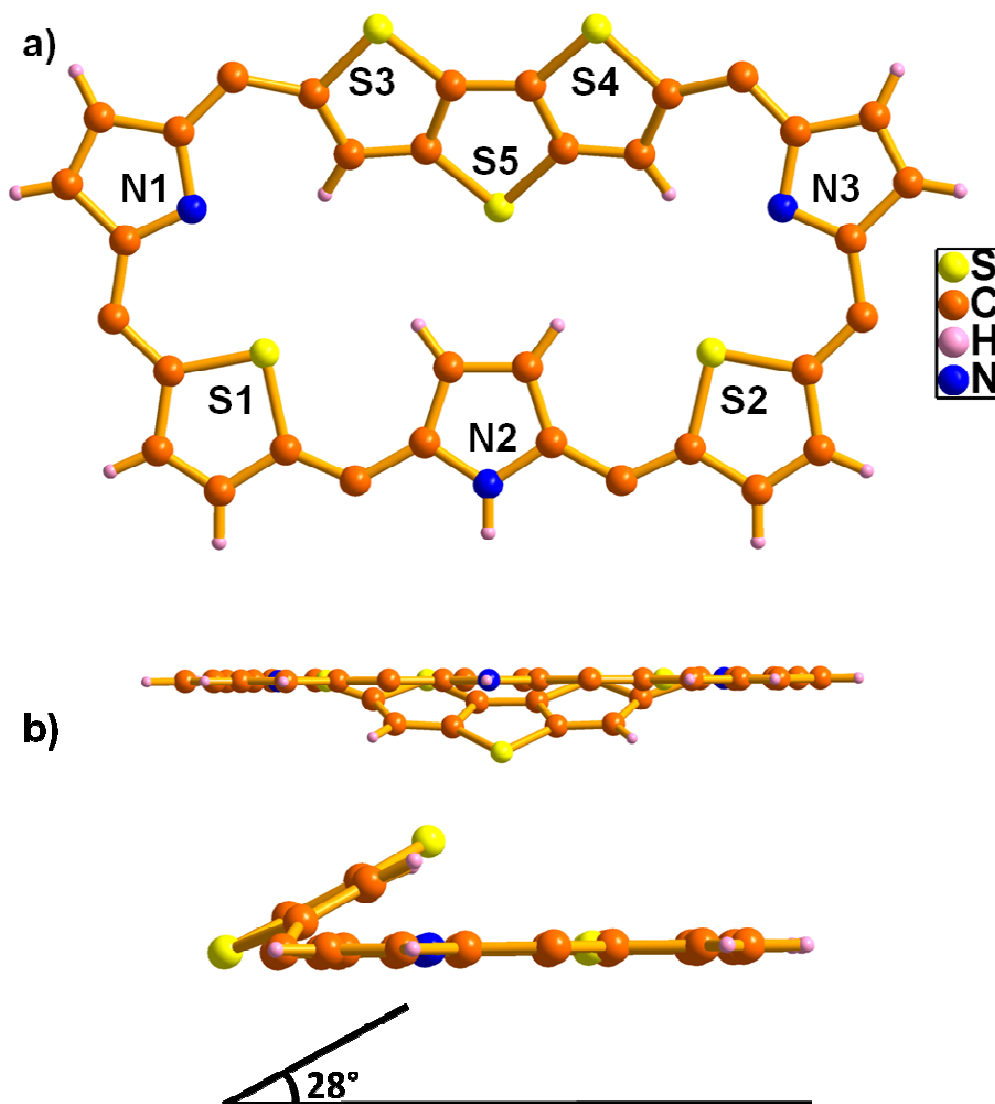


Figure 4.34: Single crystal X-ray structure of **15** a) Top view and b) side view. The *meso*-mesityl groups are omitted for clarity.

4.9.5 Electrochemistry of Fused Sapphyrin and Heptaphyrin:

The redox behaviors of the sapphyrin and heptaphyrin were studied by cyclic voltammetry using 0.1M TBAP (tetra-*n*-butylammonium hexafluorophosphate) as supporting electrolyte in dry CH₂Cl₂ solution. The observation of two reversible oxidation and two reversible reduction couple suggests the aromatic nature of this sapphyrins. The ΔE_{redox} value calculated from the electrochemical data of 1.55 V for **13** and 1.536 for **14** (Figure 4.35 and 36) indicates a reduction in the HOMO-LUMO gap consistent with the observed red-shift in the absorption spectra. On the other hand, two quasi-reversible two quasi-reversible oxidation and reduction peaks peaks obtained for the heptaphyrin supports the antiaromatic electronic structure (Figure 4.37). [116,119]

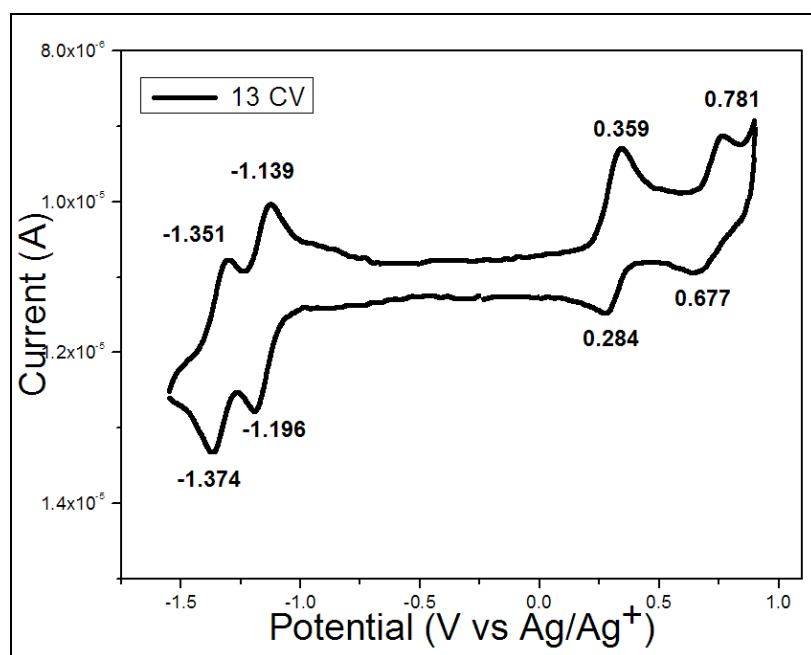


Figure 4.35: Cyclic Voltammogram of **13** in CH₂Cl₂ contains 0.1 M TBAPF₆ with Scan rate of 50 mV/s

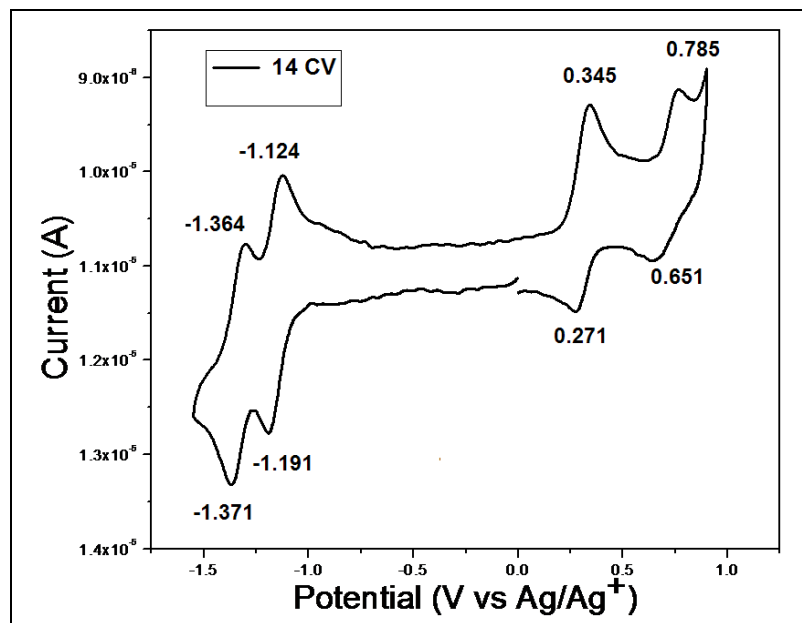


Figure 4.36: Cyclic Voltammogram of **14** in CH_2Cl_2 contains 0.1 M TBAPF_6 with Scan rate of 50 mV/s

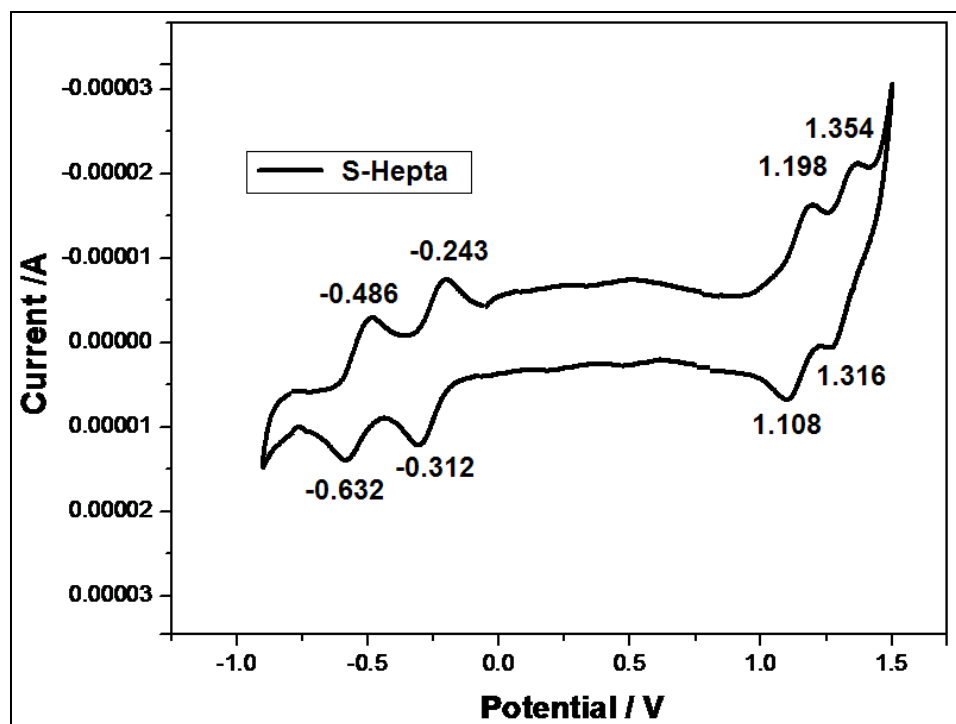


Figure 4.37: Cyclic Voltammogram of **15** in CH_2Cl_2 in CH_2Cl_2 contains 0.1 M TBAPF_6 with Scan rate of 50 mV/s

4.10 Conclusion

We have successfully synthesized and characterized two doubly fused 36π octaphyrins which exhibit the structural change upon protonation. The spectral analysis clearly demonstrates that change in the structure from a twisted figure-eight to an extended open form, where the non-aromatic structure is switched over to anti-aromatic upon protonation. We believe that the breaking of two intramolecular hydrogen bonding network (N-H...N) in freebase form and reformation of six intermolecular hydrogen bonding network (N-H...O, N-H...F, C-H...F) with counter anion is the driving force for such structural change upon protonation.

The excited state dynamics also give some insights into structural change upon protonation. Flexible figure-eight conformation of free-base form is responsible for short singlet excited state lifetime since the flexibility provides an effective nonradiative decay pathway. However, in the diprotonated state, the presence of rigid frame work due to intermolecular H-bonding and the presence of rigid DTT moiety partially destroys the effective non-radiative decay pathway and is responsible for the small increase in the singlet excited state lifetime. The moderate increase in the TPA cross section value upon protonation suggests that the perturbation of π electrons by femtosecond laser light is more effective in an extended structure relative to the twisted figure-eight structure [107,115].

We have demonstrated the one-pot synthesis of mono-fused sapphyrin and heptaphyrin heptaphyrin. The synthetic methodology adopted here is simple and straightforward. The fused sapphyrins maintains planarity and exhibit inverted thiophene in sulphur case and two different conformer in the selenium derivative. There is a drastic structural change observed between the freebase and protonated fused heptaphyrin macrocycle, however both the species maintain the anti-aromatic character.

4.11 Experimental Procedure:

4.11.1 Octaphyrins:

To 0.250 g of DTT-dipyrrane (0.42 mmol), 200 ml of dry CH_2Cl_2 was added and the mixture was degassed by bubbling nitrogen gas. To this solution 0.052 ml (1 equiv) of pentafluorobenzaldehyde was added and the reaction mixture was stirred for about 15 min at 278 K. Then 0.024 g (0.3 equiv) of *p*-TSA was added and stirring was continued for 2 hrs. To the reaction mixture 0.144 g of DDQ (1.5 equiv) was added and stirring was continued for further 2 hrs. The crude product obtained was purified by column chromatography over basic alumina followed by silica gel [100-200 mesh] with CH_2Cl_2 /hexane [20:80, Vol/Vol]. The pink color fraction was identified as product, after evaporation by vacuum yielded (07-10 %) green color solid.

9: ESI-MS: m/z (%): m/z calcd for $\text{C}_{78}\text{H}_{42}\text{F}_{10}\text{N}_4\text{S}_6+\text{H}^+$: 1417.1652; found: 1417.1589; elemental analysis calcd (%) for $\text{C}_{78}\text{H}_{42}\text{F}_{10}\text{N}_4\text{S}_6$: C 66.09, H 2.99, N 3.95; found: C 65.97, H 2.96, N 3.93. UV/Vis (CH_2Cl_2): λ_{max} [nm] (ϵ [$10^5\text{M}^{-1}\text{cm}^{-1}$]): 368 (0.243), 524 (0.331), 608 (0.222) 724 (0.101); ^1H NMR (400 MHz, CDCl_3 , 25° C, TMS) δ [ppm]: 15.48 (br, s, 2H), 9.38 (s, 2H), 6.85 (s, 2H), 7.41 (d, $^3J=7.2\text{Hz}$, 8H), 7.25 (d, $^3J=7.2\text{Hz}$, 8H), 6.34-6.29 (m, 4H), 5.87 (m, 4H), 2.48 (s, 6H), 2.45 (s, 6H).

9.H⁺, TFA/ CH_2Cl_2 : λ_{max} [nm] (ϵ [$10^5\text{M}^{-1}\text{cm}^{-1}$]): 452 (0.149), 568 (0.481), 696 (0.635) 816 (0.0784), 1136 (0.025) 1232 (0.0275); **(9.2H⁺)**, TFA/ CH_2Cl_2 : λ_{max} [nm] (ϵ [$10^5\text{M}^{-1}\text{cm}^{-1}$]): 416 (0.103), 632 (1.09), 701 (0.939) 992 (0.013);

9.2H⁺: ^1H NMR (400 MHz, TFA/ CDCl_3 , 25° C, TMS) δ [ppm]: 18.69 (br, s, 2H), 15.98 (d, $^3J=5.2\text{Hz}$, 2H), 15.84 (d, $^3J=5.2\text{Hz}$, 2H), 6.77 (d, $^3J=8\text{Hz}$, 4H), 6.60 (d, $^3J=8\text{Hz}$, 4H), 6.29 (d, $^3J=8\text{Hz}$, 4H), 5.98 (d, $^3J=8\text{Hz}$, 4H), 4.59 (d, $^3J=5.2\text{Hz}$, 2H), 4.13 (d, $^3J=5.2\text{Hz}$, 2H), 4.17 (s, 2H), 4.08 (s, 2H), 2.09 (s, 6H), 2.0 (s, 6H).

10: ESI-MS: m/z (%): m/z calcd for $C_{86}H_{58}F_{10}N_4S_6+H^+$: 1529.2904; found: 1529.287; elemental analysis calcd (%) for $C_{86}H_{58}F_{10}N_4S_6$: C 67.52, H 3.82, N 3.66; found: C 67.48, H 3.81, N 3.68. UV/Vis (CH_2Cl_2): λ_{max} [nm] ($\epsilon[10^5M^{-1}cm^{-1}]$): 348 (0.708), 528 (1.513), 680 (0.276); 1H NMR (400 MHz, $CDCl_3$, $25^\circ C$, TMS) δ [ppm]: 16.24 (br, s, 2H), 9.69 (s, 2H), 6.606 (s, 2H), 7.34 (s, 2H), 7.14 (s, 2H), 6.93 (s, 2H), 6.81 (s, 2H), 6.17-6.00 (m, 4H), 5.81 (m, 4H), 3.68 (s, 6H), 3.03 (s, 6H), 2.54 (s, 6H), 2.38 (s, 6H), 1.71 (s, 6H), 1.53 (s, 6H).

(**10.H⁺**, TFA/ CH_2Cl_2): λ_{max} [nm] ($\epsilon[10^5M^{-1}cm^{-1}]$): 392 (0.744), 688 (2.953), 816 (0.488) 1188 (0.291), 1176 (0.306); (**10.2H⁺**, TFA/ CH_2Cl_2): λ_{max} [nm] ($\epsilon[10^5M^{-1}cm^{-1}]$): 388 (0.338), 640 (1.963), 688 (2.908) 816 (0.177), 1152 (0.1368);

10.2H⁺: 1H NMR (400 MHz, TFA/ $CDCl_3$, $25^\circ C$, TMS) δ [ppm]: 23.03 (br, s, 2H), 17.84 (d, $^3J=5.6Hz$, 2H), 17.67 (d, $^3J=5.6Hz$, 2H), 6.38 (s, 4H), 6.25 (s, 4H), 3.79 (d, $^3J=5.6Hz$, 2H), 3.55 (d, $^3J=5.6Hz$, 2H), 3.09 (s, 2H), 2.90 (s, 2H), 2.07 (s, 12H), 1.96 (s, 12H), 1.90 (s, 6H), 1.81 (s, 6H).

4.11.2 Fused sapphyrin and heptaphyrin.

DTT-diol **6** (1 equiv) and Thiophen-tripyrane **11** (1 equiv) were dissolved in dry CH_2Cl_2 (200 mL) and stirred in an inert atmosphere for 10 min. The acid catalyst *p*-Toluene sulphonic acid (0.3 equiv) was added to this solution and continued stirring for further 90 min at ambient temperature. *p*-Chloroanil (1.5 equiv) was added to the above solution and the solution was opened to air, and then heated to reflux for 2 hrs. The solvent was evaporated by reduced pressure under rotary evaporator. The residue was purified by first basic alumina column followed by neutral alumina column, the brownish greenish brown color band eluted by CH_2Cl_2 : hexane (10:90) was identified as sapphyrin **13** in 10% yield and the second blue band (CH_2Cl_2 : hexane, 15:85) was identified as fused heptaphyrin **15** in 06 % yield.

13: ESI-MS: m/z calcd for $C_{60}H_{52}N_2S_4+H^+$: 929.3013; found: 929.3019; UV/Vis (CH_2Cl_2): λ_{max} [nm] ($\epsilon[10^5M^{-1}cm^{-1}]$): 495 (0.58), 661 (0.12); 1H NMR (400 MHz, $CDCl_3$, $25^\circ C$, TMS) δ [ppm]: 8.49 (s, 2H), 8.10 (d, 2H), 7.81 (d, $^3J=4Hz$, 2H), 7.19 (s, 4H), 7.09 (d, $^3J=4Hz$, 4H), 2.54 (s, 6H), 2.47 (s, 6H), 2.15 (s, 2H), 2.09 (s, 12H), 1.09 (s, 12H)

13.2H⁺: λ_{max} [nm] ($\epsilon[10^5M^{-1}cm^{-1}]$): 521 (0.81), 766 (0.18);

14: ESI-MS: m/z calcd for $C_{60}H_{52}N_2S_3Se$: 976.2458; found: 976.2469; Uv/Vis (CH_2Cl_2): λ_{max} [nm] ($\epsilon[10^5M^{-1}cm^{-1}]$): 501 (0.59), 653 (0.08);

SE-1: 8.94 (s, 2H), 8.51 (s, 2H), 7.99 (d, 2H), 7.67 (d, $^3J=4Hz$, 2H), 7.16 (s, 4H), 7.15 (s, 4H); SE-2: 8.24 (s, 2H), 7.87 (d, $^3J=4Hz$, 2H), 7.50 (s, 2H), 7.11(s, 4H), 6.99 (s, 4H), 2.12 (s, 2H).

14.2H⁺: λ_{max} [nm] ($\epsilon[10^5M^{-1}cm^{-1}]$): 530 (0.83), 766 (0.121);

15: ESI-MS: m/z calcd for $C_{88}H_{79}N_3S_5+H^+$: 1337.4878; found: 1338.4881;

UV/Vis (CH_2Cl_2): λ_{max} [nm] ($\epsilon [10^4M^{-1}cm^{-1}]$): 502 (0.805), 597 (0.427);

1H NMR (400 MHz, $CDCl_3$, $25^\circ C$, TMS) δ [ppm]: 15.68 (s, 2H), 12.86 (s, 2H), 7.53 (d, $^3J=12Hz, 2H$), 7.13 (d, $^3J=12Hz$, 2H), 6.68 (s, 4H), 6.65 (s, 4H), 6.35 (s, 4H), 5.24 (d, $^3J=4Hz$, 2H), 4.79 (d, $^3J=4Hz$, 2H), 4.47 (s, 2H), 2.26 (s, 12H), 2.12 (s, 6H), 2.01 (s, 12H), 1.89 (s, 6H), 1.43 (s, 12H), 1.37 (s, 6H)

15.2H⁺: UV/Vis (CH_2Cl_2): λ_{max} [nm] ($\epsilon[10^4M^{-1}cm^{-1}]$): 574 (0.797), 651 (0.761);

1H NMR (400 MHz, $CDCl_3$, $25^\circ C$, TMS) δ [ppm]: 9.35 (s, br, 2H), 7.42 (s, 2H), 7.40 (s, 2H), 7.37 (d, $^3J=4Hz$, 2H), 7.34 (d, $^3J=4Hz$, 2H), 7.14 (d, $^3J=4Hz$, 2H), 7.12 (d, $^3J=4Hz$, 2H), 6.17 (s, 2H), 6.15 (s, 2H), 5.66 (s, 2H), 2.17 (s, 12H), 1.75 (s, 6H), 1.45 (s, 12H), 1.40 (s, 6H), 1.30 (s, 6H), 1.27 (s, 12H).

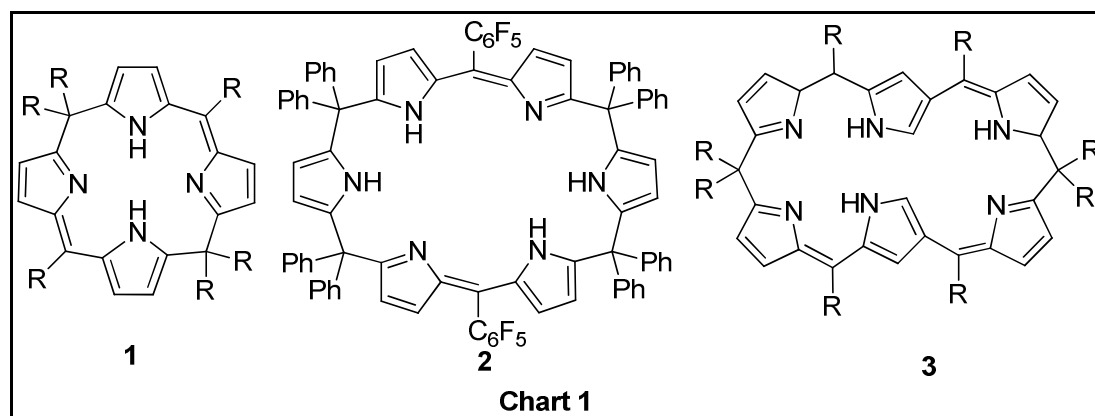
4.12 Crystal data for 10, 9.2H⁺ and 15

Parameters	10	9.2H ⁺	15
Solvent of crystallization	CH ₂ Cl ₂ /Heptane	CHCl ₃ /Toluene	CHCl ₃ / Hexane
Empirical formula	C ₈₆ H ₅₈ F ₁₀ N ₄ S ₆	C ₉₂ H ₅₂ F ₂₂ N ₄ O ₈ S ₆	C ₈₈ H ₇₉ N ₃ S ₅
M_w	1529.72	1951.74	1338.84
T [K]	100	100K	296(2)
λ [Å]	0.71073	0.71073	0.71073
Crystal system	Monoclinic	Triclinic	Triclinic
Space group	P2(1)/n	P-1	P-1
a [Å]	21.663(5)	15.7709(10)	8.9864(12)
b [Å]	11.548(5)	16.2964(10)	14.484(2)
c [Å]	30.366(5)	18.4599(10)	40.078(5)
α [°]	90.000(5)	76.714(3)	90.144(10)
β [°]	98.728(5)	77.234(3)	90.062(7)
γ [°]	90.000(5)	62.191(3)	107.934(7)
V [Å ³]	7509(4)	4048.3(4)	4963.2(12)
Z, ρ_{calcd} [Mg m ⁻³]	1.154	1.138	1.138
μ (MoK α) [mm ⁻¹]	0.256	0.284	0.076
F (000)	3152	1980	1416
Crystal size [mm]	0.13 × 0.09 × 0.08	0.3 × 0.11 × 0.08	0.11 × 0.09 × 0.07
θ range for data collection [°]	2.37 to 25.38	2.29 to 25.07	1.94 to 26.49
Reflections collected	26629	41691	27734
Refinement method	Full-matrix least-squares on F ²	Full-matrix least-squares on F ²	Full-matrix least-squares on F ²
Data / restraints / parameters	7676 / 0 / 967	14706 / 0 / 1195	4628 / 8 / 277
Goodness-of-fit on F ²	1.090	1.046	0.960
Final R indices [I > 2 σ (I)]	R1 = 0.0692	R1 = 0.0923	R1 = 0.0716
R indices (all data)	wR2 = 0.1209	wR2 = 0.1665	wR2 = 0.2268

Calix[2]thia[4]pyrin: An Expanded Calixpyrin with AIEE and Anion Receptor Properties

5.1 Introduction

Calixpyrins, a hybrid of calixpyrrole and porphyrin are receiving attention in recent years because of their conformational flexibility to adopt various non-planar conformations. The conformations depending on the number of pyrrole rings and nature of their linkage in a cyclic structure [60,61]. Structurally, they contain both sp^2 and sp^3 hybridized *meso* carbon links which connects the pyrrole rings. The presence of sp^3 hybridized *meso* carbon centers disrupts the π -conjugation and allows the macrocycle to adopt non-planar conformation [60-62]. Since they have properties analogues to both porphyrins and calixpyrroles, they find applications as metal ion receptors, anion complexing agents [70-72,76] and exhibit rich coordination chemistry [120,121]

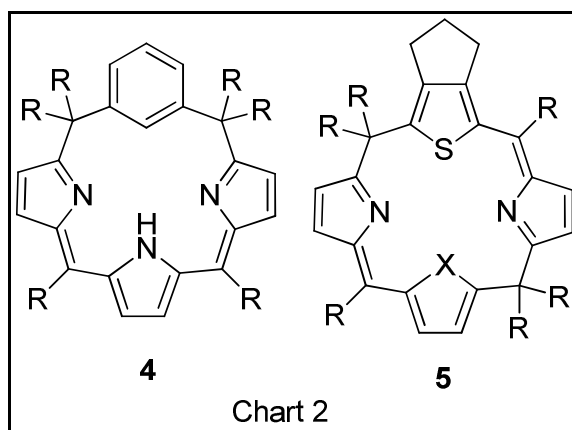


Even though, calixpyrins were reported by various research groups with decent yield [122], general synthetic protocols for synthesis of one sp^3 hybridized *meso* carbon, two sp^3 hybridized *meso* carbons **1** and three sp^3 hybridized *meso* carbons were reported by Sessler and co-workers,[60-62] and all the structure of macrocycles were confirmed by single crystal X-ray structure analyses. Till date, series of expanded calixpyrins containing five to

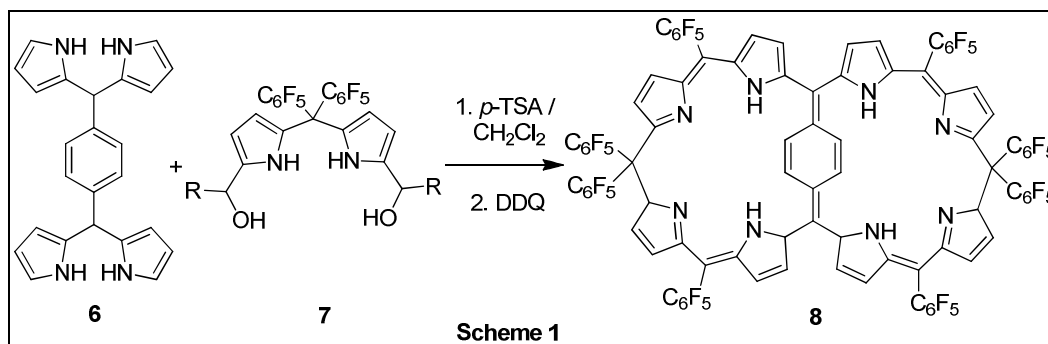
twenty eight pyrrole rings were reported in the literature [123]. In particular, calix[6]pyrrolins **2**, binds strongly with anions [63]. Furuta and co-workers have synthesized the novel N-Confused calixpyrin **3** which on metallation with platinum exhibits the NIR-emission. [124]

5.2 Core-modified calixpyrin

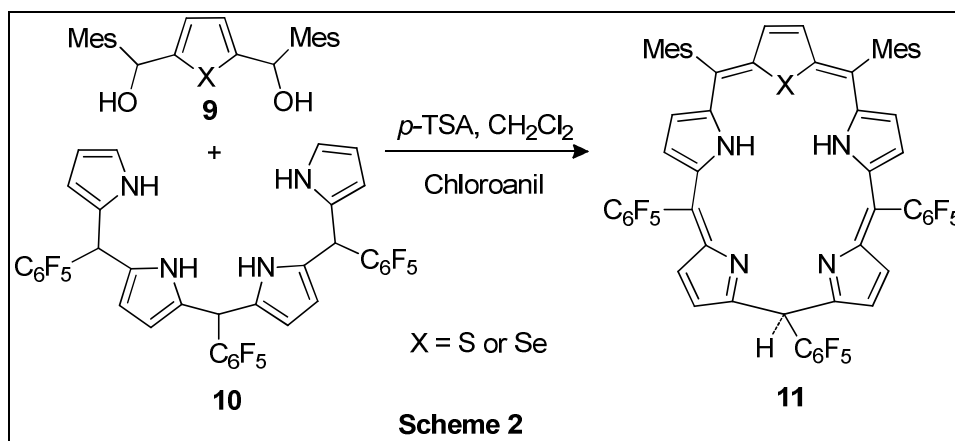
However, the synthesis of core-modified calixpyrins and their expanded derivatives are still in its infancy stage. Latos-Grażyński and co-workers demonstrated the synthesis and coordination chemistry of *m*-benzene ring incorporated porphodimethene **4**, where C.-H. Hung et.al reported binding ability of **4** which senses exclusively the Zn (II) ions [65]. Matano et.al reported synthesis of thiophene and furan containing calixpyrin **5**, their Pd complexes and also examined the catalytic activity of the respective metal complexes.



Osuka and co-workers described the synthesis of an internally 1,4-phenylene-bridged calixpyrins analogues. The condensation of 1,4-phenylene bis-dipyrromethane **6** with dipyrromethane-diol **7** in the presence of methanesulphonic acid followed by *p*-chloranil oxidation gave the bridged calixpyrin **8**. [57]

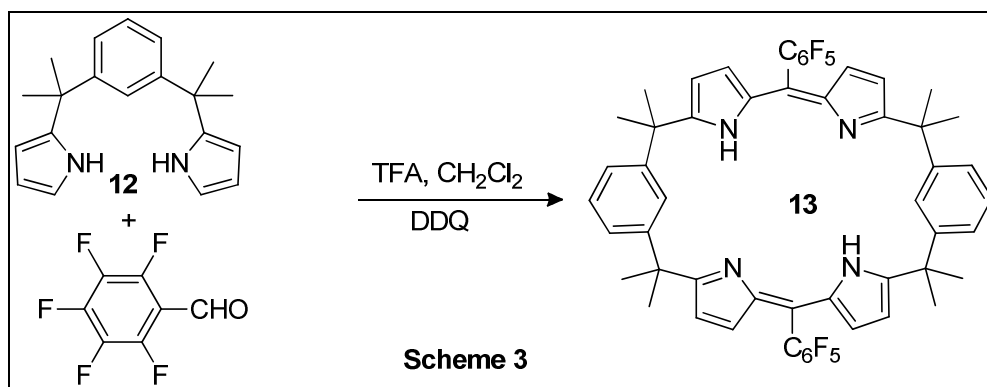


In 2008, our group demonstrated the synthesis of porphomonomethene type core modified expanded calixpyrin **11**. Reaction of thiophene-diol **9** with tetrapyrromethane **10** in presence of *p*-TSA followed by oxidation with *p*-chloranil leads to the formation of calixthia[5]pyrin or calixseleno[5]pyrin as green metallic seen color as single product (Scheme 2).

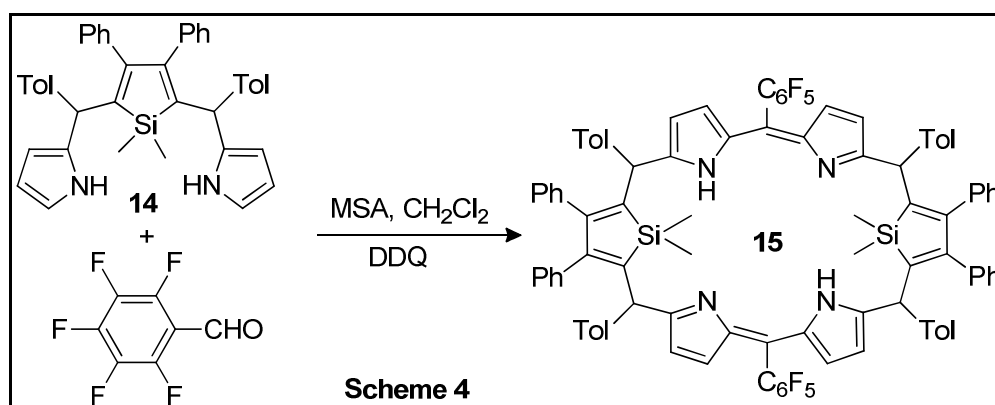


However, change of the oxidant from *p*-chloranil to stronger oxidant 2,3-dichloro-5,6-dicyano-*p*-benzoquinone (DDQ) under the same condition afforded calixpyrin (**11**), in addition to the formation of N-fused thiapentapyrin or N-fused selenapentapyrin. Thus, by controlling the nature of the oxidant used, it is possible to synthesize either calix[5]pyrin or the N-fused core-modified pentapyrin by this methodology.[125]

Recently, Srinivasan and co-workers reported synthesis of calix[2]-*m*-benzo[4]pyrin **13**. Reaction of bis-pyrrolyl benzene **12** with pentafluorobenzaldehyde in the presence of trifluoroacetic acid (TFA) followed by DDQ oxidation afforded **13** (Scheme 3). They have also demonstrated the aggregation induced enhanced emission (AIEE) and utilized this property as a probe for the detection of Hg(II) ions both in solution and solid state with excellent selectivity over 100 equiv of other metal ions.[126]



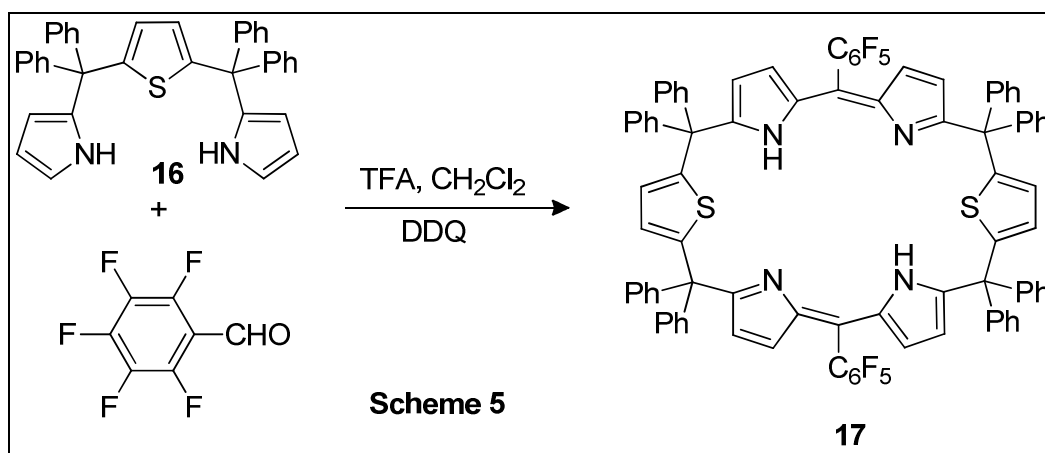
In 2012, Latos-Grażyński and co-workers reported the synthesis and characterization of calix[2]sila[4]pyrins **15** [127]. Reaction of 16-silatripyrrane **14** with pentafluorobenzaldehyde in the presence of methane sulphonic acid (MSA) followed by oxidation with DDQ gave 31,34-disilahexaphyrinoid – a four times reduced derivative of 31,34-disilahexaphyrin which contains two silole units surrounded by four tetrahedrally hybridized *meso* carbon (Scheme 3). The folded macrocyclic conformation from crystal analysis revealed that the silole rings were perpendicular to each other and the silole rings remain perpendicular to each other. The steric hindrance of bulky substituents at silicon atoms and β -positions of siloles prevented aromatization. Only one *meso* diastereomer (5*S*, 15*S*, 20*R*, 30*R*) was isolated and subsequently identified by 1D and 2D NMR techniques.



5.2 Core-modified expanded calixpyrin: Synthesis of Calix[2]thia[4]pyrin

The synthesis of calix[2]thia[4]pyrin **17** is outlined in scheme (Scheme 5). The synthetic methodology followed here is basically an acid-catalyzed condensation reaction of

appropriate precursors. Stirring a dichloromethane solution of bis-pyrrolyl thiophene **16** with **12** in the presence of trifluoroacetic acid (TFA) followed by oxidation with DDQ resulted in calix[2]thia[4]phyrin **17** in 20% yield and trace amount of higher analogue, calix[3]thia[6]phyrin **18**. The desired product **17** was purified further and is highly soluble in common organic solvents, however, insoluble in water.



5.3 Result and discussions:

5.3.1 Mass Spectral Analysis

The exact composition of **17** and its higher analogue **18** were established by ESI-MS which showed molecular ion peaks for **17** at 1446.4105 (Figure 5.1) and **18** at m/z 2168.5085 $[M+2H^+]$ (Figure 5.2).

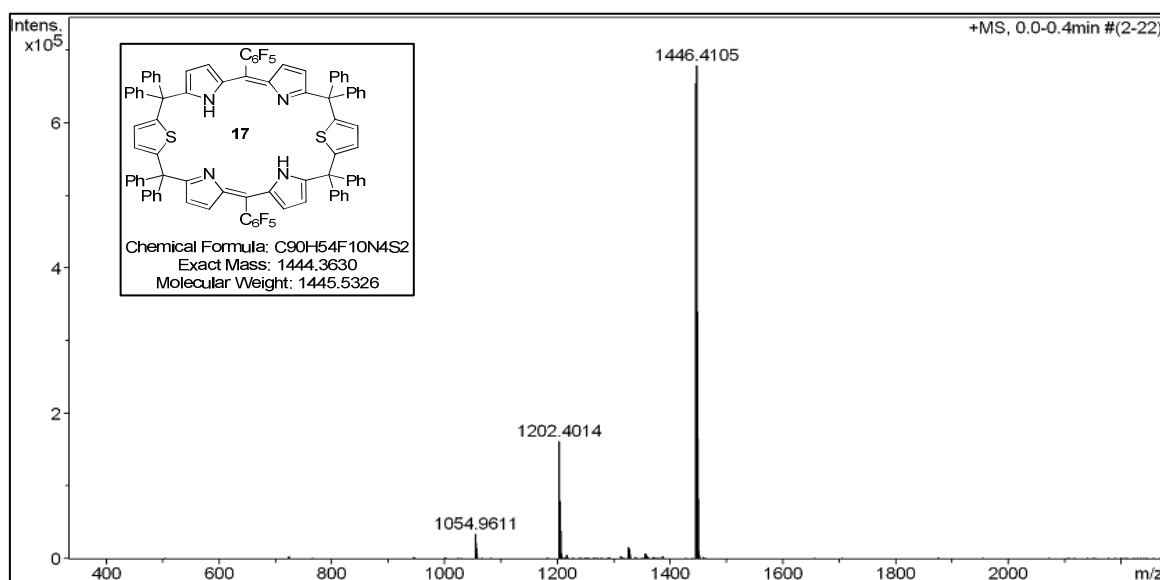
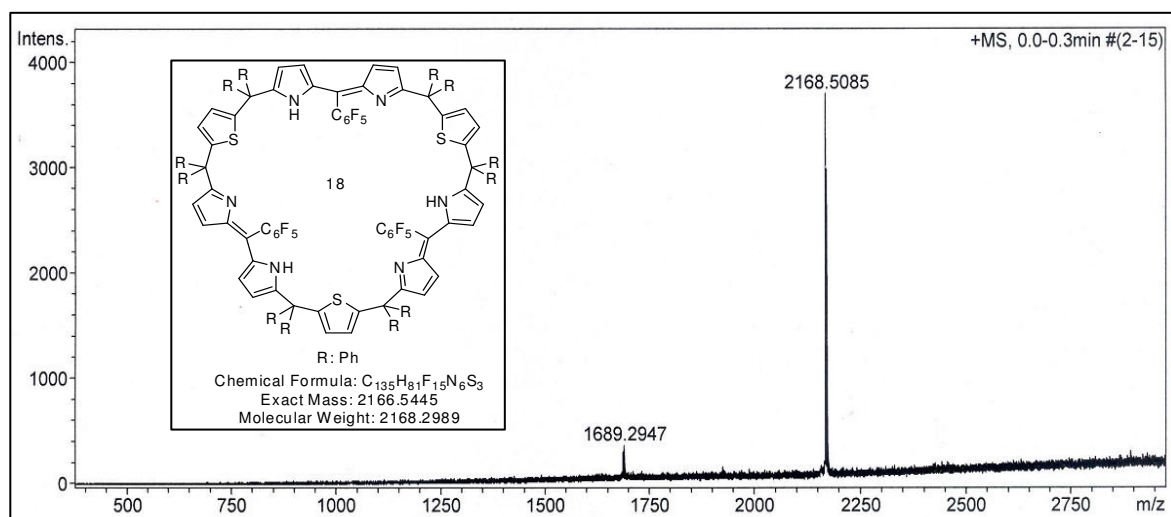
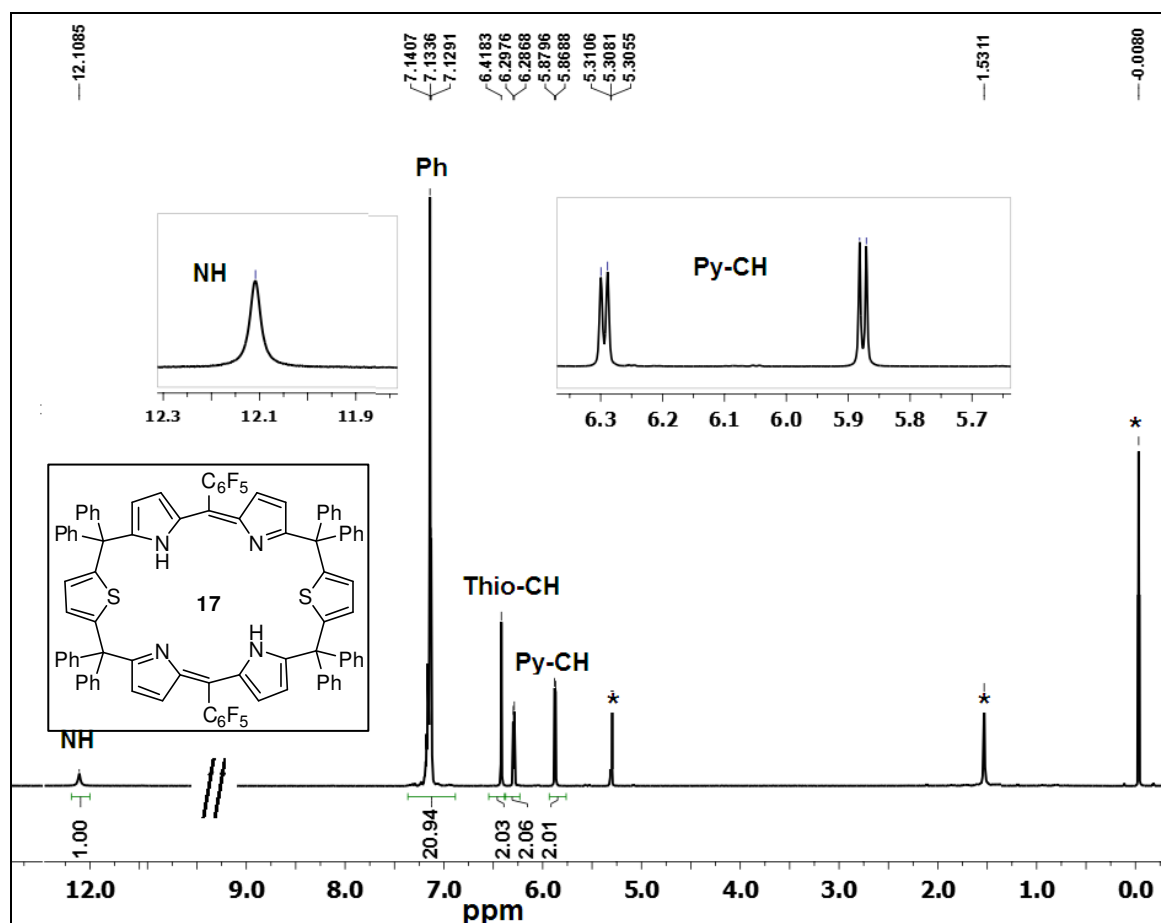


Figure 5.1: ESI-Mass spectrum of **17**

Figure 5.2: ESI-Mass spectrum of **18**

5.3.2 NMR characterization

The ^1H NMR spectrum of **17** in CD_2Cl_2 at room temperature substantiates the expected structure (Figure 5.3).

Figure 5.3: ^1H NMR spectrum of **17** in CD_2Cl_2 at 298K.

The pyrrole NH protons resonated as a broad singlet at 12.10 ppm and the assignment was confirmed by D₂O exchange experiment. The unusual downfield shift of the NH proton suggested a strong intramolecular hydrogen-bonding interaction with the imine nitrogens. The doublets at 6.30 and 5.88 ppm corresponds to the four β -CH protons of two dipyrin rings connected through the *meso*-pentafluorophenyl substituted methene bridge and the assignment was confirmed from ¹H-¹H COSY spectral analysis. The remaining four β -CH protons of the thiophene ring appeared as a sharp singlet at 6.42 ppm. Furthermore, as compared to **16**, the downfield shift of pyrrolic NH protons in **17** and the absence of two α -CH protons in the pyrrolic rings which are observed in **16** at 6.72 ppm clearly suggested the typical π -conjugation between the amine and imine pyrrole nitrogens and the formation of the macrocycle. The *meso*-phenyl protons are resonated as a multiplet at 7.15 ppm.

5.4 Aggregation Induced Enhanced Emission:

The electronic spectral analyses of **17** in dilute acetonitrile solution exhibit a band at 449 nm which is attributed to π - π^* transition of the dipyrin moiety (Figure 5.4).

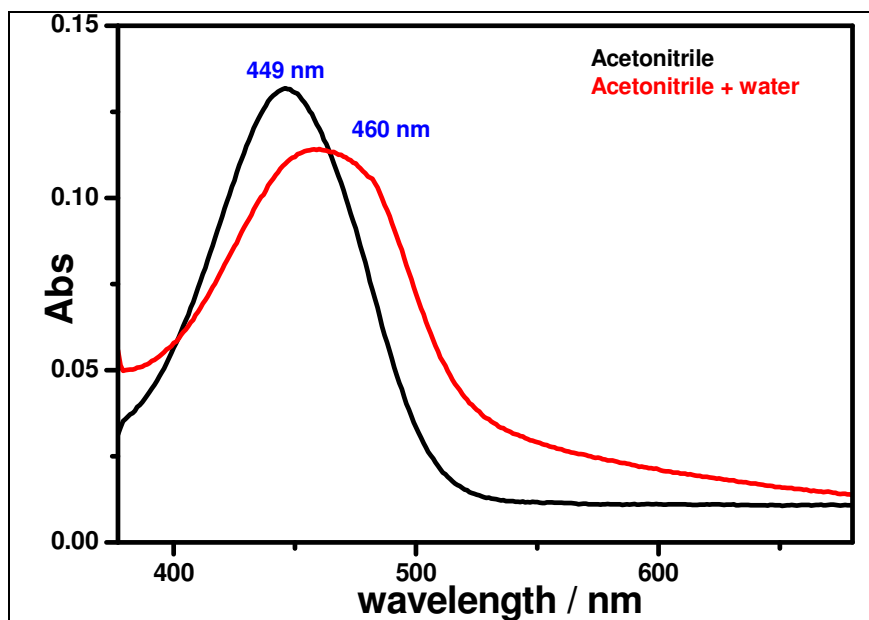


Figure 5.4: Absorption spectra of **17** in acetonitrile and acetonitrile/water mixture

Upon excitation at 449 nm, the emission spectrum in dilute acetonitrile shows a weak band at 538 nm and the results are comparable with the similar type of calixphyrins which are already known in the literature [73-76]. We observed an anomalous behavior in the absorption and emission spectrum of **17** upon increasing the percentage of water in the solvent mixture.

Upon increasing addition of water, the absorption band at 449 nm is broadened and experiences a bathochromic shift to 460 nm (Figure 5.5). On the other hand, in the emission spectral analysis, the weak emission band remains unchanged up to 50% of acetonitrile/water mixture and as the water content increases from 50% to 90%, the emission intensity at 538 nm is enhanced (Figure 5.6). These observations clearly indicate an AIEE property of **17**. The intensity variation suggests that the **17** starts to congregate at a water fraction of 50% and the aggregation continues to increase as the water fraction increases from 50% to 90% water mixture (Figure 5.7).

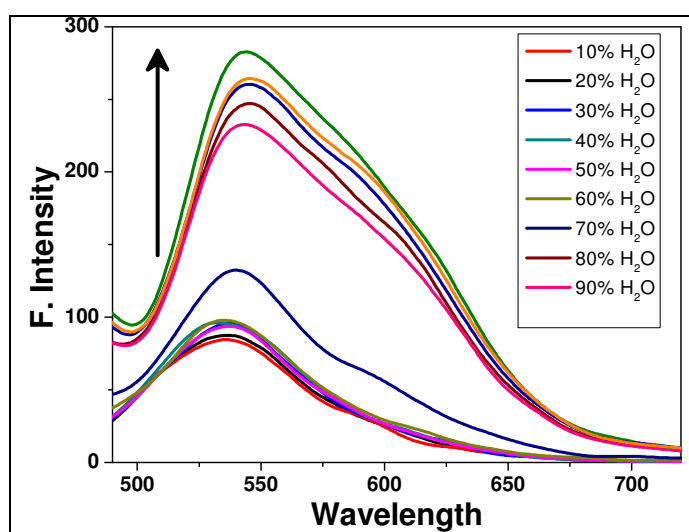


Figure 5.5: Emission spectra of **17** in acetonitrile/water mixtures with different fractions of water ($f_w=0-90$ vol%).

To have a quantitative picture of the emission enhancement upon aggregation, we estimated photoluminescence (PL) quantum yields (Φ_F) of **17** in acetonitrile and acetonitrile/water mixture (1:9 v/v) and found that Φ_F of the latter (6.9×10^{-3}) is fivefold higher than that of the former (1.38×10^{-3}). Basically, when the water content is increased to

50%, a critical point is reached, at which addition of small amount of water significantly promotes efficient calixpyrin self-aggregation leads to increase in the emission intensity.

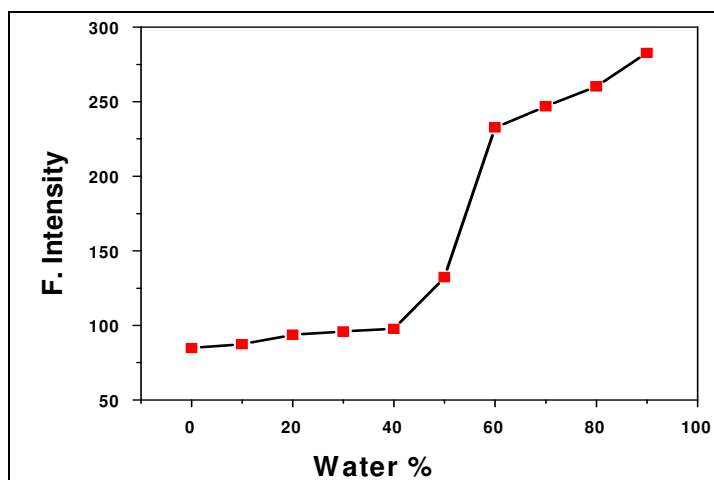


Figure 5.6: Changes in the emission intensities of **17** with the water content in the acetonitrile/water mixtures.

Further, the effect of temperature on the emission spectra of **17** in the same solvent mixture (1:9 v/v) was also investigated (Figure 5.7). Upon lowering the temperature from 75 °C to 25 °C, the emission intensity at 538 nm further enhances due to increase in aggregate formation, while rising the temperature decreases the intensity due to disaggregation of the molecules. These results suggest that the aggregate state of the compound at low temperature changed into monomer-like state at high temperatures.

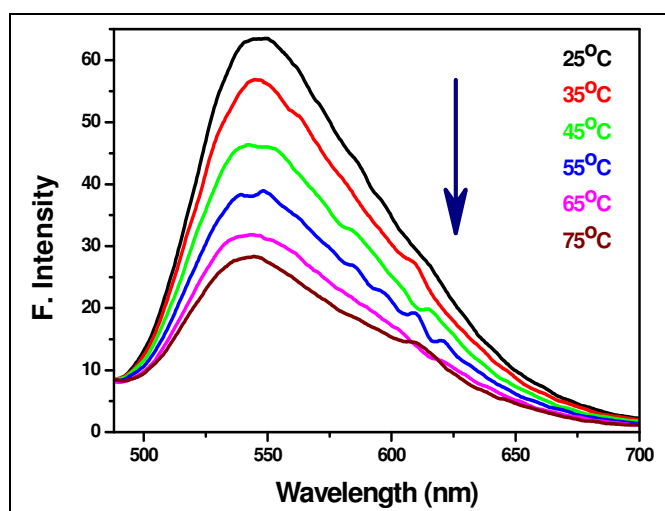


Figure 5.7: Temperature effect on the emission peak intensity of **17** in acetonitrile/water (1:9 v/v), ($\lambda_{\text{ex}} = 449 \text{ nm}$)

As the temperature decreases from higher to lower, the thermally induced or activated intramolecular rotations of the *meso*-phenyl and pentafluorophenyl groups are gradually restricted. Thus, reduction in thermal energy decreases the intramolecular rotation (IMR) of the *meso*-aryl groups and rigidifies the macrocycle as a whole, thereby enhancing the solution emission. Overall, the aggregates at low temperatures are more rigid and more emissive than the free monomer. The single crystal X-ray studies of **17** further confirm the restriction in intramolecular rotations during aggregation.

The aggregate formation of **17** was further confirmed from the microscopic analysis scanning electron microscope (SEM) and dynamic light scattering (DLS) studies. The cubic shaped aggregates were observed from the SEM analysis with the size ranging from 0.38-2.08 μm (Figure 5.8). By using different percentage of acetonitrile/water mixtures, the nanoparticles of average diameter from 150 nm (30:70) to 122 nm (10:90) were detected from the DLS studies (Figure 9-10). The reduction in the nanoparticles size upon increasing the fraction leads to an effective restriction in the IMR of the flurophore, resulting in enhanced emission.

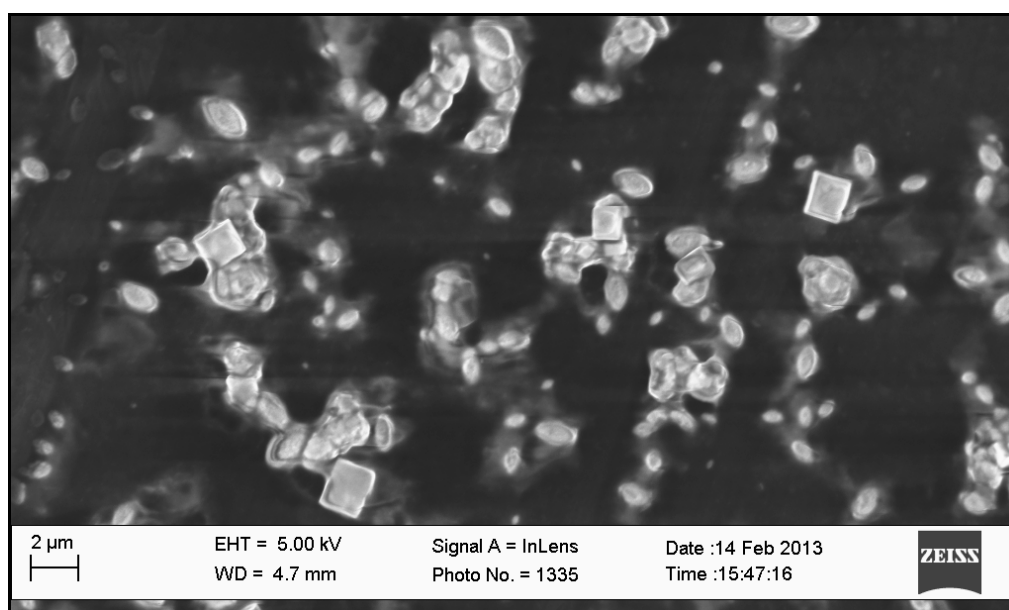


Figure 5.8: SEM image of **17** in acetonitrile/water mixture (10:90) at 278 K

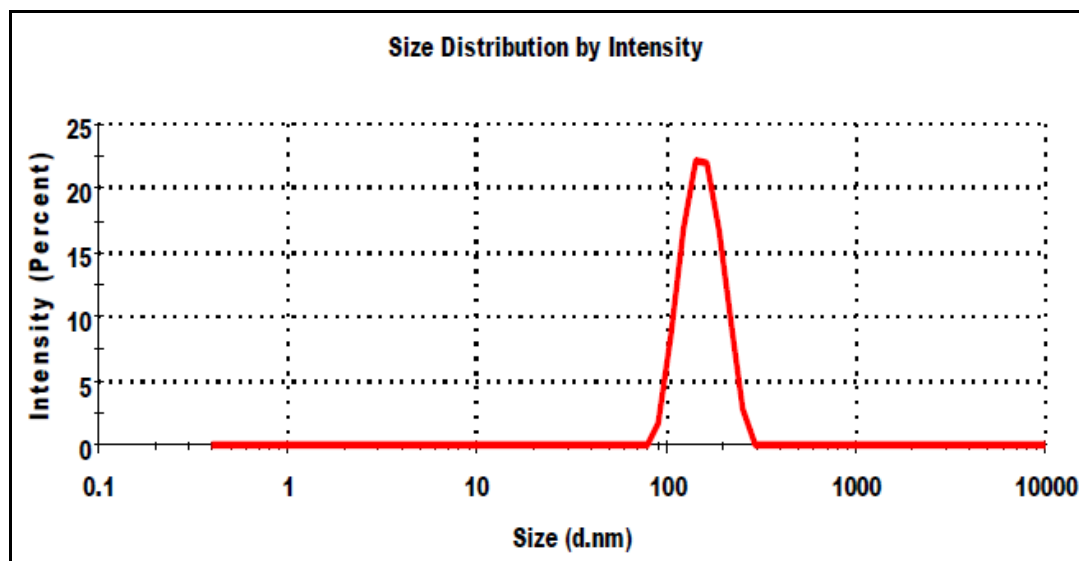


Figure 5.9: DLS measurement of **17** (6×10^{-6} M) in acetonitrile/water mixture (30:70) at 278 K

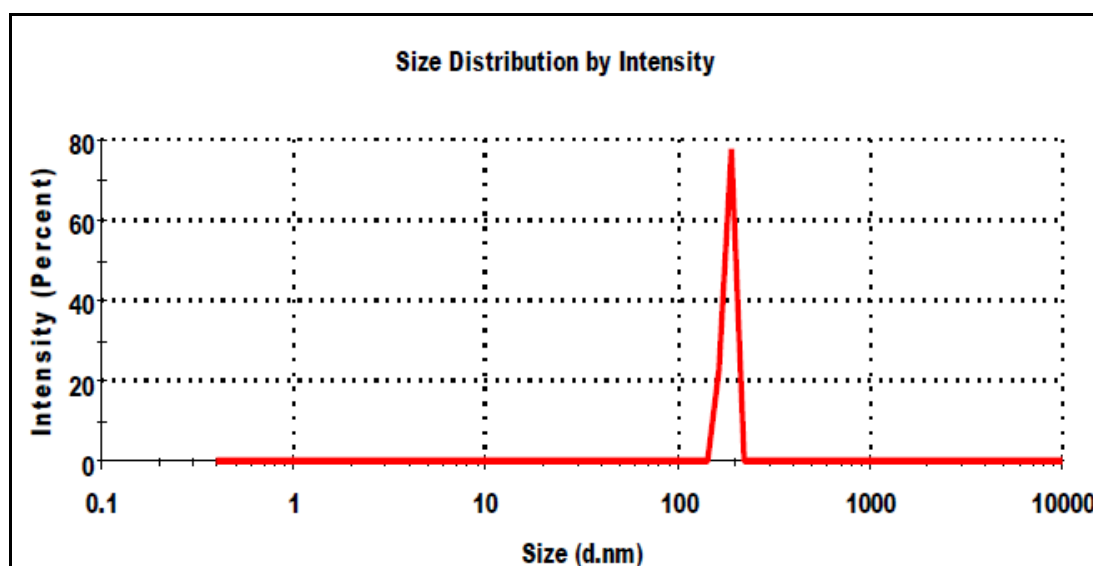


Figure 5.10: DLS measurement of **17** (6×10^{-6} M) in acetonitrile/water mixture (10:90) at 278 K

5.5 Single crystal X-ray analysis of **17**:

The single crystal X-ray structure of **17** is shown in Figure 5.11. The molecule is located on a crystallographic two fold axis. As predicted from the spectral analysis, **17** contains two bis-pyrrolyl thiophene moieties, connected by pentafluorophenyl groups incorporated methene bridge, while the remaining four *meso* positions are occupied by two phenyl rings on each *meso*-carbon atoms. There are two intramolecular hydrogen bonding

interaction observed in **17**, where the interaction is between; (i) the amine (N2-H2) and imine pyrrolic nitrogens (N1) which are present in the dipyrin moieties, and (ii) thiophene ring β -CH (C8-H8) and the phenylic π -cloud (Ph(π)) of one of the *meso*-phenyl units (Figure 5.12a). The distance and angle of N2-H2...N1 and C8-H8...Ph(π) are 2.23Å, 122° and 2.70Å, 152°, respectively. The pyrrole units in the dipyrin moieties are deviated by 15°, whereas thiophene and the *meso*-pentafluorophenyl units are perpendicular to the mean dipyrin plane by 84° and 90° respectively, and adopt a chair-like conformation which is shown in Figure 5.12b.

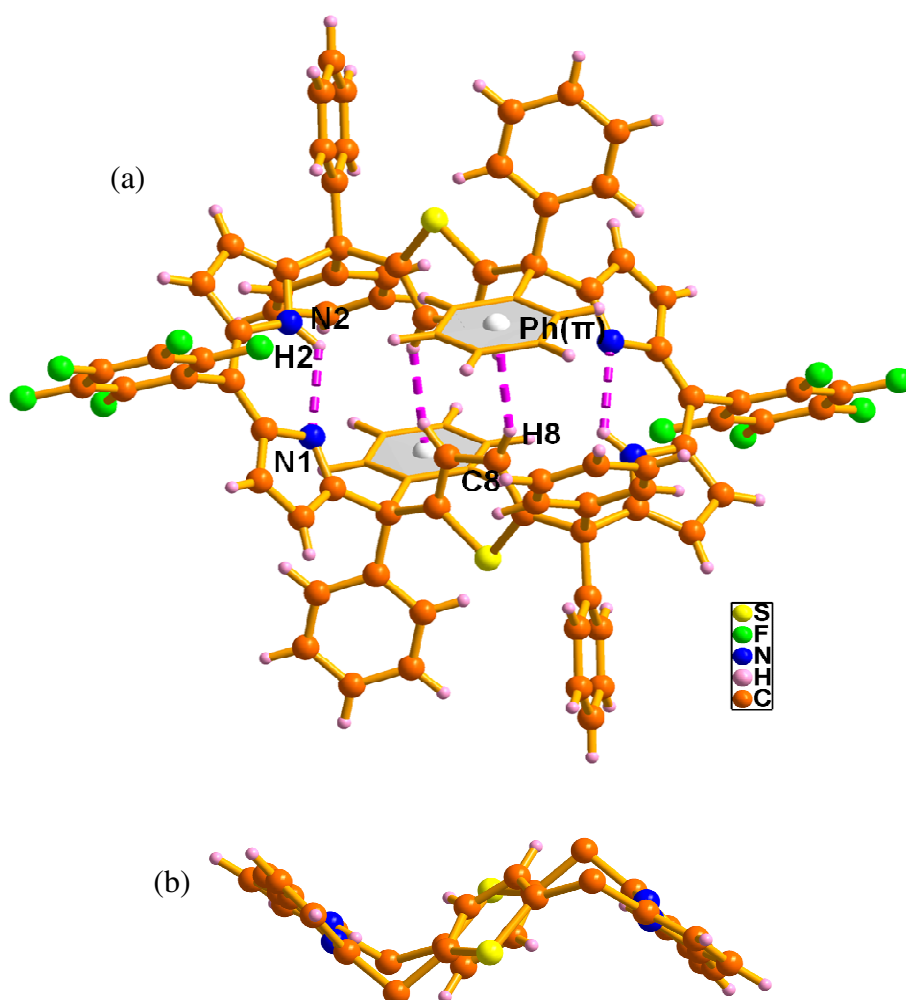


Figure 5.11: Single crystal X-ray structure of **17**. (a) Top view with intramolecular hydrogen bonding interaction and (b) side view. The *meso*-aryl groups are omitted for clarity in the side view

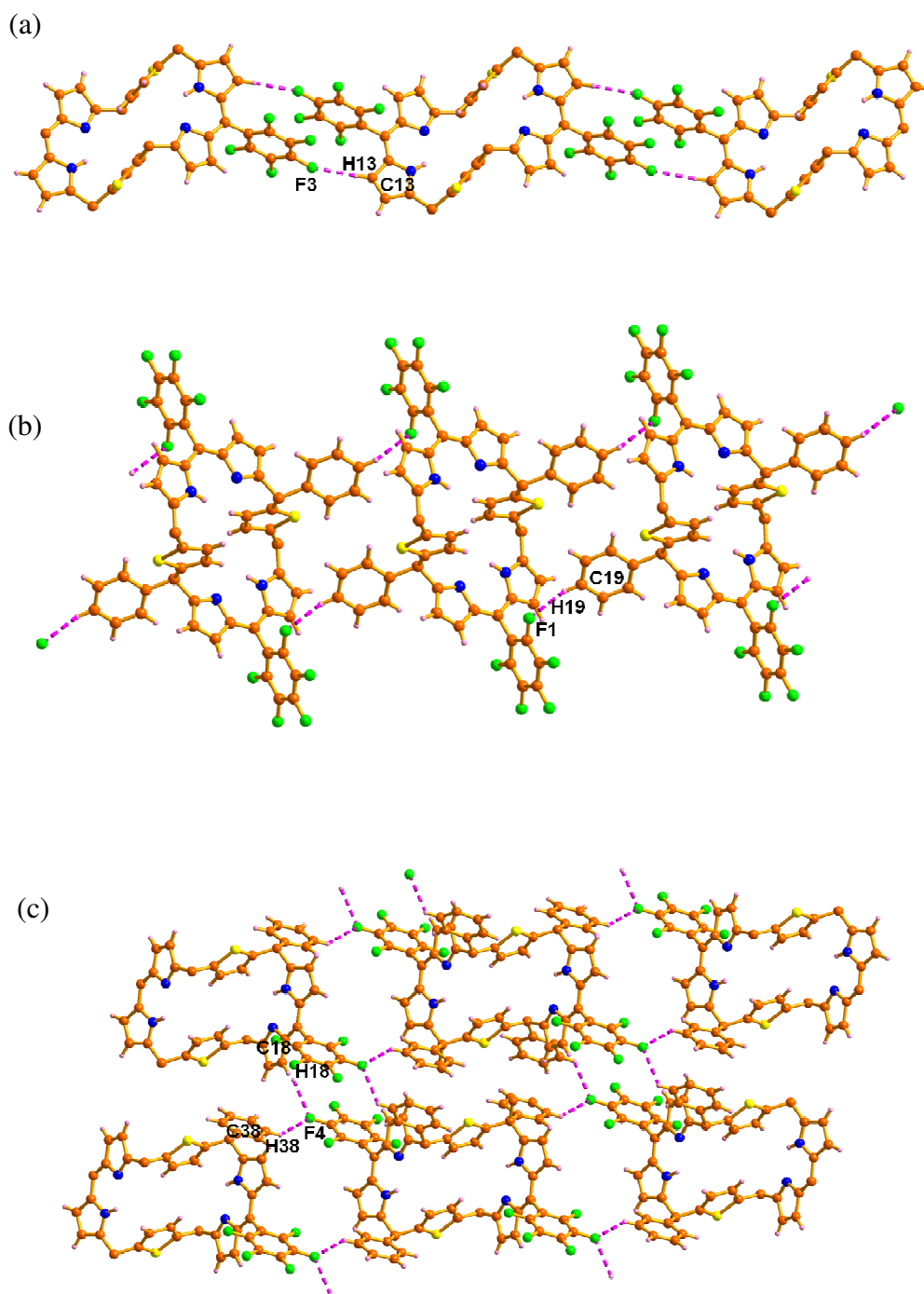


Figure 5.12: One-dimensional arrays of **17**. The intermolecular hydrogen bonding interactions of (a) C13-H13...F3, (b) C19-H19...F1 and (c) C18-H18...F4 and C38-H38...F4 with the distances and angles are: (a) 2.53 Å, 171°; (b) 2.87 Å, 133°; (c) 2.64 Å, 124° and 2.73 Å, 136°. The *meso*-aryl groups which are not involved in the hydrogen bonding interactions are omitted for clarity.

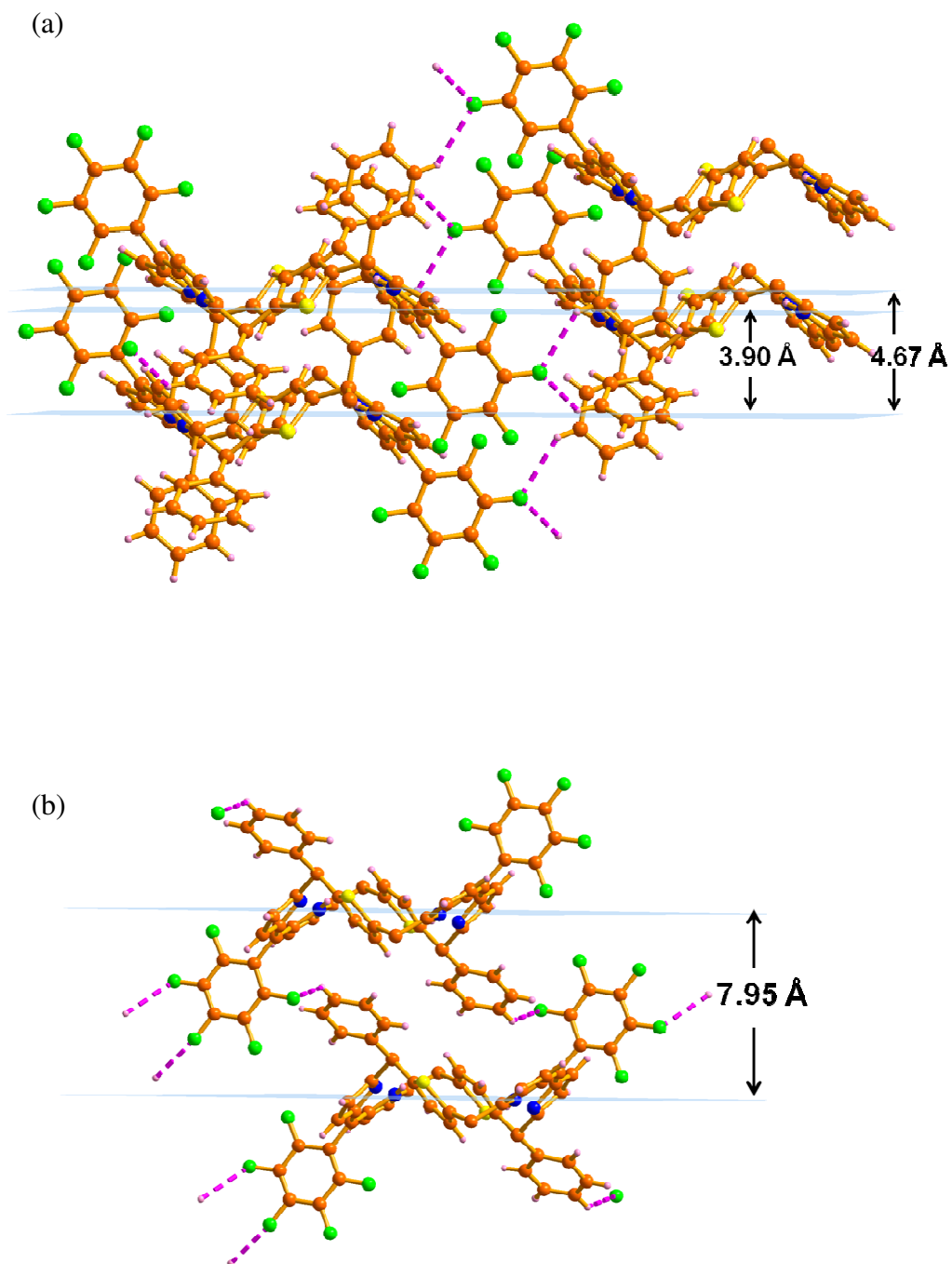


Figure 5.13: a) Two-dimensional arrays of **17**. b) The interplane distances (plane generated by the *meso*-carbon atoms such as C5, C10, C15, C5', C10' C15'). The distances are between three units (a) and two units (b) of **17**.

Fluorine atoms in the pentafluorophenyl units generate three one-dimensional arrays through intermolecular hydrogen bonding interactions; (i) F3 atom with pyrrolic β -CH unit

(C13-H13) (Figure 5.12a) ; (ii) F1 atom with one of the *meso*-phenyl CHs (C19-H19) (Figure 5.12b); and (iii) F4 atom with *meso*-phenyl CHs such as C18-H18 and C38-H38 with the distances and angles of C13-H13...F3, C19-H19...F1, C18-H18...F4 and C38-H38...F4 (Figure 5.12c) are: 2.53Å, 171°; 2.87Å, 133°; 2.64Å, 124° and 2.73Å, respectively. By combining these one-dimensional arrays, **17** generates two-dimensional supramolecular assembly in the solid state as shown in Figure 5.13. Further, the interplane distances (plane generated by the *meso*-carbon atoms such as C5, C10, C15, C5', C10' C15') between the two units of macrocycles are from 3.90 to 7.95 Å, which accommodate all the aryl units together and restrict the intramolecular rotation within them. Overall, both the intramolecular interaction between dipyrin unit, thiophene and the *meso*-phenyl unit and intermolecular interaction between the *meso*-phenyl units, pyrrolic and pentafluorophenyl units restrict the intramolecular rotation in the solid state and leads to enhanced emission, as observed in the aggregated state.

5.6 Anion binding properties of **17**:

In fact, the calixpyrins are well known in the literature that it binds with the cation, however, only limited reports on the anionic receptor properties [89]. In this section, we mainly concentrate on such property. The larger and flexible cavity size of **17** prompted us to explore the receptor properties of the macrocycle. The acidic nature of the calixpyrrole readily binds with various tetrabutyl ammonium salts; [89,128] however in order to generate calixpyrin anion complex, in addition to the regular amine nitrogens, the imine nitrogens are further protonated to generate an efficient receptor species, which promotes not only the hydrogen bonding, but also the electrostatic interaction. Therefore, protonation of the basic nitrogens in **17** leads to the formation of diprotonated species which creates a driving force to attract various anions towards its cavity.

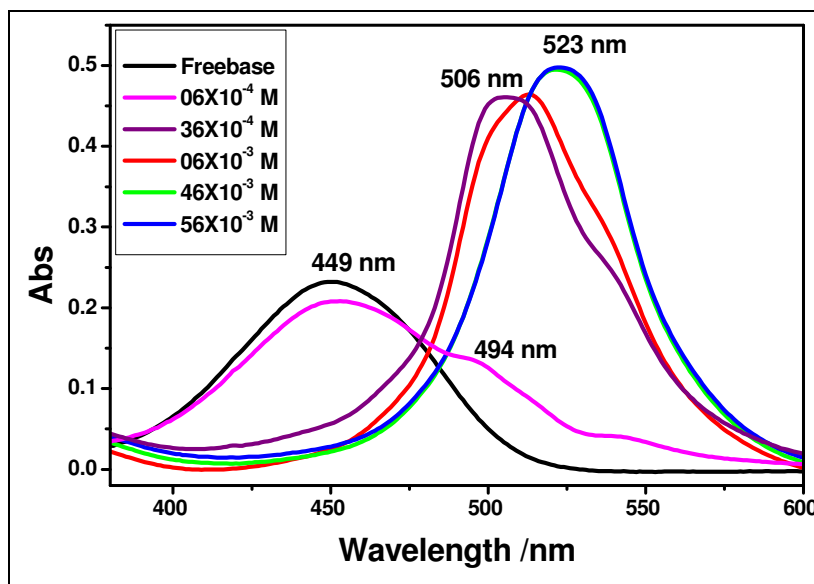


Figure 5.14: Absorption spectral changes of **17** in CH_2Cl_2 upon addition of TFA. (a) Step-wise formation of mono-, di protonated species and anion bound species; (b) Titration experiment between **17** in CH_2Cl_2 with TFA.

As discussed, **17** reported here has an $\pi-\pi^*$ absorption in the visible region and hence we have made use of electronic spectra to monitor the anion complexation. The preliminary qualitative experiment was performed by using dichloromethane solution of **17** with increasing concentration of trifluoroacetic acid. As the acid concentration increases, the band at 449 nm gradually decreases and the new band appears at 494 nm with a bathochromic shift of 45 nm which suggests the formation of monoprotinated species, as there are two species exists which are in dynamic equilibrium. Further increasing the concentration of the acid, the band at 494 nm is red shifted and the new band appears at 506 nm with the shift value of 12 nm, which reveals the formation of diprotinated species of **17**. Upon increasing the concentration of the acid further, the band is further shifted to 523 nm which suggests the extent of binding of CF_3CO_2^- ion with **17** (Figure 5.14). Overall, the preliminary binding studies reveal the formation of the mono-, di- protonated species and the binding of anion with **17**. The results encouraged us to perform the binding studies with various anions such as perchlorate (Figure 5.15, 5.16), sulphate (Figure 5.17,5.18), nitrate (Figure 5.19, 5.20) and

chloride (Figure 5.21 and 5.22) with the dichloromethane solution of **17** and the results are presented in (Scheme 6). For all these experiments, we maintained the concentrations of **17** at 6×10^{-6} M and the following observations have been made:

- (i) Addition of different amounts of anions (for example, 6×10^{-4} – 6×10^{-2} M HClO₄) to **17** solution at constant concentration results in a decrease in the absorbance at 449 nm and the simultaneous appearance of a new band at 516 to 523 nm. Thus effectively, the anion complexation results in the red shift of about 67 to 74 nm and the magnitude of this red shift is different for different anions. For example, upon increasing the concentration of perchlorate ion, the band at 449 nm is shifted to 523 nm and the color of solution changes from pale yellow to pink color which is shown in Figure 5.15.
- (ii) The isosbestic point for all the anion complexes are observed between 483 to 490 nm. The isosbestic point suggests the presence of equilibrium between the **17** and **17**.anion complex (Figure 5.15, 5.17, 5.19, 5.21)
- (iii) The binding constant values (calculated by using Benesi-Hildebrand equation) [129] vary from 3.78×10^2 M⁻¹ to 2.50×10^4 M⁻¹ with ClO₄⁻ ion showing strongest binding and Job's plot reveal 1 : 1 binding between **17** and the anions (Figure 5.16). The Job's plot and Benesi-Hildebrand plot for other anions are shown in Figure 5.16, 5.18, 5.20, 5.22 respectively.
- (iv) The binding constant depends on the compatibility of cavity size of the receptor; the size of the anion and the number of H-bonding (both regular hydrogens and protonated hydrogens) sites available.[130] A comparison of binding constants suggests that the sulphate and perchlorate anions bind stronger as compared to nitrate and chloride anions. For example, the binding constant of perchlorate anion is sixty six fold higher when compared to the

chloride anion presumably suggesting that the cavity size is more suitable for the tetrahedral anions.

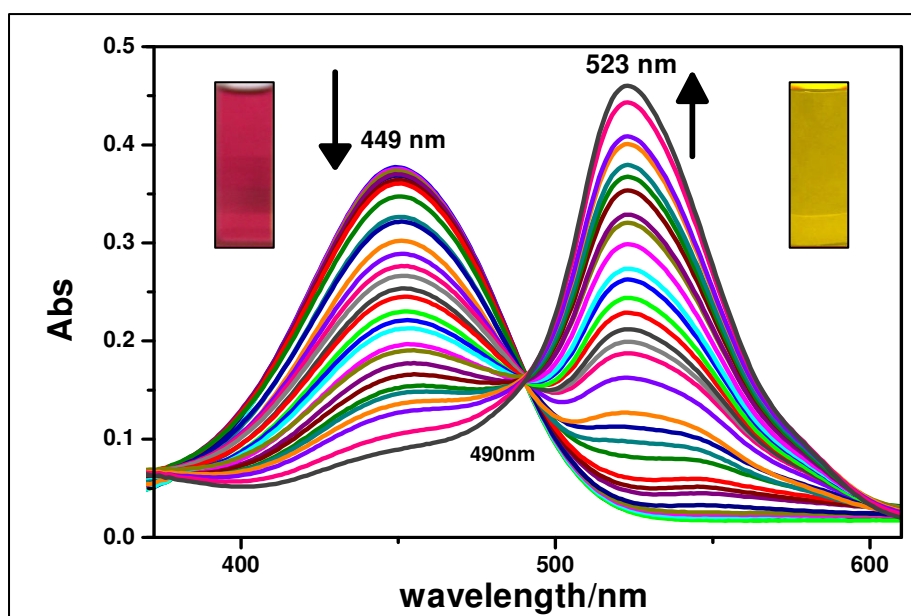


Figure 5.15: Absorption spectral as well as color changes of **17** in CH_2Cl_2 upon addition of HClO_4

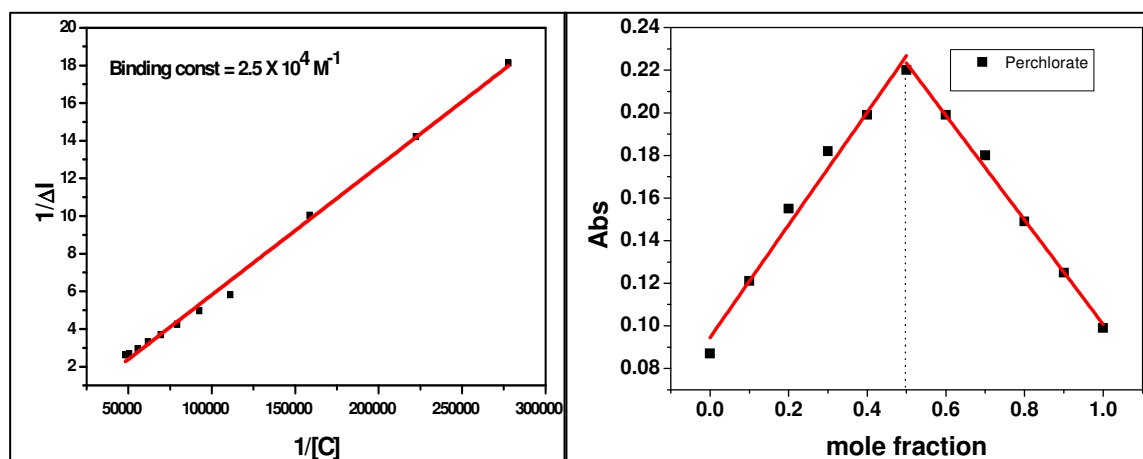


Figure 5.16: Job's plot for **17.C1O4**. and Benesi-Hildebrand plot for **17.C1O4**.

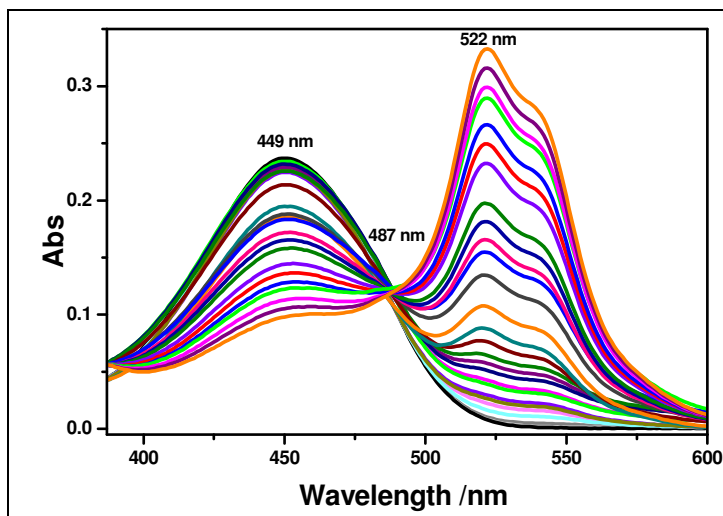


Figure 5.17: Absorption spectral changes of **17** upon addition of H₂SO₄

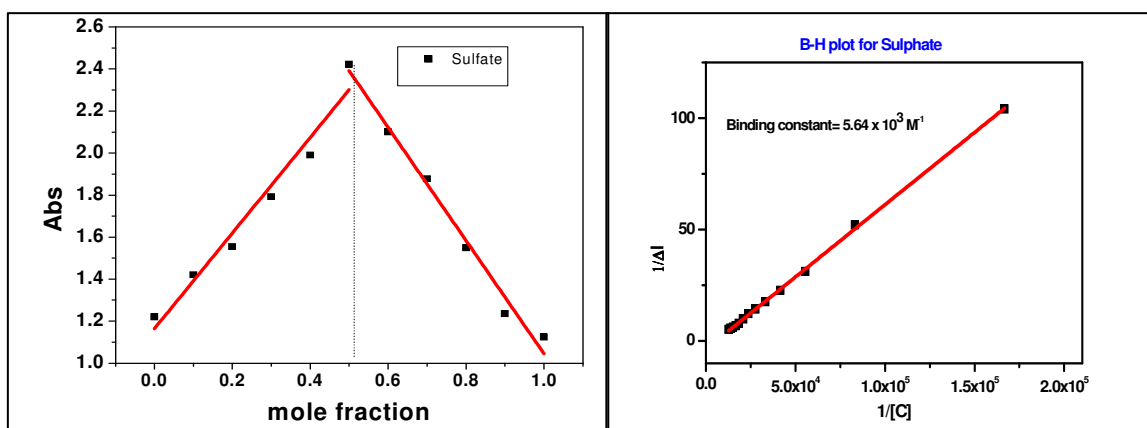


Figure 5.18: Job's plot for **17.SO₄⁻²** and Benesi-Hildebrand plot for **17.SO₄⁻²**

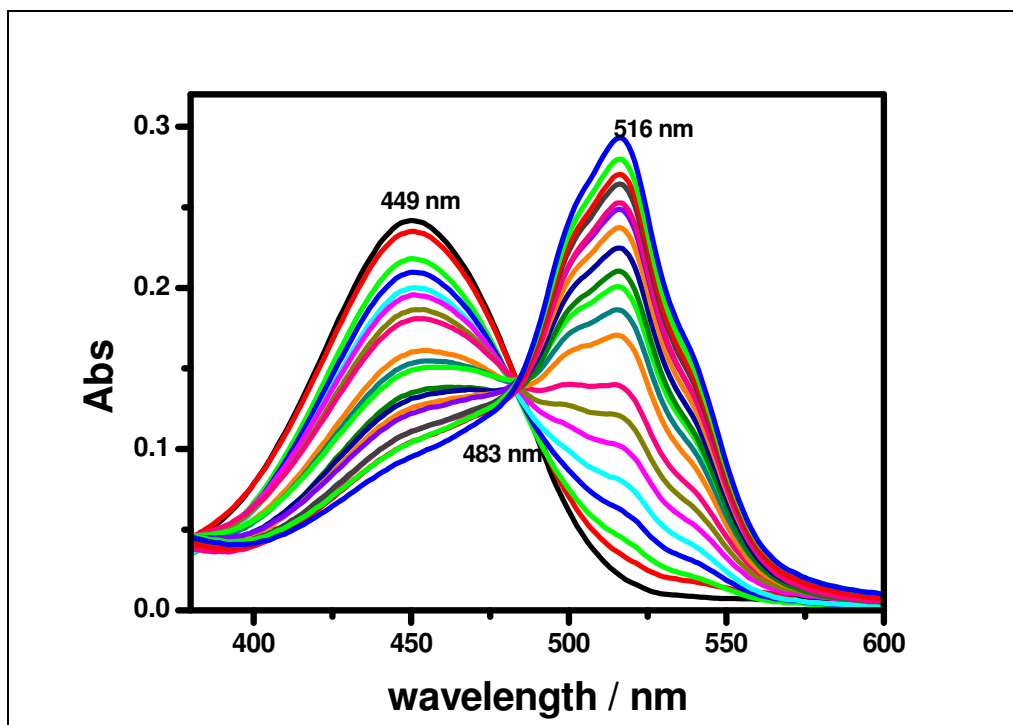


Figure 5.19: Absorption spectral changes of 17 upon addition of HNO₃

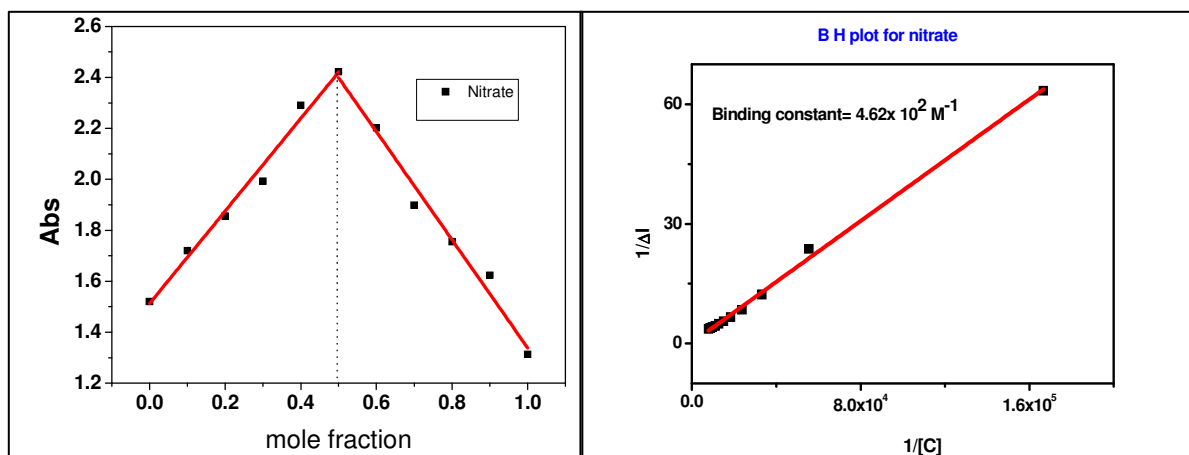
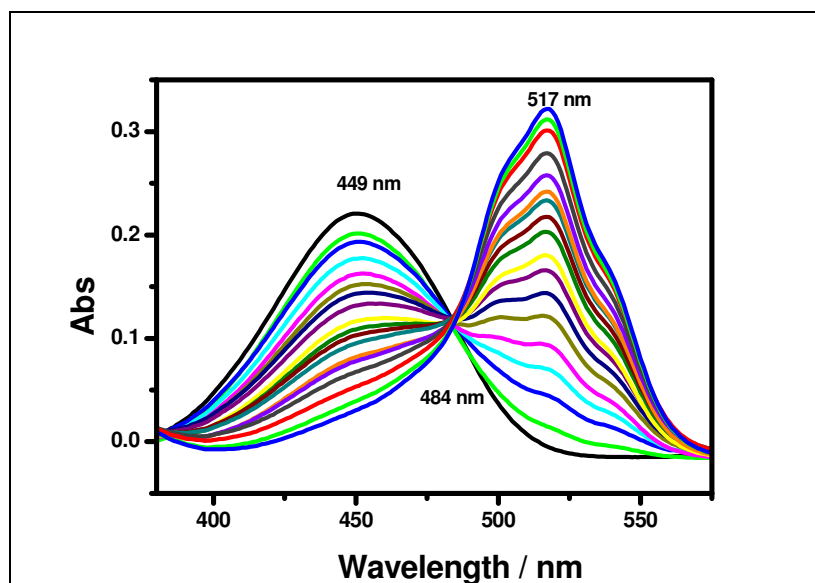
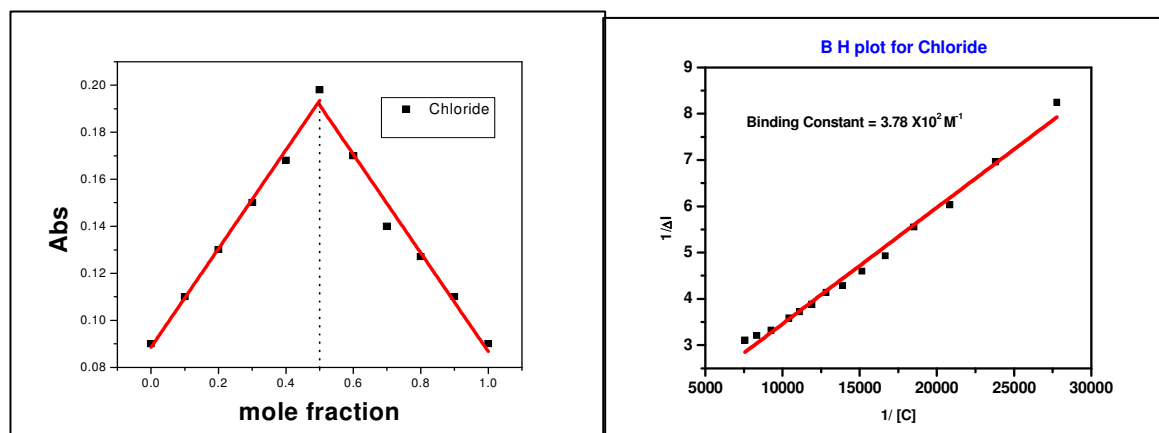
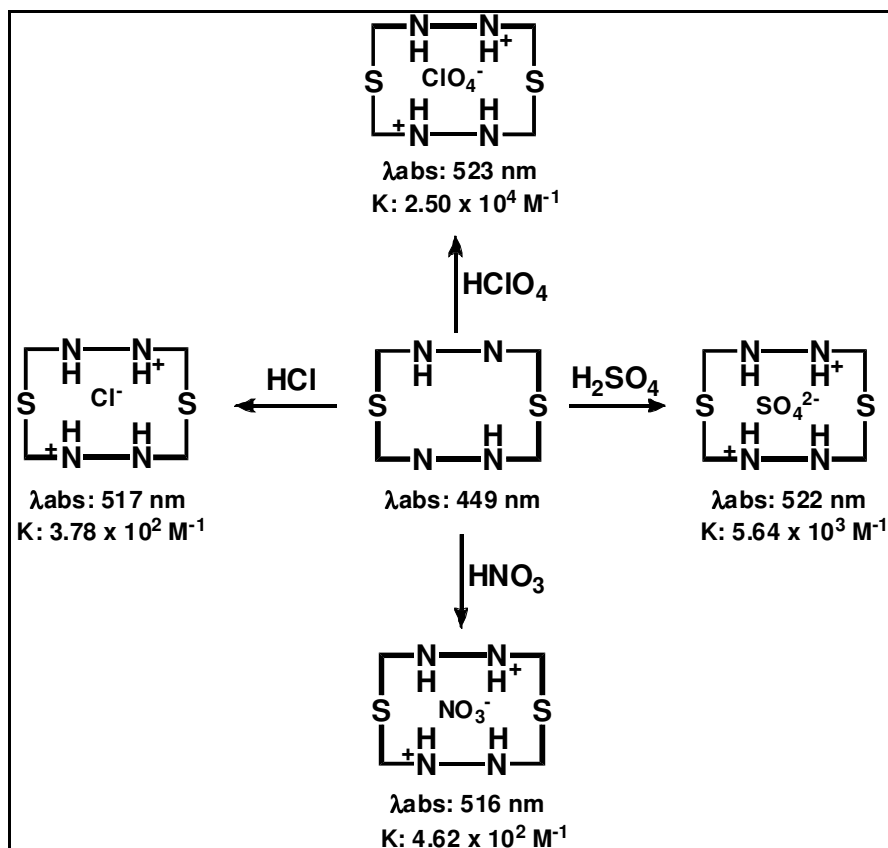


Figure 5.20: Job's plot for 17.NO₃⁻ and Benesi-Hildebrand plot for 17. NO₃⁻

Figure 5.21: Absorption spectral changes of **17** upon addition of HClFigure 5.22: Job's plot for **17.Cl⁻** and Benesi-Hildebrand plot for **17.Cl⁻**



Scheme 6: Binding of anions with **17**. The binding constants of absorption maxima and anion complexes are also shown.

5.7 Single crystal X-ray structural analysis of **17** with perchlorate anion

The final confirmation of anion binding has come from single crystal X-ray structure analysis, where, the calixpyrin crystallizes in the monoclinic system with P-1 space group and the structure is shown in Figure 5.23. As observed from the electronic spectral analysis, we expected 1:1 binding mode for anions with **17**, where all the four NHs of **17** supposed to bind with an anion. However, the crystal analysis shows that the unit cell contains two units of **17** with three ClO_4^- ions. The excess addition of the anions during crystallization affords both 1:1 and 1:2 binding mode in the solid state. All the intramolecular hydrogen bonds observed in freebase **17** (Figure 5.11a) are replaced by intermolecular hydrogen bonds with ClO_4^- anions, where one of the units binds with two ClO_4^- anions in 1:2 ratio (Figure 5.23 and 24). The pyrrole units (N1-H1 and N4-H4A) in one of the bis-pyrrolyl thiophene units is

pointing upward and binds with O7 and O6 of one of the ClO_4^- ion with the distances and angles of N1-H1...O7 and N4-N4A...O6 are 2.19, 2.06 Å and 163, 175° respectively.

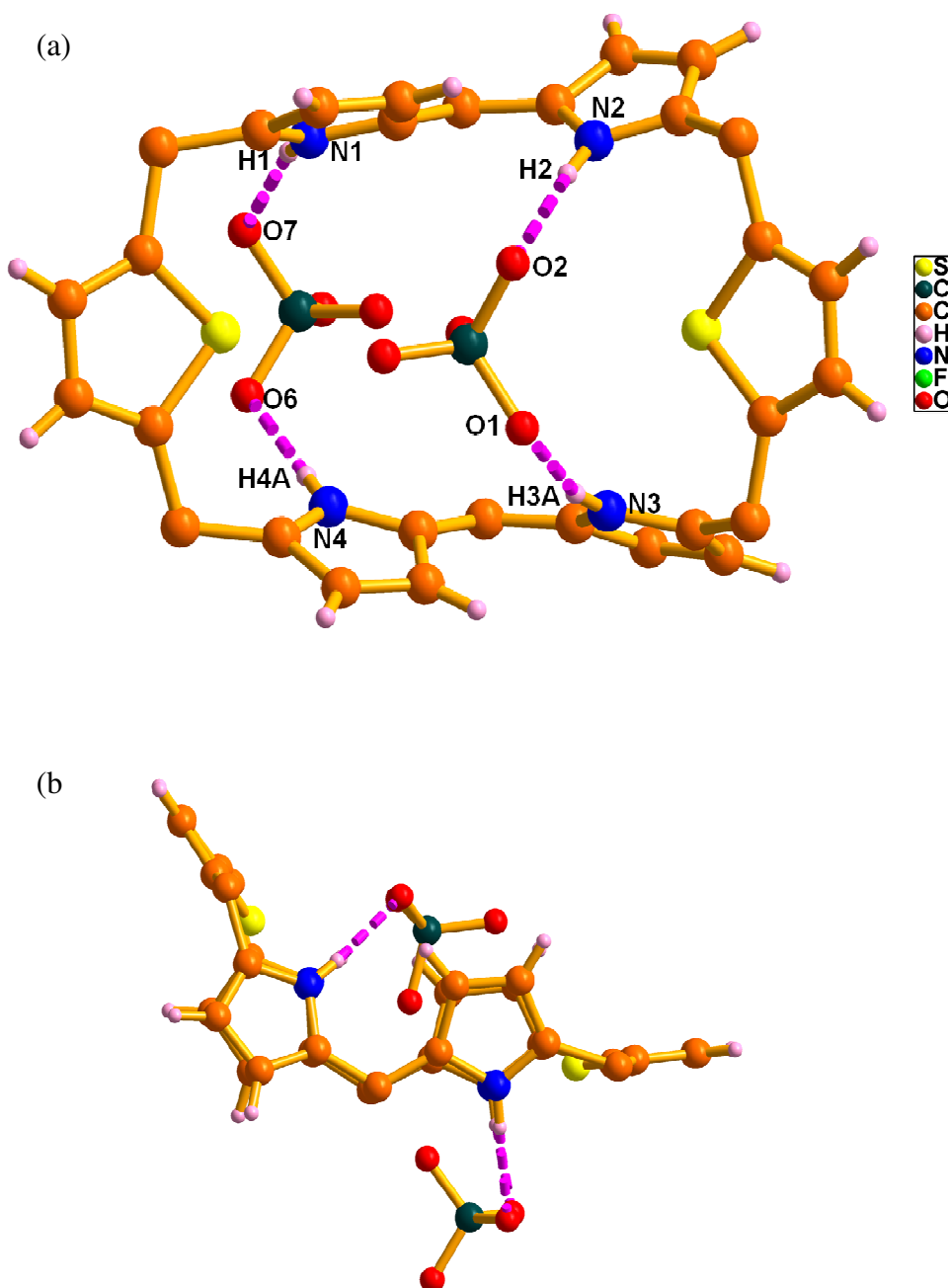


Figure 5.23: Single crystal X-ray structure of **17.2H⁺⁺** (with ClO_4^- anion). (a) Top view and (b) side view with 1:2 intermolecular hydrogen bonding interaction with ClO_4^- ions. The *meso*-aryl groups are omitted for clarity.

The pyrrole units (N2-H2 and N3-H3A) in the second bis-pyrrolyl thiophene unit is pointing downward and binds with second ClO_4^- ion (O2 and O1) with the distances and angles of N2-H2...O2 and N3-H3A...O1 are 2.14, 1.96 Å and 175, 166° respectively (Figure 5.24). On the other hand, the second **17** unit in the unit cell binds with only one ClO_4^- ion in 1:1 ratio (Figure 5.25), where one set of the pyrrole units binds with the third ClO_4^- ion with the distances and angles of N5-H5A...O14 and N7-H7A...O15 are 2.01, 2.11Å and 166, 174°, and leave the second bis-pyrrolyl thiophene unit empty.

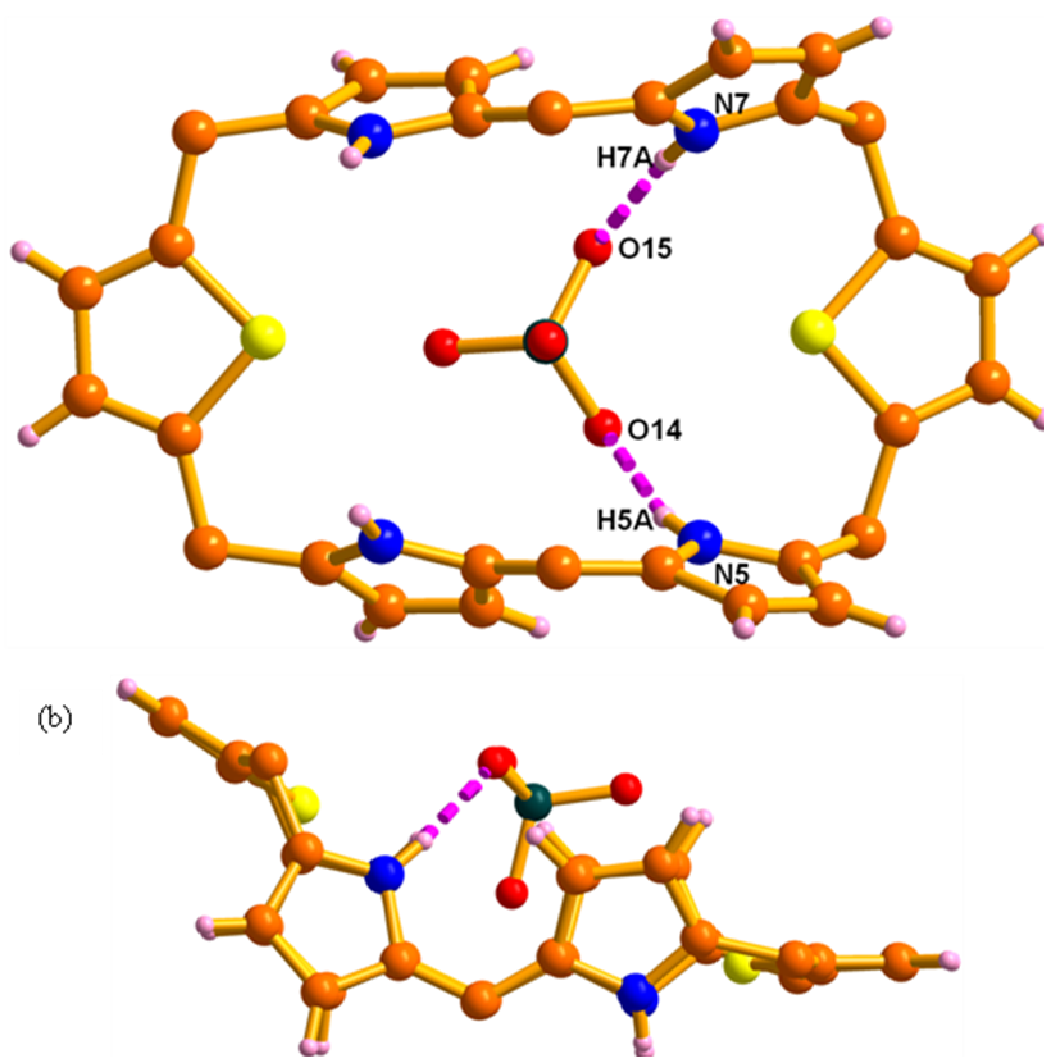


Figure 5.24: Single crystal X-ray structure of **17.2H⁺⁺** (with ClO_4^- anion). (a) Top view and (b) side view with 1:1 intermolecular hydrogen bonding interaction with ClO_4^- ions. The *meso*-aryl groups are omitted for clarity.

5.8 Conclusion

In summary, we have successfully synthesized the core-modified expanded calixphyrins by a simple synthetic strategy. The steric crowding by the *meso* phenyl substitution on the sp^3 carbons not only restricts the intramolecular rotations inducing AIEE effect but also forces the macrocycle to adopt a distorted chair like conformation in the solid state. Thus, it is possible to create strongly luminescent materials by increasing the number of sp^3 *meso* carbon bridges in the larger systems such as nona- and deca-calixphyrins. Furthermore, the anion binding properties reported here suggest that macrocycles such as **17** has stronger affinity for tetrahedral ions. However, in order to achieve specificity and selectivity, one has to modify the macrocycle cleft, the site of anion binding by appropriate peripheral substitutions. Studies in this direction are in progress in the laboratory.

5.9 Experimental section

5.9.1 Synthesis of Calix[2]thia[4]phyrin (**17**)

Pentafluorobenzaldehyde (0.089 mg, 0.46 mmol) was added to a solution of bis-pyrrolyl thiophene (**16**) (250 mg, 0.46 mmol) in dry dichloromethane (250 mL) in argon atmosphere. Followed by the addition of TFA (0.21 mL, 0.0028 mmol) and stirred for 2h in dark condition. Then 2,3-dichloro-5,6-dicyano-1,4-benzoquinone (DDQ) (0.312 mg, 1.37 mmol) was added and the reaction mixture was opened to air. The organic layer was then extracted with dichloromethane and washed with brine, then dried over anhydrous sodium sulphate. The solvent was removed using rotary evaporator. The crude product was repeatedly purified by basic alumina column chromatography. The compound was eluted with petroleum ether: dichloromethane (19:1) gave yellow solid in 20% yield.

mp: 233-235 °C (decomposition); ESI-MS: m/z calcd for $C_{90}H_{54}F_{10}N_4S_2+2H^+$: 1446.3787; Found: 1446.4105; elemental analysis: Calcd for $C_{90}H_{54}F_{10}N_4S_2$: C, 74.78; H, 3.77; N, 3.88.

Found: C, 74.74; H, 3.79; N 3.86; IR (CH₂Cl₂) v 3428, 2921, 2851, 1622, 1464, 1044; UV/Vis (CH₂Cl₂): λ_{\max} [nm] (ϵ [10⁴M⁻¹cm⁻¹]): 449 (1.39). ¹H NMR (400 MHz, CDCl₃, 298 K) δ ppm: 12.10 (brs, 2H), 7.14-7.12(m, 40H), 6.41 (s, 4H), 6.28 (d, ³J=4.3Hz, 4H), 5.86 (d, ³J=4.3Hz, 4H).

5.10.1 Crystallographic data of 17 and 17.2H⁺⁺ (with ClO₄ ion):

Parameters	17	17.2H ⁺⁺ (with ClO ₄ ion)
Solvent of crystallization	CHCl ₃ / Hexane	CH ₃ CN / Hexane
Empirical formula	C ₄₅ H ₂₇ F ₅ N ₂ S	C ₁₈₁ H ₁₁₃ Cl ₇ F ₂₀ N ₈ O ₁₉ S ₄
M_w	722.75	3460.18
T [K]	100	100
λ [Å]	0.71073	0.71073
Crystal system	triclinic	monoclinic
Space group	P-1	Pc
a [Å]	11.812 Å	17.6848 Å,
b [Å]	12.254 Å	21.470 Å,
c [Å]	16.871 Å	20.6857 Å
α [°]	86.203°	90.000(5)
β [°]	72.152°	99.421(5)
γ [°]	63.842°	90.000(5)
V [Å ³]	2079.6	7748.1
Z, ρ_{calcd} [Mg m ⁻³]	1.154	1.483
μ (MoK α) [mm ⁻¹]	0.131	0.076
$F(000)$	744	3540
Crystal size [mm]	0.10 × 0.09 × 0.09	0.11 × 0.08 × 0.07
θ range for data collection [°]	2.65 to 25.57	1.91 to 25.36
Reflections collected	26629	68396
Refinement method	Full-matrix least-squares on F^2	Full-matrix least-squares on F^2
Data / restraints / parameters	7676 / 0 / 478	25895 / 20 / 2152
Goodness-of-fit on F^2	0.945	1.031
Final R indices [$I > 2\sigma(I)$]	R1 = 0.0692 { $I > 2\sigma(I)$ }	R1 = 0.0814 { $I > 2\sigma(I)$ }
R indices (all data)	R _w = 0.1815	R _w = 0.1112

-
- [1] Smith, K. M. *Porphyryns and Metalloporphyryns*, Elsevier, Amsterdam, 1975.
- [2] Buchler, J. W. *The Porphyrins*, D. Dolphin (Ed.), Academic, New York, Vol. 1, Part A, Structure and Synthesis, 1978.
- [3] Mashiko, T. S. *Comprehensive Coordination Chemistry*, Geoffery and Wilkinson (Eds.), Vo1.2, Pergamon Press, Oxford, 1987.
- [4] Smith, E. L.; Hill, R. L.; Lehman, I. R.; Lef Kowitz, R. J.; Handler, P.; White, A.; *Principles of Biochemistry- General Aspects*, McGraw-Hill Inc., Singapore 1983.
- [5] Stępień, M.; Latos-Grażyński, L. *Aromaticity and Tautomerism in porphyrins and porphyrinoids, Aromaticity in heterocyclic compounds*, Krygowski, T.M.; Cyranski, M. K. (Eds.), Springer, 2009.
- [6] Kadish, K. M.; Smith, K. M.; Guillard, R. *The porphyrin handbook*, Vol. 1-3, Academic press, San Diego, CA, 2000.
- [7] Chandrashekar, T. K.; Venkatraman, V. *Acc. Chem. Res.* **2003**, *36*, 676–691.
- [8] Sessler, J. L.; Weghorn, S. J. *Expanded, Contracted & Isomeric Porphyrins; Tetrahedron Organic Chemistry Series*, Vol. 15, Pergamon, New York, 1995.
- [9] Jasat, A.; Dolphin, D. *Chem. Rev.* **1997**, *97*, 2267.
- [10] Sessler, J. L.; Burrell, A. K. *Top. Curr. Chem.* **1992**, *161*, 177-273
- [11] Sessler, J. L.; Seidel, D. *Angew. Chem. Int. Ed.* **2003**, *42*, 5134-5174.
- [12] Bonnett, R. *Chem. Soc. Rev.* **1995**, *24*, 19–33.
- [13] Winter, M. B.; Klemm, P. J.; Phillips-Piro, C. M.; Raymond, K. N.; Marletta, M. A. *Inorg. Chem.* **2013**, *52*, 2277-2292.
- [14] Senge, M. O.; Fazekas, M.; Notaras, E. G. A.; Blau, W. J.; Zawadzka, M.; Locos, O. B.; Mhuircheartaigh, M. N. *Adv. mater.* **2007**, *19*, 2737-2748.
- [15] Shin, J.-Y.; Kim, K.S.; Yoon, M.-C.; Lim, J. M.; Yoon, Z. S.; Osuka, A.; Kim, D. *Chem. Soc. Rev.* **2010**, *39*, 2751-2773.
- [16] Marder, S. R. *Chem. Commun.*, **2006**, 131–134.
- [17] Kim, K. S.; Lim, J. M.; Osuka, A.; Kim, D. *J. Photochem. Photobiol. C.* **2008**, *9*, 13–28.
- [18] Rath, H.; Sankar, J.; Prabhuraja, V.; Chandrashekar, T. K.; Nag, A.; Goswami, D. *J. Am. Chem. Soc.* **2005**, *127*, 11608-11611.

- [19] Srinivasan, A.; Reddy, M. V. R.; Narayanan, S. J.; Sridevi, B.; Pushpan, K. S.; Ravikumar, M.; Chandrashekar, T. K. *Angew. Chem. Int. Ed.* **1997**, *36*, 2598-2602.
- [20] Sridevi, B.; Narayanan, S. J.; Rao, R.; Chandrashekar, T. K.; Englich, U.; Ruhlandt-Senge, K. *Inorg. Chem.* **2000**, *39*, 3669-3675.
- [21] Bauer, V. J.; Clive, L. J.; Dolphin, D.; Paine, J. B.; Harris, F. L.; King, M. M.; Loder, J.; Wang, S. C.; Woodward, R. B. *J. Am. Chem. Soc.* **1983**, *105*, 6429-6436.
- [22] Vogel, E.; Bröring, M.; Fink, J.; Rosen, D.; Schmickler, H.; Lex, J.; Chan, K. W. K.; Wu, Y. D.; Plattner, D. A.; Nendel, M.; Houk, K. N. *Angew. Chem. Int. Ed.* **1995**, *34*, 2511-2514.
- [23] Neves, M. G. P. M. S.; Martins, R. M.; Tomé, A. C.; Silvestre, A. J. D.; Silva, A. M. S.; Félix, V.; Cavaleiro, J. A. S.; Drew, M. G. B. *Chem. Commun.* **1999**, 385-386.
- [24] Narayanan, S. J.; Sridevi, B.; Chandrashekar, T. K.; Vij, A.; Roy, R. *J. Am. Chem. Soc.* **1999**, *121*, 9053-9068.
- [25] Sessler, J. L.; Seidel, D.; Lynch, V. *J. Am. Chem. Soc.* **1999**, *121*, 11257-11258.
- [26] Kamimura, Y.; Shimizu, S.; Osuka, A. *Chem. Eur. J.* **2007**, *13*, 1620-1628.
- [27] Sessler, J. L.; Weghorn, S. J.; Lynch, V.; Johnson, M. R. *Angew. Chem. Int. Ed.* **1994**, *33*, 1509-1512.
- [28] Setsune, J.; Katakami, Y.; Iizuna, N. *J. Am. Chem. Soc.* **1999**, *121*, 8957-8958.
- [29] Misra, R.; Chandrashekar, T. K. *Acc. Chem. Res.* **2008**, *41*, 265-279.
- [30] Chmielewski, P. J.; Latos-Grażyński, L.; Rachlewicz, K. *Chem. Eur. J.* **1995**, *1*, 68-75.
- [31] Park, J. K.; Yoon, Z. S.; Yoon, M.-C.; Kim, K. S.; Mori, S.; Shin, J.-Y.; Osuka, A.; Kim, D. *J. Am. Chem. Soc.* **2008**, *130*, 1824-1829.
- [32] Anand, V. G.; Pushpan, S. K.; Venkatraman, S.; Dey, A.; Chandrashekar, T. K.; Joshi, B. S.; Roy, R.; Teng, W.; Senge, K. R. *J. Am. Chem. Soc.* **2001**, *123*, 8620-8621.
- [33] Vogel, E.; Pohl, M.; Schmickler, H.; Lex, J. *Angew. Chem. Int. Ed.* **1991**, *30*, 1693-1697.
- [34] Reddy, J. S.; Anand, V. G. *J. Am. Chem. Soc.* **2008**, *130*, 3718-3719.
- [35] Heilbronner, E. *Tetrahedron. Lett.* **1964**, *29*, 1923-1926.

- [36] Ajami, D.; Oeckler, O.; Simon, A.; Herges, R. *Nature*, **2003**, 819-821.
- [37] Stępień, M.; Latos-Grażyński, L.; Sprutta, N.; Chwalisz, P.; Szterenber, L. *Angew. Chem. Int. Ed.* **2007**, *46*, 7869-7873.
- [38] Yoon, Z. S.; Osuka, A.; Kim, D. *Nat. Chem.* **2009**, *1*, 113-122.
- [39] Sankar, J.; Mori, S.; Saito, S.; Rath, H.; Suzuki, M.; Inokuma, Y.; Shinokubo, H.; Kim, K. S.; Yoon, Z. S.; Shin, J.-Y.; Lim, J. M.; Matsuzaki, Y.; Matsushita, O.; Muranaka, A.; Kobayashi, N.; Kim, D.; Osuka, A. *J. Am. Chem. Soc.* **2008**, *130*, 13568-13579.
- [40] Saito, S.; Shin, J.-Y.; Lim, J. M.; Kim, K. S.; Kim, D.; Osuka, A. *Angew. Chem. Int. Ed.* **2008**, *47*, 9657-9691.
- [41] Shin, J.-Y.; Kim, K. S.; Yoon, M.-C.; Lim, J. M.; Yoon, Z. S.; Osuka, A.; Kim, D. *Chem. Soc. Rev.* **2010**, *39*, 2751-2789.
- [42] Lim, J. M.; Yoon, Z. S.; Shin, J.-Y.; Kim, K. S.; Yoon, M.-C.; Kim, D. *Chem. Commun.* **2009**, 261-282.
- [43] Boyd, R. W. *Nonlinear optics*, Third edition, Academic Press.
- [44] Williams, D. J. *Angew. Chem. Int. Ed.* **1984**, *23*, 690-703.
- [45] Misra, R.; Kumar, R.; Chandrashekar, T. K.; Suresh, C. H.; Nag, A.; Goswami, D. *J. Am. Chem. Soc.* **2006**, *128*, 16083-16098.
- [46] Misra, R.; Kumar, R.; Chandrashekar, T. K.; Nag, A.; Goswami, D. *Org. Lett.* **2006**, *8*, 629-631.
- [47] Shetti, V. S.; Kee, S.-Y.; Lee, C.-H. *Chem. Asian. J.* **2013**, 1-6.
- [48] Kumar, R.; Misra, R.; Chandrashekar, T. K.; Suresh, E. *Chem. Commun.* **2007**, 43-45.
- [49] Furuta, H.; Ishizuka, T.; Osuka, A.; Ogawa, T. *J. Am. Chem. Soc.* **2000**, *122*, 5748-5757.
- [50] Shin, J. Y.; Furuta, H.; Osuka, A. *Angew. Chem. Int. Ed.* **2001**, *40*, 619-621.
- [51] Panda, P. K.; Kang, Y.-J.; Lee, C.-H. *Angew. Chem. Int. Ed.* **2005**, *44*, 4053-4055.
- [52] Cho, D.-G.; Plitt, P.; Kim, S. K.; Lynch, V.; Hong, S.-J.; Lee, C.-H.; Sessler, J. L. *J. Am. Chem. Soc.* **2008**, *130*, 10502-10503.
- [53] Chandrashekar, T. K.; Prabhuraja, V.; Gokulnath, S.; Sabarinathan, R.; Srinivasan, A. *Chem. Commun.* **2010**, *46*, 5915-5921.

- [54] Ryan, A.; Gehrold, A.; Perusitti, R.; Pinteá, M.; Fazekas, M.; Locos, O. B.; Blaikie, F.; Senge, M. O. *Eur. J. Org. Chem.* **2011**, 5817–5844.
- [55] Song, J.; Jang, S. Y.; Yamaguchi, S.; Sankar, J.; Hiroto, S.; Aratani, N.; Shin, J. Y.; Easwaramoorthi, S.; Kim, K. S.; Kim, D.; Shinokubo, H.; Osuka, A. *Angew. Chem. Int. Ed.* **2008**, *47*, 6004–6007.
- [56] Mitsushige, Y.; Yamaguchi, S.; Lee, B. S.; Sung, Y. M.; Kuhri, S.; Schierl, C. A.; Guldi, D. M.; Kim, D.; Matsuo, Y. *J. Am. Chem. Soc.* **2012**, *134*, 16540–1654.
- [57] Anand, V. G.; Saito, S.; Shimizu, S.; Osuka, A. *Angew. Chem. Int. Ed.* **2005**, *44*, 7244–7248.
- [58] Suzuki, M.; Osuka, A. *J. Am. Chem. Soc.* **2007**, *129*, 464–465.
- [59] Yoon, M. C.; Cho, S.; Suzuki, M.; Osuka, A.; Kim, D. *J. Am. Chem. Soc.* **2009**, *131*, 7360–7367.
- [60] Sessler, J. L.; Zimmerman, R. S.; Bucher, C.; Král, V.; Andrioletti, B. *Pure. Appl. Chem.* **2001**, *73*, 1041–1057.
- [61] Král, V.; Sessler, J. L.; Zimmerman, R. S.; Seidel, D.; Lynch, V.; Andrioletti, B. *Angew. Chem. Int. Ed.* **2000**, *39*, 1055–1058.
- [62] Sessler, J. L.; Camiolo, S.; Gale, P. A. *Coord. Chem. Rev.* **2003**, *240*, 7–55.
- [63] Bucher, C.; Zimmerman, R. S.; Lynch, V.; Král, V.; Sessler, J. L. *J. Am. Chem. Soc.* **2001**, *123*, 2099–2100.
- [64] Stępień, M.; Latos-Grażyński, L.; Szterenber, L.; Panek, J.; Latajka, Z. *J. Am. Chem. Soc.* **2004**, *126*, 4566–4580.
- [65] Hung, C.-H.; Chang, G.-F.; Kumar, A.; Lin, G.-F.; Luo, L.-Y.; Chinga, E. W.-G. D. *Chem. Commun.* **2008**, 978–980.
- [66] Gupta, I.; Fröhlich, R.; Ravikanth, M. *Chem. Commun.* **2006**, 3726–3729.
- [67] Bucher, L.; Zimmerman, R. S.; Lynch, V.; Sessler, J. L. *Chem. Commun.* **2003**, 1646–1647.
- [68] Matano, Y.; Miyajima, T.; Nakabuchi, T.; Imahori, H.; Ochi, Y.; Sakaki, S. *J. Am. Chem. Soc.* **2006**, *128*, 11760–11761.
- [69] Matano, Y.; Miyajima, T.; Ochi, N.; Nakao, Y.; Sakaki, S.; Imahori, H. *J. Org. Chem.* **2008**, *73*, 5139–5142.
- [70] Beer, P. D.; Gale, P. A. *Angew. Chem. Int. Ed.* **2001**, *40*, 486–516.

- [71] Finnigan, E. M.; Giordani, S.; Senge, M. O.; McCabe, T. J. *Phys. Chem. A* **2010**, *114*, 2464–2470.
- [72] Jha, S. C.; Lorch, M.; Lewis, R. A.; Archibald, S. J.; Boyle, R. W. *Org. Biomol. Chem.* **2007**, *5*, 1970–1974.
- [73] Zeng, Q.; Li, Z.; Dong, Y.; Di, C.; Qin, A.; Hong, Y.; Ji, L.; Zhu, Z.; Jim, C. K. W.; Yu, G.; Li, Q.; Li, Z.; Liu, Y.; Qin, J.; Tang, B. Z. *Chem. Commun.* **2007**, 70–72.
- [74] Hong, Y.; Lama, J. W. Y.; Tang, B. Z. *Chem. Commun.* **2009**, 4332–4353.
- [75] Yuan, W. Z.; Lu, P.; Chen, S.; Lam, J. W. Y.; Wang, Z.; Liu, Y.; Kwok, H. S.; Ma, Y.; Tang, B. Z. *Adv. Mater.* **2010**, *22*, 2159–2163.
- [76] Salini, P. S.; Thomas, A. P.; Sabarinathan, R.; Ramakrishnan, S.; Sreedevi, K. C. G.; Reddy, M. L. P.; Srinivasan, A. *Chem. Eur. J.* **2011**, *17*, 6598–6601.
- [77] Furniss, B. S. Vogel's text book of practical organic chemistry, Ed: ELBS and Longmann, 4th edition, 1978.
- [78] Riddick, J. A.; Bunger, W. B. Organic solvents in technique of organic chemistry, 3rd edition, Wiley. New York, 1970.
- [79] Becke, A. D. *J. Chem. Phys.* **1993**, *98*, 1372–1376.
- [80] Lee, C.; Yang, W.; Parr, R. G. *Phys. Rev. B.* **1988**, *37*, 785–789.
- [81] Krygowski, T. M.; Cyranski, M. K. *Chem. Rev.* **2001**, *101*, 1385–1390.
- [82] Schleyer, P. V. R.; Maerker, C.; Dransfeld, A.; Jiao, H.; Hommes, N. J. R. *J. Am. Chem. Soc.* **1996**, *118*, 6317–6320.
- [83] Sheldrick, G. M. SHELXS-93f, Universitat Gottingen, 1993.
- [84] Frey, J.; Bond, A. D.; Holmes, A. B. *Chem. Commun.* **2002**, 2424–2429.
- [85] Srinivasan, A.; Pushpan, S. K.; Kumar, R.; Mahajan, S.; Chandrashekar, T. K.; Ramamurthy, P. *J. Chem. Soc. Perkin Trans.* **1999**, *2*, 961–968.
- [86] Sridevi, B.; Narayanan, S. J.; Srinivasan, A.; Reddy, M. V.; Chandrashekar, T. K. *J. Porphy. Phthalocyanines.* **1998**, *02*, 69–78.
- [87] Sankar, J.; Rath, H.; Prabhuraja, V.; Chandrashekar, T. K.; Vittal, J. J. *J. Org. Chem.* **2004**, *69*, 5135–5138.
- [88] Orlewska, C.; Maes, W.; Toppet, S.; Dehaen, W. *Tetrahedron Lett.* **2005**, *46*, 6067–6070.
- [89] Dehaen, W. *Top. Heterocycl. Chem.* **2010**, *24*, 75–102.
- [90] Suzuki, M.; Osuka, A. *Chem. Eur. J.* **2003**, *13*, 196–202.

- [91] Saito, S.; Osuka, A. *Angew. Chem. Int. Ed.* **2011**, *50*, 4342–4373.
- [92] Stępień, M.; Sprutta, N.; Latos-Grażyński, L. *Angew. Chem. Int. Ed.* **2011**, *50*, 4288–4340.
- [93] Mori, H.; Lim, J. M.; Kim, D.; Osuka, A. *Angew. Chem. Int. Ed.* **2013**, *52*, 12997–13001.
- [94] Ulman, A.; Manassen, J. *J. Am. Chem. Soc.* **1975**, *97*, 6540 – 6544.
- [95] Neves, M. G. P. M. S.; Martins R. M.; Tomé, A. C.; Silvestre, A. J. D.; Silva, A. M. S.; Félix, V.; Cavaleiro, J. A. S.; Drew, M. G. B. *Chem. Commun.* **1999**, 385 – 386.
- [96] Berera, R.; Grondelle, R. V.; Kennis, J. T. M. *Photosynth. Res.* **2009**, *101*, 105-118.
- [97] Schleyer, P. v. R.; Maerker, C.; Dransfeld, A.; Jiao, N.; Hommes, J. R. E. *J. Am. Chem. Soc.* **1996**, *118*, 6317-6318.
- [98] Yoon, M.-C.; Misra, R.; Yoon, Z. S.; Kim, K. S.; Lim, J. M.; Chandrashekar, T. K.; Kim, D. *J. Phys. Chem. B.* **2008**, *112*, 6900-6911.
- [99] Karthik, G.; Sneha, M.; Raja, V. P.; Lim, J. M.; Kim, D.; Srinivasan, A; Chandrashekar, T. K. *Chem. Eur. J.* **2013**, *19*, 1886–1890.
- [100] Kadish, K. M.; Smith, K. M.; Guillard, R. The porphyrin handbook, Electron Transfer, Vol. 6, Academic press, San Diego, CA, 2000.
- [101] Toganoh, M.; Kimura, T.; Uno, H.; Furuta, H. *Angew. Chem. Int. Ed.* **2008**, *47*, 8913–8916.
- [102] Furuta, H.; Ishizuka, T.; Osuka, A.; Ogawa, T. *J. Am. Chem. Soc.* **1999**, *121*, 2945–2946.
- [103] Song, J.; Aratani, N.; Heo, J. H.; Kim, D.; Shinokubo, H.; Osuka, A. *J. Am. Chem. Soc.* **2010**, *132*, 11868–11869.
- [104] Pawlicki, M.; Morisue, M.; Davis, N. K. S.; McLean, D. G.; Haley, J. E.; Beuerman, E.; Drobizhev, M.; Rebane, A.; Thompson, A. L.; Pascu, S. I.; Accorsi, G.; Armaroli, N.; Anderson, H. L. *Chem. Sci.* **2012**, *3*, 1541-1555.
- [105] Castro, C.; Karney, W. L. *J. Phy. Org. Chem.* **2012**, *25*, 612–619.
- [106] Tokuji, S.; Shin, J.-Y.; Kim, K. S.; Lim, J. M.; Youfu, K.; Saito, S.; Kim, D.; Osuka, A. *J. Am. Chem. Soc.* **2009**, *131*, 7240–7241.
- [107] Lim, J.M.; Shin, J.-Y.; Tanaka, Y.; Saito, S.; Osuka, A.; Kim, D. *J. Am. Chem. Soc.* **2010**, *132*, 3105-3114.

- [108] Zhang, Z.; Lim, J. M.; Ishida, M.; Roznyatovskiy, V.; Lynch, V.; Gong, H. Y.; Yang, X.; Kim, D.; Sessler, J. L. *J. Am. Chem. Soc.* **2012**, *134*, 4076-4081.
- [109] Stępień, M.; Sprutta, N.; Latos-Grażyński, L. *Angew. Chem. Int. Ed.* **2011**, *50*, 4288-4314.
- [110] Gouterman, M. *J. Mol. Spectrosc.* **1961**, *6*, 138-162.
- [111] Wallenborn, E. U.; Haldimann, R. F.; Klarner F.-G. Diederich, F. *Chem. Eur. J.* **1998**, *4*, 2258-2271.
- [112] Tanaka, Y.; Saito, S.; Mori, S.; Aratani, N.; Shinokubo, H.; Shibata, N.; Higuchi, Y.; Yoon, Z. S.; Kim, K. S.; Noh, S. B.; Park, J. K.; Kim, D.; Osuka, A. *Angew. Chem. Int. Ed.* **2008**, *47*, 681-698.
- [113] Park, J. K.; Yoon, Z. S.; Yoon, M.; Kim, K. S.; Mori, S.; Shin, J. Y.; Osuka, A.; Kim, D. *J. Am. Chem. Soc.* **2008**, *130*, 1824-1825.
- [114] Kim, O.; Lee, K.; Woo, H. Y.; Kim, K.; He, G. S.; Swiatkiewicz, J.; Prasad, P. N. *Chem. Mat.* **2000**, *12*, 284-286.
- [115] Keinan, S.; Therien, M. J.; Beratan, D. N.; Yang, W. *J. Phy. Chem. A.* **2008**, *112*, 12203-12207.
- [116] Anand, V. G.; Pushpan, S. K.; Venkatraman, S.; Narayanan, S. J.; Dey, A.; Chandrashekar, T. K.; Roy, R.; Joshi, B. S.; Deepa, S.; Sastry, G. N. *J. Org. Chem.* **2002**, *67*, 6309-6319.
- [117] Mori, H.; Sung, Y. M.; Lee, B. S.; Kim, D.; Osuka, A. *Angew. Chem. Int. Ed.* **2012**, *51*, 12459-12463.
- [118] Alonso, M.; Geerlings, P.; De Proft, F. *Chem. Eur. J.* **2013**, *19*, 1617-1628.
- [119] Anand, V. G.; Pushpan, S. K.; Srinivasan, A.; Narayanan, S. J.; Sridevi, B.; Chandrashekar, T. K.; Roy, R.; Joshi, B. S. *Org. Lett.* **2000**, *2*, 3829-3832.
- [120] Matano, Y.; Fujita, M.; Miyajima, T.; Imahori, H. *Organometallics.* **2009**, *28*, 6213-6217.
- [121] Ochi, N.; Nakao, Y.; Sato, H.; Matano, Y.; Imahori, H.; Sakaki, S. *J. Am. Chem. Soc.* **2009**, *131*, 10955-10963.
- [122] Bucher, C.; Seidel, D.; Lynch, V.; Kral, V.; Sessler, J. L. *J. Org. Lett.* **2000**, *2*, 3103-3106.
- [123] Orlewska, C.; Maes, W.; Toppet, S.; Dehaen, W. *Tetrahedron Lett.* **2005**, *46*, 6067-6070.

-
- [124] Furuta, H.; Ishizuka, T.; Osuka, A.; Uwatoko, Y.; Ishikawa, Y. *Angew. Chem. Int. Ed.* **2001**, *40*, 2323–2325.
- [125] Gokulnath, S.; Chandrashekar, T. K. *Org. Lett.* **2008**, *10*, 637–640.
- [126] Salini, P. S.; Holaday, M. G. D.; Reddy, M. L. P.; Suresh, C. H.; Srinivasan, A. *Chem. Commun.* **2013**, *49*, 2213–2215.
- [127] Skonieczny, J.; Latos-Grażyński, L.; Szterenber, L. *Org. biomol. Chem.* **2012**, *10*, 3463–3471.
- [128] Finnigan, E. M.; Giordani, S.; Senge, M. O.; McCabe, T. *J. Phys. Chem. A* **2010**, *114*, 2464–2470.
- [129] Benesi, H. A.; Hildebrand, J. H. *J. Am. Chem. Soc.* **1949**, *71*, 2703–2705.
- [130] Kumar, M. R.; Chandrashekar, T. K. *J. Incl. Phenom. Macro. Chem.* **1999**, *35*, 553–582.